HYBRID MEMS FOR TRANSIENT MICROSYSTEMS AND CHIP-SCALE GAS SENSORS

A Dissertation

Presented to the Faculty of the Graduate School

of Cornell University

in Partial Fulfillment of the Requirements for the Degree of

Doctor of Philosophy

by

Ved Vishwas Gund

August 2017

HYBRID MEMS FOR TRANSIENT MICROSYSTEMS AND CHIP-SCALE GAS SENSORS

Ved Vishwas Gund, Ph.D.

Cornell University 2017

This dissertation presents research performed in two broad areas of Micro Electro Mechanical Systems (MEMS): transient vaporizable electronics and chip-scale gas sensors. Transient polymer-based vaporizable electronics and MEMS for controlled disappearing of microsystems are presented in the first half of the dissertation. Components for gas sensing with ion-mobility spectrometry are presented in the second half.

For vaporizable polymer-based electronics, the key MEMS component is a graphene-on-silicon nitride single-shot valve presented here. The valve is triggered thermo-mechanically with 142 mW input power in 15 milliseconds using 2.2 mJ of energy - a 100× reduction from previous reports in literature. It is used for exposing highly reactive pristine alkali metals such as rubidium and cesium to ambient oxygen for exothermic vaporization of the polymer substrate. An architecture for integrating the alkali metals with sodium biflouride ($NaHF_2$) etch sources for etching electronics on oxide substrates is also presented. In addition to demonstrating a transient system, the graphene-on-nitride membrane is also used as a thermo-gravimetry platform for multi-mode characterization of picograms of polymer. The atomically thin graphene sheet serves as a resistive heater for ramping temperature on the nitride membrane. During this, the resistance variation of the graphene is used for electrical characterization of the polymer-graphene surface interactions. The polymer vaporization as a result

of temperature ramping on the nitride is sensed mechanically as a resonance frequency shift of the membrane. Finally, a novel architecture for producing controlled transience of silicon-based electronics is presented. Polypropylene carbonate (PPC) is used as a connective layer to hold a silicon substrate intact. PPC can be vaporized to selectively remove parts of the substrate, on demand, using localized integrated thin-film heaters.

The key component of the ion-mobility based gas sensors is the multi-electrode ion-detector array developed in this thesis. Laser-micromachining is used for direct maskless patterning of silicon wafers, to define the detector array topology. The sensor uses a lateral electric field to separate gases on different electrode-islands of the array, based on their ion-mobility and a transimpedance amplifier is used to sense the current generated due to the ions. High-aspect ratio channels are realized using vertical stacking of patterned silicon structures, which are used for obtaining distinct signatures of different gas mixtures for pattern-based recognition. To produce flow of ions of the gas to be analyzed, a thin-film piezoelectric bimorph cantilever of length 1000 μm is fabricated and used as an ion-pump. The micro-fabricated lead zirconate titanate (PZT) on silicon dioxide beams are able to produce flow rates up to 186 $\mu L/min$ min and flow velocity as high as 7 cm/sec. A sense cantilever of length 800 μm is co-fabricated with the drive pump to sense lateral air-motion and provide feedback for turbulent air-flow in the device. To produce the ion species from the neutral gas molecules for detection with the IMS array, a pyroelectric lithium niobate ($LiNbO_3$) ionizer is developed. The ionizer uses an integrated resistive heater for producing an average ion current of 9.36 pA during the stochastic ionization process and peak ion current as high as 44.8 nA. All system components operate at < 5V, for compatibility with low-voltage CMOS platform requirements. This

is crucial for integration in portable electronics such as laptops and cell-phones the target for these sensors.

BIOGRAPHICAL SKETCH

Ved Gund was born on October 2nd, 1989 in Nagpur, India to Vaishali and Vishwas Gund. He spent his early life in Pune, India and attended Loyola High School. He started college at Stanford University in California in 2007, where he majored in Electrical Engineering. At Stanford, he conducted research in the Very Low Frequency (VLF) lab working on simulations and circuit design for a micro-satellite particle detector. He also spent a summer at Ecole Polytechnique Federale de Lausanne (EPFL) in Switzerland working in the PARSA lab on computer architecture. He graduated from Stanford in 2011 with a Bachelors degree and a co-terminal Masters degree in Electrical Engineering. In August 2011, he began his PhD at Cornell University in the SonicMEMS laboratory under the supervision of Prof. Amit Lal. His doctoral research has focused on self-destructing vaporizable electronics, microsystems and sensors for defense and environmental applications and components for chip-scale gas sensing using ion-mobility spectrometry.

To Aai

ACKNOWLEDGEMENTS

I would like to express my profound gratitude to my academic advisor, Prof. Amit Lal, for his support and guidance throughout my time at Cornell. He has been an incredible motivator for me. His unparalleled hunger and drive to keep pushing boundaries, think and go beyond the ordinary is something I strive to continue learning from him beyond my time in graduate school. He is ever the optimist in terms of what can be achieved but also extremely rigorous in his approach. As a leader and visionary in the field of MEMS, his ability to think beyond the normal and realize it by means of rigorous hypothesis and testing is astounding - I aspire to imbibe these qualities within me, through my life. I would also like to thank my thesis committee members, Prof. Chris Ober, Prof. Alyosha Molnar and Prof. Debdeep Jena for their advice and support throughout my graduate career. I would like to especially thank Prof. Sunil Bhave for piquing my interest in MEMS as a new graduate student at Cornell when he taught ECE 4320, and for encouraging me to pursue research in the field.

Members of SonicMEMS laboratory who have been actively involved with my projects are crucial contributors to my research. Alex Ruyack and Dr. Serhan Ardanuc have helped me make the science-fiction of vanishing electronics into a reality. I would like to extend special thanks to Dr. Katie Camera and Amanda Leonardi from Prof. Ober's group who tirelessly provided me with polymer substrates and films that were key to all of my experiments. Dr. K. B. Vinayakumar, Dr. Yue Shi, Nathan Lambert and Sonal Lodha were instrumental in helping me with the gas sensor project at various stages. Of course all members of SonicMEMS, past and present, made day-to-day lab-life extremely enjoyable - Dr. Jason Hoople, Dr. Po-Cheng Chen, Earth Visarute Pinrod, Justin

Kuo, Sachin Nadig, Mamdouh Abdelmajeed, Adarsh Ravi, Leanna Pancoast, Dr. Nabi Shalabi, Di Ni, Dr. Kwame Amponsah, Dr. Benyamin Davaji, Tiffany St. Bernard, Dr. Yuerui Lu, Dr. Hadi Hosseinzadegan and Dr. Sarvani Piratla. I have consolidated and nurtured my love for teaching and mentorship at Cornell - it has been a pleasure working with and learning from some exceptional summer research interns, as well as the students I have interacted with in my two semesters as a teaching assistant. I would like to acknowledge Scott Coldren, Sue Bulkley, Charlene Lee, Daniel Richter and Patty Gonyea for their kindness and patience in helping me out with all of the administrative parts associated with my work. Their promptness was key in meeting deadlines and getting through stressful times. I would also like to thank the funding agencies who made my research and doctoral studies possible - first Qualcomm and then Intel for funding the chip-scale sensors, the National Science Foundation for radioactive materials-based self-powered devices, and the Defense Advanced Research Projects Agency (DARPA) and Dr. Troy Olsson for the majority of this work on chip-scale transient electronics.

My time in Ithaca was extremely special thanks to fellow ECE graduate students who are, at this point, some of my closest friends. I would like to particularly thank Dr. Suren Jaysuriya, Dr. Avik Dutt, Aseema Mohanty, Dr. Kevin Luke, Dr. Steven Miller, Dr. Shreyas Shah, Ajay Bhat, Dr. Tanay Gosavi, Levon Atoyan, Joey Engelbrecht, Sophia Rocco, Ed Szoka, Tayyar Rzayev, Rose Agger, and Brian Calderon. My special thanks to Tanay and Dr. Krishna Jayant for introducing me to Prof. Amit Lal's lab and students, when I was a new student at Cornell and for being my early mentors when I was still finding my feet around Ithaca. Friends in Ithaca have made me feel extremely loved and cared for during my time at Cornell. My roommates for four years, Shreyas

Honrao and Chaitanya Joshi, were the best partners in crime I could ask for - their moves away from Ithaca were hard transitions for me. Chaitali Joshi and Avik Dutt were and continue to be the best sounding boards and friends I have. Pankaj Singh, Aniket Kakatkar, Prateek Sehgal, Arzoo Katiyar, Neeraj Kulkarni, Pragya Sharma and Pooja Gudibanda have ensured that I am able to balance my work with a healthy life outside of lab.

I would like to specially thank my mentors Linda Tompkins and Anne Poduska and colleagues Aravind Natarajan, John Foo, Jansen Smith, Reece Kearney, Anna Srapionyan, Brendan Anderson and Elizabeth Case, at Cornell Engineering Learning Initiatives (ELI). They have helped me work towards being a more considerate, caring and kinder person. With our common goal of making teaching an enjoyable experience for teaching assistants, students and, indirectly, professors, I have had a wonderful opportunity to learn from and work with these incredibly caring people.

Perhaps, the biggest self-discovery I have made during my PhD is not related to my work. It the discovery of my love and passion for distance running. This would not have been possible without my coaches and great friends Michael Lam, Julianne Quinn, and Alexander Looi, as well as all my other training partners - Rob, Scott, Matt, Kristina, Jullien, Chelsea, Cassidy, Rich, Rachel, Adam, Alex among others. They have made the pounding of pavement and the joy of Ithaca trails extremely memorable. Anyone who knows me, knows how involved I am with the local running community. As groups, the Cornell Running Club, High Noon Athletics Club and the Finger Lakes Runners Club have given me a sense of belonging to Ithaca more than any other place I have lived in - I will forever carry the memories from group runs, races, and volunteering with me.

There is no exaggeration when I say that Vivek Athalye, Dr. Ivan Papusha and Dr. Geoff Schiebinger are my best friends who continue to inspire and support me through everything - they have been the constants in a whirlwind of changes over the last few years. Finally, I would like to thank my parents, my Maa, Kakuli, and my cousins Nishant and Preeti for their unconditional love and support throughout my life.

TABLE OF CONTENTS

Biographical Sketch . . . iii
Dedication . . . iv
Acknowledgements . . . v
Table of Contents . . . ix
List of Tables . . . xiii
List of Figures . . . xiv

1 Introduction **1**
1.1 Sensors in the Information Age . . . 1
1.2 Transient Electronics - Existing Technology . . . 5
1.2.1 Early Transient Systems - Corrosion and Impact-based Self-Destruction . . . 6
1.2.2 Transient Electronics on Flexible Polymer Substrates . . . 8
1.2.3 Post-processing Chips for Transience . . . 10
1.2.4 Array-based Polymer Transient System with Embedded Etch Sources . . . 14
1.2.5 MEMS Gas Sensors . . . 15
1.2.6 Calorimetric Gas Sensors . . . 18
1.2.7 Opto-Chemical Sensors . . . 18
1.2.8 Photo-Ionization Sensors . . . 19
1.2.9 Electrochemical Gas Sensors . . . 19
1.2.10 Mass-based Gas Sensors . . . 22
1.2.11 Resonators for Mass-Sensing . . . 23
1.2.12 Ion Mobility Spectrometry . . . 24
1.2.13 Ion-Mobility Spectrometer Array . . . 26

2 Single-Use Thermo-Mechanically Triggered Graphene-on-Nitride Valves for Transient Electronics **29**
2.1 Introduction . . . 29
2.2 Device Design . . . 31
2.2.1 Electrical Analysis . . . 33
2.2.2 Thermal Analysis . . . 37
2.2.3 Thermo-mechanical Stress Analysis . . . 40
2.3 Valve Fabrication . . . 44
2.4 Experiments . . . 47
2.4.1 I-V Measurements of Graphene Resistors . . . 47
2.4.2 Valve Out-of-plane Deflection . . . 48
2.4.3 Surface Topography of Fractured Valve Surface . . . 51
2.4.4 Pulsed-powered Triggering . . . 52
2.4.5 Valve-Sealing Test . . . 55
2.4.6 High Speed Visualization of the Triggering Mechanism . . . 56
2.5 Discussion . . . 57

2.5.1 Need for One-shot Valves . . . 58
2.5.2 Role of Graphene in Triggering . . . 59
2.5.3 Device Scaling . . . 60
2.5.4 Electrode Design . . . 63
2.5.5 Role of Si_xN_y . . . 64
2.6 Conclusions . . . 65

3 Transient Micro-Packets for Silicon Dioxide and Polymer-Based Vaporizable Electronics 66
3.1 System Architecture . . . 66
3.2 Transience Energetics . . . 70
3.3 Test Assembly . . . 72
3.3.1 VPC transience test . . . 73
3.3.2 Oxide transience test . . . 74
3.4 Experimental Results . . . 74
3.4.1 VPC transience . . . 74
3.4.2 Oxide transience . . . 77
3.5 Polymer Molding . . . 79
3.6 Conclusions . . . 82

4 Bi-Modal Graphene Polymer Interface Characterization Platform For Vaporizable Electronics 86
4.1 Introduction . . . 87
4.2 Device Concept . . . 89
4.3 Electrical Sensing . . . 90
4.4 Mechanical Sensing . . . 90
4.5 Device Fabrication . . . 92
4.6 Polycarbonate synthesis . . . 93
4.7 Testing And Results . . . 94
4.7.1 Unloaded Device - Characterization . . . 94
4.7.2 Polymer-loaded Devices - Resistive Sensing . . . 96
4.7.3 Polymer-loaded Devices - Mass Sensing . . . 97
4.7.4 Bi-Modal Sensing . . . 99
4.8 Conclusions . . . 100

5 Electronic Singulation of Silicon Pillars from Flexible Substrates Utilizing Vaporizable Polymer 102
5.1 Introduction . . . 102
5.2 PoP Architecture . . . 106
5.2.1 PPC for Flexible Substrate . . . 106
5.2.2 PoP Thermal Model . . . 110
5.2.3 Graphene Interconnects between Pillars . . . 117
5.2.4 Graphene PPC Piezoresistive Accelerometer . . . 118
5.3 PoP Fabrication Process . . . 119

5.3.1 Passivation and Tethering . . . 122
5.3.2 Metallization for heaters . . . 123
5.3.3 Lithography on PPC Membranes . . . 124
5.4 Experiment Results . . . 125
5.4.1 Quasi-Static Heating of PPC Polymer . . . 125
5.4.2 Pulse-Powered Triggering . . . 127
5.4.3 Graphene Interconnects Resistance During Heating . . . 128
5.4.4 Graphene Piezoresistive Accelerometer . . . 132
5.5 Discussion . . . 135
5.5.1 Technology Translation to CMOS . . . 135
5.5.2 Graphene for Interconnects and Sensors . . . 135
5.6 Conclusion . . . 137

6 Low-voltage Ion Mobility Spectrometer Array 138
6.1 Introduction . . . 138
6.2 Ion-Mobility Spectrometry . . . 139
6.3 Device Design . . . 140
6.4 Device Fabrication . . . 143
6.4.1 Direct-pattern Maskless Laser Micromachining . . . 146
6.5 Device Test Setup . . . 146
6.6 Experimental Results . . . 147
6.7 Conclusion . . . 151

7 Thin Film Piezoelectric Sense-Actuate Fan Pair 152
7.1 Micro-scale Gas Pumping . . . 152
7.2 Piezo-fan Model . . . 155
7.3 Device Fabrication . . . 158
7.4 Device Testing . . . 160
7.4.1 PZT Characterization . . . 160
7.5 Flow Measurements . . . 162
7.6 Sense Fan Measurements . . . 164
7.7 Conclusions . . . 167

8 Enhanced Lithium Niobate Pyroelectric Ionizer for Chip-Scale Ion Mobility-based Gas Sensing 169
8.1 Introduction . . . 169
8.2 Device Design . . . 171
8.3 Experimental Section . . . 173
8.4 Results and Discussion . . . 174
8.5 Conclusions and Future Work . . . 177

A Electrical and Thermo-Mechanical Analysis of Graphene-on-Nitride Single-Shot Valves 179

Bibliography **186**

LIST OF TABLES

1.1 Summary of Previous Approaches to Transience 13
1.2 Summary of Gas Sensing Techniques 27

2.1 Comparison of valve performance 30
2.2 Device Dimensions and Parameters 33
2.3 Thermo-Mechanical Stress Analysis 41
2.4 Sealing Test Analysis 56
2.5 Device Scaling and Valve Triggering 63

5.1 Device Dimensions and Physical Parameters 112
5.2 Summary of Interconnect Triggering 132

7.1 Summary of flow-velocities, flow rates and mechanical to air-mass flow power transfer efficiencies 163
7.2 Comparison of this work with previous reports for chip-scale fans and pumps 164

LIST OF FIGURES

1.1 Galvanic systems for self-destruction of metal containers. 7
1.2 Transient electronics on silk substrates with magnesium and silicon based components. 9
1.3 PPA-based transient substrates with UV exposure to trigger degradation. 10
1.4 Micro-fluidic add-on to oxide-based substrate for triggered chemical corrosion to produce chip transience. 11
1.5 Mechanical-shattering of chips by post-processing grooves on the backside filled with thermally expanding high-stress material. 12
1.6 Unit-cell for transient microsystems (Vaporizable Polymer Composite) (top): VPC substrate cavities are alternatingly filled with rubidium and sodium biflouride ($NaHF_2$), sealed by graphene-on-nitride valves with CMOS electronics as the backing layer. Time evolution of system transience (bottom): Valves are triggered on millisecond time scales, exposing Rb to oxygen. This releases heat to decompose the VPC and the salt, which releases HF to etch the oxide. The final residue is silicon nitride, metal micro and nano fragments, and salt. 16
1.7 Molecules used for the opto-chemical detection of HCl down to 5 ppm concentrations by Nakagawa et al. 20
1.8 Taguchi's SnO_2 electrochemical gas sensor. The exposed electrode was used for gas sensing. 21
1.9 Multi-stage GC sensor with a pre-concentrator, pump and chromatographic sensor integrated with MEMS fabrication. 23
1.10 Vapor-analyte detection using arrays of SAW device sensors. . . 24
1.11 Ion-mobility Spectrometer Principle of Operation: Ions of the target analyte flow in a drift-tube against an opposing flow of buffer gas and are separated on the basis of their mobility 25

2.1 Schematic of a 750×750 μm^2 valve with a cross section of a unit element used in the analysis. Top view of the graphene-on-nitride valve with the periodically repeating nickel fingers. The zoomed-in graphic shows the one of the repeating element which is modeled and the corresponding equivalent electrical circuit. 32

2.2 3D view of the valve element and the corresponding COMSOL model for it which is analyzed and the corresponding electric potential on the surface and the current density (top). The normalized mid-axis current density for this device is plotted as a function of the distance along the mid-axis. The jagged lines in the plot are a result of the distributed geometry used in analyzing the valve element. 35
2.3 Equivalent thermal circuit for the valve element. 38
2.4 Estimated increase in the temperature of region II of the valve vs. input current and corresponding change in total element resistance vs. temperature due to the TCR of graphene. 40
2.5 Nickel-nitride bimorph used for estimating valve deflection and the temperature gradient assumed along the X-axis. 42
2.6 Analytically estimated stress produced in the valve element versus input current in one finger of the nickel electrode. Based on the yield strength of the nitride film, the current needed to fracture it can analytically determined from the graph. 45
2.7 Device Fabrication Process - 1. 500 μm silicon wafer. 2. 360 nm LPCVD silicon nitride (Si_xN_y) deposited on both sides of the wafer. 3. RIE etch to pattern nitride on the backside 4. 45 nm nickel deposited by lift-off for contact to graphene. 5. KOH etching with 30 % by weight solution in DI water. 6. Graphene transfer and patterning with oxygen plasma for confining it to the membrane region for the valves. 46
2.8 A). Analytical model and experimental data for change in valve temperature above ambient as a function of input current in one nickel finger and B). the corresponding change in graphene resistance. C). Characteristic IR images of the valve surface with FLIR T300 IR camera, close to room temperature and during a quasi-static temperature ramp. 49
2.9 A). Surface topography maps with the Polytek Topography Measurement System (TMS) of the center of the valve with quasi-static heating at four different temperatures. IR measurements to record the temperature were done separately to characterize the valve temperature as a function of input power. B). Deflection along the mid-axis of the valve for increasing valve temperatures C). Analytical and experimental data for valve surface deflection vs. peak temperature on the valve surface. 50
2.10 Optical micrographs of the valve A). before and B). after triggering. C). Valve surface topography characterized with white-light interferometry D). Plot of the surface deflection along the traced outline on the valve surface in B. 51
2.11 Equivalent thermal circuit of the valve for pulse-powered fracturing. 53

2.12 A. Setup for pulse-powered triggering with a series resistor to capture trigger time B. Trigger power and trigger energy as a function of trigger time 54
2.13 Setup for measuring the sealing test in vacuum with the valve-syringe assembly 56
2.14 Optical photographs of the high speed camera triggering sequence of images of a membrane fracture 58
2.15 Device scaling and power requirements as a function of silicon nitride membrane thickness 63

3.1 A). Unit-cell for transience: VPC substrate cavities are alternatingly filled with rubidium and sodium biflouride ($NaHF_2$), sealed by graphene-on-nitride valves with CMOS electronics as the backing layer. B). Time evolution of system transience: Valves are triggered on millisecond time scales, exposing Rb to oxygen. This releases heat to decompose the VPC and the salt, which releases HF to etch the oxide. The final residue is minimal and consists of silicon nitride, metal fragments. 67
3.2 Analytical model for energy and stoichiometry constraints for a $(500\ \mu m)^3$ micro-packet vs. Rb fill factor in it. Heat of polymer vaporization is 110 kJ/mol and heat capacity is 1.2 $kJ/(kg.K)$. Rubidium energy is calculated from the enthalpy of formation of Rb2O equal to -169.5 kJ/mol. Oxide thickness is assumed to be 10 μm. 69
3.3 Top: Schematic of the test-structure for VPC transience. Bottom: An optical image of a 2×2 valve array tested for transience with Rb deposited inside valves, with connections to the valve via wirebonds. 72
3.4 $NaHF_2$ micro-packet test structures for oxide etching: A). with 1 μm oxide on bulk silicon and B). 5 μm thick oxide substrate commercial die embedded in $NaHF_2$. On the bottom, optical images of both test structures are shown. Both assemblies use a nitride-membrane with integrated Ni heater and $NaHF_2$ manually packaged in the chambers. 75
3.5 A). Optical micrograph of test structure 100 nL Rb is sealed by the valve and the VPC (not seen in this picture) is used as a backing layer B). Optical micrograph of a valve post-triggering shows 95% vaporization confirmed with image processing C). IR image of the polymer backside during Rb oxidation the elevated VPC temperature shows energy transfer from Rb to the substrate D). Best vaporization performance of 500 nL Rb in -packet produces 5.2mm^2 (determined with image-processing) etching of 125 μm thick polymer. 30% of polymer is etched below the tested valves (shown in inset) 77

3.6 A). Temperature profile of membrane surface vs. time for oxide-etching test of 1 μm thermal oxide on bulk silicon. B). IR image of the chip, confirming that the achieved peak temperature of $> 189^oC$ exceeds the temperature required for $NaHF_2$ decomposition C). Optical image of the substrate after etching shows exposed silicon which is an etch stop for HF etching D). Profilometry of the etched oxide substrate 1 μm confirms the depth of the etching 78
3.7 (Top) Honeywell thinned chip optical micropgraphs before and after $NaHF_2$ etch tests. (Bottom) Schematic of the die cross-section showing oxide sandwiched between polyimide and silicon which makes it necessary for in situ produced HF to etch laterally 80
3.8 Method for making VPC molds using a double-inversion SU-8 and PDMS based casting process. SU-8 is patterned lithographically, and used to make a negative/reverse PDMS mold. This is then used for casting polymer to make the VPC with the same structure as the SU-8. The optical image on the bottom right shows a 2×2 array and a single chamber made using this process. This method can be extended to making larger arrays 81
3.9 A). Optical image of a wafer with SU-8 patterned on it, for using the SU-8 as a PDMS mold. B). SEM image of a single 300 $\mu m \times 300$ μm chamber, designed for holding Rb. C). Honeycomb lattice made of SU-8 for making an array of Rb chambers 83
3.10 A). Method for realizing nitride on VPC with Rb chambers using SU-8 and PDMS molding and solution casting of VPC. B). Method of processing substrates with 100 nL Rb droplets inside the glovebox to build the desired nitride on VPC structures with no silicon. The nitride used for alignment can be cleaved by a sharp tip or a laser. 84

4.1 Polymer surface-interactions with the atomically-thin graphene are sensed electrically with graphene resistivity modulation. The mass-loss and vaporization are sensed mechanically with membrane resonance-frequency shift. 87
4.2 Characterization platform with spun-on analyte polymer for thermal cycling 89
4.3 Schematic of the membrane showing various thermal parameters and the half-membrane model to calculate its thermal time constant. 92
4.4 Unloaded device fundamental resonance frequency measurement. 95
4.5 Control-measurement of unloaded membrane resonance frequency shift and graphene resistance change vs. input power. . . 95

4.6 A). Temperature calibration of Si_xN_y membrane devices with serpentine calibration nickel resistors to obtain temperature versus power data in air and vacuum. B). IR camera images of the membrane with calibration resistor, during voltage-ramp in air (blue curve in A) 96
4.7 Graphene resistance change due to spun-on polymer, before thermal degradation, varies by 10x between VPC and VPC+PAG. After mass-loss at high input-powers, the graphene is cleaned and both resistance converges to pristine graphene-on-nitride resistance. 97
4.8 Resonance frequency vs. time during voltage-ramp of the graphene. Regions of only spring softening (low input power), and spring softening followed by mass-degradation (high input power) are shown 98
4.9 Polymer mass-loss % vs. input power - A) Low input-power with no material loss B) Onset of material loss, also seen optically C) Rapid polymer degradation sensed as a large frequency-shift D) Polymer degradation completed over graphene-heater. Measured 70 and 33 % mass-loss was verified by image processing . 99
4.10 Bi-modal polymer characterization - The platform gives complementary electrical and mechanical signals in different input-power regimes, shown by dotted vertical lines, for sensing graphene-polymer surface interactions, mass-degradation, and surface cleaning. 100

5.1 System Structure A). Standard CMOS and MEMS on silicon substrate B). Post processing to pattern oxide on the top to passivate electronics and pattern metal heaters associated with each island C). Transfer of the PPC handle layer with graphene for interconnects. The PPC holds silicon islands together. D). Example of a triggered pillar with PPC surrounding it vaporized, but other chip components intact 107
5.2 A). Polyproplyene carbonate B). PAG used to lower degradation temperature of PPC 108
5.3 TGA curves of PPC and PPC with 5 wt. % PAG 110
5.4 Schematic of the analyzed device - 3D view of the pillar array with heaters and PPC handle layer (left) and top view of the array with various dimensions and relevant thermal resistances for conductive losses to the substrate 110
5.5 Equivalent thermal circuit for the corner silicon pillar of the PoP array. 115

5.6 Simulation results from COMSOL Multiphysics: The temperatures of the target pillar, adjacent pillars and center pillar as a function of input power to the heater associated with the target pillar. Representative 3D images of the device heating at 24 and 40 mW input power are shown below. 116
5.7 Analysis of graphene interconnects formed between pillars with Ti/Au metal heaters as contacts to the interconnects 117
5.8 A. Graphene piezoresistor between adjacent pillars used for acceleration sensing B. Fundamental breathing mode resonance of the membrane with pillars at 174.1 Hz 119
5.9 PoP Fabrication Process: 1). PECVD oxide deposition 2). Ti/Au heater metal evaporation with lift-off 3). RIE for backside oxide patterning 4). DRIE etch of bulk silicon 5). Graphene transfer with PPC handle layer 6). BOE etching of top oxide to realize final structure. 120
5.10 SEM of a fabricated 3×3 PoP Array 122
5.11 Optical micrograph of nickel heaters used in a 3×3 array of pillars (left)and zoom-in image of faults in the metal at the anchor. This problem is resolved by replacing nickel with gold on titanium thin films. 124
5.12 A). Test setup used for quasi-static triggering of pillars. The IR camera (not shown here) is used to monitor the device temperature from the top side B). Measured peak surface temperature vs. input power and expected profiles from analytical model and COMSOL simulations C). IR camera images of the device during heating at 57.7 and 86.2 ^oC 126
5.13 Comparison of device heating with exposed PPC and untreated PPC. 127
5.14 (Top) Setup for measuring the triggering time and energy of the device. A Keithley 2400 was used as a voltage source for device under test (DUT) with heater resistance 20Ω in series with a resistor R_s of 22Ω. The voltage across Rs was measured with a National Instruments NIDAQ USB-6259. (Bottom) Triggering sequence captured with a Keyence high speed camera (2000 fps) shows the different stages of triggering a single pillar A). Voltage not applied and the device is intact B). Voltage applied across the series combination starts vaporizing the polymer, heater still intact C). Polymer vaporizes detaching the silicon pillar D). Metal heater fractures and produces an open circuit, no longer conducting current. 129
5.15 A. Setup for testing transience of interconnects between metal heaters associated with pillars A and B. A resistor of 3 $k\Omega$ was placed in series with the interconnect and the voltage across the interconnect was monitored. B. Equivalent circuit for the setup. 130

5.16 A). Temperature of pillar B versus input power for triggering and breaking graphene interconnect, measured using IR camera B). Increase in voltage measured across the series resistor as graphene interconnect is vaporized C). Optical micrograph of triggered devices D). Sequence of IR camera images during triggering 131
5.17 Shaker table setup for measuring the accelerometer response of the PoP membrane device with a 10× amplifier and 60 Hz notch filter followed by data acquisition. 134

6.1 Ion-mobility analysis in drift tube with one planar electrode for measuring travel-time of different ions, $m_1 < m_2 < m_3$, in opposing buffer gas m_B. Electrons present in the drift tube are accelerated towards the positive electrode thereby producing no signal at the output 140
6.2 Ion-mobility analysis in constant lateral flow velocity with transverse E-field for spatial mass spectrometry providing spatial and temporal resolution of multiple species 141
6.3 COMSOL simulations of E-field lines in the device showing a cross-section. The zoomed areas show the reduced effect of the E-field curvature effect around the edges as the aspect ratio is tripled from 0.5 to 1.5 for a fixed channel width of 1 mm 143
6.4 Fabrication process flow and assembly for stacked IMS array device. 144
6.5 a). SEM images of laser cut device features for individual electrodes b). Surface roughness of 10 um due to laser cutting c). Photo of assembled 2-layer ion-mobility spectrometer array. Square through-holes were used for optical alignment of layers on the PCB with vertical pins, which were eventually removed . 145
6.6 Device current as a function of electrode voltage (tested on electrode 2) for different ionizing powers which vary the ion-concentrations produced. Ion-current saturation occurs in transverse E-field at approx. 1.9V 148
6.7 Spectrometry of ion-species based on ion mobility Comparison of average current (nA) sensed as a function of electrode number on one-layer(left) and two-layer(right) devices for ionization of air. The stacked-device device has enhanced sensing due to effective confinement of ions in channel 149
6.8 Detection of acetone-vapor in air comparison of the signals from ionization of air (left) and an air-acetone mixture (right). A strong current on electrode 4 in the air-acetone mixture indicates the acetone signal 150

7.1 Chip scale ion-mobility gas sensor schematic - IMS array gas sensor, radioactive 63Ni film for gas ionization integrated with piezoelectric sense-actuate microfans for producing ion-flow . . 155
7.2 Process flow for fabrication of sense-actuate fan pairs 159
7.3 Transmission Electron Micrography (TEM) of the cross-section of the device layer stack 160
7.4 Scanning electron micrograph (SEM) of the unreleased sense-actuate fan-pair 161
7.5 Plot of measured maximum air-velocity with RTD sensor element at the tip of the drive fan as a function of frequency for 800 μm and 1000 μm long piezofans 164
7.6 Plot of measured maximum air-velocity with RTD sensor element at the tip of the drive fan and expected $V^{\frac{5}{6}}$ dependence . . . 165
7.7 Sense-fan time-domain voltage output for different drive voltages on the actuator at resonance 166
7.8 DC flow sense indicating constant lateral air-stream force and AC fluctuation showing increasing flutter/turbulence as actuator drive is increased 167
7.9 FFT of the AC signals with a peak at 1108Hz, which is twice the resonant drive frequency 168

8.1 Ion-mobility based gas-sensor architecture modified to incorporate the $LiNbO_3$ ionizer. 170
8.2 Schematic of thermal cycling of the crystal vs. time and corresponding ionization detected. The relative polarization of the $LiNBO_3$ crystal in the four different phases are also shown 1. room temperature; 2. heating cycle; 3. steady-state elevated temperature; 4. cooling cycle 171
8.3 Equivalent circuit of the crystal before (A) and after (B) attaching copper electrodes to increase ionization events. 172
8.4 Experimental setup used to measure the ionization events 174
8.5 Measured ionization events (A) Crystal surface (B) Crystal with copper foils attached 175
8.6 Increase in ionization events due to electrode 176
8.7 (A) Ionization events in heating and cooling cycle (B) Temperature control using control circuitry and an integrated temperature sensor 177
8.8 Ionization count per 150 second cycle as a function of heating power. 178

CHAPTER 1

INTRODUCTION

1.1 Sensors in the Information Age

The invention of the transistor [1] in 1947 as a metal-oxide-semiconductor (MOS) device was seminal in enabling the transition from mechanical and analog electronic technology to high density and low power digital computation. This period extended from the 1950s to the 1970s and is called the Digital Revolution, responsible for ushering in the Information Age. The Information Age has led to a proliferation of the use of digital logic circuits and analog devices, and technologies which rely on them - the computer, internet, cell-phones, tablets. In this period, the major emphasis in the design, production and use of silicon-based electronics has been to make computation faster, cheaper and energy-efficient all at the same time. This revolution has followed computational power growth predicted by the now famous Moore's Law. Gordon Moore, the co-founder of Fairchild Semiconductor and Intel, predicted in an internal paper that the number of transistors and components on an integrated circuit would double every 18-24 months. This prediction was expected to be a result of device shrinking as a result of advancement in lithography, and has been consistent up until recently when it has slowed down [2]. Many claim that one way to keep increasing the value of ICs is to go towards "More than Moore's Law" by adding new functionality on-chip. Technological advancements made in new ways to fabricate micro-mechanical structures have lead to exponential growth in Micro Electro Mechanical Systems (MEMS)-based sensors and actuators.

Much in the way that silicon has revolutionized computation, it has also been responsible for miniaturization of sensors and actuators by taking advantage of its attractive mechanical properties and device scaling due to lithography [3]. The ability to leverage the processing methods, materials and microfabrication technology that led to the proliferation of digital circuits has also led to the development of MEMS. In order to making moving parts for sensors and actuators, complementary processing techniques have been realized to support pre-established MOS planar process flows. This is achieved by preferentially etching one material relative to another to make suspended structures that are free to move. One of the first such demonstrations was done at UC Berkeley by Roger Howe and Richard Muller in 1982 when they fabricated suspended polycrystalline silicon beams, produced by etching an underlying silicon dioxide layer [4]. This work follows the first CMOS structure made by Harvey Nathanson in metal cantilevers with resonant gates [5]. Following this, a large variety of MEMS sensors and actuators have been developed including accelerometers, gyroscopes, pressure sensors, ink-jet printers, optical switches, digital micro-mirrors for DLPs,ultra-sound for bio-medical devices [6, 7, 8, 9, 10, 11]. These devices have competed with, and in many cases, replaced conventional macro-scale sensors due to their reduced costs, compatibility with batch-fabrication, improved sensitivity and CMOS-integration. The burgeoning sensor market and the integration of sensors in hand-held electronics has led to the Internet-of-Things (IoT) - the ability to connect computational blocks in daily-use sensors to the internet, and send and receive measured data. The IoT emphasizes multi-sensor integration on a unified platform for extensive data collection rather than improving the sensitivity of isolated sensors [12], although the ability to have IoT connectivity and improved sensors continues to

drive research and development.

The rapid growth of the IoT has also presented challenges in terms of the security of sensors and devices, and information acquired by them. By connecting them to the cloud, all of the information, devices and individuals connected to them are at a risk of data compromise by means of software hacking. This is a major concern for defense and financial applications where the loss of this personal data can lead to disastrous results. As a result, data encryption is critical and has been traditionally accomplished with software keys and encryption [13]. To further enhance security, hardware layers of protection and encryption have been an attractive addition to such sensitive information and devices. It is highly desirable that chips which acquire and store sensitive information can be triggered to vanish or self-destruct in situ to avoid allowing adversaries to access that data as well as the electronics.

Another important function of IoT sensors with regards to security is detection of toxic and volatile gases. This is critical in locations of high security such as airports and military facilities where toxic vapor monitoring for small quantities of harmful gases and bio-warfare agents is important for the safety of large number of lives. IoT gas sensors which can be miniaturized and designed to be portable for integration in platforms such as smart-phones and tablets are also useful in food processing facilities and in the automation industry. The ability to leverage MEMS technology to make portable sensors in a network spanning a large area is important for gas sensing. The wireless sensor nodes eliminate the need for bulky table-top sensors and reduce the cost of these sensors by batch-fabricating large quantities of these sensors on a single wafer. The processing time of miniature gas sensors can be smaller owing to reduced sample size, with

trade-offs in accuracy and sensitivity.

Chapters 2-5 of this thesis puts forth a methodology for the design, microfabrication and testing of transient microsystems using polymer substrates integrated with MEMS actuators and sensors. Silicon is the material of choice for conventional electronics because of its robustness and minimized performance variance over a wide range of temperatures and environmental conditions. The use of polymers as substrate material, whose physical and chemical properties can be tailored accurately based on their constituents, allows for the design of electronics and sensors which can be made to sublimate controllably and precisely. This is done at relatively low temperatures of $110 - 270\ ^oC$, whereas most polymers vaporize and catch fires at higher temperatures and leave behind visible residue. Chapters 6-8 present an ion-mobility spectrometry (IMS) as a tool for multi-species gas detection. In order to separate gases in a mixture, an IMS array is used for applying a lateral electric field and using a constant flow of ions into the device to obtain signatures of the mixtures using current detection. Low-voltage operable components necessary for producing ions from neutral molecules (an ionizer), producing a steady flow of ions in the device channel (an ion pump), and the IMS sensor for detecting ions from mixtures of gases (an ion-detector array) are presented which can be integrated for a gas analysis system.

The remainder of this chapter presents an overview of the research in the relatively nascent field of transient electronics and challenges associated with designing transient electronics. For gas sensors, this chapter addresses the existing technology for precision gas-sensing as well as chip-scale gas sensors that have been realized as a result of MEMS devices and their limitations.

1.2 Transient Electronics - Existing Technology

Modern silicon electronics are highlighted by their robust operation over a wide range of operation conditions and in harsh environments. The choice of silicon as a substrate for electronics is primarily an outcome of its physical invariance and little degradation in performance over a wide range of operating conditions, and for providing a stable oxide that enables CMOS circuits. However, today opportunities exist at the other end of the robustness spectrum where electronics must be designed for useful operation over a small range of temperatures and conditions, but can be made to vanish, vaporize or fall apart irrecoverably in a controlled manner. A few years ago this was akin to science-fiction or the plot for movies like the *Mission Impossible* series where agent Ethan Hunt often gets a secure, encrypted messaged in a cassette which self-destructs. However, today electronics packaging and interfacing with non-electronic materials is at an advanced stage of research where it is feasible to design self-destructing or transience electronic packages. While explosive destruction of systems is always possible, obtaining results with significant heating that generate IR signatures, audio cues and causes fires is not considered a controlled approach to transience. Hence, we can define transience in electronics as the ability to controllably trigger the vanishing of a part of or an entire chip, on-demand. The solution at the heart of such transient system is incorporating the appropriate etch sources, heat sources, or mechanical design which allows the electronics to function as they would under ordinary circumstances but produce transience upon receipt of an external trigger. The next few sections of this chapter attempt to describe the history of transient systems as well as their evolution over time.

1.2.1 Early Transient Systems - Corrosion and Impact-based Self-Destruction

The earliest reports of transience are from galvanic systems to fabricate self-destructing containers [14]. This was targeted to address the rise of waste storage containers in natural and man-made environments. The large variance in the deterioration time of metal-containers that are discarded led to accumulation of such containers, and was a growing concern in the 1970s. Container contamination continues to be a problem with a larger array of other materials today, most notably plastics. As a solution, metal laminate of two layers of dissimilar metals, electronically connected, were used which deteriorated on contact with moisture. Positioned between the metal layers was a minimum of one layer of an electrolyte-forming composition capable of establishing ionic communication between the metal layers when the composition is contacted with moisture. When the electrolyte-forming composition was contacted by sufficient moisture to provide ionic conduction between the metal layers, a galvanic cell is formed having the unique property of simultaneously deteriorating at both the anode and cathode. Figure 1.1 shows a sketch of the galvanic cell and the metal laminate. While targeted towards a noble application of keeping the environment clean, the reliance on moisture for triggering the deterioration of containers posed two problems: 1). It did not eliminate the variance in the time needed to eliminate these containers, instead relying on moisture content in air. 2). It led to possible uncontrolled deterioration of containers that were actively in use.

Another early example of a self-destructing system is an impact-based detonator which used a piezoelectric fuse responsive to sound waves for explosion

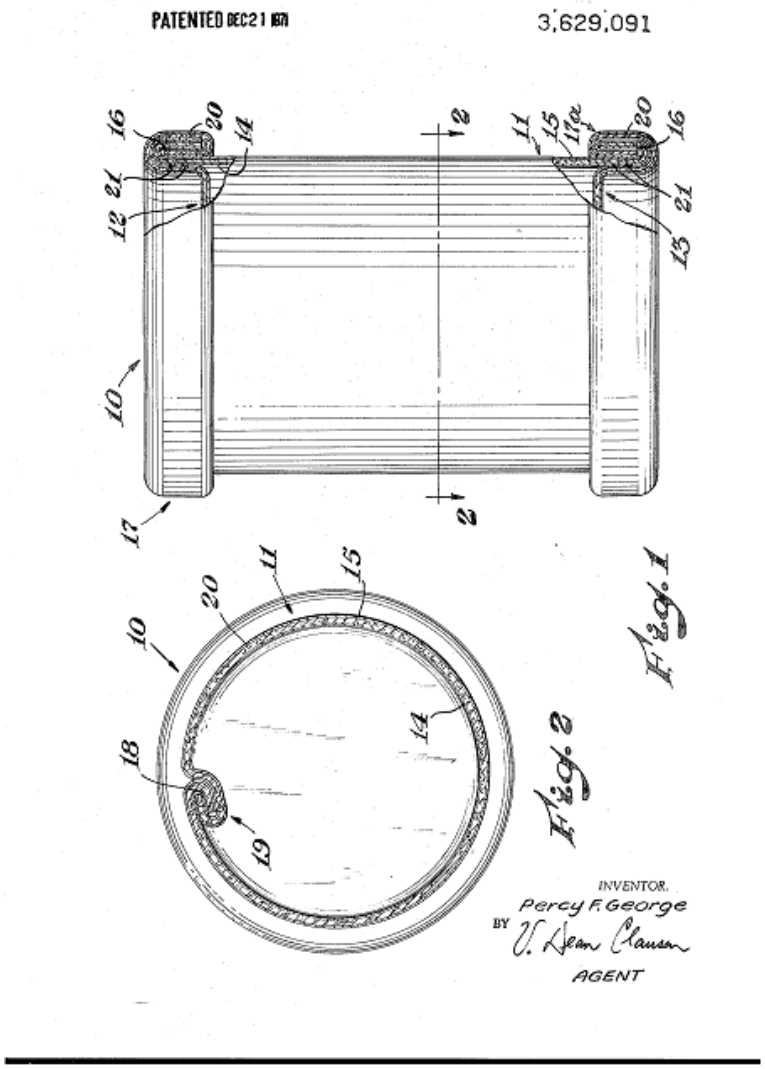

Figure 1.1: Galvanic systems for self-destruction of metal containers.

of the device [15]. The device included means for responding to impact such as macro-scale inertial or tilt sensors, the firing or dropping of which led to a sonic wave generation. After a predetermined time delay, the sonic wave produced by the generator would be transmitted to the piezoelectric fuse for detonation of the explosive device, thereby ensuring destruction of the device. A key concern with such a system for covert or defense operations is the audio trigger

produced by the explosion of the device. An accidental impact or triggering of the device while in operation would also be dangerous potentially harming the users.

Over the years, research in self-destructing system has been limited without an obvious need to design transient systems. However, with the growth of the IoT, implantable biomedical devices, and increasing security concerns associated with large wireless networks constantly interfacing with humans, there is a growing desire to incorporate transience mechanisms in chips. This must be done without modifying their functionality, to ensure that the chips vanish when they are no longer needed or when tampering or unwanted acquisition is detected.

1.2.2 Transient Electronics on Flexible Polymer Substrates

Research on transient electronics has been revived in recent times, led by demonstrations from researchers at the University of Illinois Urbana Champagne in Prof. John Rogers' group. The Rogers group first demonstrated electronics made entirely of silicon/silicon dioxide and magnesium (Mg)/magnesium oxide (MgO) on solution casted silk substrates. The silk substrates have inductors, capacitors, transistors, resistors and diodes made of combinations of silicon and magnesium and their oxides with magnesium interconnects. Chip components are patterned using transfer printing, physical vapor deposition with hard-masks and as shown in Figure 1.2 [16]. All of the components, ranging from the inductors, capacitors, resistors, diodes, transistors, interconnects, and crossovers, to the substrate and encapsulation, disintegrate

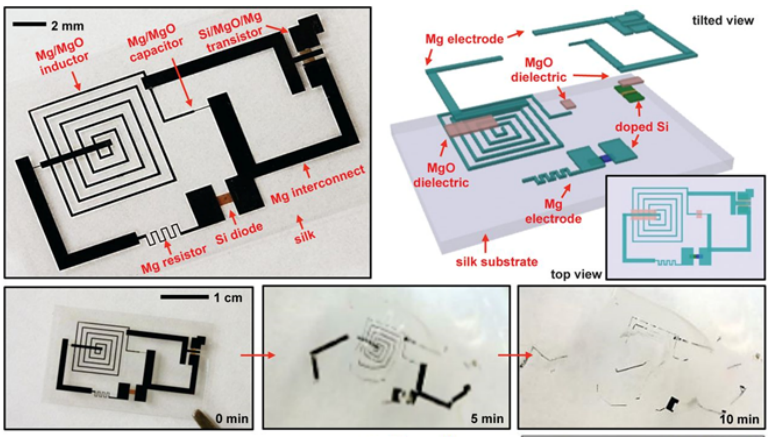

Figure 1.2: Transient electronics on silk substrates with magnesium and silicon based components.

and dissolve when immersed in deionized (DI) water. The transience times for the substrates can be increased or decreased by tuning the number of encapsulating and packaging layers. The electronics' performance, fabricated on unconventional silk substrates is limited in comparison to well-developed silicon and silicon dioxide-based processes - the speed of operation is lower, device sizes are larger and circuit complexity is limited by the ability to realize multi-layer interconnects. The transience of the substrates also depends on the availability of DI water, not naturally found outside research facilities. Thin film silicon-based electronics on poly(phthalaldehyde) (PPA) with photo-acid generators to control the rate of vanishing on exposures to specific wavelengths and intensities of light, have also been shown to produce effective transience shown in Figure 1.3 [17]. The limitation for these optically transient materials is long transience durations (up to several hours) and reliance on external ultra-violet (UV) light stimulation to activate the PPA degradation.

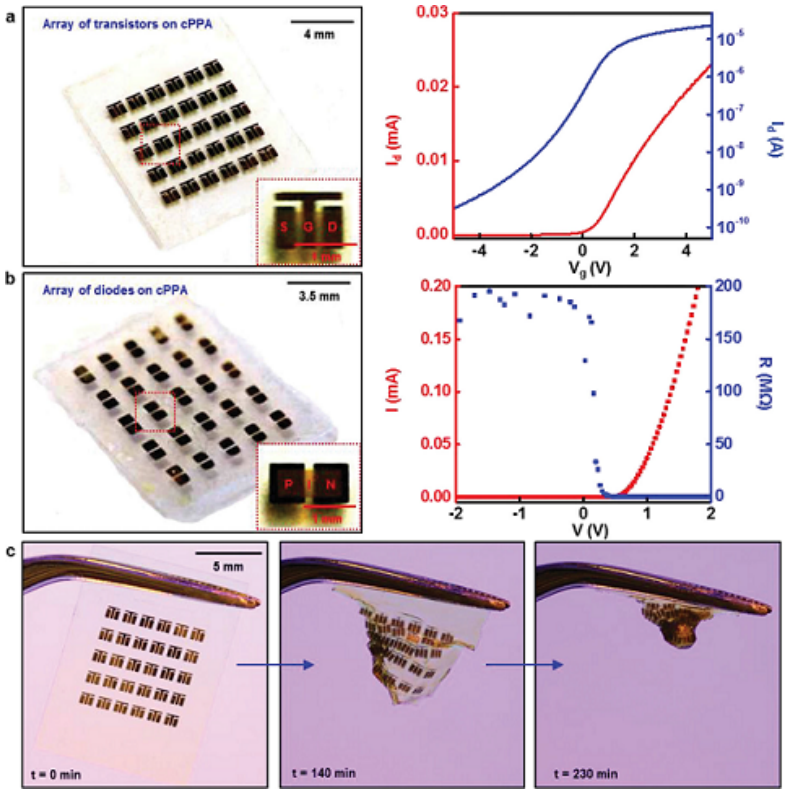

Figure 1.3: PPA-based transient substrates with UV exposure to trigger degradation.

1.2.3 Post-processing Chips for Transience

To better incorporate transience and reduce the transience time, researchers have chosen to post-process standard CMOS/MEMS dies with add-on transience functionality. Instead of changing the electronic materials and substrates, post-processing techniques modify the standard substrates to make them compatible for transience. Researchers at the University of Utah have developed a microfluidic device for transience of microchips. The microfluidic chamber, which destroys a target chip, is placed right above it and releases a highly corrosive chemical agent on the chip, which otherwise remains safely contained in a reservoir [18]. In this case, a micro-fabricated polymer membrane (SU-8) is

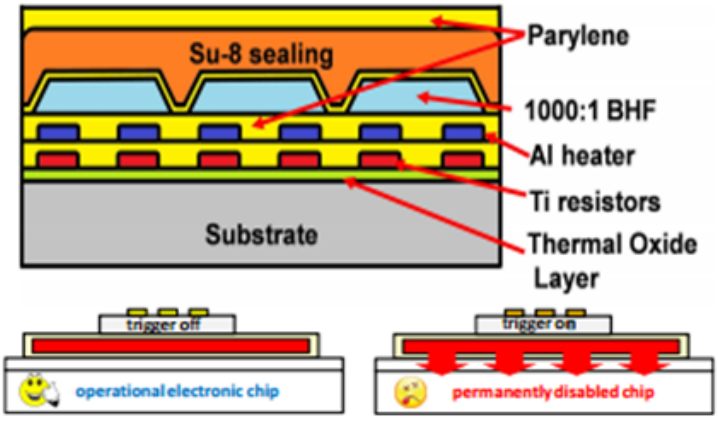

Figure 1.4: Micro-fluidic add-on to oxide-based substrate for triggered chemical corrosion to produce chip transience.

used to separate the chemical agent, hydrofluoric acid (HF), from the oxide substrate, shown in Figure 1.4. Thin-film aluminum heaters are used to delaminate the SU-8 when transience is triggered to released the HF and etch the oxide. By confining the HF to the chip-package, a very high transience efficiency can be achieved since none of the HF is lost to the ambient. By using a reservoir of the HF etchant instead of a distributed system or an array, it is conceivable that transience could be halted if the reservoir is detached from the package, rendering the self-destruction invalid.

Transience can also be realized by mechanically shattering an electronic chip into extremely tiny particles (e.g. $< 100\ \mu m$) that are separated from each other by large lengths, thus making it impossible to recover and re-assemble the chip. Fast transience is achieved by post-processing standard ASIC to etch grooves on the backside of its substrate and filling these grooves with thermally active material [19]. The thermal material expands significantly at elevated temperatures due to its high temperature of expansion coefficient (TEC), producing large stresses in the substrate (Figure 1.5). As a result of heating on the scale

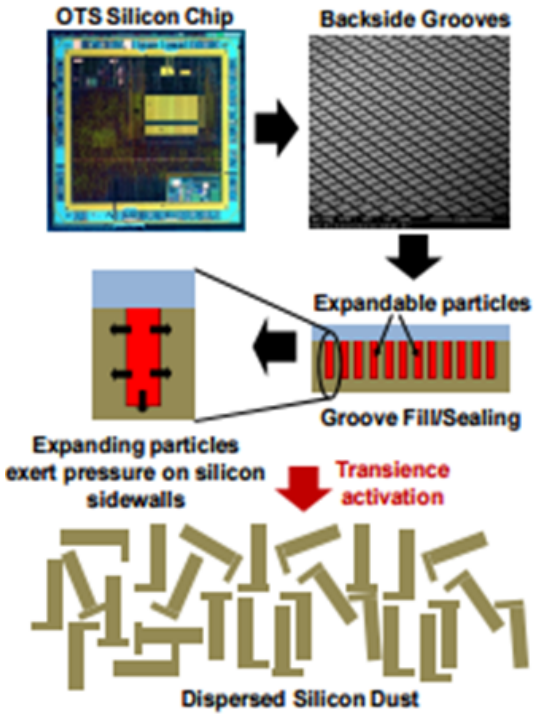

Figure 1.5: Mechanical-shattering of chips by post-processing grooves on the backside filled with thermally expanding high-stress material.

of a few minutes, the chip shatters into micro-scale pieces, achieving transience via mechanical fracturing. This method of transience is limited by the power requirements of the system. The demonstration used a macroscopic table-top heater, showing the need for large heating power over extended time durations, which is not feasible for a deployable standalone sensor for environmental monitoring or for defense applications.

Table 1.1: Summary of Previous Approaches to Transience

Ref.	**Approach**	**Transience Time**	**Advantage**	**Limitation**
[14]	Galvanic reaction	~ 2 days	No fuel source, zero power	Dependence on humidity, variability in transience time
[15]	Impact-based detonation	Few seconds	Predetermined time delay between impact and detonation	Accidental damage causing triggering, audio and visual cues from triggering
[16]	Dissolution in DI water	10 minutes	No residue from transience	Need DI water, electronics have modest performance
[17]	Degradation in UV	3 hours	Silicon-based electronics	Needs sustained UV exposure
[18]	Corrosion with etchant	15 seconds	Post-processing of chips	Detachable reservoir possibly renders transience invalid
[19]	Mechanical shattering	2 minutes	Post-processing of chips	Uses macroscopic heater

1.2.4 Array-based Polymer Transient System with Embedded Etch Sources

Table 1.1 summarizes the previously used approach to transience, the time of transience in each case, and the advantages and limitations of each approach. An architecture of a self-destructing standalone chip is an array of transient sub-blocks. Each sub-block has self-contained heating or etch sources which achieve sub-block transience in a controlled manner. This approach is scalable to larger systems by tiling of the sub-blocks. Transience presented in this work uses the oxidation of high purity, high power-density alkali metals such as Rb or Cs stored in micro-cavities to vaporize the sub-blocks shown in Figure 1.6. Large heat of oxidation for alkali metals is a result of their low ionization energies, making them highly susceptible to self-triggered oxidation. Although silicon could be vaporized, its high melting point and even higher boiling point would need too large a volume of fuel to reach that temperature. Hence, this work uses a low-decomposition temperature polymer as the substrate material which vaporizes at temperatures in the 120-200 °C range, leaving behind minimal residue. These specialized polymers are fortified with photo-acid generator (PAG), to further reduce the vaporization temperatures [20]. The heating and resulting vaporization of the polymer substrate requires that the Rb is sealed sealed hermetically. When transience is required, the Rb needs to be exposed to ambient oxygen to start oxidation and heating to vaporize the polymer. The valve must be triggered reliably, consuming low power as the energy is likely to be supplied by an energy-limited battery. To achieve fast transience, vaporization initiation or triggering time must also be minimized with minimal latency. The desired component to meet all of the constraints is a valve that seals the

Rb inside polymer micro-cavities, and is triggered with very low power and energy, in short durations to expose it to atmospheric oxygen. Additional reactive elements can be placed in the heated chamber to initiate chemical reactions for transience of electronics. Sodium biflouride $NaHF_2$, co-packaged with the Rb, also heats up during Rb oxidation and decomposes to produce HF, which etches silicon dioxide layers in the electronics. Chapter 2 of this thesis presents the design, analysis and testing of a single-shot valve made with graphene transferred on a silicon nitride membrane and its performance compatible with the requirements of the proposed transience platform. Chapter 3 describes the design and testing of the integrated transient system, including the valve, polymer substrate, Rb and $NaHF_2$ and results from testing the transience properties. Chapter 4 presents a polymer-characterization platform that can be co-fabricated with the valves using the same structural layers. This platform incorporates bi-modal sensors for frequency-based mass sensing and resistance-based surface interaction monitoring on the transient substrate. Finally, in the discussion on transient electronics, a novel architecture for controlled detachment of silicon micro-parts from polymer-based substrates is presented in chapter 5. This device architecture is targeted towards controlled transience of silicon substrates, to selectively remove or destroy parts of CMOS or MEMS dies while keeping the rest of the substrate intact. Such a topology could also potentially be used for micro-robotics delivery and directed drug-delivery applications.

1.2.5 MEMS Gas Sensors

The ability to detect trace concentrations of gases is important in industrial and medical monitoring systems, and is often a critical component to ensure the

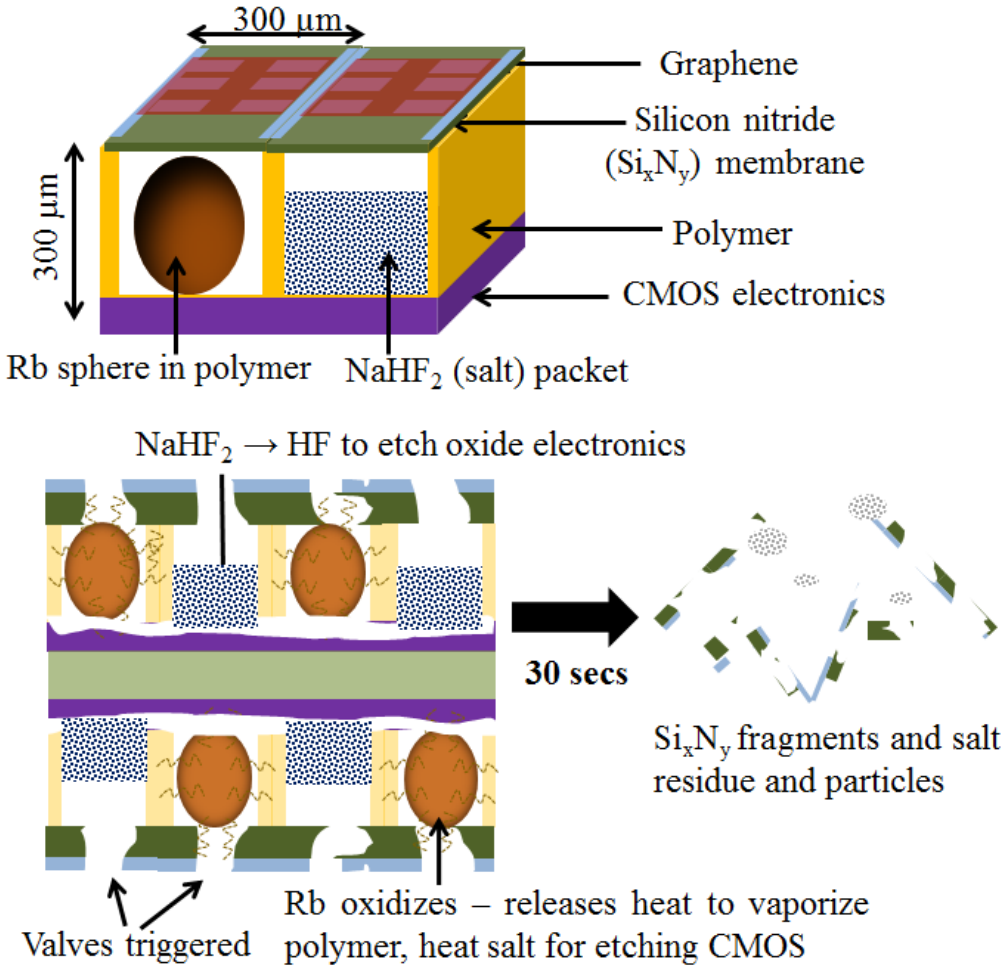

Figure 1.6: Unit-cell for transient microsystems (Vaporizable Polymer Composite) (top): VPC substrate cavities are alternatingly filled with rubidium and sodium biflouride ($NaHF_2$), sealed by graphene-on-nitride valves with CMOS electronics as the backing layer. Time evolution of system transience (bottom): Valves are triggered on millisecond time scales, exposing Rb to oxygen. This releases heat to decompose the VPC and the salt, which releases HF to etch the oxide. The final residue is silicon nitride, metal micro and nano fragments, and salt.

safety of people in many applications. These include monitoring of emission contents in industrial and automotive production, detection of toxic gases and equipment cleanliness in food packaging, identification of biological warfare agents at locations of high security such as airports, medical applications, and environmental studies for the regulation of respective gas concentrations [21].

The earliest example gas "sensors" were canaries [22], used by coal miners when they would dig tunnels and be at risks of exposure to CO_2, CO, and CH_4. Miners would bring canaries down in the mines and if they stopped singing and eventually died, it would be an indicator of the presence of toxic gases. In the late 1800s and early 1900s, gas sensors were used for detecting carbon monoxide and carbon dioxide with paper-based sensors using color changes [23]. Such sensors were did not provide quantitative estimates for the concentrations of gases and had undetermined minimum detectable concentrations. Over the last century, various qualitative and quantitative methods of gas sensing have been developed with an increased emphasis on multi-species detection using portable gas sensors. Examples of traditional methods of gas detection are [24]: calorimetric sensors which measure thermal conductivity changes of a gaseous mixture [21], opto-chemical sensors based on optical fluorescence or variation of optical absorption spectra [25], electrochemical cells [26] and MOS semiconductor films based on modulation of cell current as a result of surface redox reactions involving analyte [27], etc. The next few sections look at various gas sensing techniques and their advantages and limitations.

1.2.6 Calorimetric Gas Sensors

Calorimetric gas sensors measure the concentrations of combustible gas analytes by measuring thermal responses of sensing elements. For example, sensing elements can be thermometers which measure the temperature rise resulting from the oxidation process on a catalytic element [28]. Kirchner and co-authors demonstrated the use of MEMS calorimetric sensors that are catalytically activated, and have sensor calibration using passivated devices for differential sensing of peroxide[29]. These sensors have been used for flammable gases, when the temperature rise is high. Calorimetric sensors are less suited for the detection of toxic, odorless, colorless non-flammable gases.

1.2.7 Opto-Chemical Sensors

Opto-chemical sensors can operate at room temperature eliminating the need to heat gases. Various opto-chemical sensors have been reported for operation at room temperature that measure toxic gas emission down to the ppb and ppm levels [30, 31, 32, 33]. These sensors operate by measuring the optical absorbance and reflectance of organic compounds in both gas phase and adsorbed state on the surface. For example, free-base tetraphenylporphines and their response to adsorbed compounds can be detected at 550-600 nm wavelength [34] (organic compounds shown in Figure 1.7). The measurements are reversible and repeatable since the chemical-bonding of the adsorbed molecules of interest can be specifically controlled and the extent of the adsorption can be measured by the optical spectra. These sensors can be miniaturized to the scale of a few molecules for detection of very low concentrations of gases ($< 5\ ppm$). An issue

with photonic gas sensors is the requirement of a lase or an LED, which are not easily integrated onto CMOS [35].

1.2.8 Photo-Ionization Sensors

Photoionization sensors use a vacuum UV-wavelength light source to ionize target analytes [36]. Typical UV light-source wavelengths correspond to photo energies in the range of 10-12 eV, which is larger than the bonding energy in atoms. The electronics for detection can be transimpedance amplifiers for ion-current gain and can accurately determine the gas concentration.If the work function of the target molecules (ϕ) is lower than the ionization energy of the light sources (E_{source}), electrons are extracted and ions are formed according due to the photoelectric effect with the energy of the electrons ($E_{electron}$) and ions (E_{ion}) given by:

$$E_{electron} + E_{ion} = \frac{1}{2} m_e v_e^2 + \frac{1}{2} m_{ion} v_{ion}^2 = E_{source} - \phi \tag{1.1}$$

The operation of the sensors requires a filtered light source such as plasma lamps which constrains the miniaturization or portability of the full system. The sensors can be limited in photo-ionization in cases where total energy needed for ionization is greater than the that of photons emitted from the plasma lamps.

1.2.9 Electrochemical Gas Sensors

Electrochemical sensors (or semiconductor sensors) are extremely popular owing to their feasibility for integration with electronics, fabrication on standard

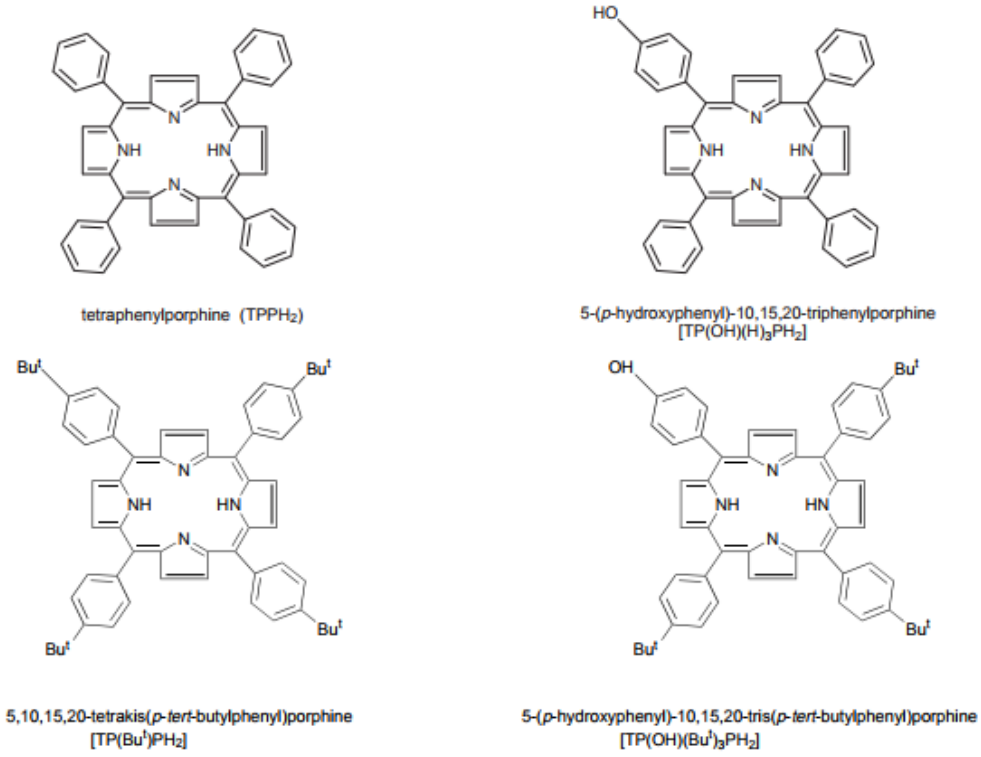

Figure 1.7: Molecules used for the opto-chemical detection of HCl down to 5 ppm concentrations by Nakagawa et al.

semiconductor substrates and electrical sensing with well-developed CMOS circuits. Brattain and Bardeen at Bell las first observed that germanium (Ge) film-resistance depends on the gas concentrations in their local atmosphere, as well as the humidity and moisture content [37]. The first demonstration of electrochemical sensors was by Seyama in 1962 which used zinc oxide (ZnO) thin films as resistive sensors for toluene, benzene and ethanol [38]. The operating temperature of 485 ^{o}C of these devices is required to create sufficient sensitivity due to the large bandgap of ZnO. Following this early work , a number of noble metals, semiconductors, and metal oxides have been demonstrated as highly effective materials for gas sensors. Most notably, Taguchi fabricated and demonstrated

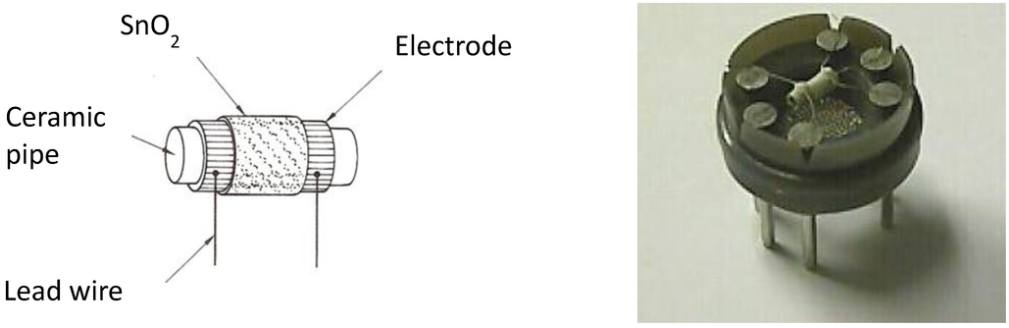

Figure 1.8: Taguchi's SnO_2 electrochemical gas sensor. The exposed electrode was used for gas sensing.

tin oxide (SnO_2) gas sensors which were found to have ultra-high sensitivity, lower operating temperatures ($< 300\ ^oC$) and thermal stability over multiple sensing cycles [39]. These sensors continue to be used and only recently have been challenged in performance and temperature of operation by 1-D nanowire-based [40, 41, 42, 43, 44] and semiconductor sensors using thin films such as that of graphene [45, 46]. With extremely high sensitivity, ultra-low concentration gas detection, and fast response times, these sensors are extremely useful for species-specific gas-sensing with low-voltages, even with miniaturization of the sensor to the nanoscale. Like calorimetric sensors, a major limitation or barrier to multi-functional gas sensing with electro-chemical sensors is the need for functionalization of the sensor and array-based sensing to detect multiple gases [37, 39]. Hysteresis due to surface modification and corrosion leading to sensor performance degradation are also concerns with regards to electro-chemical sensors.

1.2.10 Mass-based Gas Sensors

Mass-based sensors have risen to prominence in the last few years as a result of harnessing MEMS technology to miniaturize gas chromatography (GC) to the micro-scale. Recent efforts have been made to develop field-portable and meso-scale GC systems to provide portability and near real time analysis capability [47, 48]. One example of mass-based sensors is Micro Gas Analyzers (MGAs). The operation principle of an MGA is also relatively simple - a pre-concentrator made by coating metal heaters with functionalizing polymers is used for adsorbing and concentration analyte molecules. At sufficient concentration of the adsorbed analytes, they are flown in long drift tubes, designed with deep reactive ion-etching (DRIE) with effective lengths on the scale of centimeters to separate the various components of the adsorbed gases based on their travel times in the drift tubes. The diffusivity is specific to the mass of the compounds or gases sensed, and hence high resolution in separation of gases with similar masses can be achieved. Collaborative work from the groups of Prof. Zellers, Prof. Najafi and Prof. Gianchandani at the University of Michigan have realized micro-scale peristaltic pumps, pre-concentrators and gas chromatographs with reduced dead volume of gases, lower thermal mass of heaters and low operation power with sensing time on the order of $\sim$ 10 minutes to make portable gas chromatographs as shown in Figure 1.9 [49, 50, 51, 52]. In spite of being miniaturized and designed for low-voltage and low-power platforms, the sensing-time is limited by the travel time of molecules in the drift tubes and can be a limiting factor where high throughput sensing is needed.

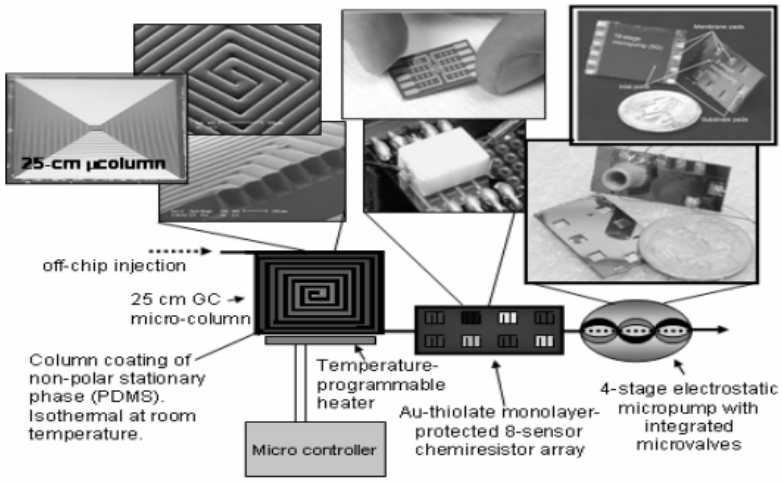

Figure 1.9: Multi-stage GC sensor with a pre-concentrator, pump and chromatographic sensor integrated with MEMS fabrication.

1.2.11 Resonators for Mass-Sensing

Quartz Crystal Microbalances (QCMs) can be used for gas sensing by measuring the shift in resonance frequency of on a quartz crystal connected used in an oscillator configuration. The shift in frequency depends on the mass adsorbed on the surface of the crystal as:

$$\frac{\Delta f}{f} = -\frac{\Delta m}{2m} \tag{1.2}$$

Work from Prof. Zellers' group has also investigated mass-based gas-sensing using surface acoustic wave (SAW) devices as resonant sensors [53] (shown in Figure 1.10). Integrated arrays of polymer-coated flexural plate wave sensors have been designed with each element of the array used for sensing a specific gas. With high-frequency resonators the shift in frequency Δf from the resonance frequency f_{res} can measure up to 300 pb concentration of organic compounds such as ethanol and toluene [54, 55]. The need for array-based sensing with elements tuned for each target analyte limits the miniaturization and semi-

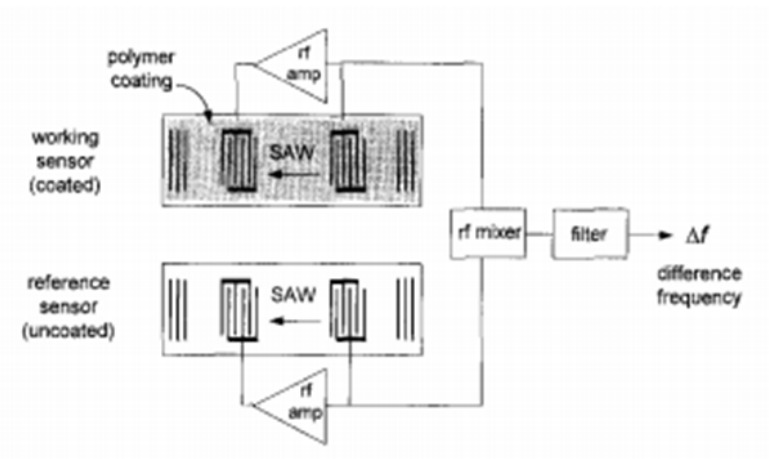

Figure 1.10: Vapor-analyte detection using arrays of SAW device sensors.

conductor real estate required for the sensors. Making each sense element of an array suitable for a target gas results in a large overall sensor.

1.2.12 Ion Mobility Spectrometry

Ion-mobility spectrometry (IMS) is an analytical technique that separates and identifies ions of volatile organic compounds (VOCs) in the gas phase based on their mobility in the gas phase. While the molecular mass alone is an important differentiator for sensing, charge with mass provide a dual reference for detection and are more desirable to be used simultaneously for gas sensing. The basic principle of operation of IMS is shown in Figure 1.11 [56]. The target analytes fed into the IMS fluidic channel are ionized at the input of the channel. An ion-shutter is used for filtering the ions followed by flowing the gas in an opposing flow of a buffer gas. The velocity of the ions in the IMS channel for an applied electric-field E and ion-mobility μ is:

$$v = \mu E \tag{1.3}$$

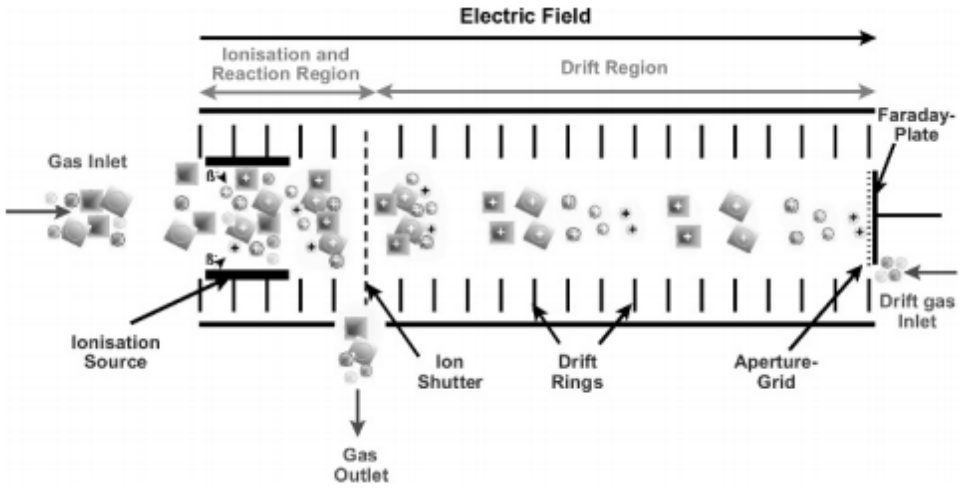

Figure 1.11: Ion-mobility Spectrometer Principle of Operation: Ions of the target analyte flow in a drift-tube against an opposing flow of buffer gas and are separated on the basis of their mobility

Based on the gas-mobility and the collision cross-section with the buffer gas, the travel time in the drift tube of a few centimeters can vary for different gases. At the end of the fluidic channel the current from the ion-bunches of each gas element is detected with a Faraday plate, and other signal processing hardware such as the transimpedance amplifiers.

Traditionally, IMS has been used for military and security applications due to its high sensitivity, lack of hysteresis in sensor performance, and ability to detect multiple gases in an analyte mixture with high resolution [57]. In order to miniaturize mobility-based sensing for portable and hand-held electronics, MEMS technology offers approaches to increase performance and reduce SWAP (size, weight and power). Various efforts have targeted hand-held IMS devices with electron-spray ionization (creating aerosols from liquids for macromolecular species), high-field asymmetry for ion-separation (applying asymmetric signal amplitude and duty cycle RF fields on the ions in the IMS fluidic channel

for guiding them) and secondary ion-cluster detection (Using the collision of ions with other neutral molecules which produces a cascade of secondary ions, leading to signal enhancement)[58, 59, 60]. MEMS quadrupoles have been used for ion-trapping and detection for further miniaturization of IMS [61, 62]. All of these efforts have been limited by the need to produce high voltages on-chip for one or more of producing E-fields necessary to separate ions, producing ions from ambient VOC molecules or for pumping these ions. The ability to realize high-aspect ratio structures is also a challenge with DRIE being a common method of fabrication. Also, with the traditional architecture of a single-detector for sensing the ion-flux, high bandwidth electronics are a necessity because the same detector is used to identify various ion-bunches falling on the detector. Table 1.2 summarizes the methods of gas sensing used as well as their advantages and limitations to motivate the research of IMS devices for gas-sensing using MEMS.

1.2.13 Ion-Mobility Spectrometer Array

This thesis presents a platform for miniaturization of IMS-based gas sensing using low voltages. A low-voltage operation IMS array compatible for mobile platforms is presented in chapter 6. Following this, a flow production device used in these devices, a thin-film piezoelectric fan, is presented in chapter 7. The fan uses a piezoelectric unimorph with a silicon dioxide elastic layer to realize a flapping motion and streams ions into the IMS device channel. Along with flow-production, a co-fabricated unimorph piezoelectric beam placed next to the fan is used for feedback sensing when the flow from the fan becomes turbulent and produces lateral air-motion instead of transverse motion in the device channel.

Table 1.2: Summary of Gas Sensing Techniques

Sensor	**Parameter Sensed**	**Advantage**	**Limitation**
Calorimetric	Thermal Conductivity	Thermal sensor with reference provides in situ sensing	Needs high temperature for operation, not suitable for non-flammable gases
Opto-chemical	Absorbance or Reflectance	Room-temperature operation	Need for high photon-energy lamps and lasers
Electrochemical	Resistance change	Ease of integration with CMOS and semiconductors	Hysteresis and corrosion of the sensor, gas-specific sensing
Mass-based	Travel time in drift tubes / resonance frequency shift	Multi-species detection	Slow time of detection, need for arrays of sensors
Mobility-based	Travel time of ions in E-field	Multi-species detection	Need for high voltages

Finally, to generate ions from neutral gas molecules which need to be detected, an ionization source is needed before the ions are streamed. To this effect, the thesis presents a lithium niobate-based pyroelectric ionizer in chapter 8.

CHAPTER 2

SINGLE-USE THERMO-MECHANICALLY TRIGGERED GRAPHENE-ON-NITRIDE VALVES FOR TRANSIENT ELECTRONICS

2.1 Introduction

Single-use valves are membrane barriers which prevent two environments from interacting with each other, until the membranes are removed or broken. In single-use valves, the membrane cannot be reversibly closed to the isolation state. Such valves have been previously reported in literature for a range of applications. One example of a single-use valve is where pyrotechnic actuation of a thin film energetic propellant is triggered by a micromachined silicon microheater on a dielectric membrane [63]. Joule heating of the microheater causes the propellant to combust and react with oxygen. The gaseous products of this reaction produce elevated pressures, imparting pressure impulses to fracture the membrane. The microheater and membrane have a small thermal mass, resulting in fast valve triggering times on the order of milliseconds. A challenge with this approach is that the volatile reactant fuel needs substantial heat to reach the combustion point. Another example of a single shot use is where the fuel is sealed by polythethylene (PE) and polyethylene terepthalate (PET) films which are a few tens of microns in thickness [64]. These valves trigger by melting thermosetting adhesives that connect the polymer membrane to the substrate, consequently delaminating the polymer. The heating causes expansion of the stored fluids in the chamber, and the valve action relies on the over-pressure of stored fluids inside the cavity. The time of trigger is diffusion-limited by thermal transport through the liquid. The high energy needed to overcome the

latent heat of fusion of the valve-adhesive can also increase the trigger delay and energy budget of the valve. Another example of a single-use valve that can survive harsh environments and high pressure-gradients uses melting solder or alloys for valve operation [65]. In this valve, the trigger time is very large (> 10 seconds) and the switching energy is $130\ J$. Table 2.1 compares the metrics of the previously reported valves to the one presented in this work. The table summarizes existing valve designs that are limited by high trigger power and energy and long trigger times, which we have reduced significantly.

Table 2.1: Comparison of valve performance

Work	**Trigger Time (sec)**	**Power (W)**	**Trigger Temp (C)**
[63]	25×10^{-3}	72	300
[64]	1.2	0.2-0.4	120
[65]	~ 10	13	~ 500
This work	15×10^{-3}	0.14	~ 280

This chapter presents a single-use valve with ultra-low trigger power and trigger energy using thermo-mechanical actuation of a graphene-on-nitride membrane. Graphene serves as a two-dimensional resistive heater for selectively heating various parts of the membrane, based on the placement of nickel electrodes that distribute current in graphene. Also, graphene is an additional gas-diffusion barrier on top of the silicon nitride, and protects rubidium stored in underlying polymer substrates [66]. This becomes important in the limiting case of a very thin structural layer of the membrane material (silicon nitride in this work), which could potentially have pinholes and be porous and

allow gases to permeate into the chamber. The Joule-heating of the graphene resistor produces temperature gradients, leading to thermo-mechanical stress in the valve leading to its rupture. The valve design and analysis of the thermo-mechanical membrane rupture is presented in section 2. The fabrication process for the valve is described in section 3, followed by a detailed set of experimental results and comparison to the analytical model in section 4. Section 5 discusses the experimental data validating the triggering mechanism of the valve. Section 6 summarizes the results of the work and provides concluding remarks.

2.2 Device Design

The top view of the valve schematic is shown in Figure 2.1. It consists of a square silicon nitride membrane of side a and thickness t_{SiN} with nickel electrodes of thickness t_{Ni} patterned on it. An atomically thin sheet of graphene $t = 0.4\ nm$, transferred on top, covers the square membrane. Each of the two electrodes has M metal fingers, with the inter-finger spacing in the Y-direction being λ. Joule heating of the graphene resistor is used to induce temperature gradients which deform the membrane due to thermal expansion mismatch of nickel and nitride, and consequently fracturing the membrane and triggering the valve.

The periodically repeating electrode finger geometry in the Y-direction is modeled with a single membrane element of area $a \times \lambda$ on the valve, as shown. In order to simplify the analytical model, it is assumed that the element repeats infinitely along the Y-direction. Electrodes on the left and right source and sink the current I respectively. Regions I and III have identical thermal and stress profiles, since they are symmetrically placed above and below the metal. For

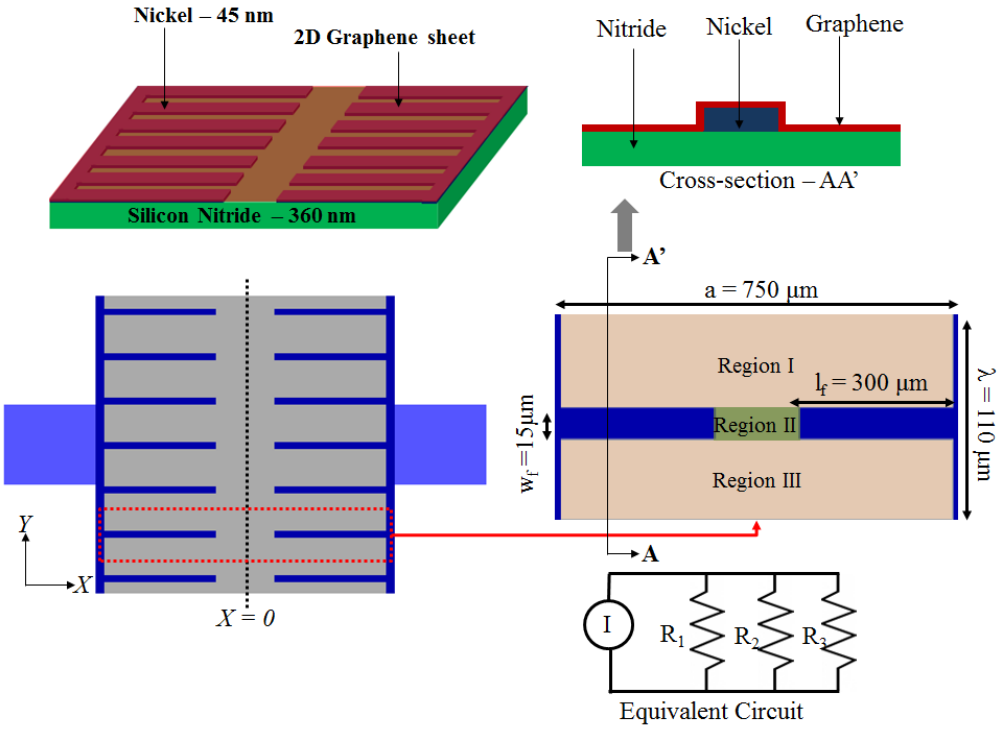

Figure 2.1: Schematic of a 750×750 μm^2 valve with a cross section of a unit element used in the analysis. Top view of the graphene-on-nitride valve with the periodically repeating nickel fingers. The zoomed-in graphic shows the one of the repeating element which is modeled and the corresponding equivalent electrical circuit.

the sake of brevity, whenever region I is analyzed, it is assumed that the same analysis applies to region III. Table 2.2 lists the device dimensions and physical parameters for the materials used to fabricate the valve. The properties and material constants for graphene are from published works and it is generally understood that the properties can vary with processes used to fabricate and transfer the graphene films.

Table 2.2: Device Dimensions and Parameters

Parameter	**Value**
Valve side length (a)	750 μm
Spacing between nickel fingers (λ)	110 μm
Finger length (L_f)	300 μm
Finger width (w_f)	15 μm
Silicon nitride thickness (t_{SiN})	360 nm
Nickel thickness (t_{Ni})	45 nm
Graphene thickness (t_{gr})	$\sim$ 0.4 nm
Young's modulus of silicon nitride (E_{SiN})	$\sim$ 290 GPa [67]
Young's modulus of nickel (E_{Ni})	$\sim$ 190 GPa [68]
Young's modulus of graphene (E_{gr})	$\sim$ 1 TPa [69]
Graphene resistivity (ρ_{gr})	$\sim$ $10^{-5}-10^{-6}$ $\Omega-cm$
Nickel resistivity (ρ_{Ni})	7×10^{-8} $\Omega - cm$

2.2.1 Electrical Analysis

The valve structure with the nickel electrodes and two-dimensional planar current flow leads to an analytically complex electrical model for the device due to the two-dimensional flow of current across electrodes. A COMSOL simulation is used to guide the analysis, while assuming that the opposing pairs of electrodes is an infinitely repeating structure in the Y-direction. Figure 2.2 shows the the two-dimensional structure and the cross-section of the valve element simulated in COMSOL and the electric potential and current density produced

on the surface as a result. The mid-axis current density is also plotted and the ratio of current densities from the edge of the element to the center, between the electrodes is ~ 1.2. In order to simplify the analytical model, it is assumed that the the currents in regions 1 and 3 flow independently of current in region 2 i.e. the three areas function like individual resistors.

The resistivity of nickel ($\rho_{Ni} = 7 \times 10^{-8}\ \Omega.m$) is much smaller than that of chemical vapor deposition (CVD) grown graphene ($\rho_{gr} > 1 \times 10^{-6}\ \Omega.m$ [70]). Further a nominal 45 nm thickness for the metal is much thicker than the $< 1\ nm$ thickness of graphene. As a result, the resistance is dominated by the graphene segment in each of the three regions. R_2 can be estimated as:

$$R_2 = \frac{\rho_{gr}(a - 2l_f)}{t_{gr} w_f} \tag{2.1}$$

and the resistance in region 1 and 3 is:

$$R_1 = R_3 = \frac{\rho_{gr} a}{t_{gr} \frac{\lambda - w_f}{2}} \tag{2.2}$$

For the fabricated device dimensions, the ratio $\frac{R_1}{R_2} = 1.58$. With the repeating boundary condition at the edge of each electrode area, the current density has a periodic profile along x = 0 in the Y-direction. The current density can be expressed in the form of a constant current density J_0 modulated by a sinusoidal J_m.

$$J(y) = J_0 + J_m cos(k_1 y) \tag{2.3}$$

The current density is maximum between the fingers where the graphene resistance is the lowest, and minimum along the top and bottom boundaries where resistance is highest. For the element under consideration, one can assume that the current does not vary significantly within each of the three regions being analyzed. As a result, the currents in each of three regions can be expressed as:

$$I_1 = I_3 = I_0 - \Delta I \tag{2.4}$$

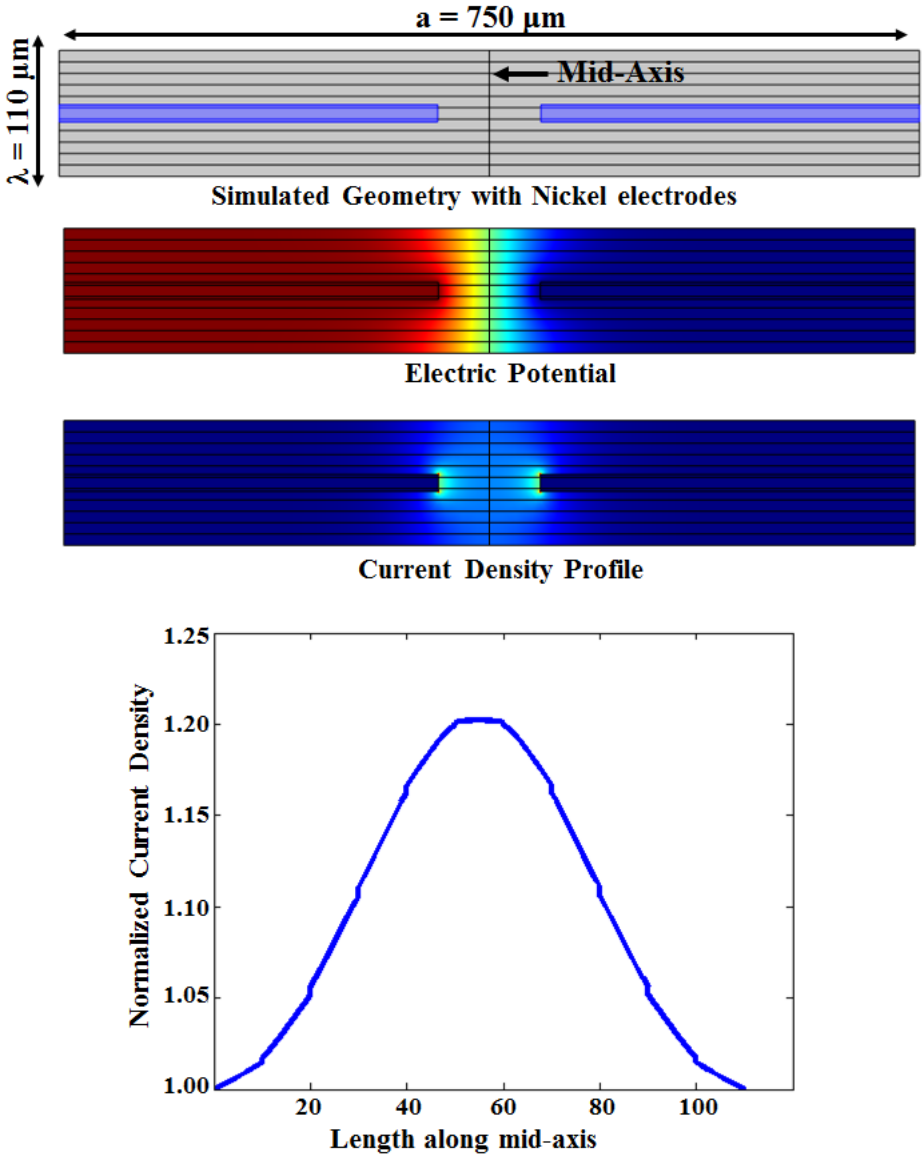

Figure 2.2: 3D view of the valve element and the corresponding COMSOL model for it which is analyzed and the corresponding electric potential on the surface and the current density (top). The normalized mid-axis current density for this device is plotted as a function of the distance along the mid-axis. The jagged lines in the plot are a result of the distributed geometry used in analyzing the valve element.

$$I_2 = I_0 + \Delta I \tag{2.5}$$

The power dissipated due to Joule heating in each segment is

$$P_i = I_i^2 R_i \tag{2.6}$$

Additionally, the sum of the currents is equal to the total current input on the left side of the element.

$$I_1 + I_2 + I_3 = I \tag{2.7}$$

The resistivity of graphene, ρ_{gr}, depends on the local temperature T [71] and varies significantly with temperature. For a constant band-gap E_i in the graphene, the resistivity is given by:

$$\rho_{gr}(T) \sim exp(+E_i/2k_BT) \tag{2.8}$$

Where k_B is the Boltzmann constant. This can be linearized using the Taylor-series approximation as:

$$\rho_{gr}(T) \approx \rho_0(1 + \alpha\Delta T) \tag{2.9}$$

Here, α, the the temperature coefficient of resistance (TCR) can be approximated as $E_i/2k_BT^2$. Pristine defect-free graphene is a zero-bandgap material [72]. The band-gap can be non-zero when by applying an Electric field across graphene [73], adding impurities or with different boundary conditions than free-standing films [74]. The value of α as reported previously in [71] varies between $-1.2 \times 10^{-3}/K$ and $-3.7 \times 10^{-3}/K$, based on the percentages of single and bi-layer content of the graphene films respectively. This rage of CTE is in close agreement with the predicted temperature-dependence of graphene resistivity from theory [75].

2.2.2 Thermal Analysis

The change in temperature ΔT_i in any region of the element is a continuous function of X and Y along the surface of the element. A simplified lumped model can be used to analyze the valve with discrete thermal properties while including thermal resistors for interactions between these regions:

$$\Delta T_i = P_i R_{th,i} \tag{2.10}$$

P_i is the Joule heating in that region of the analyzed element and $R_{th,i}$ is the thermal resistance between the part of the valve being heated and the substrate, which is at T_0. The lateral dimensions of the the nitride and the graphene film are the same, so the product of thermal conductivity (κ) and material thickness (t) determine the thermal resistance. Graphene has a very high thermal conductivity of 4.8×10^4 $W/(m.K)$ [76], but has a sub-nm thickness of 0.4 nm [77]. Silicon nitride has a thermal conductivity of 30 $W/(m.K)$ but is 360 nm thick so the κt product is much $6\times$ larger for nitride. As a result, the thermal resistance of the graphene in parallel with the nitride is much larger and is ignored for the calculation of temperature increase. For the analysis, we can assume that the silicon frame around the membrane has a thermal sink at room temperature.

$$R_{th,1} = R_{th,3} = \frac{1}{\kappa_{SiN}} \frac{a}{2t_{SiN}(\lambda - w_f)} \tag{2.11}$$

For region II, the thermal resistance to the substrate is a parallel combination of the nitride membrane and nickel electrode finger:

$$R_{th,2} = \frac{1}{\kappa_{SiN}} \frac{a}{4t_{SiN}w_f} \| \frac{1}{\kappa_{Ni}} \frac{l_f}{2t_{Ni}w_f} \tag{2.12}$$

The Joule-heating of the graphene resistor in each region changes the resistivity , which in turn affects the heating power produced in the region and its local

temperature. Additionally, there is heat flow between the different regions of the repeating element due to the different temperatures across the elements limited by $R_{th,21}$. The equivalent thermal circuit that models the different channels of heat flow is shown in Figure 2.3.

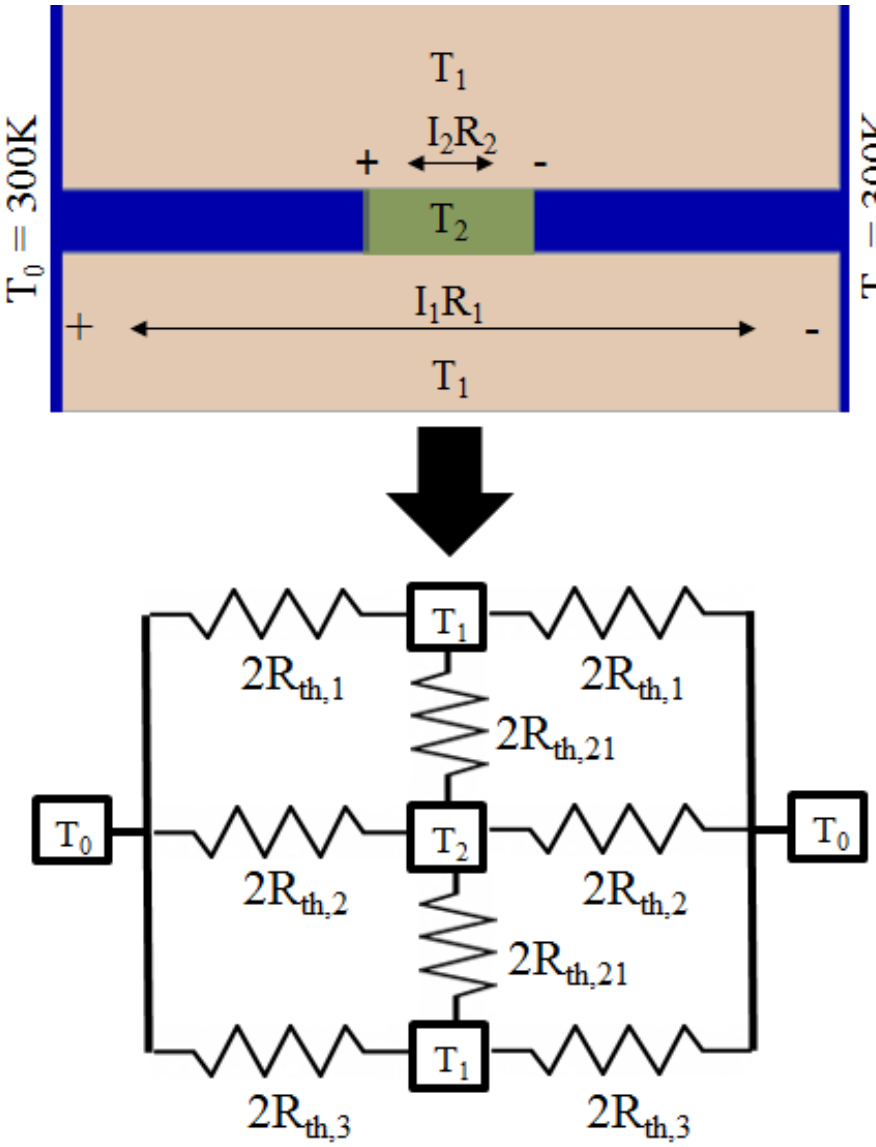

Figure 2.3: Equivalent thermal circuit for the valve element.

To determine the temperature in the different parts of the element and the graphene resistances which depends on the temperature,a system of coupled

equations must be solved. For each region, R_i is the nominal electrical resistance at room temperature, $R_{th,i}$ is the thermal resistances to the substrate, I_i is the current flowing through the graphene resistor, ΔT_i is the change in temperature of the region.

1. Kirchoff's current law (KCL) requires the total current flowing through the difference resistors to be equal to the input current:

$$2I_1 + I_2 = I \tag{2.13}$$

2. Kirchoff's voltage law (KVL) requires the potential drop across the resistors to be the same:

$$I_1 R_1(1 + \alpha\Delta T_1) = I_2 R_2(1 + \alpha\Delta T_2) \tag{2.14}$$

3. The change in temperature is the input power times thermal resistance:

$$I_1^2 R_1(1 + \alpha\Delta T_1) = \frac{\Delta T_1}{R_{th,1}} + \frac{\Delta T_1 - \Delta T_2}{R_{th,21}} \tag{2.15}$$

$$I_2^2 R_2(1 + \alpha\Delta T_2) = \frac{\Delta T_2}{R_{th,2}} + \frac{\Delta T_2 - \Delta T_1}{R_{th,21}} \tag{2.16}$$

   The second term in each of the above equation accounts for heat flow between the different regions of the membrane.

This system of coupled equations was solved numerically in MATLAB since the change in temperature is implicitly defined in terms of source current and element resistance, which in turn depends on the temperature. Figure 2.4A shows the predicted change in temperature of regions I and II as a function of input current to the element. The temperatures of the two regions do not differ, until at high source current $> 0.8\ mA$, as shown in the zoom-in plot. Figure 2.4B plots

resistance-dependence of the element versus average change in temperature. In the above analysis, the piezo-resistive change in graphene resistance is not considered since temperature alone accounts for a > 4× change from the baseline resistance.

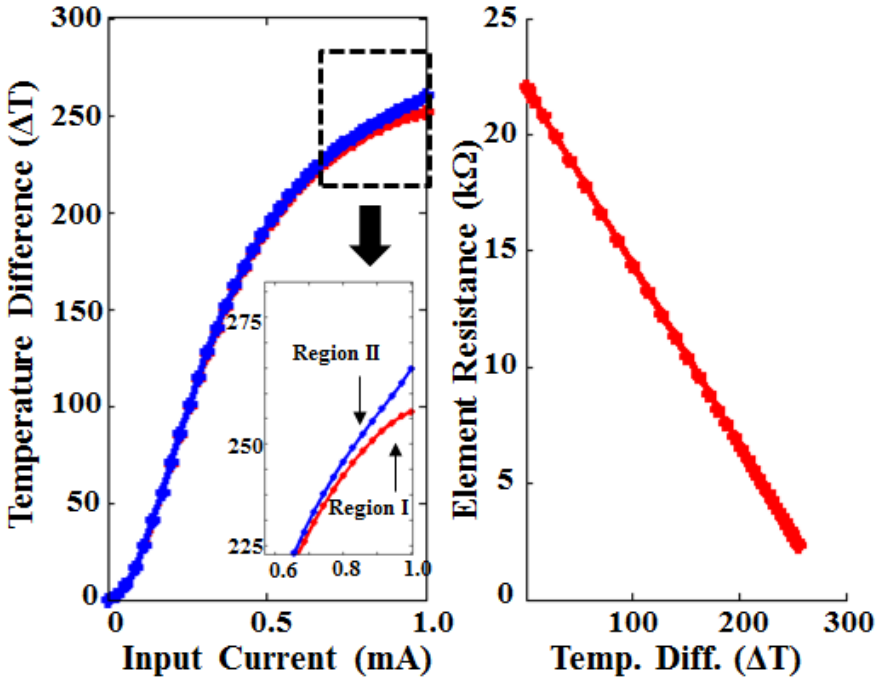

Figure 2.4: Estimated increase in the temperature of region II of the valve vs. input current and corresponding change in total element resistance vs. temperature due to the TCR of graphene.

2.2.3 Thermo-mechanical Stress Analysis

The out-of-plane deflection produced in the membrane element and the corresponding thermal stresses generated can be estimated using the temperatures obtained from the analysis above as a function of source current, shown in Figure 2.4. The dynamic and static constituent equations for the bending of beams

made with two layers have been derived previously [78]. In the previous analyses, one layer is piezoelectric and the second layer is purely elastic. Closed form solutions for the radius of curvature of such a beam have also been derived [79]. This bimorph analysis has also been extended to multi-layer stacks [80]. All of these analyses trace back to Timoshenko's analysis [81] of the deflection of a thermal bimorph, made of materials with different thermal expansion coefficients and Young's moduli. The thermo-mechanical stress analysis presented here uses Timoschenko's thermal bimorph analysis for the nickel-nitride bimorph of the valve structure. The thermal stress varies along the membrane and a closed-form solution can is analytically difficult to achieve. Instead a simpler one-dimensional model of stress is used. This model neglects the graphene because of its significantly lower thickness compared to nickel and nitride.

Table 2.3: Thermo-Mechanical Stress Analysis

Parameter	**Value**
Thermal expansion coefficient of silicon nitride α_{SiN}	3.3 $ppm/^oC$
Thermal expansion coefficient of nitride α_{SiN}	13 $ppm/^oC$
Ratio of thicknesses of nickel and nitride $m = \frac{E_{Ni}}{E_{SiN}}$	0.125
Ratio of Young's moduli of nickel and nitride $n = \frac{t_{Ni}}{t_{SiN}}$	0.645
total thickness of the stack $h = t_{SiN} + t_{Ni}$	405 nm

The element is analyzed as a beam with two fixed ends and a point load at the center due to the heating. Due to the symmetry of this structure, one

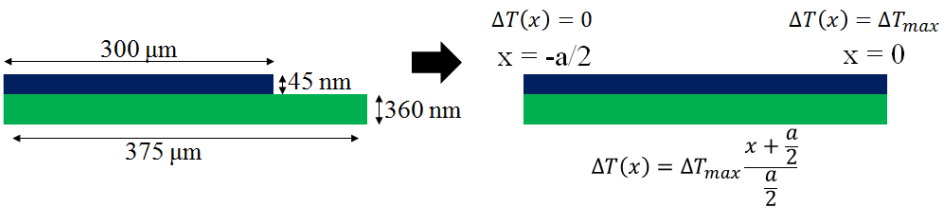

Figure 2.5: Nickel-nitride bimorph used for estimating valve deflection and the temperature gradient assumed along the X-axis.

can analyze half of it about $x = 0$. In this device, the length of a nickel finger $L_f = 300\ \mu m$ and half the valve dimension $\frac{a}{2} = 375\ \mu m$ are comparable. To further simplify the analysis, the deflection of the element is determined assuming the nickel extends to the center of the membrane. The radius of curvature, ρ, for this bimorph is given by [81]:

$$\rho = \frac{6(\alpha_{SiN} - \alpha_{Ni})\Delta T(1+m)^2}{h(3(1+m)^2 + (1+mn)(m^2 + \frac{1}{mn}))} \tag{2.17}$$

The parameters used here are summarized in Table 2.3. The temperature dependence on distance from the mid-axis of the valve can be approximated to be linear because the power dissipation predominantly occurs at the center of the valve where the graphene resistance is the highest (shown in Figure 2.5). Thus, the temperature difference ΔT from the substrate varies as:

$$\Delta T(x) = \Delta T_{max} \frac{x + \frac{a}{2}}{\frac{a}{2}} \tag{2.18}$$

Where ΔT_{max} is the maximum temperature, at the center of the valve ($x = 0$). The radius of curvature can be approximated as $\frac{1}{\rho} = \frac{d^2y}{dx^2}$, derived for small deflections,and can be integrated twice to determine the deflection, applying the fixed-free boundary conditions. The effective spring constant for a clamped-clamped beam is 64 times that of fixed-free beam of the same length [82]. The radius of curvature of a clamped-clamped beam with a force applied at the center, does not have the same form as the fixed-free beam but the final peak dis-

placement is determined using the effective spring constant of the structure.

$$\frac{d^2y}{dx^2} = B\Delta T_{max}\frac{x+\frac{a}{2}}{\frac{a}{2}} \tag{2.19}$$

Here B is the constant multiplier in the expression for radius of curvature:

$$B = \frac{6(\alpha_{SiN} - \alpha_{Ni})(1+m)^2}{h(3(1+m)^2 + (1+mn)(m^2 + \frac{1}{mn}))} \tag{2.20}$$

Integrating twice and setting $\frac{dy}{dx}(x = \frac{-a}{2}) = 0$ and $y(x = \frac{-a}{2}) = 0$,

$$y(x=0) = B\Delta T_{max}\frac{\frac{(x+\frac{a}{2})^3}{6}}{\frac{a}{2}} = B\Delta T_{max}\frac{a^2}{24} \tag{2.21}$$

The expected deflection amplitude is:

$$y_{max} = \frac{1}{64}B\Delta T_{max}\frac{a^2}{24} \tag{2.22}$$

Region II of the membrane element is mechanically coupled to the regions I and II. The same analysis applies for regions I and III where the bimorph is formed by graphene and nitride. However, the thickness of Si_xN_y is 100× of graphene, even though graphene's Young's modulus is 5× higher. The value of the parameter B in equation 2.20 is $B = 10.56$ for the nickel-nitride bimorph whereas for that of the graphene-nitride bimorph $B = 0.662$. So the bending produced due to the heating of the graphene-nitride bimorph is negligible compared to the nickel-nitride bimorph.

For a given temperature difference ΔT between the center of the valve and substrate, the maximum bending stress produced [81] is:

$$\sigma_{bend} = \frac{6}{h^2}\frac{3}{2}(E_{Ni}I_1 + E_{SiN}I_2)\frac{(\alpha_2 - \alpha_1)\Delta T}{h} \tag{2.23}$$

Here the moments of inertia $I_1 = \frac{t_{Ni}^3}{12}$ and $I_2 = \frac{t_{SiN}^3}{12}$ are normalized to the width of the bimorph.

The expected bending stress plotted as a function of input current is plotted in Figure 2.6. This stress occurs in between the electrodes. Several papers have previously reported the yield strength of silicon nitride previously between 100−2400 MPa depending on processing temperature, deposition process used (low pressure, atmospheric pressure, plasma enhanced), density of resultant nitride produced and the thickness of the films [83, 84, 85, 86]. The typical yield strength of thin-film LPVCVD silicon nitride is $\sim 300 - 400\ MPa$ [85, 86]. Based on process parameter variations leading to a range of yield strengths from 300 MPa to 400 MPa, the required source currents to trigger the element vary from 0.54 mA to 0.92 mA. Since the simplified analysis does not account for the length of the nickel finger being less than half the membrane length, the actual current required to fracture the valve is expected to be higher.

2.3 Valve Fabrication

The valve fabrication process is shown in Figure 2.7. A 360 nm thick low-pressure chemical vapor deposition (LPCVD) silicon nitride is deposited on double-side polished $1 - 10\ \Omega - cm$ resistivity n-type doped silicon substrates of 0.5 mm thickness (step 2). The Si_xN_y film on the backside is patterned with a reactive ion-etch (RIE) of CHF_3/O_2 to expose silicon for eventual release of nitride membranes on the front side (step 3). Next, a 45-nm thick nickel was evaporated on the front side of the wafer and patterned to form electrodes using a lift-off process (step 4). After this, 30 % KOH by weight in DI water at 85 ^oC was used to etch the exposed silicon from the backside while protecting the frontside using an AMMT holder (step 5).

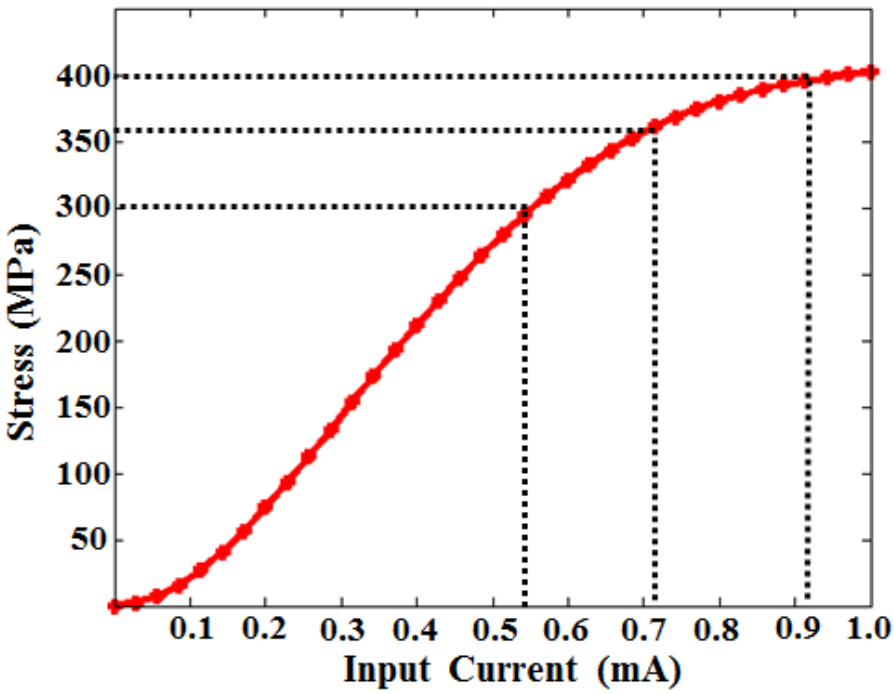

Figure 2.6: Analytically estimated stress produced in the valve element versus input current in one finger of the nickel electrode. Based on the yield strength of the nitride film, the current needed to fracture it can analytically determined from the graph.

Graphene was grown on a 25 μm-thick copper foil in a FirstNano carbon nanotube/graphene furnace with CVD capability, by flowing methane and hydrogen at 1000^oC. The graphene was confirmed by Raman spectroscopy with a laser at 488 nm [69]. Based on the peaks for graphite, defects and the 2D peak, a $\sim$ 70 : 30 ratio of single layer to bilayer graphene was determined for the films fabricated. To transfer the graphene on the devices, a graphene transfer process was used with Poly(methyl methacrylate) (PMMA) [70] as a handle layer (not shown). PMMA was spun on top of the copper foil using a dummy silicon wafer as a holder for the foil. This was followed by etching of copper in ferric chloride and rinsing in multiple DI water baths to clean the graphene of contaminants such as chloride ions. The graphene-PMMA stack was trans-

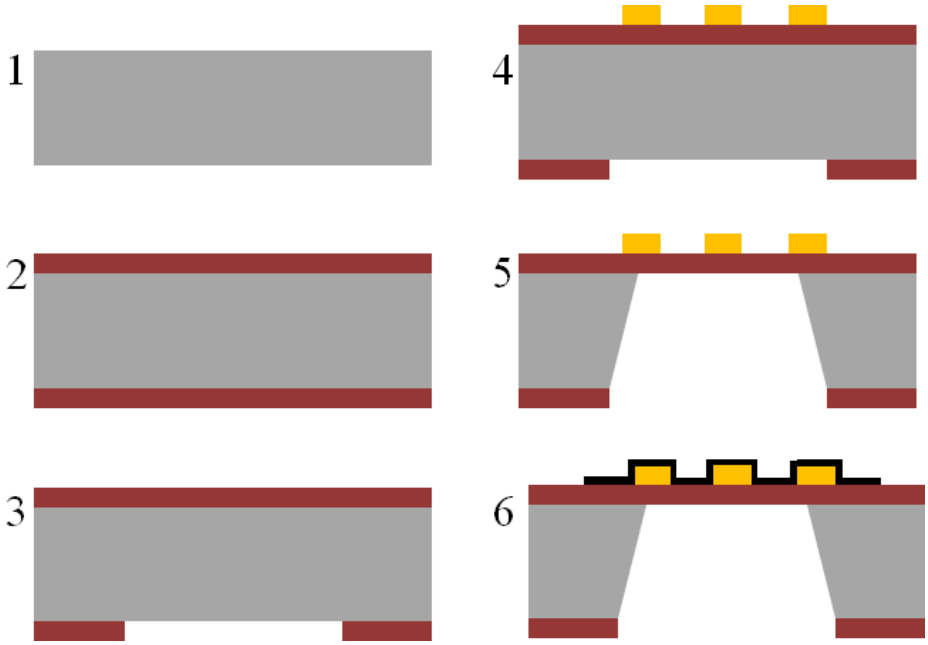

Figure 2.7: Device Fabrication Process - 1. 500 μm silicon wafer. 2. 360 nm LPCVD silicon nitride (Si_xN_y) deposited on both sides of the wafer. 3. RIE etch to pattern nitride on the backside 4. 45 nm nickel deposited by lift-off for contact to graphene. 5. KOH etching with 30 % by weight solution in DI water. 6. Graphene transfer and patterning with oxygen plasma for confining it to the membrane region for the valves.

ferred to the nitride membrane (step 6). SPR 220 3.0 photo-resist was spun-coat and patterned on top of the graphene-PMMA stack, and was patterned by contact lithography followed by RIE etching with O_2 plasma to confine graphene to the nitride membrane. The etch was terminated on the nitride on the top-side to form the valve membranes. The devices were adhesively bonded to the PC boards, and wirebonds were made from the PCB to the metal contacts on the valve electrodes.

2.4 Experiments

2.4.1 I-V Measurements of Graphene Resistors

To characterize Joule heating of the graphene resistors of the valve as a function of input power, a Keithley 2400 was used to source current quasi-statically through the graphene. This allows the valve to thermally equilibriate at each current value. A compliance voltage of 210 V was set for the resistors. The graphene resistor is on a membrane of $(750 \times 750)\ \mu m^2$and there are 7 metal fingers, the total current is distributed between the fingers in parallel. The valve surface temperature was measured with a FLIR T300 IR camera, with a 5 mm working distance objective lens without any magnification. Figure 2.8A shows the measured peak valve surface temperature and as well as the temperature predicted by the analytical model, as a function of input current in one finger. Figure 2.8B shows the measured graphene resistance versus temperature of one valve-element modeled in the previous section and the expected resistance from analytical calculations. The $30 \times 30\ \mu m^2$ pixel size of the IR camera limits the effective resolution temperature gradients and differences on the different parts of the valve. Figure 2.8C shows representative IR images of the valve surface at $T = 23.5\ ^oC$ and $T = 88.7\ ^oC$ respectively. The measured temperature trend matches the analytical model with good agreement, given the approximate 1D nature of the model.

It has been shown that graphene resistance is governed by band-gap renormalization and the carrier scattering on phonons [71]. Band-gap renormalization is the change in the intrinsic band-gap of the material due to the presence of impurities and dopants. In graphene, this occurs during the transfer process

using $FeCl_3$ which dopes the graphene with chloride ions. The measured resistance tracks the expected resistance from room temperature to $T = 200\ ^oC$. Beyond this temperature, there is substantial deviation from the expected decreased. This deviation may be attributed to the model used, which assumes linear dependence of resistance on temperature and ignores higher order effects such as a positive TCR coefficient with ΔT^2-dependence. Additionally, based on the conditions used for graphene-growth, the competing effect of increase in carriers in graphene with temperature (leading to decrease in resistance) and increase in phononic interactions with the lattice (leading to increase in resistance) may lead to a plateauing of the resistance, as observed in the device. Experimentally, it was observed that the peak power required to fracture the valve with quasi-static power ramp is 29.5 mW with 0.91 mA input current in the element (or 6.5 mA total driven current in the valve). This is on the upper end of the range in the analysis, predicting a yield strength of $\sim$ 395 MPa.

2.4.2 Valve Out-of-plane Deflection

A Polytek Topography Measurement System (TMS) was used to measure the surface deflection along the mid-axis of the valve as a function of change in graphene current-driven temperature, and compared this to the analytical model for membrane deflection. Figure 2.9A shows color-coded deflections for the central region of the membrane between fingers. As the power across the graphene resistor is increased, the peak-to-peak valve deflection increases as the thermo-mechanical stresses increase with increasing temperature. The deflection along the mid-axis is plotted in Figure 2.9B, and the data matches the analytically predicted peak-deflection closely (Figure 2.9C). The slope of the data

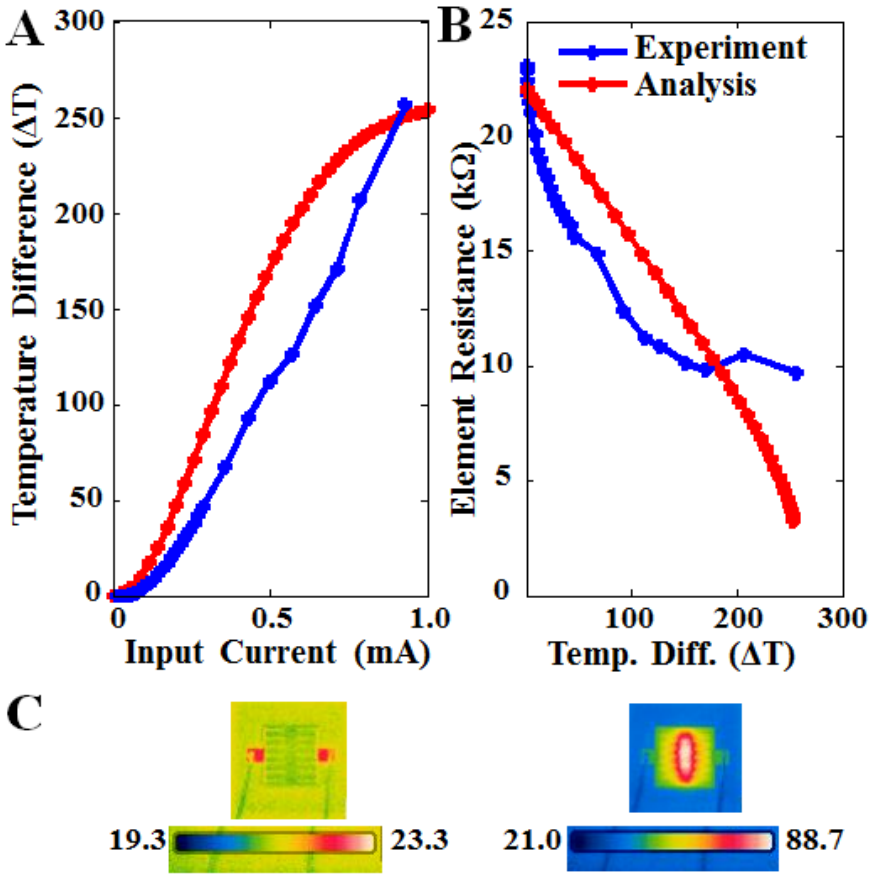

Figure 2.8: A). Analytical model and experimental data for change in valve temperature above ambient as a function of input current in one nickel finger and B). the corresponding change in graphene resistance. C). Characteristic IR images of the valve surface with FLIR T300 IR camera, close to room temperature and during a quasi-static temperature ramp.

indicates a 8 $nm/^oC$ rate of peak displacement. It was observed that at much higher input powers, the deflection profile no longer follows the periodic profile enforced by the electrode fingers. The maximum measured peak-to-peak displacement before the valve fracturing is 4.1 μm for $\Delta T = 240\ ^oC$ but the periodic deflection along the mid-axis has a longer wavelength than the inter-electrode spacing at this input power. This is a potential outcome of the mem-

brane buckling out of plane leading to minimization of surface energy due to bending [87].

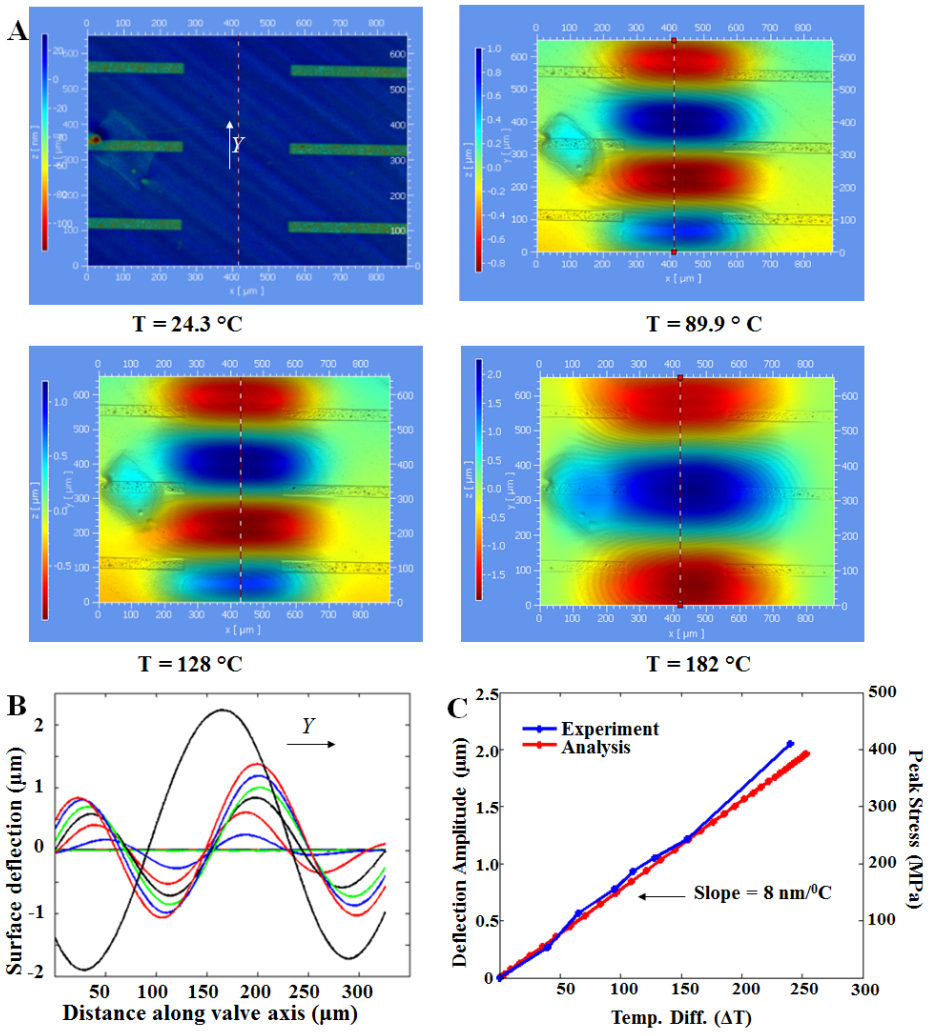

Figure 2.9: A). Surface topography maps with the Polytek Topography Measurement System (TMS) of the center of the valve with quasi-static heating at four different temperatures. IR measurements to record the temperature were done separately to characterize the valve temperature as a function of input power. B). Deflection along the mid-axis of the valve for increasing valve temperatures C). Analytical and experimental data for valve surface deflection vs. peak temperature on the valve surface.

2.4.3 Surface Topography of Fractured Valve Surface

In order to verify the fracturing of the graphene-on-nitride valve with thermo-mechanical stress, the valve surface was optically imaged before and after triggering (Figure 2.10A and B). As seen in Figure 2.10B, the central portion of the valve is completely removed upon valve-triggering. Figure 2.10C shows the optically imaged topography, using the TMS, on the part of the valve enclosed by the dotted line in B. The peak-to-peak nitride fragment deflection are > $40\mu m$, measured in figure 2.10D.

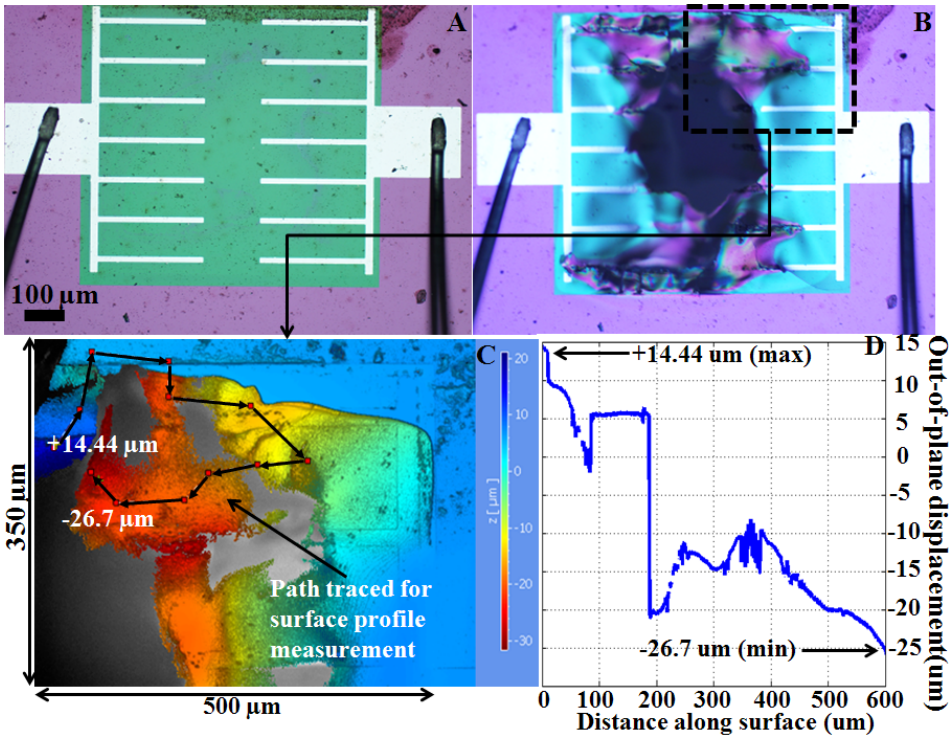

Figure 2.10: Optical micrographs of the valve A). before and B). after triggering. C). Valve surface topography characterized with white-light interferometry D). Plot of the surface deflection along the traced outline on the valve surface in B.

2.4.4 Pulsed-powered Triggering

Quasi-static valve triggering has low fracture-power but requires high total energy because the power is ramped slowly to maintain a slowly increasing temperature. This slow rate leads to steady state energy loss to the silicon frame used for anchoring the valve. In order to reduce the total energy required for triggering the valve, higher power can be pulsed into the graphene resistor for a shorter duration of time to minimize the thermal losses. The optimal rate of heating is related to the thermal time constant of the valve $\tau_{thermal}$. The thermal time constant of the valve membrane is the time it takes to reach $\frac{1}{e}$ of the steady state temperature for a step input for the circuit shown in Figure 2.11. Pulsing current through the graphene any faster than this time constant does not allow the temperature changes to occur any faster, while consuming higher input power. Thus, the total energy consumption needed for fracturing can be minimized by actuation on the time scales of the membrane thermal constant.

$$\tau_{thermal} = R_{th}C_{th} \tag{2.24}$$

$R_{th} = 4.87 \times 10^4 K/W$ is the thermal resistance estimated in the device design section and C_{th} is the total thermal capacitance of the element made of nickel and silicon nitride films.

$$C_{th} = \Sigma \rho_i V_i C_{p,i} \tag{2.25}$$

Here, ρ is the density of each material, V is its volume and C_p is the heat capacity for each element i.e. silicon nitride, nickel, graphene in the summation of thermal capacitances. For the membrane under consideration, $C_{th} = 6.97 \times 10^{-8} J/K$, leading to the thermal time constant $\tau_{thermal} = 3.4\ msec$.

For the purpose of confirming lowering of the total energy, the valves were

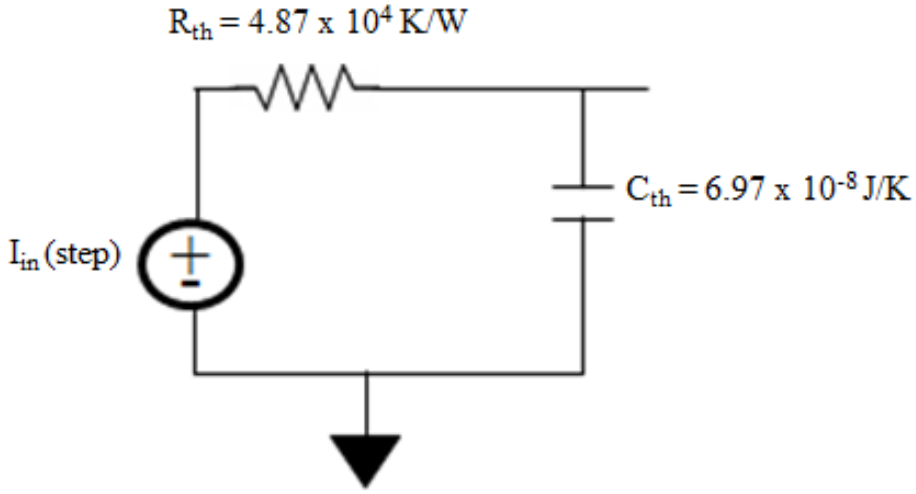

Figure 2.11: Equivalent thermal circuit of the valve for pulse-powered fracturing.

fractured with increasing powers, corresponding to decreasing fracture times. The setup for pulse-powered triggering is shown in Figure 2.12A. The device under test (DUT) is connected in series with a resistor of comparable resistance to that of the graphene resistor. Current is pulsed through the DUT and the duration for which the series resistor conducts is measured on the oscilloscope. For the duration the DUT is intact and the graphene conducts current, a voltage is produced across the series resistor. The Joule heating power is:

$$P_{in} = I^2 R \tag{2.26}$$

Here, the current I is varied to test the fracture time for various input powers and for a nominal graphene resistance of $R = 3k\Omega$. As soon as the membrane fractures, the resistor stops conducting. This duration of actuation as a function of input power and the total energy of valve triggering are plotted in 2.12B [88]. As expected, the trigger power increases as the trigger duration decreases. However, there is a net saving in energy since the duration of fracturing greatly compensates for the power expended. The benefits of pulse-powered trigger-

ing are experimentally optimized to minimize the expended energy for a trigger time of 12.45 $msec$ with P_{in} = 142 mW. At higher P_{in}, the increase in power outweighs the trigger time, leading to increase in trigger energy. The analytical model assumes that the thermal expansion coefficient of graphene is linear whereas experimentally, a quadratic dependence was observed at temperatures above 120^oC. The exact resistance-temperature dependence varies depending on the process used for graphene growth. This is a possible reason in the estimated bending stress being higher than what is actually needed during triggering.

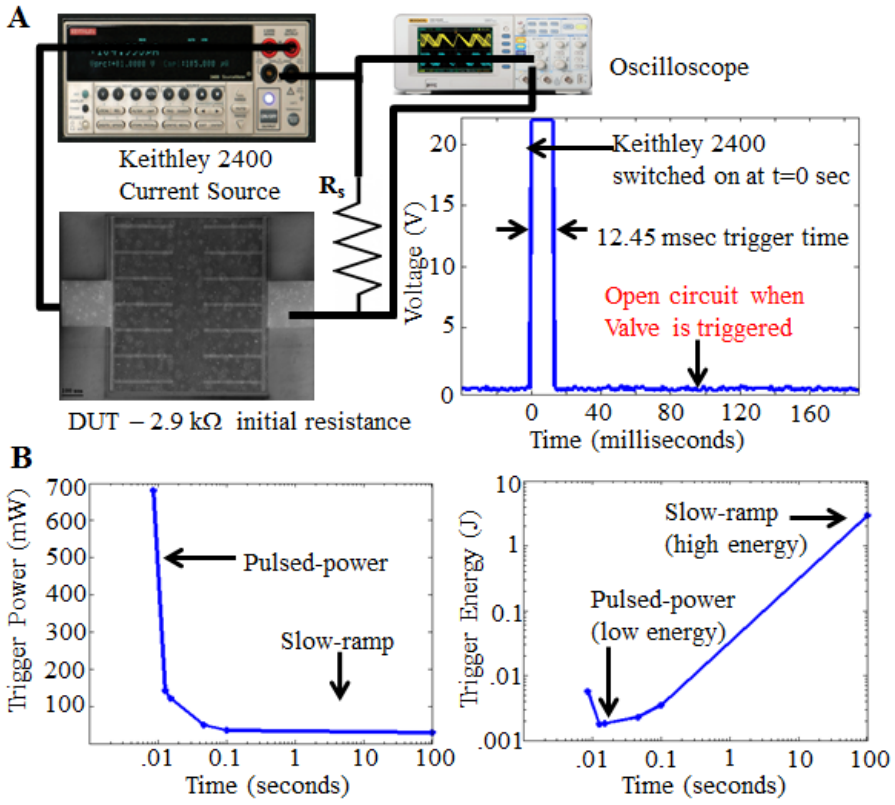

Figure 2.12: A. Setup for pulse-powered triggering with a series resistor to capture trigger time B. Trigger power and trigger energy as a function of trigger time

2.4.5 Valve-Sealing Test

The valve's seal against standard gases, particularly oxygen, at standard temperature and pressure is an important aspect of the valve. The setup for testing the valve as a seal is shown in Figure 2.13. A syringe with 3 ml air at atmospheric pressure was adhesively bonded to the backside of a valve with epoxy glue. $V_1 = 3$ ml of air at atmospheric pressure ($P = 10^5$ bar) corresponds to $n_1 = 0.12$ millimoles (mmol) of air according to the ideal gas law:

$$PV = nRT \tag{2.27}$$

$R = 8.314$ J/(mol.K) is the gas constant and the ambient temperature was T = 300 K. The test structure was then left alone for 12 hours to allow for leaks, if any. This assembly was then placed in a vacuum-chamber with a total volume of $V_2 = 1650$ ml and the chamber was pumped to $P_2 = 4$ mbar. The number of moles of air inside the chamber n_2 was calculated as:

$$n_2 = \frac{P_2 V_2}{RT} = 0.25\ mmol \tag{2.28}$$

The valve was then triggered, releasing the sealed air inside the syringe. Assuming there were no leaks before triggering, the chamber and the syringe had a total of $n_1 + n_2 = 0.37$ mmol of air. The final gas pressure in the chamber was expected to be:

$$P_{final} = \frac{(n_1 + n_2)RT}{V_2} = 5.9\ mbar \tag{2.29}$$

The final volume is V_2, the total volume of the chamber since the syringe volume is accounted for inside the chamber. The analysis for triggering is included in Table 2.4. The sensitivity of the pressure gauge is 0.1 *mbar*. The initial observed pressure spike to 5.4 *mbar* is less than the expected 5.9 *mbar*. This is due to the finite time taken by the air released from the syringe to reach the pressure gauge. Within a few minutes, the pressure reaches ~ 6 *mbar*, as expected.

Table 2.4: Sealing Test Analysis

Before Triggering			
Region	**Pressure (bar)**	**Volume (ml)**	**Millimoles of air (mmol)**
Chamber	4×10^{-3}	1650	0.25
Valve-Syringe	1	3	0.12
After Triggering			
Final total volume (ml)		1650	
Total air in chamber (mmol)		0.37	
Expected pressure (bar)		5.9×10^{-3}	
Observed instantaneous pressure (bar)		5.4×10^{-3}	

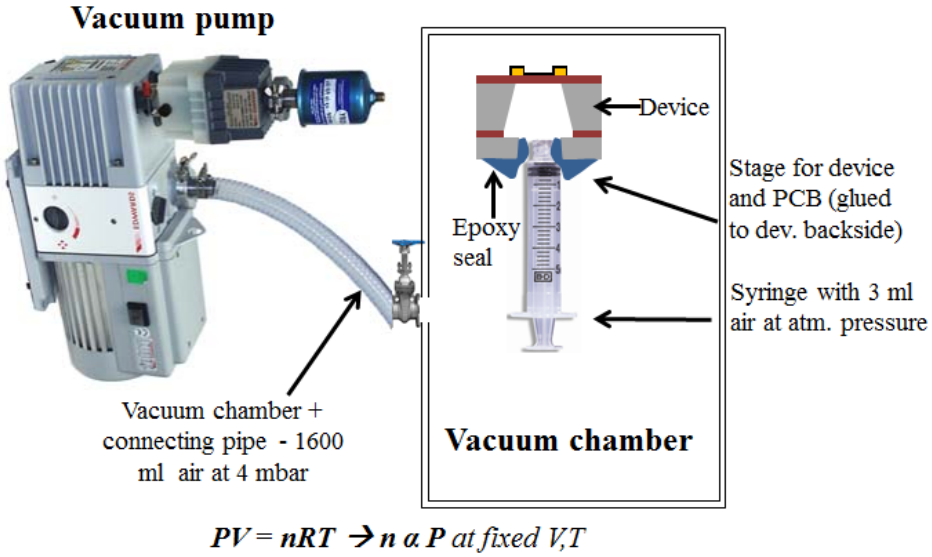

Figure 2.13: Setup for measuring the sealing test in vacuum with the valve-syringe assembly

2.4.6 High Speed Visualization of the Triggering Mechanism

A Keyence VW-9000 High Speed Microscope was used to image the valve surface and observe the triggering. Figure 2.14 shows the triggering highlight. The

camera records images at 23,000 frames per second with a frame time of 43.5 μs. As the current is driven through the graphene, the heating is initially limited by the thermal time constant of the material (1-2). As the valve surface temperature increases, the valve surface deflects out-of-the-plane (3) producing bending moments along and orthogonal to the fingers and maximum stress between the pairs of electrodes. The analysis in section 2 treats the fingers as an infinitely repeating periodic structure, orthogonal to the direction of current flow. However, the fabricated device has a termination at the top and bottom due to the clamped boundary of the membrane. The exact location of membrane fracture between the fingers depends on local variations in the nitride stress, but occurs predominantly between the pairs of fingers closest to the anchor where the stress is highest. Consequently, the nitride membrane cracks in this region when the stress σ_{bend} given in equation 2.23 exceeds the yield stress of nitride (4-5). This cracks propagates along the mid-axis of the membrane where the stress is maximum (6-8), according to 2.23 at $x = 0$. The total time of valve-fracture is approximately 10 milliseconds, in agreement with the time estimated from pulse-powered triggering with electrical measurements. The high speed microscope imaging thus helps validate the predictions from the analytical model.

2.5 Discussion

The single-shot valve presented here employs thermo-mechanical triggering produced by Joule heating of the graphene resistor. This section discusses the need for single-shot valves to expose reactive materials, the rationale for the use of graphene for the resistive heater and silicon nitride for the structural material as well as device scaling parameters for future designs.

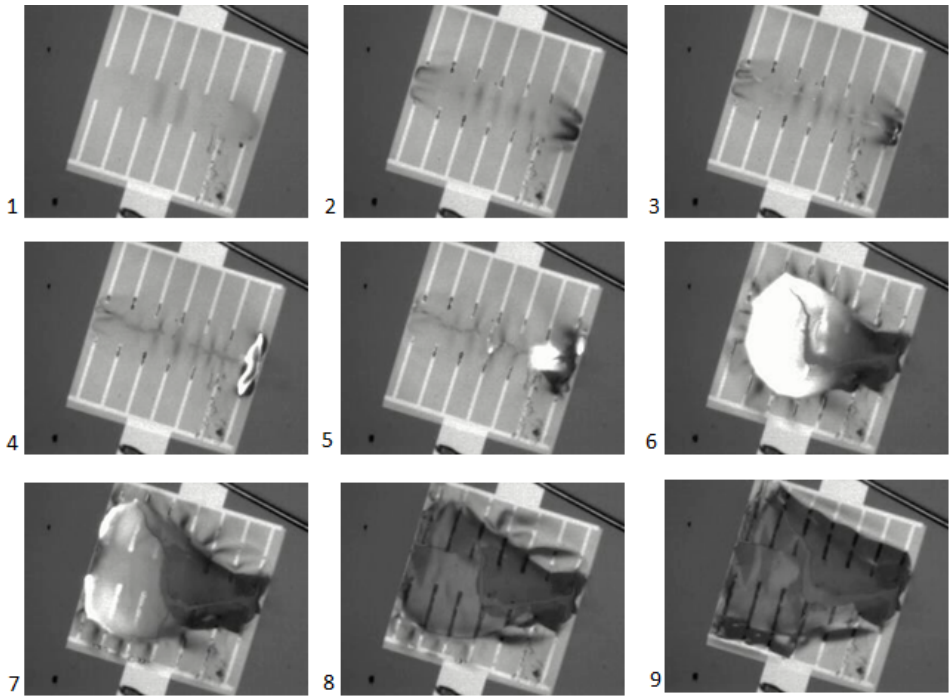

Figure 2.14: Optical photographs of the high speed camera triggering sequence of images of a membrane fracture

2.5.1 Need for One-shot Valves

Many applications need valves for protecting reactive materials from the ambient air for long-time storage without the need for re-filling the material that is stored within. There can often be a long lead-time between packaging of reactive materials inside the valves and eventually exposing them. During the period from packaging to valve-triggering, it is key that the valve remains intact and provides an effective barrier while also ensuring that it opens up on-demand and with high yield and reliability. Some examples of applications that need single-shot valves with these constraints are:

1. Reactive fuel storage in small space systems such as nano-satellites, which must survive large shocks or high pressure gradients across them [64, 89].

2. Chemical analysis or ingestible biomedical drug delivery systems for precisely controlled one-time delivery of specific volumes of drugs [65].
3. Reactive alkali metal storage for vaporization of transient electronics which must be hermetically sealed from atmospheric oxygen before being exposed for exothermic oxidation and substrate vaporization [90].

MEMS valves that have been previously developed for single-use applications are for systems have targeted high-pressure differential operation [65], relied on over-pressure of stored fluids [64] for operation or used pyrotechnic actuation which can minimize the energy of actuation with volatile fuel-based propulsion [63]. Multi-use MEMS valves have also been reported with piezoelectric [91], photo-sensitive [92] and electrostatic [93] actuation with low-power and energy but they do not have large requirements for mechanical motion of the valve material. The valve design reported here uses one-shot fracturing of Si_xN_y membranes with thermo-mechanical stress generation to produce large cavities $> 200\ \mu m \times 200 \mu m$, at the end of life-time of transient electronics with low-power.

2.5.2 Role of Graphene in Triggering

Graphene was initially chosen as the valve material because it provide an effective barrier to gas diffusion [66]. This is important for sealing against atmospheric oxygen in applications such as highly volatile alkali metals polymer packages for vaporizable electronics [90]. The graphene barrier becomes especially useful in the limiting case of ultra-thin nitride membranes as the structural layer for the valve material, where diffusion of gases through pin-holes in the nitride may be a concern. However, the 360 nm thick nitride of the valves

provides an effective barrier on its own.

This paper demonstrates a utility of high current-carrying capacity of graphene. Graphene is critical for the valve-functionality as a two-dimensional heater with high current-carrying capacity (10^8 A/cm^2) which is several orders of magnitude higher than present-day metal interconnects [94], while minimizing the membrane stiffness. For example, copper has a maximum current density J_{max} = 500 A/cm^2 which is 6 orders of magnitude smaller than that of graphene [94]. This mitigates the possibility of failure in triggering due to local oxidation of the metal or electro-migration [95] which causes the metal to melt or produces faults in it without triggering. For valve-fracturing between a given pair of electrode fingers, the maximum current density with 1 mA current flowing in a finger is 1.6×10^4 A/cm^2. This is lower than the current-carrying limit of graphene but large to trigger failure of valves with just metal heaters. Valves with nickel metal heaters for triggering have also been fabricated, but these valves do not demonstrate fracturing and have failure due to faults in the metal at high source currents. The graphene-on-nitride valves have 100% success in triggering with > 200 devices tested. Graphene as a 2-D resistor is an ideal resistive heater for the thermo-mechanical fracturing of the valve.

2.5.3 Device Scaling

With the parameters used to express device dimensions and parameters such as drive current I and heating power P_{in}, scaling laws can be determine for the device. The electrical resistance for Joule heating is dependent only on the

graphene thermal coefficient of resistance (α) and scales as:

$$R_{elec} \propto a(1 + \alpha\Delta T) \tag{2.30}$$

The input power depends on the drive current I and resistance as:

$$P_{in} \propto I^2 a(1 + \alpha\Delta T) \tag{2.31}$$

The increase in temperature ΔT is proportional to the thermal resistance. For valves with silicon nitride thinner than 150 nm, the graphene thermal resistance is comparable to that of nitride because the ratio of the products of thermal conductivity (κ) and thickness (t) for nitride and graphene is ~ 2, and the graphene resistance adds in parallel to the nitride resistance. The thermal resistance is:

$$R_{therm} \propto \frac{a}{1 + Ct_{SiN}} \tag{2.32}$$

Here, C is a constant which accounts for graphene resistance and thermal parameters such as conductivities of silicon and nickel, since the thickness of graphene does not scale. The change in temperature is:

$$\Delta T \propto P_{in} \frac{a}{1 + Ct_{SiN}} \tag{2.33}$$

Combining equations 2.31, 2.32 and 2.33, the dependence of Joule heating power produced as a function of input current is:

$$P_{in} \propto I^2 a(1 + \alpha P_{in} \frac{a}{1 + Ct_{SiN}}) \tag{2.34}$$

Using equation 2.23, the stress-dependence on the metal and nitride thickness is:

$$\sigma_{bend} \propto \frac{E_{Ni} I_1 + E_{SiN} I_2}{h^3} \Delta T \tag{2.35}$$

For $t_{Ni} = 45\ nm$, the contribution to the stress from $I_1 = \frac{t_{Ni}^2}{12}$ is much smaller than the $I_2 = \frac{t_{SiN}^2}{12}$ even for $t_{SiN} = 100\ nm$, the smallest thickness of valves used in the

design here. So the I_1 term is ignored, especially since $E_{Ni} < E_{SiN}$. By combining equations 2.33 and 2.35, the approximate stress-dependence can be written as:

$$\sigma_{bend} \propto \frac{E_{SiN}}{(1 + \frac{t_{Ni}}{t_{SiN}})^3} P_{in} \frac{a}{1 + Ct_{SiN}} \tag{2.36}$$

Equations 2.34 and 2.36 can be co-optimized to minimize the power required for triggering and bending stress. Since the proportionality terms include P_{in}, a closed-form expression cannot be derived for optimum parameters but a design space of parameters can be extracted from this scaling. To harness the benefit of graphene as barrier to gases as well as to reduce the triggering power further, it is necessary to reduce the nitride thickness. Valves with the same lateral dimensions but with reduced thicknesses of 200 *nm* and 100 *nm* have also been tested. For these thicknesses, The graphene thermal resistance is not negligible compared to the nitride. Table 2.5 compares the steady-state triggering power for valves of different thicknesses and compares them to analytical expected trigger powers using equation 2.36, assuming that the required stress is nominally 360 *MPa* for triggering the nitride. The trigger powers predicted analytically are lower than experimental values but show the same trend. In the limiting case of no silicon nitride, only graphene contributes to the thermal resistance and the expected trigger power is 6.7 *mW*, as shown in Figure 2.15. However, the analytical model is no longer valid since the nickel-nitride bimorph no longer exists at this point. Also, the thinner nitride membranes are more susceptible to damage during fabrication since they are more fragile and can impact device yield.

Table 2.5: Device Scaling and Valve Triggering

Nitride Thickness (nm)	Estimated Trigger (mW)	Experimental trigger (mW)
360 *nm*	17.15	29.5
200 *nm*	12.1	18.2
100 *nm*	8.7	13

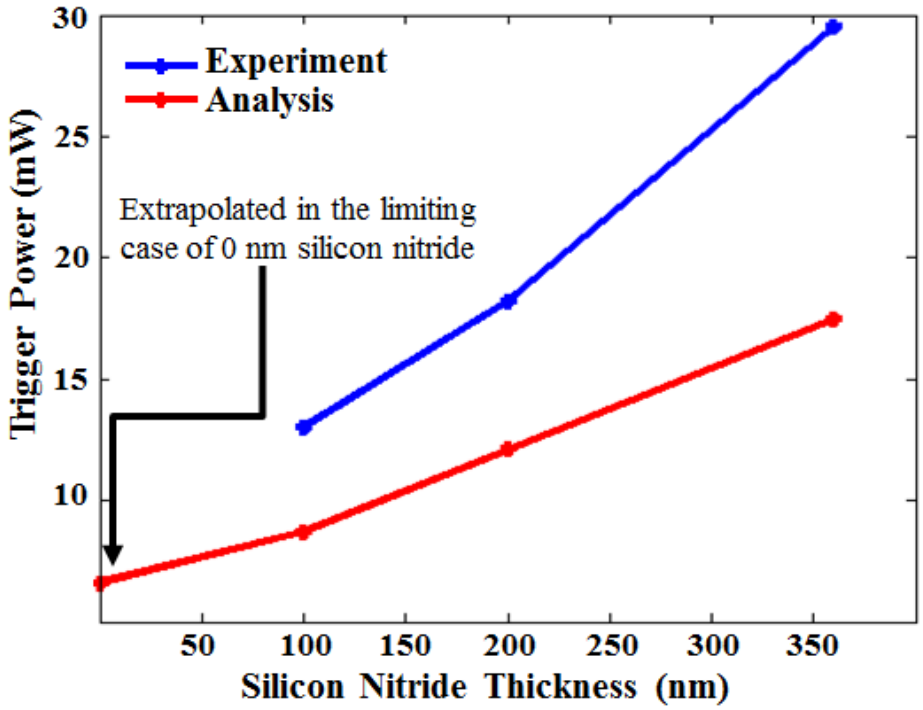

Figure 2.15: Device scaling and power requirements as a function of silicon nitride membrane thickness

2.5.4 Electrode Design

Nickel is the material of choice for the electrodes, because it has low contact resistance and reduced Ohmic losses for interfacing with graphene [96, 97]. Also,

it provides a large contrast in thermal expansion coefficient with that of silicon nitride to provide large membrane actuation to fracture the valve for the same input power. The electrode finger width w_f and the inter-finger spacing λ_f set the ratio of the resistance for regions I-III in the analysis in section II. Qualitatively, the ratio $\frac{w}{\lambda_f}$ is small, the power dissipation from Joule heating occurs at the center of the valve but the graphene resistance also decreases quickly due to the negative thermal coefficient of resistance of graphene. For a large $\frac{w}{\lambda_f}$, the thermal gradient between regions I and II of the membrane is small and higher power will be needed to fracture the membrane. The current design uses $\frac{w}{\lambda_f} = 0.13$. In future designs, the parameter $\frac{w}{\lambda_f}$ can be tuned to reduce the triggering power further.

2.5.5 Role of Si_xN_y

The single-trigger valve presented here has significantly lower power and lower trigger energy compared to previously reported valves in literature [63, 64, 65]. The major reason for reduced energetics requirements is the triggering mechanism that relies on stress-based fracturing, unlike other valves which rely on melting of adhesives or seals and need to overcome large latent heats of fusion of the adhesive material. The melting point of silicon nitride is 1900^oC [98]. By using Si_xN_y as the membrane material for thermo-mechanical triggering, it is only necessary to achieve the maximum required temperature of $\sim 250^oC$ locally to generate the yield stress required to fracture the valve without needing to melt or vaporize the membrane material. This ensures that the valve trigger power and triggering energy is substantially lower.

2.6 Conclusions

In this work, the design, analysis and testing of a novel single shot graphene-on-nitride valve based on thermo-mechanical fracture of tensile silicon nitride membranes is presented. The design of the electrode geometry and the resultant thermo-mechanical triggering mechanism achieved by using a two-dimensional resistive heater such as graphene is analytically derived and confirmed with experiments. The valve serves as an ideal barrier to standard gases at room temperature, including oxygen, for sealing applications such as fuels for pristine reactive alkali metals for vaporizable electronics [90].The trigger power of the valve is $64 - 142mW$ in $15. \pm 43.9$ milliseconds, giving a very low input trigger energy requirement of $2.2\ mJ$.

CHAPTER 3

TRANSIENT MICRO-PACKETS FOR SILICON DIOXIDE AND POLYMER-BASED VAPORIZABLE ELECTRONICS

In the last chapter, a single shot valve which fractures thermo-mechanically and initiates transience in polymer-based vaporizable electronics, was presented [99]. This valve is the key MEMS component and trigger for each unit cell of the arrayed transient substrate. This chapter presents the integration of the valve with polymer micro-packets of high purity rubidium (Rb) and sodium biflouride, $NaHF_2$, which form the unit-cell for the substrate. The stored nano-liter quantities of Rb are exposed on-demand to oxidize it exothermically. The co-packaged $NaHF_2$ also dissociates at 160^oC to release hydrofluoric acid. The heat generated from the Rb reaction is thus used for two purposes: 1). Vaporizing the polymer substrate close to 180^oC. 2). Decomposing the salt to release the acid necessary for etching the oxide-based electronics. With co-packaging of rubidium and $NaHF_2$, a pathway to fully transient packaged electronics is demonstrated. In order to minimize and eventually eliminate non-transient silicon from the system, polymer molding method using SU-8 and PDMS has also been presented.

3.1 System Architecture

Figure 3.1A shows the unit cell of the vaporizable system architecture. The vaporizable polycarbonate (VPC) substrate is composed of a polymer blend, where 30% of the blend is a polycarbonate synthesized based on previous procedures [100], and 70% is poly-(propylene carbonate) PPC, material provided by Novomer Inc. Specific details of the synthesis of this polymer are presented

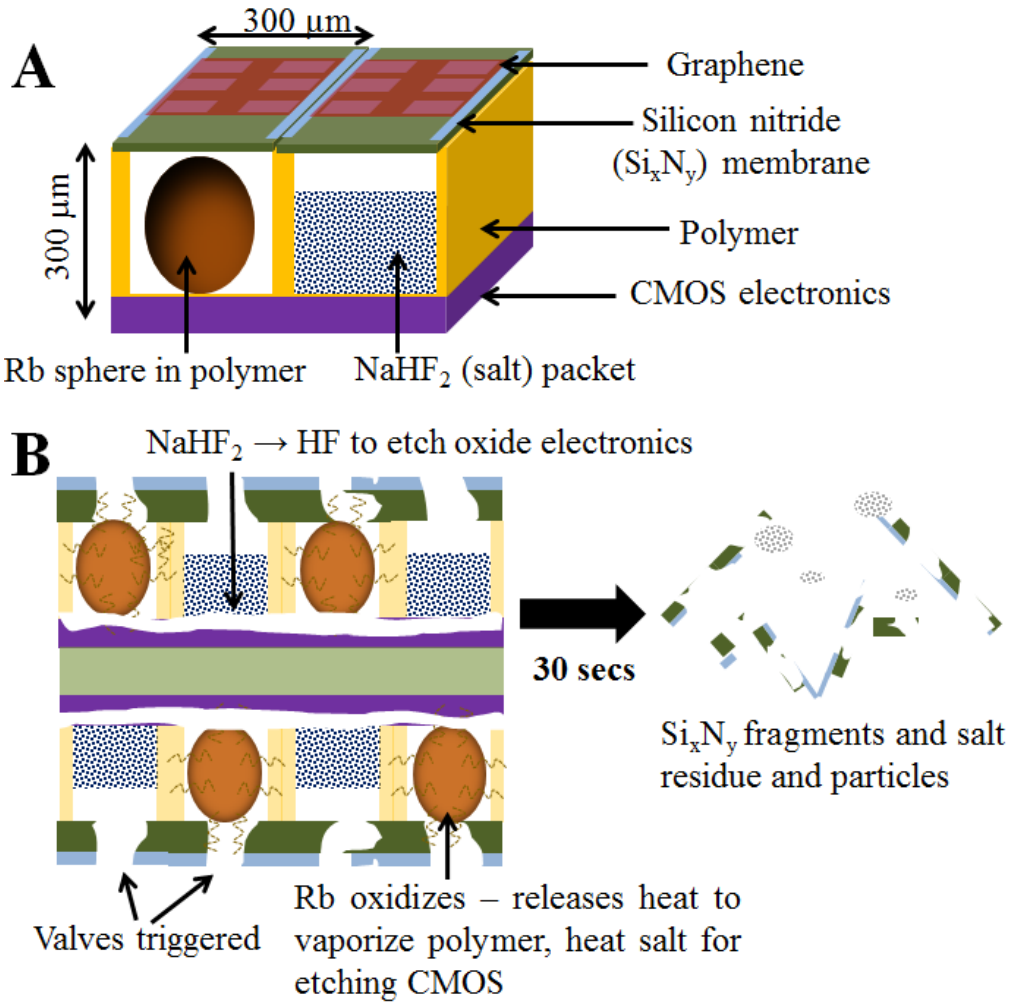

Figure 3.1: A). Unit-cell for transience: VPC substrate cavities are alternatingly filled with rubidium and sodium biflouride ($NaHF_2$), sealed by graphene-on-nitride valves with CMOS electronics as the backing layer. B). Time evolution of system transience: Valves are triggered on millisecond time scales, exposing Rb to oxygen. This releases heat to decompose the VPC and the salt, which releases HF to etch the oxide. The final residue is minimal and consists of silicon nitride, metal fragments.

in [101]. This polymer is designed to be mechanically and thermally stable under standard operating conditions, but to vaporize at 180^oC in the presence of an acid catalyst. Nanoliter droplets of Rb are stored in one polymer chamber, which constitutes one half of the transience unit cell. In order to raise the substrate temperature and vaporize, energy from the exothermic oxidation of Rb is used. Previous research in the *Sonic*MEMS Laboratory has demonstrated wax micropackets of rubidium for long term storage of rubidium [102]. Rb is also a high specific-power density reactive alkali metal, which has been shown to be an excellent fuel for micro-combustion [103]. It oxidizes exothermically and releases sufficient heat, which is used to vaporize the substrate. To protect the Rb from oxygen and atmospheric moisture during ordinary conditions as well as to enable triggered transience, it is critical to have an impermeable seal that can be triggered irreversibly. This is accomplished by the graphene-on-nitride single-shot micro-valves [99].

The CMOS electronics used in the system presented here are obtained from Honeywell and are conventionally fabricated on 5 μm silicon dioxide (SiO_2) substrate, with a handle layer of 500 μm silicon. To reduce thermal mass and to realize targeted oxide substrate transience, the bulk silicon is removed with a thinning process. This leaves behind only the 5 μm oxide layer with small metal and silicon islands for the electronics. In order to etch this substrate, $NaHF_2$ is co-packaged in the other half of the unit cell. $NaHF_2$ is a stable salt at room temperature but decomposes at 160^oC to release hydrofluoric acid (HF). The energy to heat the $NaHF_2$ and release HF also comes from the Rb oxidation reaction, after it has vaporized the barrier between the two halves of the unit cell. With the VPC decomposition and oxide etching, the hygroscopic Rb-oxide (which can be Rb_2O gathers moisture rapidly from the air. Ideally, this leaves behind a clear

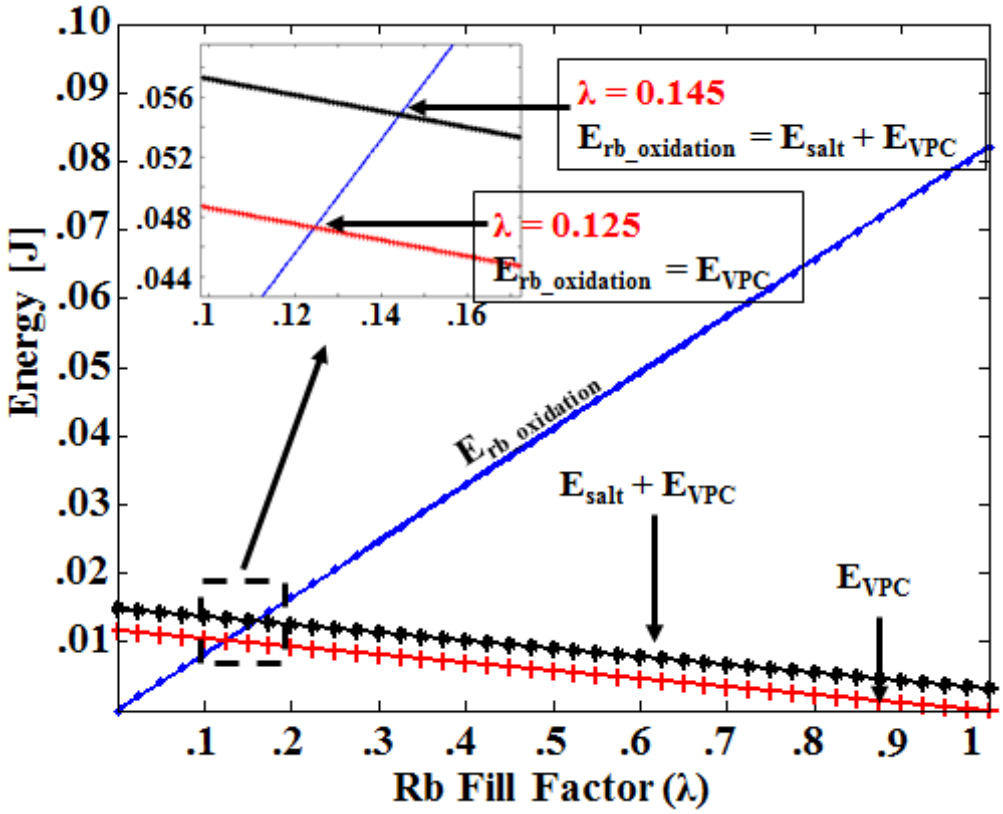

Figure 3.2: Analytical model for energy and stoichiometry constraints for a $(500\ \mu m)^3$ micro-packet vs. Rb fill factor in it. Heat of polymer vaporization is 110 kJ/mol and heat capacity is 1.2 $kJ/(kg.K)$. Rubidium energy is calculated from the enthalpy of formation of Rb2O equal to -169.5 kJ/mol. Oxide thickness is assumed to be 10 μm.

liquid along with minimal residue of silicon nitride and metal fragments from the valves which account for < 5% of the initial material, as shown in Figure 3.1B.

3.2 Transience Energetics

It is critical to choose the relative quantities of the VPC, Rb, and salt appropriately so that the energy obtained from Rb oxidation can be effectively utilized for both, vaporizing the substrate and decomposing the salt to etch the oxide electronics. The energy delivered by Rb oxidation, $E_{Rb_oxidation}$, is given by -

$$E_{Rb_oxidation} = \frac{\Delta H_f V_{Rb} \rho_{Rb}}{A_r} \tag{3.1}$$

Here, ΔH_f is the oxidation enthalpy in J/mol, V_{Rb} is the volume of the Rb droplet in m^3, ρ_{Rb} is Rb-density in kg/m^3 and A_r is the atomic weight of Rb in kg/mol. To determine the quantity of Rb required to heat and vaporize the VPC, the energy delivered by Rb is calculated and is plotted as a function of fill factor λ i.e. fraction of Rb per unit of volume, with the rest of the volume assumed to be occupied by the VPC. This is shown in Figure 3.2. For a fixed total VPC micropacket volume, V_{total} (chosen to be $(500\mu m)^3$ here), $E_{Rb_oxidation}$, scales linearly with λ -

$$V_{Rb} = \lambda V_{total} \tag{3.2}$$

Consequently, the VPC volume, V_{VPC}, in this fixed volume decreases linearly as λ increases

$$V_{VPC} = (1 - \lambda) V_{total} \tag{3.3}$$

The energy, E_{VPC}, to vaporize this VPC is given as

$$E_{VPC} = V_{VPC} \rho_{VPC} (C_p \Delta T + H_{VPC}) \tag{3.4}$$

Here, ρ_{VPC} is the VPC density in kg/m^3, C_p is its heat capacity in $J/(kg.K)$, ΔT is the temperature difference from room temperature to its vaporization temperature in Kelvin, and H_{VPC} is the VPC enthalpy of vaporization in J/kg. $\lambda = 0.0625$

is the break-even point for substrate vaporization, with energy E_{VPC}, assuming 100% energy transfer from Rb oxidation to VPC. To account for alternating chambers of $NaHF_2$ and Rb, the required FF in each Rb micro-packet is twice as much i.e. $\lambda = 0.125$. Stoichiometry constraints are imposed by the quantity of HF released from $NaHF_2$, which is required to etch the thinned oxide electronics

$$NaHF_2 \leftrightarrow NaF + HF \tag{3.5}$$

$$SiO_2 + 6HF \rightarrow H_2SiF_6 + 2H_2O \tag{3.6}$$

The energy required to decompose the salt, E_{salt}, is

$$E_{salt} = m_{salt}C_{salt}(T_{dec} - T_{room}) \tag{3.7}$$

Here, m_{salt} is the mass of $NaHF_2$ in the half VPC chamber (in kg), C_{salt} is the heat capacity of $NaHF_2$ in J/(kg.K) and T_{dec} and T_{room} are decomposition and room temperatures respectively. This analysis assumes that oxide substrate thickness is 10 μm, twice the thickness of thinned dies obtained from Honeywell, to obtain a conservative estimate of λ. This provides a reasonable upper bound on the required energy. Accounting for the chemistry and for E_{salt}, the required $\lambda = 0.145$ (shown in the inset of Figure 3.2). The analysis, hence, provides a design space of energy and stoichiometry parameters which can be tuned to achieve fully transient systems using Rb oxidation as a heat source and $NaHF_2$ oxide etching. While 100% energy transfer from Rb-oxidation is impractical due to conductive losses to the ground, convective losses to air currents and radiative losses, the required λ can be tuned to improve substrate transience based on experimentally obtained heat-transfer efficiencies. Combining this analysis with experimentally obtained efficiencies, it is possible to choose the relatively quantities of the substrate material and the fuel for transience.

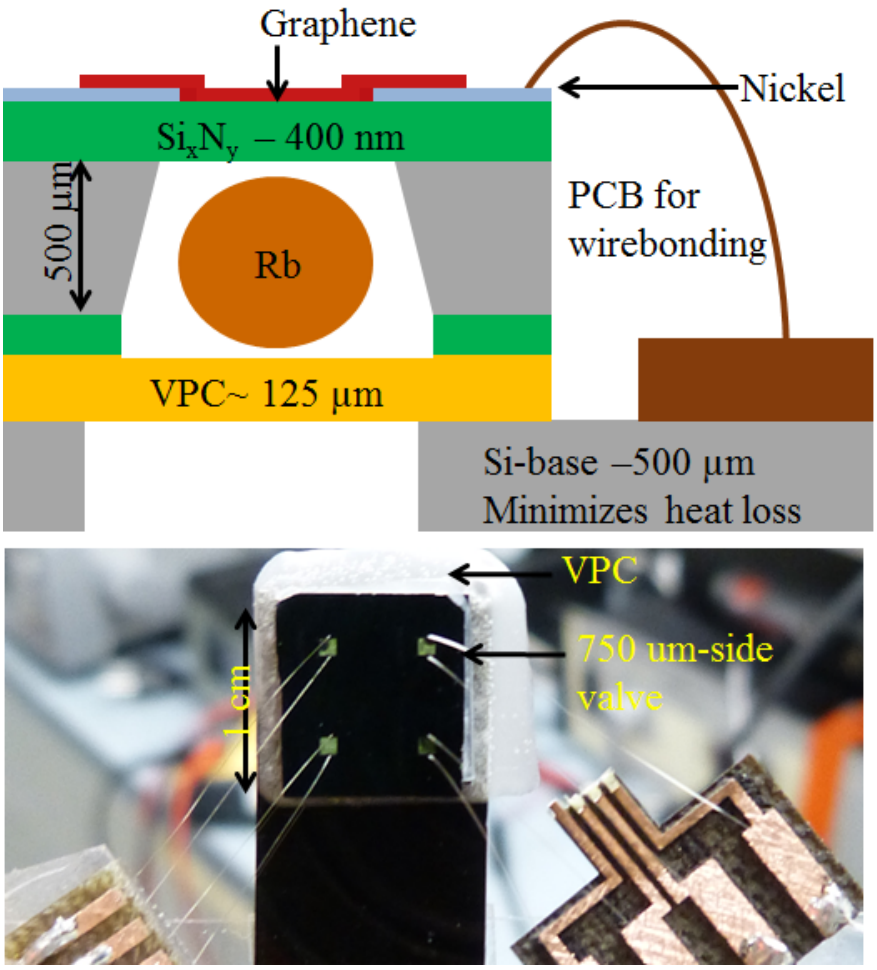

Figure 3.3: Top: Schematic of the test-structure for VPC transience. Bottom: An optical image of a 2×2 valve array tested for transience with Rb deposited inside valves, with connections to the valve via wirebonds.

3.3 Test Assembly

Two separate test structures were designed and assembled for independently quantifying VPC and oxide-electronics transience respectively.

3.3.1 VPC transience test

Figure 3.3 shows a schematic of the test-assembly and an optical image of the assembled test structure. $750 \times 750\ \mu m^2$ graphene-on-nitride micro-valves were fabricated [99] and Rb was deposited inside the micro-valves with a heated syringe inside an inert atmosphere Labconco glovebox with $<$ 0.1 ppm oxygen. The valve chamber can hold 500 nL of Rb, which is the typical quantity dispensed. The Rb is dispensed on the silicon nitride - this ensures that when the valve triggers, the surface of the Rb touching the valve also gets heated locally in order to break the thin shell of Rb_2O that forms on its surface. Rb is stored under mineral oil inside the glovebox to prevent slow oxidation over long time periods. The valve was then bonded to a $\sim 1 \times 1 cm^2$ solution casted VPC film. Solution casting of the 5 $wt\%$ VPC polymer blend, with added thermal acid generator (TAG) from dichloromethane (DCM) produced approximately 125 μm films of the desired mechanical strength and decomposition temperature $\sim 180^oC$. This film was thermally bonded, from the bottom to 0.5 mm thick silicon-spacer and from the top to a valve with Rb filled packet, respectively, by heating to 70^oC. At this temperature, the polymer blend softens sufficiently to "flow" without vaporization and can stick to the valve and the spacer. The spacer is used to minimize heat-losses and mount a PCB, which is wire-bonded to the pads on the valve for electrical contact. A USB optical microscope was used to image the top-side i.e. valve surface, and an FLIR T-300 IR camera monitors the bottom of the VPC film for temperature measurement.

3.3.2 Oxide transience test

Since the test structures do not eliminate silicon completely from the system, the Rb oxidation cannot be used in this setup to heat the $NaHF_2$. Hence, MEMS heaters must be used to locally heat and decompose $NaHF_2$ stored in the KOH-etched cavities. The graphene-on-nitride valves are thermally unstable close to 180^oC due to thermo-mechanical stresses in the nitride as discussed previously [99]. Hence 400 nm nitride membranes (3×3 and 7×7 mm^2 in this case) with nickel heaters of resistance $1k\Omega$ were used for the oxide-etching test. Two test structures were used for oxide etching. In one case, $NaHF_2$ was packaged in the valves and sealed on the backside with 1 μm thermal oxide on bulk silicon (Figure 3.4A). In the second case, a thinned 5 μm oxide substrate chip (obtained from Honeywell) was embedded in $NaHF_2$, and a glass substrate was bonded on the backside (Figure 3.4B). Both devices were wirebonded to PCBs for electrical contact. An IR camera was used to monitor the membrane temperature to ensure that sufficiently high temperatures are reached locally to decompose $NaHF_2$.

3.4 Experimental Results

3.4.1 VPC transience

Valves were triggered with an average trigger power of $\sim$ 140 mW. 100% valve triggering yield was achieved with over 150 devices tested up to now. Figure 3.5A and 3.5B show optical micrographs of valves bonded to VPC encapsulat-

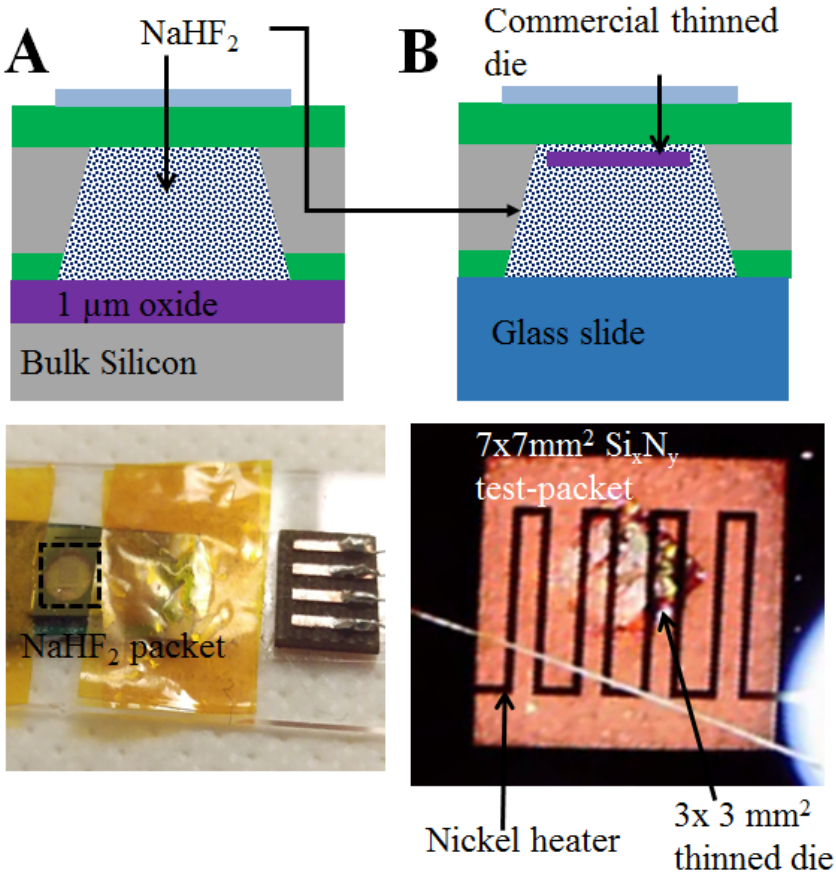

Figure 3.4: $NaHF_2$ micro-packet test structures for oxide etching: A). with 1 μm oxide on bulk silicon and B). 5 μm thick oxide substrate commercial die embedded in $NaHF_2$. On the bottom, optical images of both test structures are shown. Both assemblies use a nitride-membrane with integrated Ni heater and $NaHF_2$ manually packaged in the chambers.

ing Rb, before and after valve-triggering to demonstrate valve vaporization. IR monitoring (Figure 3.5C) shows heat being transferred from Rb oxidation to VPC. The highest performance transient devices used 500 nL Rb droplets which produce vaporization of 125 μm thick VPC substrate with the largest through-etch hole of $5.2mm^2$, larger than the base area of the valves (Figure 3.5D). The

efficiency of energy transfer from Rb to VPC is-

$$\eta = \frac{E_{VPC}}{E_{Rb_oxidation}} \tag{3.8}$$

Here, $E_{Rb_oxidation} = \frac{\Delta H_f V_{Rb} \rho_{Rb}}{A_r}$ and $E_{VPC} = V_{VPC}\rho_{VPC}(C_p\Delta T + H_{VPC})$. The best achieved energy transfer efficiency from Rb oxidation to VPC is extracted as 9.15%. Immediately, there are a few obvious sources of heat loss which can be mitigated. These are given below:

1. Since the test-structure assembly is done manually, the exact placement of the 2×2 valve-array on the VPC and bonding to the spacer is subject to variation.
2. The valves in this proof-of-concept test structure are supported on 500 μm bulk silicon, instead of polymer walls as targeted in the final structure. This leads to significant thermal losses to the silicon, since the thermal conductivity of silicon is $\kappa_{Si} = 130\ W/m.K$ and that of polymer is $\kappa_{Si} = 2 - 3\ W/m.K$. This reduces the efficiency of Rb oxidation used for VPC vaporization.
3. It is not clear if all of the Rb is oxidized to produce heat required for transience, since the Rb oxidation dynamics are stochastic and there is variability in the amount of Rb that is oxidized inside the chambers due to long-term leakage of oxygen-containing air.

By eliminating silicon in a fully-polymer system, these losses can be minimized for complete device transience, based on the analytical model developed. These are addressed in the next section of this chapter.

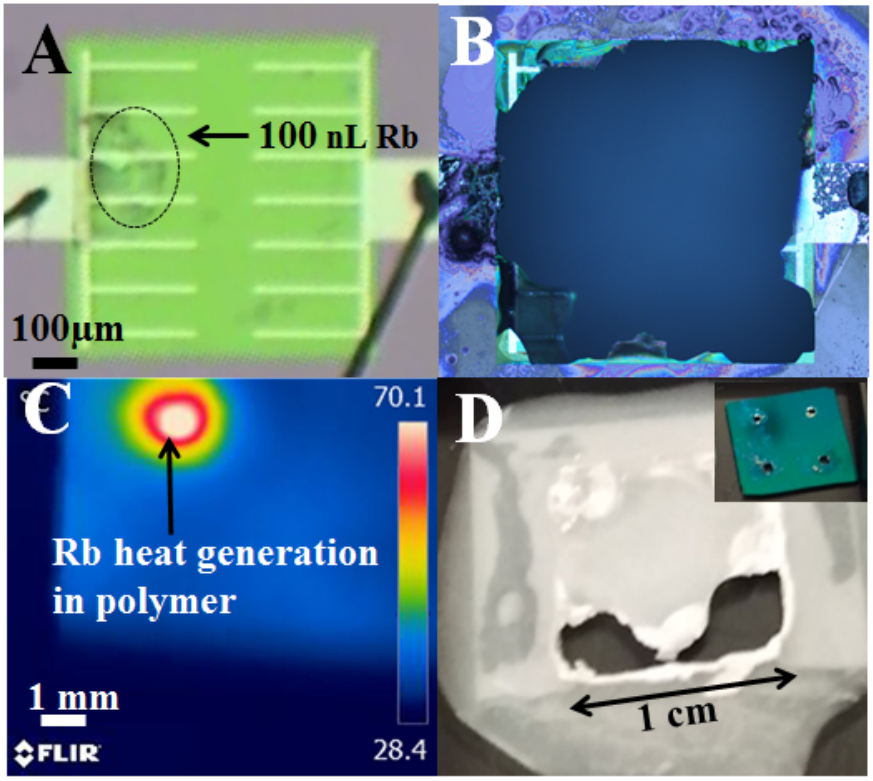

Figure 3.5: A). Optical micrograph of test structure 100 nL Rb is sealed by the valve and the VPC (not seen in this picture) is used as a backing layer B). Optical micrograph of a valve post-triggering shows 95% vaporization confirmed with image processing C). IR image of the polymer backside during Rb oxidation the elevated VPC temperature shows energy transfer from Rb to the substrate D). Best vaporization performance of 500 nL Rb in -packet produces $5.2mm^2$ (determined with image-processing) etching of 125 μm thick polymer. 30% of polymer is etched below the tested valves (shown in inset)

3.4.2 Oxide transience

Thermal oxide Etching

For testing the 1 μm oxide-on-silicon as base, thermal power was ramped across $1k\Omega$ nickel-heaters on nitride membranes. This helped achieve a local temper-

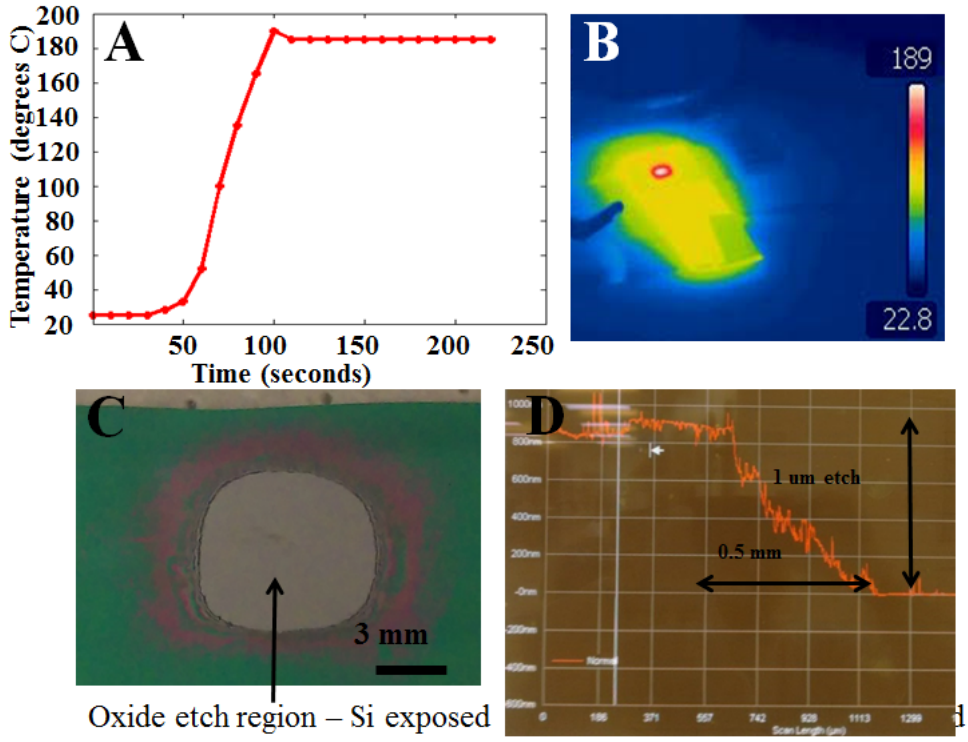

Figure 3.6: A). Temperature profile of membrane surface vs. time for oxide-etching test of 1 μm thermal oxide on bulk silicon. B). IR image of the chip, confirming that the achieved peak temperature of $> 189^oC$ exceeds the temperature required for $NaHF_2$ decomposition C). Optical image of the substrate after etching shows exposed silicon which is an etch stop for HF etching D). Profilometry of the etched oxide substrate 1 μm confirms the depth of the etching

ature $> 160^oC$, verified with an IR camera (Figure 3.6A). The maximum power dissipated for this was 450 mW. The oxide which served as the base for the packaged $NaHF_2$ was completely etch after $\sim$ 1 minute of heating (Figure 3.6B). This was verified with profilometry.

Thermal oxide Etching

5 μm thinned chips from Honeywell were tested for etching with $NaHF_2$ .The heaters were ramped to 600 mW thermally for ~ 2 minutes. The dies were monitored optically and seen to visibly deform due to stress-relief from etching of the oxide-film. Following this, oxide etch was confirmed optically (Figures 3.7). Since the thinned die has a polyimide passivation layer on top of it as well as residual bulk silicon on the bottom as shown in the bottom half of Figure 3.7, the HF produced due to $NaHF_2$ decomposition has to undercut laterally to etch the oxide. As a result, the metal wires and polyimide remain intact but discoloration of the chip due to oxide etching confirms oxide etching and hence chip function transience.

3.5 Polymer Molding

In order to eliminate silicon completely from the polymer system, it is necessary to make high aspect ratio structures of the VPC. Solution casting is able to produce films of thickness ~ 125 μm, but these films cannot be molded into the desired shapes of the micro-packets. In order to achieve this, SU-8 and PDMS molding was chosen.

SU-8 is an epoxy-based negative photo-resist. SU-8 is composed of Bisphenol A Novolac epoxy that is dissolved in an organic solvent (gamma-butyrolactone GBL or cyclopentanone, depending on the formulation) and up to 10$wt\%$ of mixed Triarylsulfonium/hexafluoroantimonate salt as the photoacid generator [104]. It can be directly patterned on silicon substrates to make high

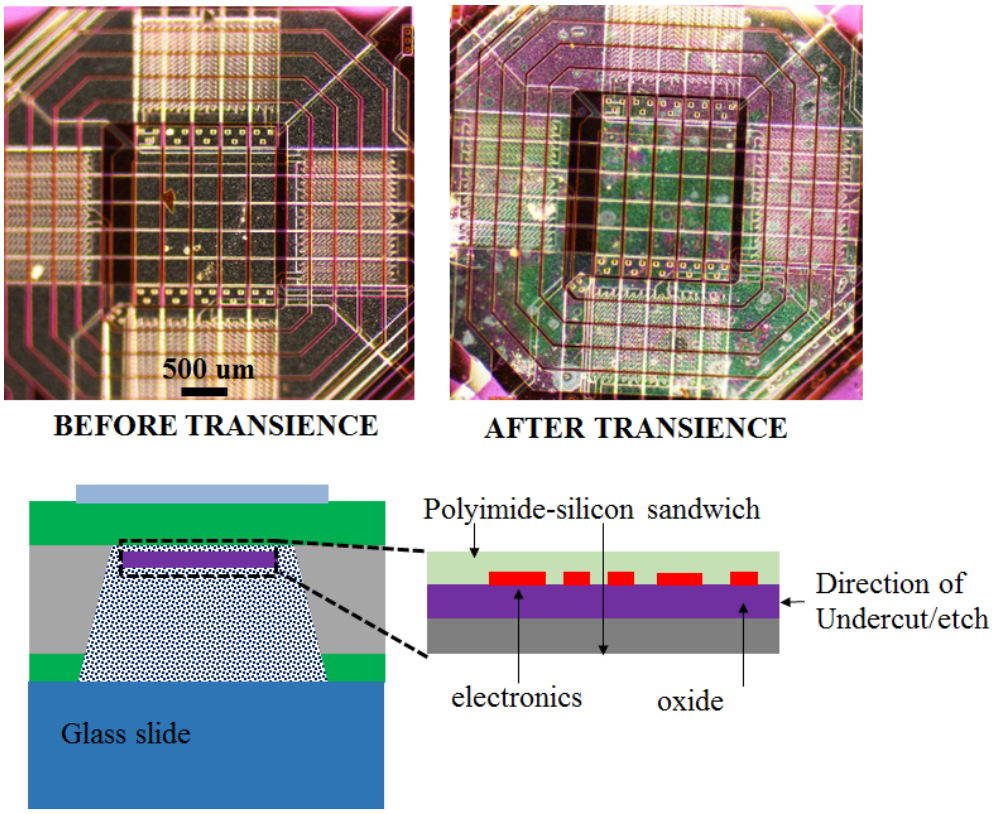

Figure 3.7: (Top) Honeywell thinned chip optical micropgraphs before and after $NaHF_2$ etch tests. (Bottom) Schematic of the die cross-section showing oxide sandwiched between polyimide and silicon which makes it necessary for in situ produced HF to etch laterally

aspect ratios with slow spin-rates (< 300 RPM) and prolonged curing time of > 24 hours, at temperatures slightly over room temperature, up to 100^oC. This was used to define the structures which would be eventually made from the VPC. After making the SU-8 mold, it was "inverted" i.e. cavities become solid structures and solid structures becomes cavities, using a negative Polydimethylsiloxane (PDMS) which is an optically clear silicone. The second negative mold of PDMS is used to realize the same structures as were made with the SU-8 by using a high weight percent DCM solution of the VPC. Instead of making a negative mold with the SU-8, it was preferred to use the double inversion since the

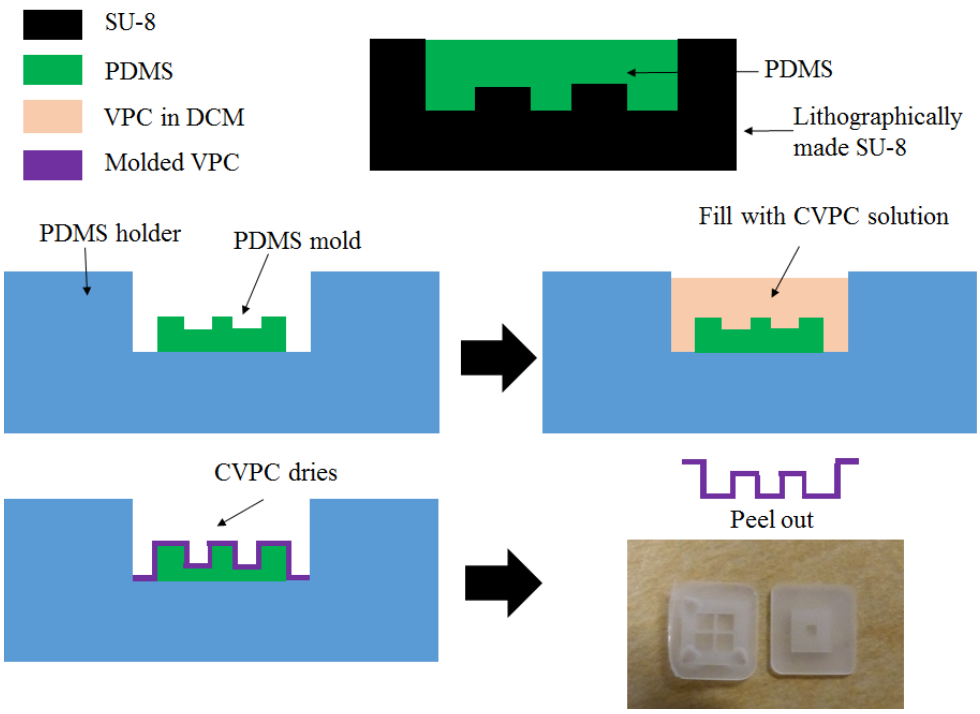

Figure 3.8: Method for making VPC molds using a double-inversion SU-8 and PDMS based casting process. SU-8 is patterned lithographically, and used to make a negative/reverse PDMS mold. This is then used for casting polymer to make the VPC with the same structure as the SU-8. The optical image on the bottom right shows a 2×2 array and a single chamber made using this process. This method can be extended to making larger arrays

polymer casting in PDMS was already established for making solution casted films with no adhesion problems. Figure 3.8 shows the process for making the VPC mold.

For the polymer packets designed here, SU-8 was coated on a silicon wafer by spinning, like photo-resist, with the following recipe:

1. 10 seconds at 250 rpm with 100 rpm/s ramp rate
2. 30 seconds at 750 rpm with 300 rpm/s ramp rate

3. 10 seconds at 0 rpm with -75 rpm/s ramp rate (ramp down)

After this, the polymer was hard-baked overnight at 65^oC with a ramp-rate of $5^oC/min$. The SU-8 was spun and left unexposed for 3 days to prevent cracking due to immediate exposure with UV light. An exposure matrix was used to optimize the exposure energy with a 11 mW/cm^2 lamp from the ABM contact aligner at the Cornell Nanoscale Facility, with 365 nm UV light. It was determined that a 288 second exposure was optimal for 560 μm thick SU-8 . No post-exposure bake was applied. For developing, MIF 726 was used with a stir-plate at the lowest stir rate to avoid peeling of the SU-8 from the silicon substrate. Figure 3.9 shows optical and SEM images of the SU-8 mold used for making the CVPC micro-packets. A PDMS mold was similarly made using standard procedures, while using the SU-8 as the skeleton structure for casting. Finally, 10% VPC polymer in DCM was solution casted in the PDMS to realize the desired polymer micro-packets. These high-aspect ratio VPC micro-packets were then filled with Rb inside the glove-box and thermally bonded to the valves at 70^oC. The yield for these structures was low $\sim$ 20% because of the stress induced in the 360 nm nitride membranes when the polymer was bonded thermally to them, but can be improved by engineering the stress in the nitride appropriately, or increasing the film thickness. Figure 3.10 shows a schematic of the procedure used for realizing these structures as well as the devices made.

3.6 Conclusions

A scalable micro-packet architecture for polymer and oxide-based vaporizable electronics has been demonstrated and tested. With integrated Rb and $NaHF_2$,

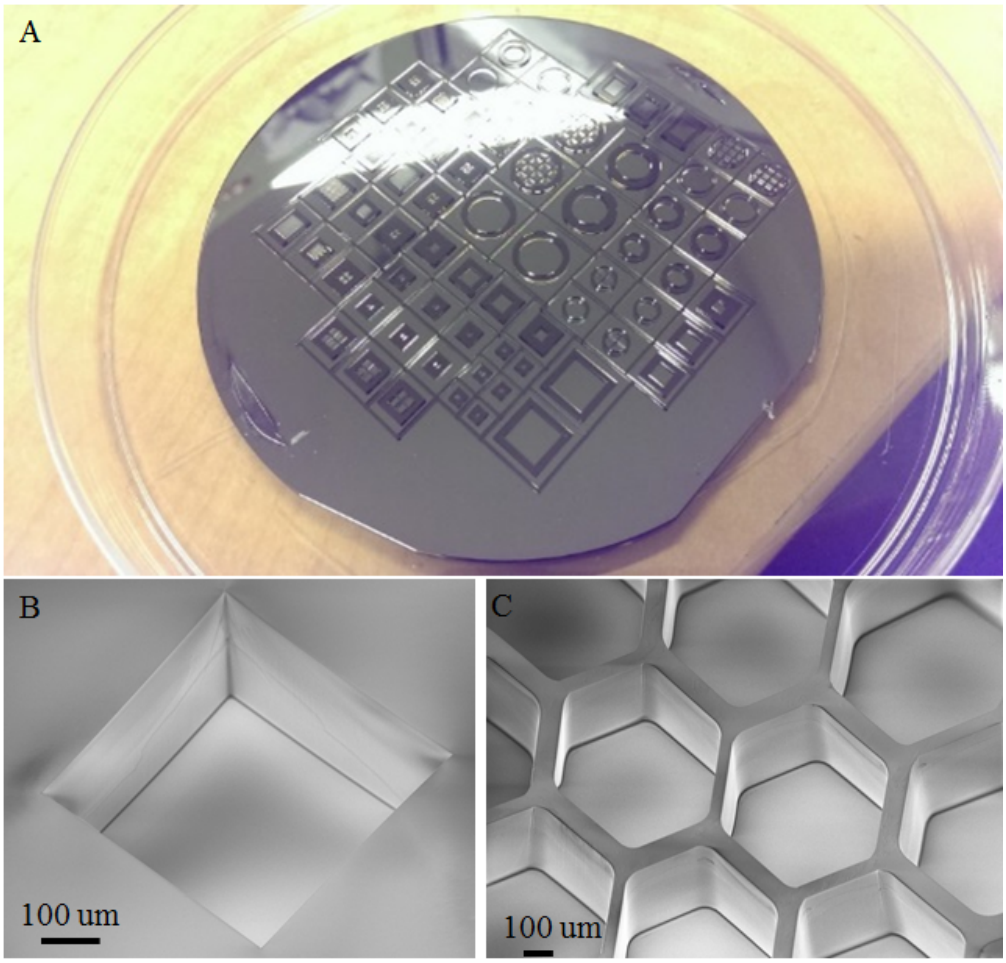

Figure 3.9: A). Optical image of a wafer with SU-8 patterned on it, for using the SU-8 as a PDMS mold. B). SEM image of a single 300 $\mu m \times 300$ μm chamber, designed for holding Rb. C). Honeycomb lattice made of SU-8 for making an array of Rb chambers

vaporization of the VPC substrate as well as etching of integrated thinned oxide-electronics is demonstrated. A fully polymer system can be realized by solution-casting VPC in PDMS molds so that silicon content in the system is zero and energy transfer from Rb-oxidation heating can be utilized for complete transience. In addition, using the energetics and stoichiometric analysis provided in this paper, the experimentally observed thermal efficiencies for transience can be determined to optimize Rb fill factor in these systems. The overall power

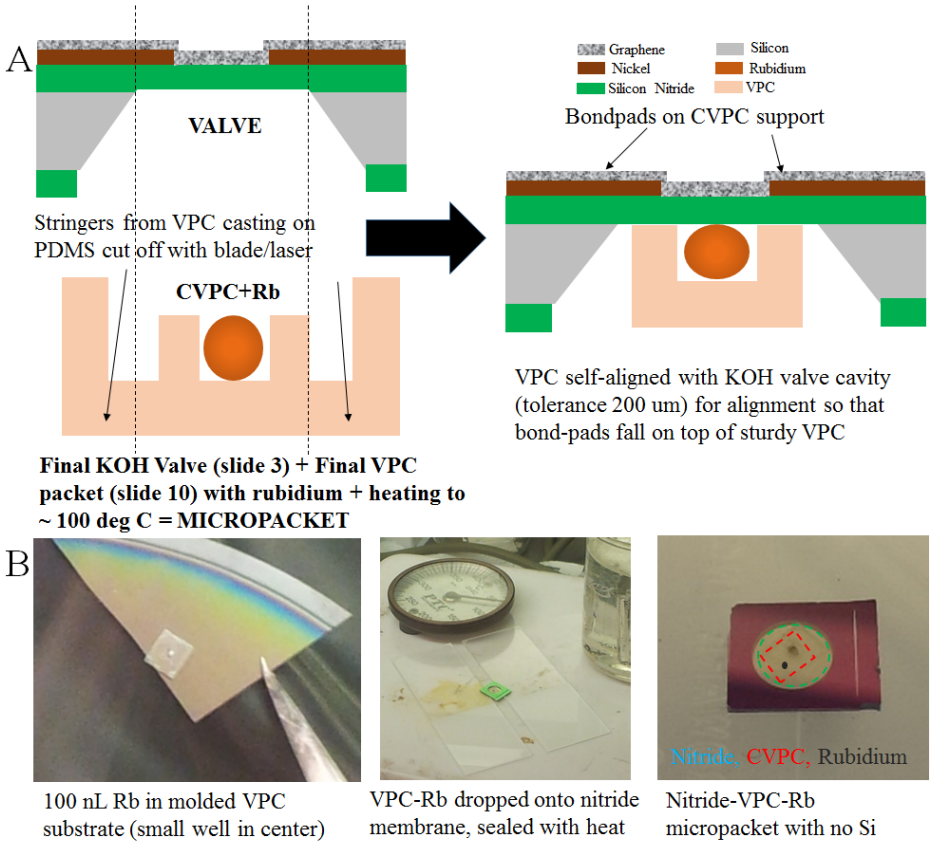

Figure 3.10: A). Method for realizing nitride on VPC with Rb chambers using SU-8 and PDMS molding and solution casting of VPC. B). Method of processing substrates with 100 nL Rb droplets inside the glovebox to build the desired nitride on VPC structures with no silicon. The nitride used for alignment can be cleaved by a sharp tip or a laser.

consumption can be reduced by co-packaging Rb and $NaHF_2$, so that Rb oxidation heat can be directed optimally into both polymer and $NaHF_2$. In the future, large arrays of molded VPC structures can be realized with nitride membranes for selectively patterned valves on the top. By wire-bonding to these on hardened substrates or indium bonding for electric contact, these devices can be tested for full transience functionality. The biggest challenge in this process lies in the hermetic sealing of Rb inside the chambers, since the thermal seal of VPC with nitride may not be leak-proof even though the valves themselves don't al-

low oxygen to permeate through them. These problems need addressing with the study of Rb oxidation chemistry and possibly using protective coating layers on Rb to preserve it for the active lifetime of the device.

CHAPTER 4

BI-MODAL GRAPHENE POLYMER INTERFACE CHARACTERIZATION PLATFORM FOR VAPORIZABLE ELECTRONICS

Characterization of physical and chemical properties of organic materials such as polycarbonates is essential for their customized design, specific to applications. This chapter presents a micromechanical resonant membrane platform with simultaneous electrical and mechanical sensing using graphene transferred on silicon nitride (Si_xN_y) to characterize thin-film analytes as shown in Figure 4.1. The analytes are deposited on top of the membrane by spin-casting them in solution. Electrical sensing is done by modulation of graphene resistance. This is a manifestation of the graphene-polymer interface changes due to dangling bond interactions between the analyte film and graphene surface. At the same time, the resonance frequency of the analyte film/graphene/Si_xN_y composite membrane changes with changes in temperature, elastic modulus of the organic analyte and mass loss due to vaporization of the analyte film. Thus a bi-modal characterization of the organic thin film can be acquired, both in the electrical and mechanical domain. This enables us to determine and optimize the organic film formulation, based on the application.

As an example, this device demonstrates a platform to distinguish between marginally different formulations of a polymer used in the design of low temperature degradable transient electronics. The major advantage of this sensor is that it uses the same fabrication process flow and design as the thermo-mechanically triggered valve for vaporizable electronics, presented in chapter 2. For co-fabrication with vaporizable devices, the platform needs no additional design layers, structures or materials. By coating the membranes with thin-film

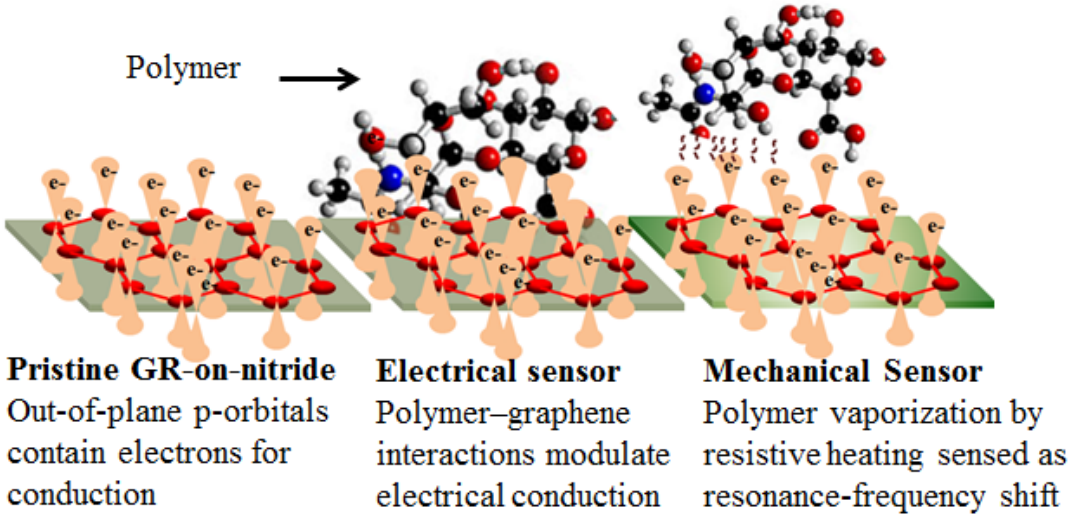

Figure 4.1: Polymer surface-interactions with the atomically-thin graphene are sensed electrically with graphene resistivity modulation. The mass-loss and vaporization are sensed mechanically with membrane resonance-frequency shift.

analytes which are light sensitive and degrade when exposed to ambient light, the device can be used as a radiation sensor for tamper-proofing in secure packages that necessitate protection from light.

4.1 Introduction

The design and synthesis of novel polycarbonates using experimental and theoretical techniques finds use in various applications. Polycarbonates are used in electronic components for insulation and as dielectrics, for macro and micro tubing, and in niche applications such as polycarbonate lenses and sterile medical storage. In MEMS microfabrication, these polymers are used in photoresists for lithography and as protective films [105]. However, no single application accounts for more than 10% of the commercial market volume for polycarbon-

ates because of the wide variety of properties offered by these materials [106]. More importantly, the capability to modify and tune their physical and chemical properties, specific to the application, with only minor changes in composition makes them extremely versatile. Small weight-percent (wt%) additives in polymer blends can drastically change their physical and material properties, and alter their response to temperature and pressure. For vaporizable polycarbonates (VPC), exposure to light of various frequencies and intensities can also change chemical properties such as surface bonds and their energies. This enables their use as passive sensors with secure physical encoding of material properties for quantitatively recording light flux intensity and temperature changes [100]. Designing polymers for such applications requires optimization of their glass-transition temperature (T_g) and decomposition temperature (T_d). The effect of the polymers on electrical conductivity of materials that they contact also needs monitoring for electronics packaging. To quickly characterize these blends while exploring a large design space of parameters for the VPC, it is impractical to synthesize large quantities of these materials. Synthesis of small quantities is desirable, and it also allow efficient use of reagents. Hence, a microscale characterization platform that can enable polymer characterization with high specificity in multiple domains is essential.

The traditional method of measuring thermal-response of analytes is Thermo-Gravimetric Analysis (TGA). Micromechanical TGA devices use resonant vibrating cantilevers, with integrated piezoresistive sensors for temperature cycling using Joule heating, and measuring corresponding mass-change with shifts in resonance frequencies [107]. However, they do not provide information on surface interactions or change in binding energies. Desorption kinetics of thin-film analytes deposited on micro-hotplate arrays have been studied

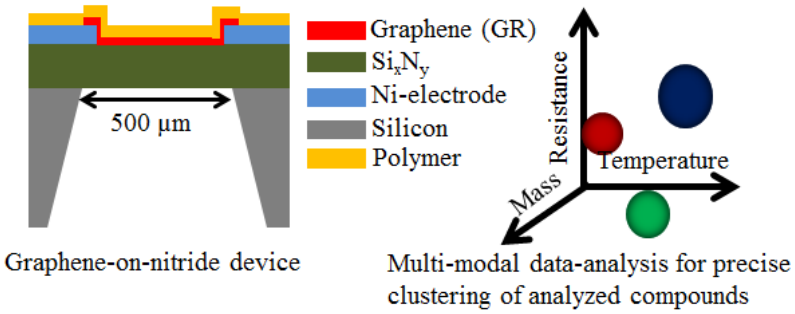

Figure 4.2: Characterization platform with spun-on analyte polymer for thermal cycling

using mass spectroscopy [108] but do not have mass-sensing capability. The device presented here is based on a bi-modal sensing approach that can simultaneously measure mass-loss and surface-interaction changes to combine the bests of both of the approaches mentioned formerly.

4.2 Device Concept

The characterization platform uses graphene transferred on a Si_xN_y membrane, with the analyte polymer spun-on, as shown in Figure 4.2. The graphene film is patterned to define electrodes for sensing its resistivity. By patterning and confining the graphene to be on the nitride membrane, thermal losses via conduction to the substrate can be minimized. A PZT plate is adhesively bonded to the back of the device to excite resonances in the membrane [109].

4.3 Electrical Sensing

Graphene is an atomically thin sheet of carbon atoms arranged in a honeycomb lattice and shows outstanding electrical properties as a zero-band gap semiconductor with high electrical conductivity [110]. Carbon atoms connected to each other in the lattice are sp^2 hybridized. The remaining p-orbital with a single electron is free for conduction. By means of dipole-electron interactions, polymers can locally bind the free electrons which are otherwise available for conduction in graphene. The resistivity of graphene can thus be reversibly modulated by molecules adsorbed and desorbed on its surface via charge-transfer. This has been used to study graphene's interactions with a variety of molecules [111], using graphene Field Effect Transistors (FETs). The device is used to measure the modulation of graphene's resistance for sensing surface-modifications during the temperature ramp, as graphene's atomic interactions with the spun-on polycarbonate change. Additionally, the graphene also serves as a resistive heater for temperature ramping with Joule heating.

4.4 Mechanical Sensing

The suspended Si_xN_y membrane is the structural layer, actuated at resonance, for mass-sensing with the device. The fundamental resonance frequency of a square membrane, f, in the stress-dominated regime is [112]:

$$f = \frac{1}{a}\sqrt{\frac{\sigma}{2\rho}} = \frac{1}{a}\sqrt{\frac{\sigma V}{2\rho m}} \tag{4.1}$$

Here, a is the length of the square, σ is the in-built stress and ρ is the density, also expressed as the ratio of mass m to volume V. The second expression yields

the relationship for mass-loss Δm to frequency-shift Δf:

$$\frac{\Delta f}{f} = -\frac{\Delta m}{2m} \tag{4.2}$$

In addition to this, there is a temperature dependence of the membrane-frequency during heating, based on changes in the composite film-stress, σ, and the membrane dimensions. Since, the membrane is clamped on all sides, and Joule heating is confined to the center of the membrane, the length a is constant to first order. The membrane resonance frequency decreases due to the reduction in tensile stress as temperature increases i.e. membrane mechanical spring softening. An effective thermal expansion coefficient (TEC) for the thickness, which can change in the center of the membrane, also needs to be accounted for. The temperature-dependence thus derived from 4.1, is:

$$\frac{1}{f}\frac{df}{dT} = \frac{1}{2\sigma}\frac{d\sigma}{dT} + \frac{3}{2}\alpha \tag{4.3}$$

Here, T is the temperature, α is the effective TEC accounting for the Si_xN_y, metal electrodes and spun-on VPC, and t is the total thickness of the layers. The thermal time constant for heating the membrane uniformly as given in [113] and as shown in Figure 4.3 :

$$\tau_{heat} = \frac{\rho C_p L^2}{12\kappa} \tag{4.4}$$

C_p is the heat capacity, ρ is the density and κ is the thermal conductivity of the composite structure. Substituting for each of these parameters, $\tau_{heat} = 3.8\ msec$ for membrane heating due to its small thermal mass.

On the other hand, the time to raise the temperature of spun-on VPC and overcome its relatively high heat of vaporization is on the scale of minutes because of the heat of vaporization required. Hence, during the initial temperature ramp, only a fast negative shifts on millisecond timescales is expected i.e. decrease in resonance frequency due to membrane heating, a result of effective

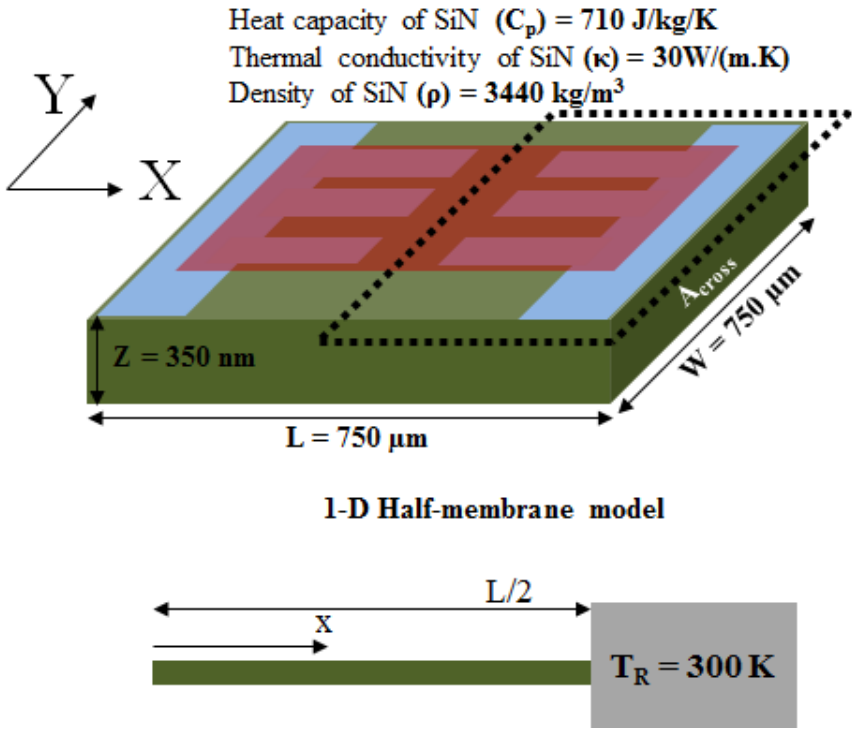

Figure 4.3: Schematic of the membrane showing various thermal parameters and the half-membrane model to calculate its thermal time constant.

spring-softening. At sufficiently high input power, it is expected that this will be followed by a slow positive shift i.e. an increase in resonance frequency as the VPC heats and vaporizes leading to mass-loss.

4.5 Device Fabrication

Chapter 2 has a detailed description of the process used for making graphene on Si_xN_y devices. The fabrication process-flow described therein was used in this work with some modifications. 45 *nm* thick nickel-electrodes were evaporated and patterned on 360 *nm* thick Si_xN_y for contact with graphene, which was transferred on top of electrodes. Graphene was also patterned by oxygen

plasma-etch only on top of the suspended Si_xN_y to minimize heat losses to the substrate for power-savings.

4.6 Polycarbonate synthesis

The polycarbonate used in this study was synthesized based on [101]. VPC was polymerized using the bis(carbonylimidazo1ide) of 2,5-dimethyl-2,5-hexanediol and 80% 1,4- and 20% 1,3-benzenedimethanol. Two different VPC test solutions were made. One consisted of 5 wt% VPC in dichloromethane (DCM) and the other contained 5 wt% VPC + 5wt% (with respect to polymer content) photoacid generator (PAG) (VPC + PAG) in DCM. A PAG, after exposure to ultraviolet (UV) light, provides an acid source, which catalyzes polycarbonates decomposition [114]. By adding PAG to one solution and not the other, two different polymer blends with different thermal properties were created. Each solution was spin coated onto a silicon wafer followed by a post-spin bake of 120^oC for 2 minutes to form a thin film of 500 nm. The VPC + PAG film was exposed to 254 nm UV light with a dose of 300 mJ/cm^2. Each film was removed from the wafer and the T_d for each was verified using a commercial TGA. VPC had a T_d of 209^oC, while the VPC + PAG had a lower T_d of 97^oC. After confirmation of different thermal properties, thin films of each blend were spun on graphene devices using the same procedure as above.

4.7 Testing And Results

4.7.1 Unloaded Device - Characterization

Square membranes of side 500 μm were tested for all experiments. Device resonance modes were excited with backside AC PZT actuation and identified with the Polytek MSA 400 laser interferometer. The fundamental mode at 293 kHz with a Q-factor of 1050 in 3 $mbar$ vacuum, shown in Figure 4.4, was used. As a control experiment, voltage was ramped across the graphene heater on an unloaded device while simultaneously monitoring membrane resonance frequency shifts and graphene resistance change. This is plotted in Figure 4.5. With no spun-on polymer, device resonance frequency decreased over millisecond time scales, as expected, due to spring-softening of the membrane with increasing heat. Graphene-resistance varied non-monotonically and approached a value of 8 $k\Omega$ at high input-power.

For temperature calibration, a Si_xN_y membrane with a serpentine nickel resistor of baseline resistance 1.46 $k\Omega$ at room temperature, was heated by voltage-ramp across the resistor. The membrane surface temperature was monitored with an FLIR T300 infra-red camera while monitoring the nickel resistance, as shown in Figure 4.6. Using this highly linear calibration data ($r^2 = 0.99$), the thermal expansion coefficient (TEC) of deposited nickel was extracted as $\alpha_{TCR} = 5.85x \times 10^{-3}/K$ with the variation from baseline resistance R_0 given by $R = R_0(1 + \alpha_{TCR}T)$. The same device was then tested for voltage-ramp in 3 mbar vacuum to obtain a temperature versus power calibration, to account for reduced heat-losses in vacuum.

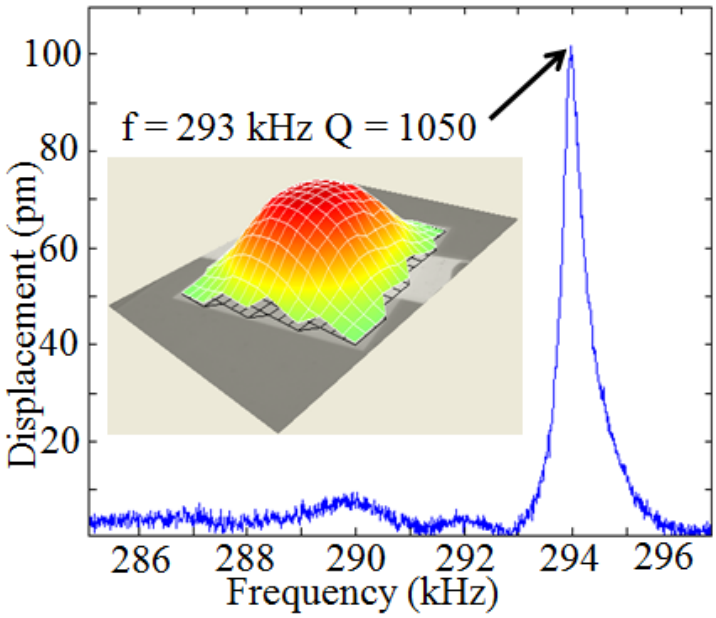

Figure 4.4: Unloaded device fundamental resonance frequency measurement.

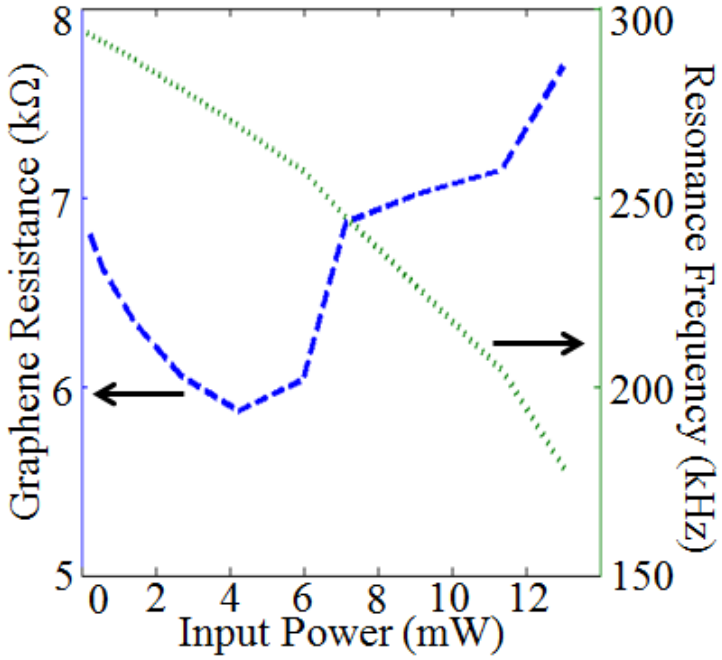

Figure 4.5: Control-measurement of unloaded membrane resonance frequency shift and graphene resistance change vs. input power.

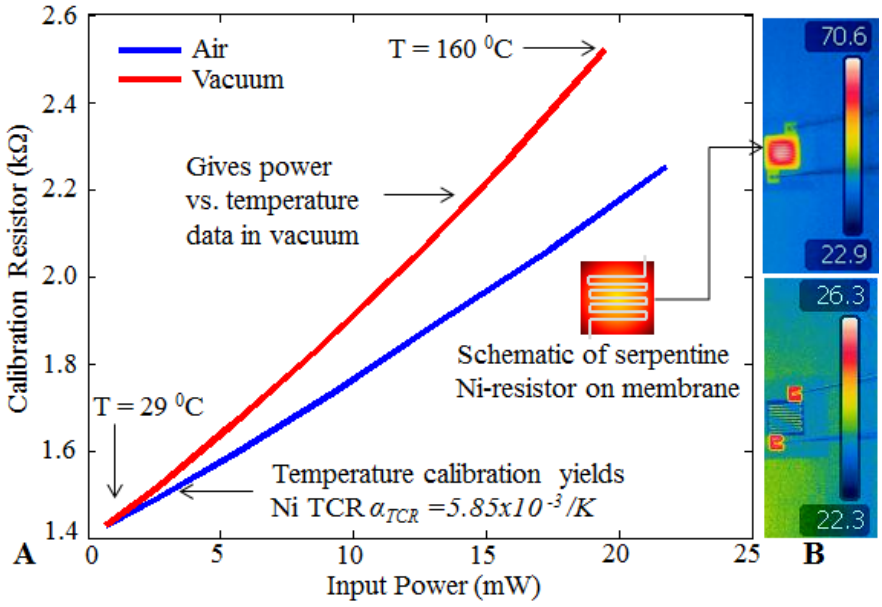

Figure 4.6: A). Temperature calibration of Si_xN_y membrane devices with serpentine calibration nickel resistors to obtain temperature versus power data in air and vacuum. B). IR camera images of the membrane with calibration resistor, during voltage-ramp in air (blue curve in A)

4.7.2 Polymer-loaded Devices - Resistive Sensing

With spun-on VPC (Device-1) and VPC+PAG (Device-2) polymer, devices were tested with voltage-ramp to heat the polymer while tracking the resonance frequency and graphene resistance. The initial resistances of the graphene on Device-1 and Device-2 before voltage-ramp were 18.6 $k\Omega$ and 2.76 $k\Omega$. This indicated high sensitivity of the graphene to small differences in the polymer, in this case the PAG, as a result of different surface interactions. Graphene resistance was modulated with increasing voltage, as VPC degraded thermally. Eventually, as the VPC is cleaned off the device surface, resistances in both devices approach that of pristine graphene on unloaded devices, shown in Figure 4.7.

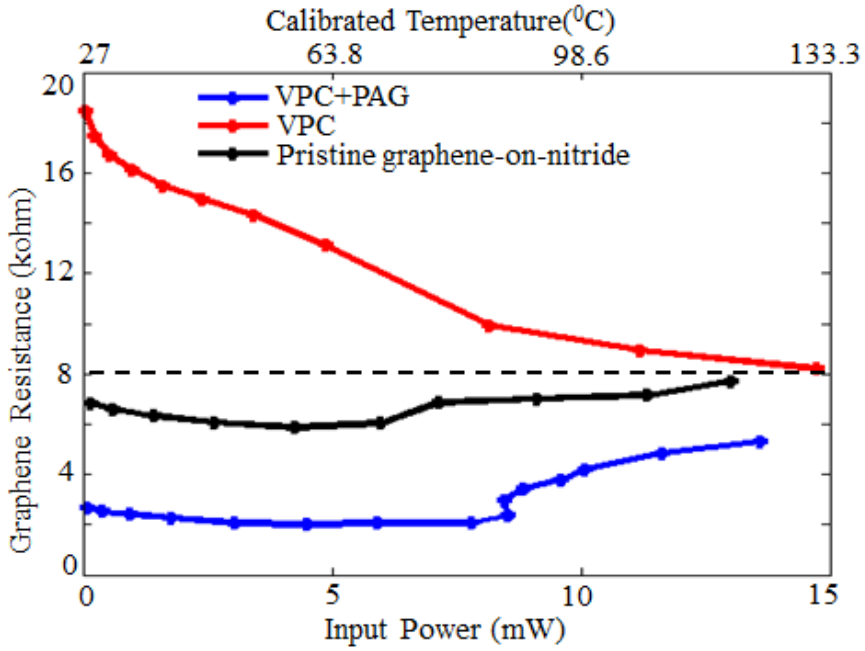

Figure 4.7: Graphene resistance change due to spun-on polymer, before thermal degradation, varies by 10x between VPC and VPC+PAG. After mass-loss at high input-powers, the graphene is cleaned and both resistance converges to pristine graphene-on-nitride resistance.

4.7.3 Polymer-loaded Devices - Mass Sensing

The initial resonance frequencies for Devices 1 and 2 were 208.9 kHz and 233.2 kHz respectively. These are lower than the unloaded device frequency of 293 kHz due to different wt% of spun-on polymers. The resonance frequency measured versus time (Figure 4.8), initially decreased on a scale of milliseconds during steps in voltage-ramp, just like the unloaded devices. However, with higher input-power, the analytes heated up sufficiently and slow-mass degradation was observed on a scale of minutes even as the power was kept constant over those intervals. This measurement is limited by device Q-factor degradation at large input power >25 mW.

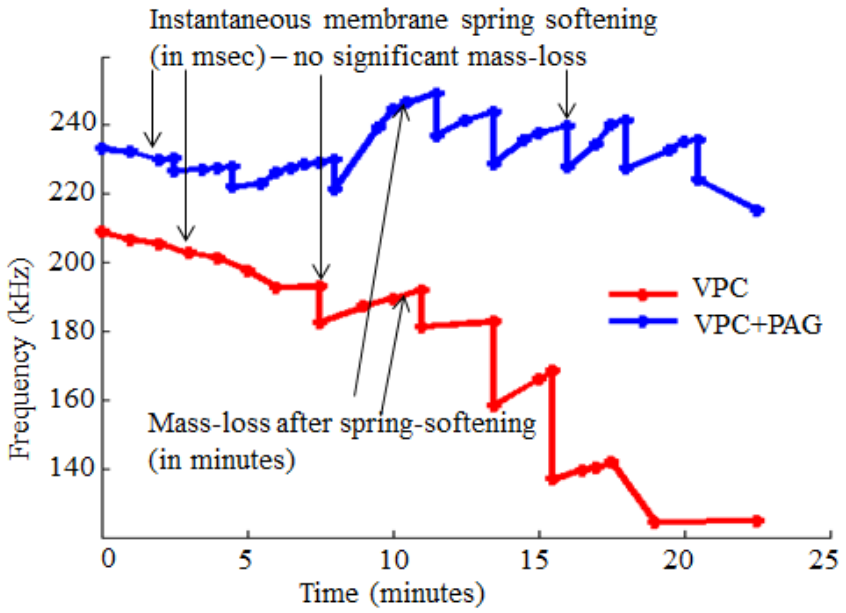

Figure 4.8: Resonance frequency vs. time during voltage-ramp of the graphene. Regions of only spring softening (low input power), and spring softening followed by mass-degradation (high input power) are shown

To measure mass-degradation versus temperature, the frequency shifts due to spring-softening were subtracted to calculate mass-loss % using equation 4.2. This helped to determine the thermal response of VPCs to increasing input power, and hence, temperature using the calibration data from Figure 4.6. Simultaneously, the membrane surface was optically monitored with the MSA-500 microscope (20×) to observe VPC vaporization. Figure 4.9 shows stages in the mass-degradation process mapped to corresponding images of the membrane for device 2. The measured mass losses for device 1 and 2 were 33 % and 70 % respectively, in reasonable agreement with values of 43.2 % and 60 % obtained by image processing results (using ImageJ software). Residual polymer on the platform, such as in Figure 4.9D, is due to inefficient heating near the anchors as a result of substrate losses. This can be improved by co-optimization

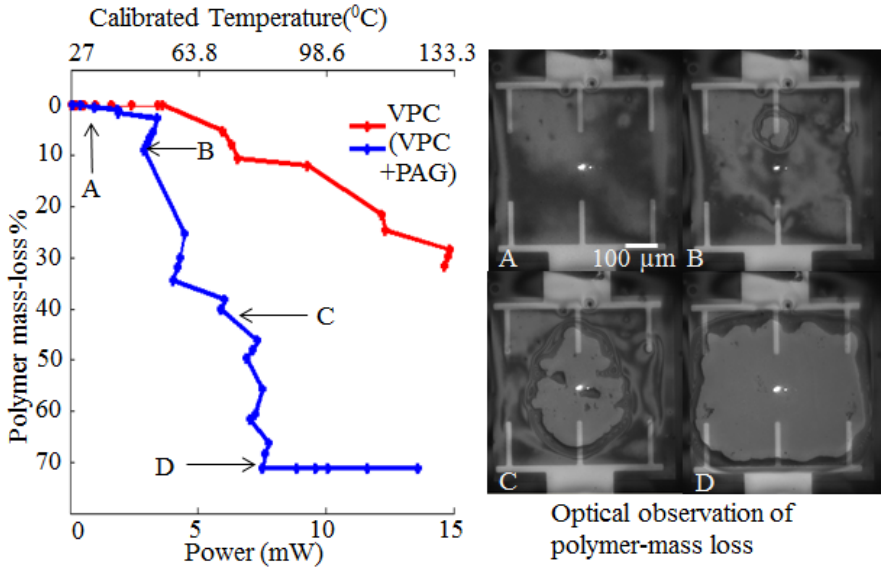

Figure 4.9: Polymer mass-loss % vs. input power - A) Low input-power with no material loss B) Onset of material loss, also seen optically C) Rapid polymer degradation sensed as a large frequency-shift D) Polymer degradation completed over graphene-heater. Measured 70 and 33 % mass-loss was verified by image processing

of the electrode design and graphene patterning.

4.7.4 Bi-Modal Sensing

By combining frequency and resistance measurements, it is possible to get a 2-dimensional signal for the thermal response of the material, for mass-loss and surface-changes. The signals for Device-2 are shown in Figure 4.10. The electrical (green curve) and mechanical (blue curve) signals are complementary to each other in this case, highlighting the advantage of sensing with more than one modality. For low input-power, there is almost no mass-degradation producing negligible frequency shifts. However, due to graphene-polymer

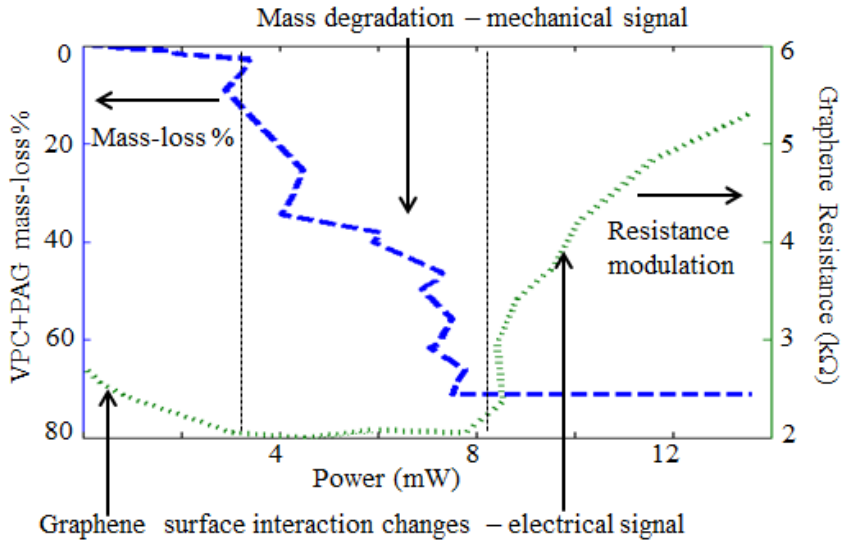

Figure 4.10: Bi-modal polymer characterization - The platform gives complementary electrical and mechanical signals in different input-power regimes, shown by dotted vertical lines, for sensing graphene-polymer surface interactions, mass-degradation, and surface cleaning.

nanoscale surface interactions, the graphene resistance is modulated significantly (by 20 %). At higher powers, mass-degradation is observed causing large frequency shifts but only small changes in graphene resistance showing minimized surface interactions. At high powers when mass-degradation is almost complete, no further frequency shifts are seen. However, as the graphene is cleaned by high current-drive annealing [115], its resistance approaches that of the unloaded device.

4.8 Conclusions

This chapter presented a bi-modal characterization platform for polymer analysis using a graphene-on-Si_xN_y sensor. While the target application is for the

analysis of VPCs for novel vaporizable electronics, the platform is broadly applicable and can be extended to the analysis of other polymers, within the stable range of temperatures of the device when it doesn't trigger thermo-mechanically like a single-shot valve. As a low-power (mW range) analysis tool, it can be used to analyze picogram quantities of polymers. For thermally degradable polymers, the device can be cleaned by ensuring that the graphene-resistance approaches that of pristine graphene while resonance frequency approaches that of the unloaded device resonance, allowing for cost effectiveness and repeatable use.

CHAPTER 5

ELECTRONIC SINGULATION OF SILICON PILLARS FROM FLEXIBLE SUBSTRATES UTILIZING VAPORIZABLE POLYMER

This chapter introduces an architecture for vaporizable electronics with an array of silicon pillars formed on a flexible polymer substrate with graphene interconnects. The pillars are linked and held together by a layer of vaporizable polymer, acid-activated polyproplyene carbonate (PPC). Individual islands have gold thin-film metal heaters associated with them. The heaters, when driven by a current, generate sufficient Joule heating power to melt and vaporize the polymer and interconnect graphene layer. The melting of the polymer can be used to increase flexibility for the array to be connected to highly curved surfaces. This work demonstrates controllable singulation of the pillars from the chip, which can be used for chip destruction by breaking a functioning CMOS circuit into non-functioning individual pillars. This work demonstrates the process flow to form a 3×3 array of 200 μm diameter silicon pillars spaced 200 μm apart, with gold heaters and graphene interconnects. In addition to singulation of the silicon pillar, breaking of graphene interconnects highlights the potential of high strength interconnects in a CMOS BEOL stack to be broken.

5.1 Introduction

Flexible electronics are attractive for Internet-of-Things (IoT) applications which need to be large-area for sense and actuate over large areas, have low rigidity, and ability to conform electronics to surfaces with high curvature and topography changes. Applications for flexible electronics include large-area low-cost displays [116], body-covering sensor arrays such as the artificial skin (e-skin)

for tactile sensing [117, 118, 119], polymer-based photovoltaics for low-cost renewable energy [120, 121] and soft, curvilinear surfaces integrated with electronics for biomedical monitoring and surgical procedures [122, 123, 124]. One existing approach to making flexible IoT electronics is to design and synthesize conducting and semi-conducting polymers on substrates that have lower rigidity than silicon, which is brittle [125]. This approach targets electronics on flexible substrates such as paper, plastic and metal foils since the substrates are available at low-cost in large area format, and provide the opportunity to significantly reduce the overall cost by taking advantage of large area electronics fabrication approaches such as roll to roll processing. Since the development of organic materials and polymers for electronics is relatively new compared to well-established semiconductor processing on rigid silicon substrates, the performance of these electronics is typically modest compared to commercial off the shelf silicon-based electronic components. A solution to overcoming the performance limitations while realizing high-quality flexible electronics is to assemble CMOS electronics onto flexible target substrates. For example, free-standing silicon-based nanoscale devices have been fabricated on silicon-on-insulator (SOI) substrates and deposited on plastic substrates by dry transfer printing and solution casting to yield devices with excellent electrical properties [126]. High performance silicon-based photonic circuits including interferometers and resonators have been realized on plastic substrates by a transfer-and-bond method [127]. Transfer printing methods combine the best properties of flexible substrates and inorganic semiconductors by mechanical flexibility with sophistication in CMOS design. The challenge with transfer printing is the alignment of the transferred electronics, optical or otherwise, to lithographically patterned structures already existing on the substrates and achieve

electrical connectivity between elements of the flexible substrates. In addition to flexibility of IoTs, there is a realization that the security of the IoT devices is also very important.

The growth of the IoT has brought forth major challenges with regards to the security of electronic devices connected as parts of extensive wireless sensor networks. The Oxford online dictionary uses the following telling example sentence in relation to IoT - "If one thing can prevent the Internet of Things from transforming the way we live and work, it will be a breakdown in security." This is especially true for defense and financial applications where secure data must be protected from hackers and potential adversaries, and medical data must be safeguarded. To safeguard against data compromise, it is critical to have secure encryption of data, and package sensors and electronics in a way that they cannot be reverse engineered. Traditionally, this has been done by means of software keys using established encryption standards [128]. In order to provide a hardware layer of security, there has been an emphasis on physical obfuscation and transience methods in recent times [129, 18, 19]. Here, the device can be destroyed completely by etching or mechanically removing parts, thus leaving residue of broken irrecoverable pieces. As a result, it is desirable to design flexible electronic systems with high-performance electronics with self-alignment of the electronics to the flexible substrates, which can be controllably singulated into small irrecoverable pieces of $10 - 100\ \mu m$ in size which would be very hard to recover if dispersed into the environment. Such a system can find use beyond defense and security applications. For example, one can envision miniaturizing micro-delivery systems with micro-drones using arrays of chips which can release small payloads on-demand [130].

This chapter presents a pillars-on-polymer (PoP) architecture for controlled detachment of silicon micro-parts from flexible polypropylene (PPC) substrates. The singulation is accomplished by a set of integrated thin-film metal heaters that can individually address controlled release of each micro-part. The PoP architecture converts silicon substrates into contiguous arrays of silicon pillars held together with a polymer which, in this paper, is the acid-activated PPC. The metal heaters are resistively heated to vaporize the PPC locally, releasing the pillar associated with the heater and singulate the pillar. Interconnects between pillars are formed with atomically thin graphene, which is transferred on the substrate using the PPC as a handle layer. The process of using PPC as a handle layer is novel compared to the established method involving PMMA [131]. Section 2 describes the device structure including details of the PPC synthesis and acid-activation for low-temperature triggering, steady-state thermal model, high-speed release, and the dual use of graphene for interconnects and as a piezoresistive material for acceleration sensing. The thermal model of the polymer is verified with a finite element analysis model of the device using COMSOL Multiphysics. Section 3 describes the device fabrication process with novel techniques used to realize the hybrid system - combining the processing of low-temperature material (PPC) with high-temperature materials (silicon, silicon dioxide, metals). Experimental results are presented in section 4 for the steady-state heating, pulse-powered release, graphene interconnect tests, and the accelerometer response. Section 5 discusses the translation of the technology and fabrication methods presented in this to CMOS integration and the use of graphene to realize transient interconnects and sensors.

5.2 PoP Architecture

The PoP device structure is shown in Figure 5.1. A standard ASIC is shown with integrated circuits and released MEMS sensors and actuators, integrated on a silicon substrate (Figure 5.1A). Without changing the functionality of the ASIC, the modified structure incorporates additional layers to obtain a transient substrate with electronic control over fragmentation of different parts of the substrate. An oxide layer is deposited and patterned on the top to passivate and protect the electronics and sensors. Then a metal layer is deposited and patterned to form the heaters on the oxide (Figure 5.1B). A PPC film, with graphene underneath, is transferred on top with the graphene serving as the interconnect between different pillars (Figure 5.1C). Each pillar has an individually addressable metal heater to trigger and remove it from the substrate, on demand. By selectively heating the PPC surrounding a silicon island, it can be removed from the substrate without affecting the other components of the chip (Figure 5.1D). With suspended silicon islands on PPC, a vaporizable accelerometer is also built into the flexible electronic IoT. A drawback of this architecture is that a portion of the silicon substrate is removed potentially reducing the density of electronics on a wafer, which can increase the cost of each chiplet. Using SOI CMOS, the DRIE etch can be terminated on the oxide to alleviate the decrease in density of electronics.

5.2.1 PPC for Flexible Substrate

PPC, shown in figure 5.2A, is an amorphous polymer commercially derived from the alternating polymerization of CO_2 and propylene oxide. It has

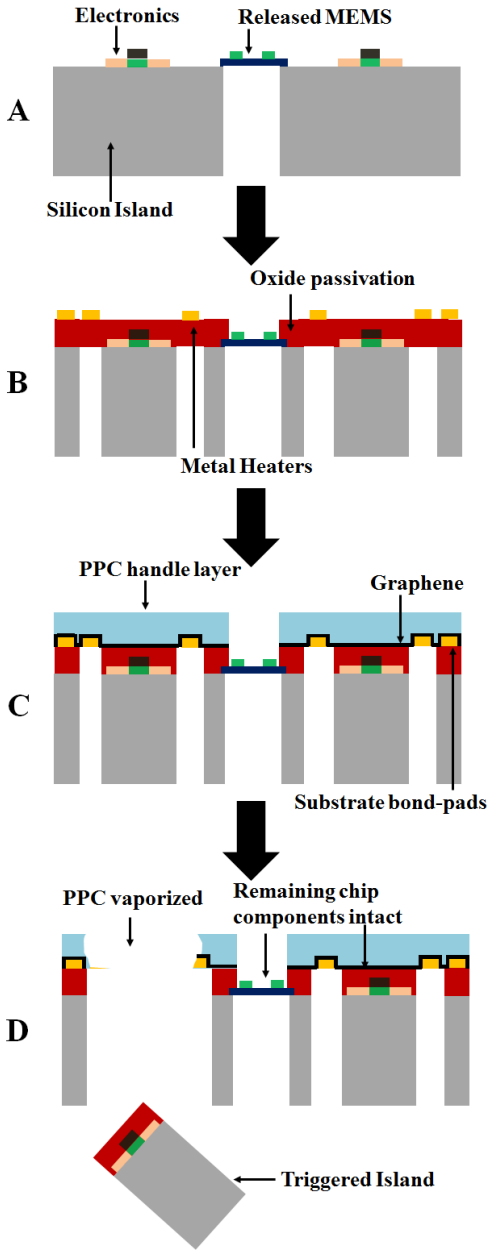

Figure 5.1: System Structure A). Standard CMOS and MEMS on silicon substrate B). Post processing to pattern oxide on the top to passivate electronics and pattern metal heaters associated with each island C). Transfer of the PPC handle layer with graphene for interconnects. The PPC holds silicon islands together. D). Example of a triggered pillar with PPC surrounding it vaporized, but other chip components intact

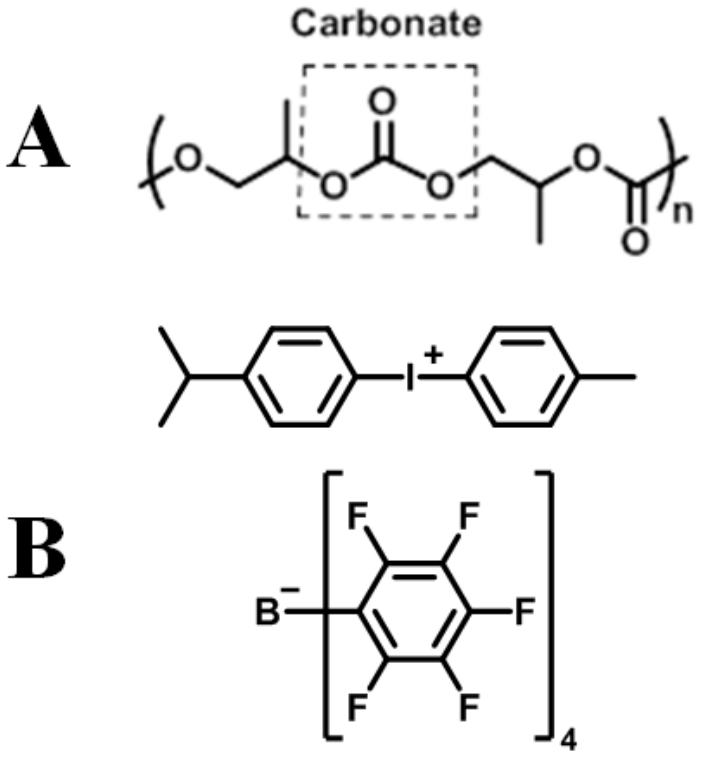

Figure 5.2: A). Polyproplyene carbonate B). PAG used to lower degradation temperature of PPC

fairly low decomposition temperature, T_d, with onset reported anywhere between 180^oC to 240^oC, stemming from the carbonate moiety in its backbone [132, 133, 134]. This decomposition temperature has led to the application of PPC as a sacrificial material in a variety of ways. It has been used for creating encapsulated air cavities, channels for microfluidic devices, and as a binder in the ceramics industry [135, 136, 137, 138, 139]. PPC undergoes two separate decomposition reactions: chain unzipping and chain scission. At low temperatures chain unzipping dominates, where free hydroxyl or carbonate chain ends attack the polymer backbone at the carbonate functionality releasing propylene carbonate. Above 200^oC, chain scission dominates causing random breaks in the backbone, releasing CO_2 and propylene glycol. The degradation of PPC is

clean leaving behind minimal residue, as the decomposition by both chain unzipping and chain scission produce volatile or low boiling point by-products. The decomposition of PPC can be tuned to lower the decomposition temperatures by blending with acidic or basic additives. Acid protonates the carbonyl oxygen, lowering the activation energy necessary for chain scission, while base can deprotonate hydroxyl and carboxylate chain ends to promote chain unzipping and directly attack at the carbonate. Both lower the onset of decomposition temperature, leading to a complete and clean decomposition at significantly lower temperatures. The use of photoacid generators (PAGs) in PPC allows for the controllable release of acid into the polymer when exposed to a dose of UV [140, 141]. Figure 5.2B shows the structure of the PAG used, which upon Deep UV exposure, releases a super-acid. This causes a significant lowering of the onset of T_d from 230^oC to 105^oC. This shift can be seen in the Thermo Gravimetry Analysis (TGA) curves shown in Figure 5.3 comparing pure PPC and exposed PPC with PAG. When the PAG containing sample is exposed to 4 mJ/cm^2 of UV exposure of 165 nm wavelength, a shift in decomposition temperature is seen. All samples were spun from PPC dissolved dichloromethane, as it is an excellent solvent for both PPC and the PAG, and has extremely low boiling point of 39.6^oC. It is quickly and completely removed during the spin coating process, eliminating the need to further bake off the solvent. Additionally, in a study of decomposition temperatures of PPC spun from several different solvents, dichloromethane showed the lowest decomposition compared to the other solvents that were screened [142].

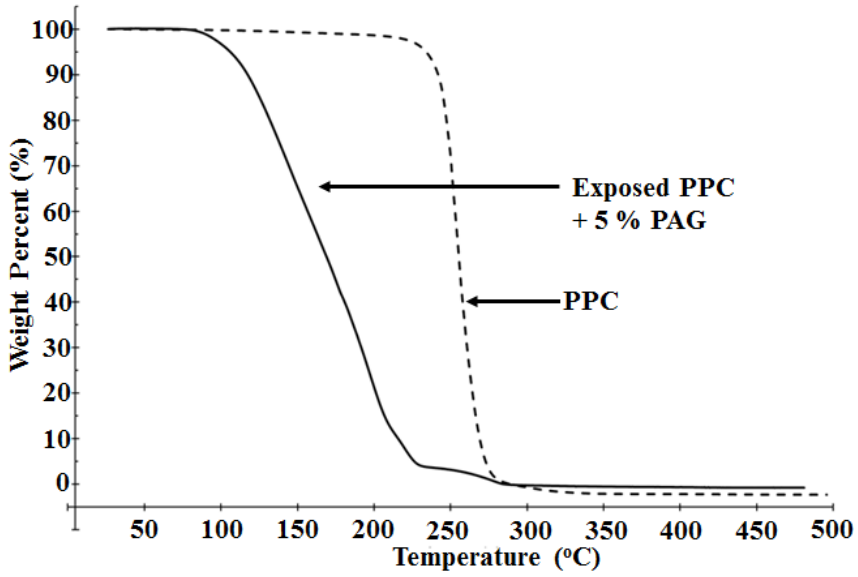

Figure 5.3: TGA curves of PPC and PPC with 5 wt. % PAG

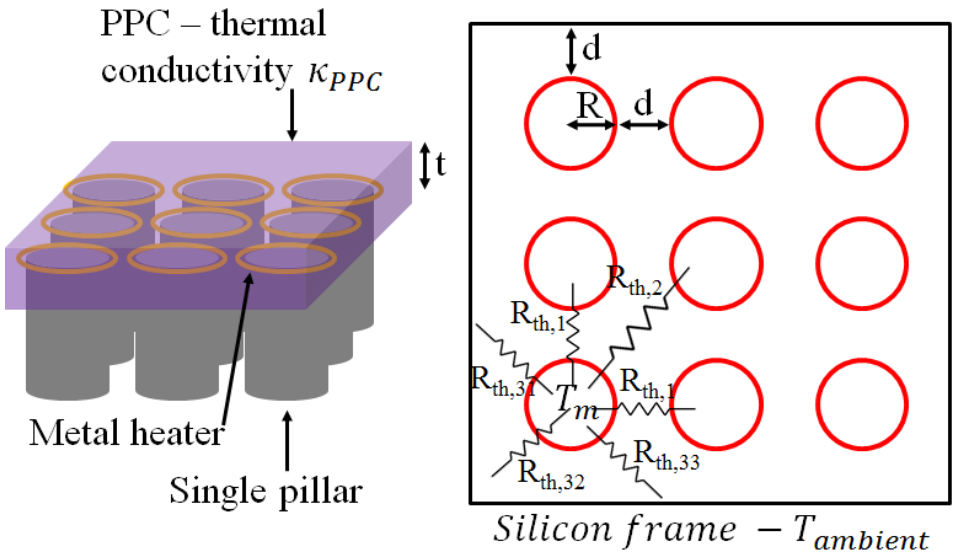

Figure 5.4: Schematic of the analyzed device - 3D view of the pillar array with heaters and PPC handle layer (left) and top view of the array with various dimensions and relevant thermal resistances for conductive losses to the substrate

5.2.2 PoP Thermal Model

Figure 5.4 shows a representative 3×3 array of silicon pillars and a top view of this structure, which is analyzed here. The pillar radius is R and the inter-pillar

spacing as well as the spacing to the edge of the substrate is d. Metal heaters are patterned on the top oxide to realize the heaters, which are used to resistively heat and melt the PPC surrounding the individual silicon pillars.

Quasi-Static Heating

The heating of the pillars and membrane as a function of steady-state input power allows the PPC to stabilize thermally at each point. The heating can be modeled using the Fourier equation of heat conduction is used [143]. Here, the heating of a pillar in the corner of the array is analyzed, and similar analyses can be applied to other pillars without loss of generality. In the steady state, the heating power input into the pillar P_{in} with the metal heater can be written as:

$$P_{in} = \Sigma \frac{T_m - T_i}{R_{th,i}} + hA(T_m - T_{ambient}) + \sigma A(T_m^4 - T_{ambient}^4) \tag{5.1}$$

The pillar temperature (T_m) is assumed to be constant throughout its bulk and A is the pillar area losing heat convectively or radiatively. The ambient temperature of the silicon frame is assumed to be $T_{ambient}$ and T_i is the temperature of the $i-th$ heat sink that contributes to conductive losses from the heater. $\frac{1}{R_{th,i}} = \frac{\kappa A_{cross}}{L}$ is the thermal resistance to each heat-sink - the substrate on which the PPC is suspended and each of the adjacent pillars. The material constants and physical parameters for PPC thermal resistors are the thermal conductivity κ_{PPC}, the cross-section area for the heat flow A_{cross}, and length of thermal resistor L. The convective losses are characterized by $h \approx 20(W/m^2K)$, where h the convective coefficient of air [144]. Radiation is included with $\sigma = 5.67 \times 10^{-8} W/(m^2K^4)$, the Stefan-Boltzmann constant of radiation. Table 5.1 lists the parameters of the system used to calculate the thermal power dissipation.

Table 5.1: Device Dimensions and Physical Parameters

Parameter	**Value**
Pillar radius (R)	100 μm
Spacing between pillars (d)	200 μm
Nominal PPC thickness (t_{PPC})	3 μm
Nominal graphene thickness ($t_{graphene}$)	0.4 nm
Area of the pillar losing heat for convection (A)	6.2×10^4 μm^2
Thermal conductivity of PPC (κ_{PPC})	22 $W/(m.K)$ [145]
Thermal conductivity of graphene ($\kappa_{graphene}$)	4.8×10^4 $W/(m.K)$ [146]
Convective loss coefficient of air	$h \approx 20(W/m^2K)$ [144]
Ambient temperature ($T_{ambient}$)	300 K

Heat conduction to the three nearest pillars and the substrate is included, assuming that the conduction to pillars further away is much smaller. The distance between the pillar under consideration and the two closest pillars varies between d (at the closest points) and $2R + d$ along the tangents on either side. On average, the length of the thermal resistors to these pillars is approximated as $\approx R + d$. Similarly, the distance to the pillar in the center is $\approx (2R + d)\sqrt{2} - R$. The adjacent pillars can be assumed to be thermally isolated from the substrate so they track the temperature changes in the target pillar. The temperatures of these pillars are lower than that of the pillar being released. Hence, the temperatures of the adjacent pillars can be assumed to have a weak linear dependence on the temperature of the pillar being heated. If the pillar under consideration

is at T_m, the temperatures of the two closest pillars is αT_m, and of the pillar in the center is βT_m. Here, α and β (both < 1) are coefficients that are determined empirically, guided by COMSOL FEA simulations. The first term in the steady-state heat transfer equation can be written as:

$$\Sigma \frac{T_m - T_i}{R_{th,i}} = 2\frac{T_m - \alpha T_m}{R_{th,1}} + \frac{T_m - \beta T_m}{R_{th,2}} + \frac{T_m - T_0}{R_{th,3}} \tag{5.2}$$

The conductive thermal resistances to the two nearest pillars ($R_{th,1}$) and the pillar in the center ($R_{th,2}$) can be approximated using a uniform rod thermal resistance ($\frac{1}{R_{th}} = \frac{\kappa A_{cross}}{L}$) resulting in:

$$\frac{1}{R_{th,1}} = \kappa_{PPC}\frac{t_{PPC}(2R)}{R+d} = \frac{2\kappa_{PPC}t_{PPC}}{1+\frac{d}{R}} \tag{5.3}$$

$$\frac{1}{R_{th,2}} = \kappa_{PPC}\frac{t_{PPC}(2R)}{(2R+d)\sqrt{2}-R} = \frac{2\kappa_{PPC}t_{PPC}}{2\sqrt{2}-1+\frac{d}{R}\sqrt{2}} \tag{5.4}$$

The thermal resistance to the silicon frame is calculated by integrating the radial elements to the substrate over the range of angles where the distance to the substrate is less than the distance to the nearest pillars over the angles from $-\pi/4$ to $\pi/4$. This equivalent resistance is:

$$\frac{1}{R_{th,3}} = 2\kappa_{PPC}t_{PPC}\left(\int_{-\frac{\pi}{4}}^{\frac{\pi}{4}} \frac{d\theta}{\frac{1+\frac{d}{R}}{cos\theta} - R}\right) \tag{5.5}$$

The membrane constitutes the PPC and graphene film underneath it, both of which contribute to to the thermal resistance. The product of thermal conductivity κ and the material thickness t for each material constitutes a relative measure of the contribution to heat conduction, since the length and width of the resistors is the same. Even though graphene has a very high thermal conductivity [146], it has a very large thermal resistance because of its sub-nm thickness [147]. The ratio of the κt product for PPC to graphene is 13.1 for the PoP structure, so

that the PPC thermal resistors dominates the conductive heat loss. Hence, it is reasonable to ignore graphene in the thermal model.

Other thermal losses are due to convection and radiation.The thermal resistance due to convection is $R_{th,convection} = \frac{1}{hA}$ where h is the convective coefficient of air and A is the area of heat transfer. The radiative losses are much smaller than the conductive and convective heat losses even at the elevated temperatures for releasing the pillar and are ignored in this analysis. Conductive heat losses from the corner pillar to the substrate at room temperature and to adjacent pillars with weak linear temperature dependence can be estimated with an equivalent thermal resistance R_{th} as:

$$\frac{1}{R_{th}} \approx 2\frac{1}{R_{th,1}} + \frac{1}{R_{th,2}} + \frac{1}{R_{th,3}} + \frac{1}{R_{th,convective}} \tag{5.6}$$

For the corner pillar under consideration, this can be estimated to be $R_{th} = 3.8 \times 10^3 \ K/W$. To achieve the PPC vaporization temperature of 170^oC [148], the necessary input power is estimated to be $P_{in} = \frac{\Delta T}{R_{th}} = 37.6 \ mW$ from this linear quasi-static thermal model. As the PPC melts and the cross-section of the polymer and its thermal conductivity changes, the transfer changes substantially. The analysis presented above is a good first estimate of the power required to reach the melting point of acid-activated PPC.

Pillar Release Using Pulse Power

To reduce the time of release and the total energy required to release a pillar, current pulses instead of a constant current, can be used to drive the heater at a time scale faster than the thermal heating time constant of the pillar to be dissipated through the anchors. For this, a power larger than the quasi-static

heating threshold (determined in the previous sub-section) is needed to release the pillar. The response time of the triggering is set by the thermal time constant of triggering $\tau = R_{th}C_{th}$ - the product of equivalent thermal resistance R_{th} and the thermal capacitance of the silicon pillar being released C_{th}. For a pillar mass m and heat capacity of silicon C_{Si}, C_{th} is:

$$C_{th} = mC_{Si} = \pi R^2 h \rho_{Si} C_{Si} = 2.85 \times 10^{-6} J/K \tag{5.7}$$

Here, the polymer and graphene thermal mass is ignored since it is much smaller than that of the silicon pillar. The numerical value of the thermal time constant for the structure investigated here is in the $10 - 11$ *msec* range. Figure 5.5 shows the equivalent thermal circuit for the device. For a steady-state peak pillar temperature $T_{max} = \frac{P_{in}}{R_{th}}$, the pillar temperature as a function of time is expected to be:

$$T_m(t) = T_{max}(1 - e^{(-t/\tau)}) \tag{5.8}$$

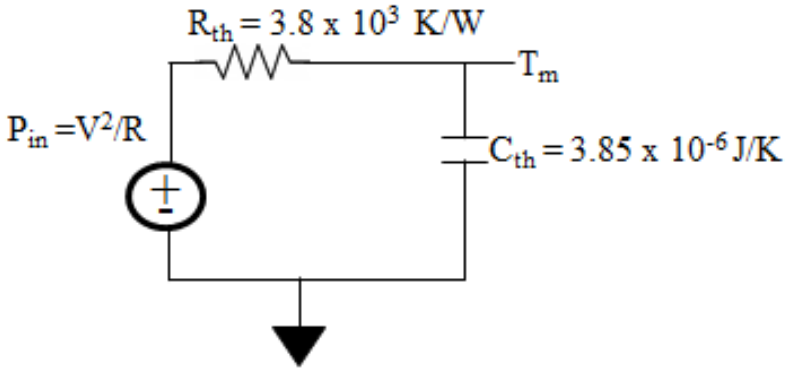

Figure 5.5: Equivalent thermal circuit for the corner silicon pillar of the PoP array.

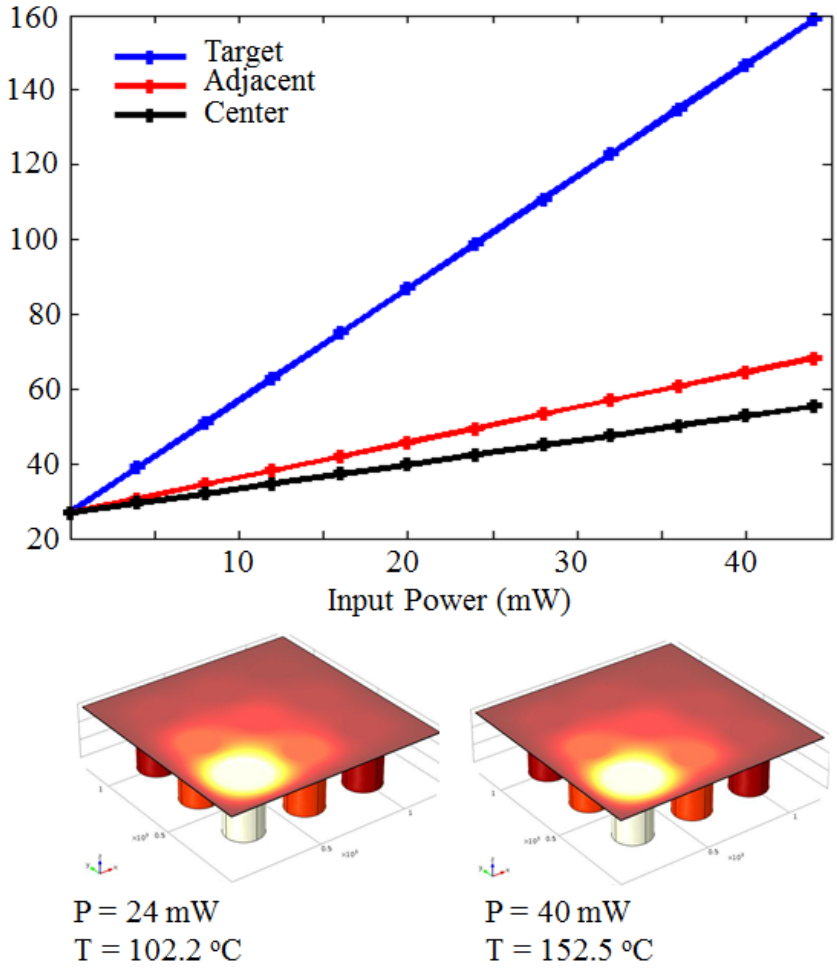

Figure 5.6: Simulation results from COMSOL Multiphysics: The temperatures of the target pillar, adjacent pillars and center pillar as a function of input power to the heater associated with the target pillar. Representative 3D images of the device heating at 24 and 40 mW input power are shown below.

COMSOL for Quasi-Static Heating

COMSOL Multiphysics was used to simulate the thermal heat flux and temperature of a 3×3 pillar array device geometry, with heating of the corner pillar. Ti/Au heaters were used for Joule heating of the PPC substrate and silicon pillars. Figure 5.6 shows the resulting temperature of the target pillar, the two

adjacent pillars and the pillar in the middle as a function of the input thermal power. These plots are used to extract the parameters α and β used in the analytical model. The extracted parameters for the weak temperature dependence of the adjacent pillars and center pillar are $\alpha = 0.21$ and $\beta = 0.31$. These values of α and β are used in the analytical model in equation 5.2.

5.2.3 Graphene Interconnects between Pillars

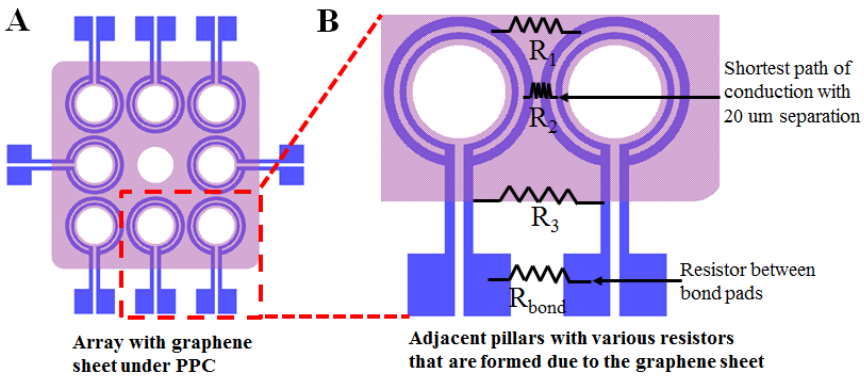

Figure 5.7: Analysis of graphene interconnects formed between pillars with Ti/Au metal heaters as contacts to the interconnects

The PoP structure uses a graphene layer under the PPC, which acts as an interconnect between the pillars. By using an atomically thin sheet of graphene for the interconnects, the connectivity between pillars can also be controllably removed by vaporizing the polymer surrounding the pillar.

The electrical interconnections between the heaters are shown in Figure 5.7A with a 3×3 array of 150 μm radius pillars. The graphene sheet connects metal heaters with Ohmic voltage drops between them, since it is not patterned during the fabrication. The region of graphene between the two heaters, analyzed here is shown in the expanded cross-section (Figure 5.7B). The net resistance is the

distributed resistance between the electrodes, which can be broken up into the four dominant discrete resistors shown in the figure. The spacing between the neighboring heaters, at the closest point of contact, is 20 μm. Since the spacing between the heaters is much larger in the other regions, a $L_1 \times W_1 = 20\ \mu m \times 100\ \mu m$ patch of graphene is considered as the equivalent resistor (R_2) between them. For graphene purchased from Graphene Supermarket, the typical sheet resistance varies between $R_{sheet} \sim 600 - 1500\Omega$ [149]. The expected resistance between the metal heaters is:

$$R_2 = R_{sheet}\frac{L_1}{W_1} \sim 120 - 300\Omega \tag{5.9}$$

When the PPC and graphene vaporize, R_2, R_3 and R_4 are broken. It is then expected that R_{bond} will dominate the resistance since it is the next smallest resistor. The area of R_{bond} is $L_2 \times W_2 = 200\ \mu m \times 170\ \mu m$ and the resistance is expected to be $\sim 705 - 1700\Omega$. As the graphene resistor heats up due to Joule heating, its resistance is expected to decrease owing to its temperature coefficient of resistance (TCR) [71]. The resistance measurements are normalized, and measured to the resistance value at room temperature to compensate for this TCR.

5.2.4 Graphene PPC Piezoresistive Accelerometer

Large-area unpatterned graphene under the PPC can be used as a piezoresistor to measure motion of the pillars. In the context of vaporizable electronics, the accelerometer is a vaporizable MEMS sensor. Graphene has been previously used as a piezoresistor for pressure and strain sensors with a range of reported gauge factors between 0.5 and 1.8×10^4 [150, 151, 152, 153], based on the method of growth, fabrication, substrate of deposition and metal contacts. The graphene

piezoresistors between the metal heaters was chosen to use the PPC substrate as an accelerometer, while the silicon pillars serve as proof masses, (Figure 5.8A). COMSOL eigenfrequency analysis was used to determine the resonance frequency of the 3×3 PoP array of side 1.8 mm with pillars of radius 100 μm and 3 μm thick PPC. The fundamental resonance of the structure with the breathing mode is expected to be at 174.1 Hz, as seen in Figure 5.8B. This exceptionally low resonance frequency is desirable from the perspective of matching to frequencies found in nature for IoTs used in environmental monitoring [154]. This is a direct outcome of the orders of magnitude lower Young's modulus for PPC, compared to typical MEMS accelerometer.

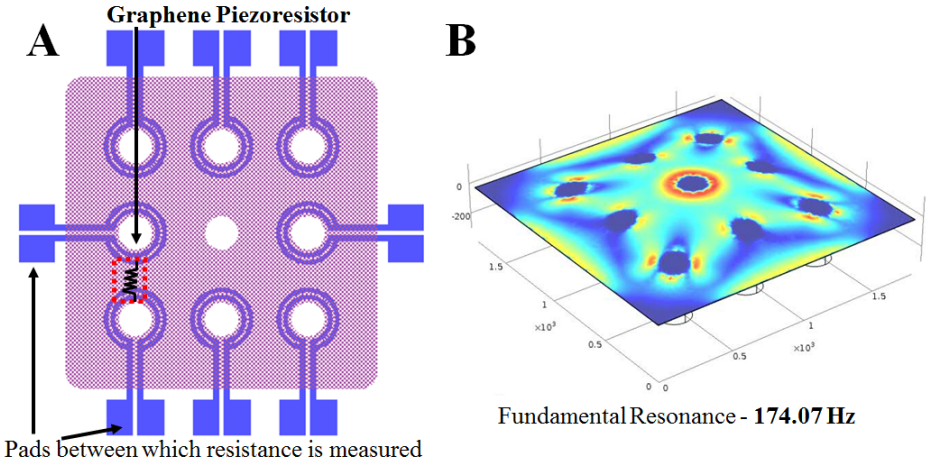

Figure 5.8: A. Graphene piezoresistor between adjacent pillars used for acceleration sensing B. Fundamental breathing mode resonance of the membrane with pillars at 174.1 Hz

5.3 PoP Fabrication Process

The PoP fabrication process flow is shown in Figure 5.9. Devices were fabricated on thinner substrates of 300 μm (instead of conventional 500 μm substrates),

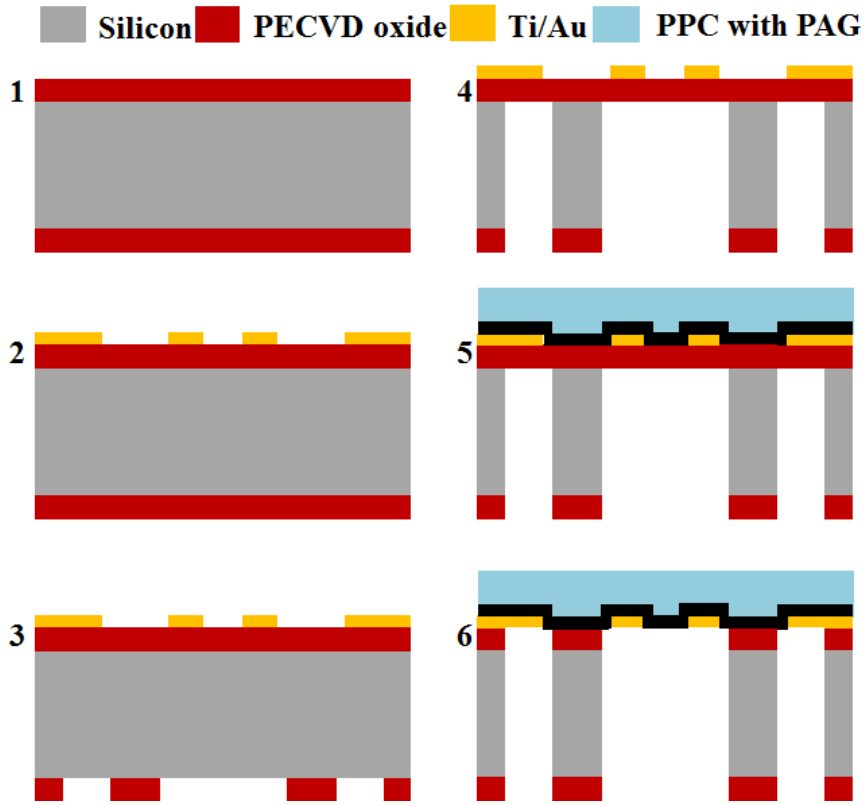

Figure 5.9: PoP Fabrication Process: 1). PECVD oxide deposition 2). Ti/Au heater metal evaporation with lift-off 3). RIE for backside oxide patterning 4). DRIE etch of bulk silicon 5). Graphene transfer with PPC handle layer 6). BOE etching of top oxide to realize final structure.

since deep reactive ion-etching (DRIE) of silicon is the bottleneck in the process. The thickness of the substrate does not influence the device design since DRIE is able to achieve very high aspect ratios as high as 70:1 with process optimization [155, 156]. Plasma Enhanced Chemical Vapor Deposition (PECVD) silicon dioxide of thickness 1 μm and 1.6 μm were deposited on 300 μm double-side polished silicon wafers to define the device-side and backside respectively. Titanium/gold (Ti/Au) metal of 15 nm and 50 nm respectively were deposited on the frontside to define the heaters. A 7 μm-thick film of SPR 220 7.0 photoresist was spun and patterned on the backside of the device for Reactive Ion Etching

(RIE) of exposed oxide with a CHF_3/O_2 plasma, terminating on silicon. Deep Reactive Ion Etching (DRIE) was used to etch silicon terminating on the 1 μm oxide on the front side, to realize an array of silicon pillars suspended on the top side of the wafer. The high aspect ratio of DRIE enables high fill-factor of silicon singulation. For the 300 μm wafer with 20:1 aspect ratio for DRIE etching, gas as small as 15 μm can be realized between pillars. A similar process flow has been previously reported for realizing isolated pillars as electronics islands, tethered together by PPC [157]. However, it did not include interconnects between the pillars to demonstrate the feasibility of a functional electronic die. Additionally, it does not incorporate any sensors. The new device design is able to overcome these limitations.

In [157], a 3 μm-thick PPC film was spin coated on the suspended devices using a 10 $wt.\%$ solution of PPC in dichloromethane (DCM) which has 5 $wt.\%$ photo-acid generator (PAG) relative to the PPC. To use the graphene film as an interconnect, the PPC was spun coated on CVD-grown graphene on 25 μm copper foil. The PPC was treated with a UV exposure dose of 4 mJ/cm^2 to reduce its vaporization temperature from 260^oC to 170^oC [148]. After this, the PPC-graphene-copper stack was placed in copper etchant to remove the coppper, followed by rinsing and cleaning the PPC-graphene layers in successive baths of DI water. This is process similar to the standard graphene transfer process using PMMA as a handle layer [131]. However, here the PPC is not simply a handle layer for transferring graphene, but is the final structural layer. The PPC-graphene layer is transferred on the top side of and allowed to dry for 24 hours.

The removal of the oxide below the PPC/graphene/metal stack is necessary

to realize the PoP structure where pillars can be individually released. Without oxide removal, the pillars remain connected to the oxide even when the PPC vaporizes. The oxide was etched with a Buffered oxide etch (BOE) solution containing 1:6 HF in DI water to realize the final devices. This step effectively transfers the metal heaters from the oxide to the PPC with graphene, leaving it adhered to the polymer. A SEM of the final device is shown in Figure 5.10. The specific choices of materials and techniques used to realize a hybrid polymer-silicon system are explained in detail in the sub-sections below.

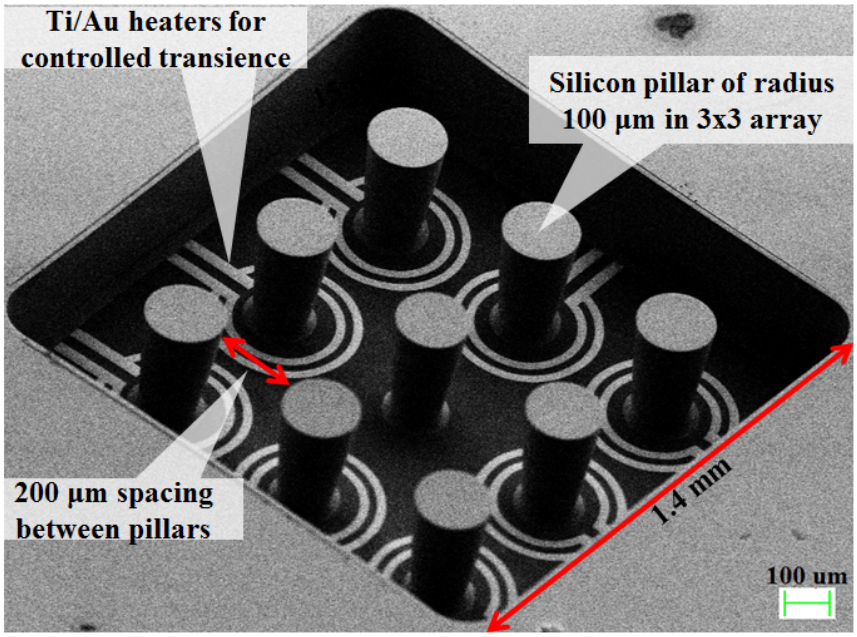

Figure 5.10: SEM of a fabricated 3×3 PoP Array

5.3.1 Passivation and Tethering

To transform a contiguous silicon chip into an array of pillars, we need a thin film to initially tether the pillars together. This film can be eventually etched to transfer pillars to the polymer. To achieve this, a 1 μm silicon dioxide film

was deposited with Plasma Enhanced Chemical Vapor Deposition (PECVD) on the front side. This oxide film holds the pillars together and is an etch-stop for DRIE [125], which is used to singulate the die into individual pillars. In the case of forming PoP on real CMOS, the oxide also serves as passivation to protect the electronics from any chemical etchants during post-processing. Previous designs have used a thinner oxide layer of 0.5 μm which lead to lower yield of devices [157]. This was a consequence of variability in DRIE etch-rates across the wafer, and fragility of the thinner membrane while spin-coating PPC. Thicker oxide of 1 μm mitigates this risk and is able to achieve close to 100% yield of devices.

5.3.2 Metallization for heaters

For graphene-on-nitride devices that we have reported previously, nickel electrodes were used for contact to the graphene [158, 159]. Nickel has been shown to have minimal contact resistance with graphene [160, 161]. Also, nickel does not react with HF which is critical to the final device functionality since the BOE etch exposes HF to the heater material after etching oxide. However, nickel thin films have high internal stress which can cause them to crack, producing faults in resistors [162]. It was observed that nickel heaters failed due to cracking at the anchors, close to the substrate where stress is high, as seen in Figure 5.11. In the future, this could be resolved by evaporating thinner nickel films or by using atomic layer deposition (ALD) films that have more controllable stress.

To solve the problem of the cracking of nickel heaters, gold (Au) metallization was used. Au metallization can also have a small contact resistance with

graphene but needs an adhesion layer of titanium for stiction. However, Ti has a favorable reaction with HF and is etched by it. Even then, this does not affect device functionality because the Ti is etched away only in the suspended regions of the heater. On the substrate where wire-bonds are connected to the metal heaters for electrical contact, Ti is sandwiched between the PPC and oxide and remains unaffected since the lateral undercut produced by the HF $\sim 1\ \mu m$ is much less than the bond-pad dimensions 100 μm. No delamination of the Au films or heater performance degradation was observed even after a 30% over-etch of the oxide in BOE.

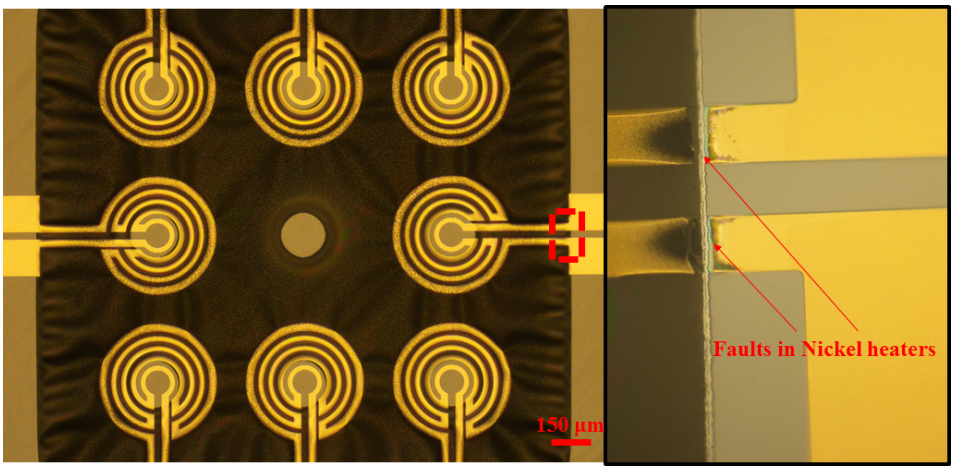

Figure 5.11: Optical micrograph of nickel heaters used in a 3×3 array of pillars (left)and zoom-in image of faults in the metal at the anchor. This problem is resolved by replacing nickel with gold on titanium thin films.

5.3.3 Lithography on PPC Membranes

The substrate temperature is increased during the DRIE of bulk silicon. Since the PAG-loaded PPC is a low temperature degradable material [148], it must be spun-on after DRIE on large area suspended membranes to ensure that it does

not vaporize during DRIE etching. This process demonstrates high yield close to (100%) on large area square oxide membranes as big as 1.8 mm in side, with silicon pillars. The PPC can be lithographically patterned with UV exposure of the areas to be removed followed by heating at $\sim 160^oC$ to produce optically defined features on the substrate.

5.4 Experiment Results

5.4.1 Quasi-Static Heating of PPC Polymer

To test the thermal model and determine the quasi-static power required to singulate a silicon pillar, PoP arrays with UV-treated PPC were tested for heating with the AU heaters. The input voltage on the Ti/Au heater was ramped steadily at 0.2 V/min, to allow the pillar to thermally equilibriate during the ramp. The pillar temperature was measured with a FLIR T300 infrared camera, as a function of input power into the heater. Figure 5.12 plots the IR camera data as well as the expected profile from the analytical model and COMSOL simulation. At 170^oC, the pillars are released by PPC vaporization.

The heating results with unexposed PPC, compared to that without the UV exposure of PPC on the PoP devices are shown in 5.13. The devices without UV exposure of the PPC require heating up to 292^oC for vaporization and release of the pillar. Figure 5.13 shows that 94.94 mW input heating power is needed to release the pillar. The thermal resistance is also seen to decrease above 170 ^oC, the temperature at which exposed PPC vaporizes. This is likely due to partial exposure of the PPC to ambient UV of the required dosage, leading to PPC

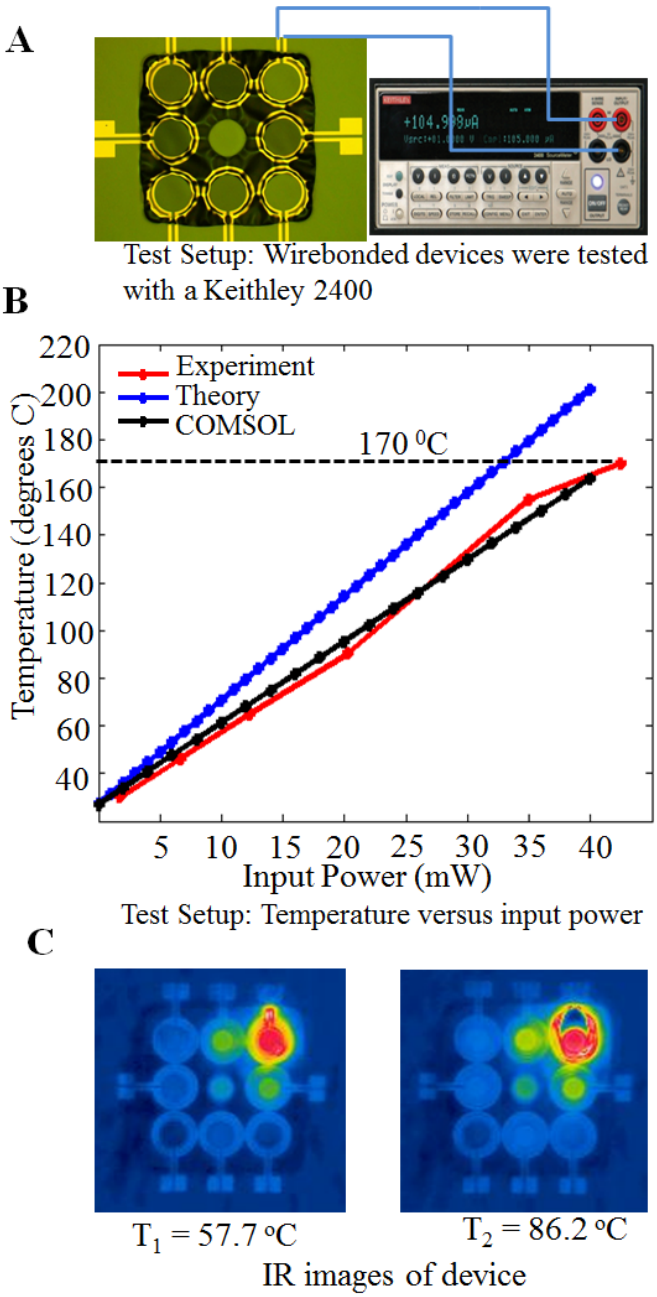

Figure 5.12: A). Test setup used for quasi-static triggering of pillars. The IR camera (not shown here) is used to monitor the device temperature from the top side B). Measured peak surface temperature vs. input power and expected profiles from analytical model and COMSOL simulations C). IR camera images of the device during heating at 57.7 and 86.2 ^{o}C

vaporization at this temperature.

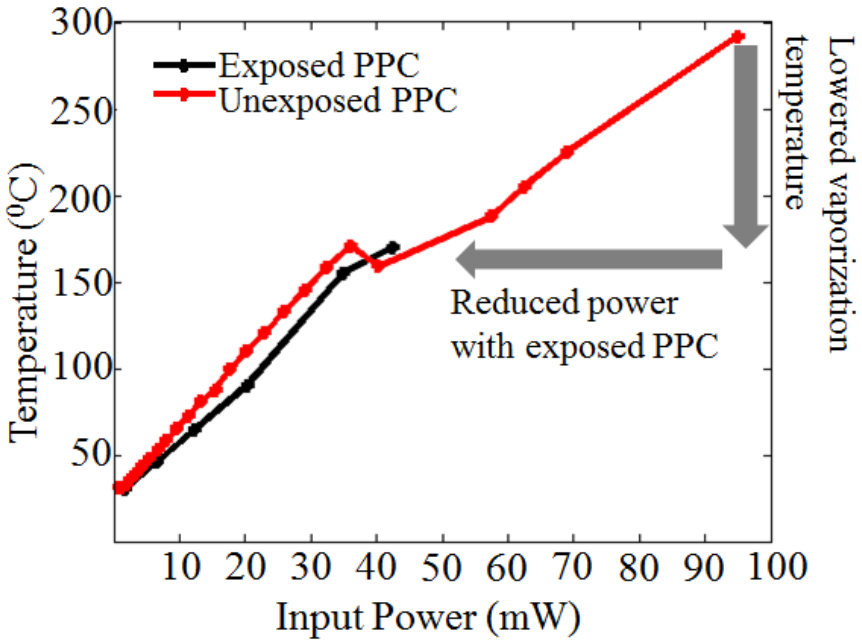

Figure 5.13: Comparison of device heating with exposed PPC and untreated PPC.

5.4.2 Pulse-Powered Triggering

To determine the effect of pulsed power heating instead of steady power input to detach the pillar, current was pulsed into the metal heaters on millisecond time scales. In this test, the 20Ω Ti/Au heater surrounding the pillar was connected in series with an off-chip 22Ω ceramic resistor. The voltage across the off-chip resistor was monitored to determine when the on-chip gold-resistor is no longer conducting. Simultaneously, a Keyence VW-9000 high speed camera was used to observe the pillar in slow motion during the release. Figure 6 shows the test setup and the voltage wave-form across the resistor during the triggering, measured with a NIDAQ USB-6259. With no input current, the pil-

lar is intact and the voltage across the resistor is zero (point A). When power is pulsed, the pillar conducts for the duration that the heater is functional (point B to C). When the polymer surrounding the pillar has completely melted and the pillar has been detached, the heater breaks producing an open circuit and the series resistor stops conducting (point D). The duration for which the heater conducts current in the case shown is 5.06 seconds. This is much longer than the analytically estimated thermal time constant of the pillar because the melting of PPC and its physical dissociation limit the time required for releasing a pillar. In some cases, the metal heater remains intact even after the pillar is released. This results in the duration of release being significantly longer than time constant, and consequently leads to higher power consumption. In future designs, the heater geometry and the pulsing profile can be optimized further to bring down the time of singulation close to the thermal time constant.

5.4.3 Graphene Interconnects Resistance During Heating

The graphene interconnects formed by resistors between the different metal heaters were tested to determine the ability to controllably break interconnects between different parts of the PoP chip. The setup for testing graphene interconnects is shown in Figure 5.15. The pair of heaters in this device were specifically chosen for this demonstration because the graphene was not patterned during fabrication. In this case, the separation between the heaters is 20 μm at the closest point of separation and this forms the graphene interconnect as explained in the device design. This resistor was measured to be 154Ω before triggering. A resistor of $R_s = 2k\Omega$ was placed in series with it with a 2V bias and the resistance across the interconnect was measured while simultaneously ramping

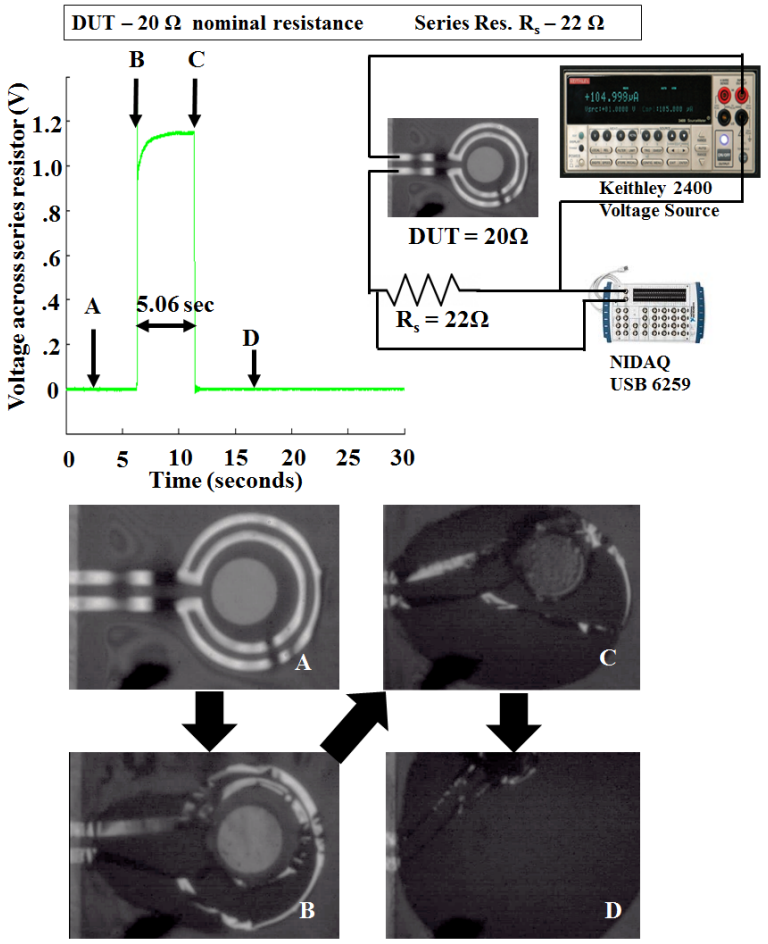

Figure 5.14: (Top) Setup for measuring the triggering time and energy of the device. A Keithley 2400 was used as a voltage source for device under test (DUT) with heater resistance 20Ω in series with a resistor R_s of 22Ω. The voltage across Rs was measured with a National Instruments NIDAQ USB-6259. (Bottom) Triggering sequence captured with a Keyence high speed camera (2000 fps) shows the different stages of triggering a single pillar A). Voltage not applied and the device is intact B). Voltage applied across the series combination starts vaporizing the polymer, heater still intact C). Polymer vaporizes detaching the silicon pillar D). Metal heater fractures and produces an open circuit, no longer conducting current.

power with Joule heating across the heater surrounding pillar B.

Figure 5.16A shows the data for power-ramp across the heater surround-

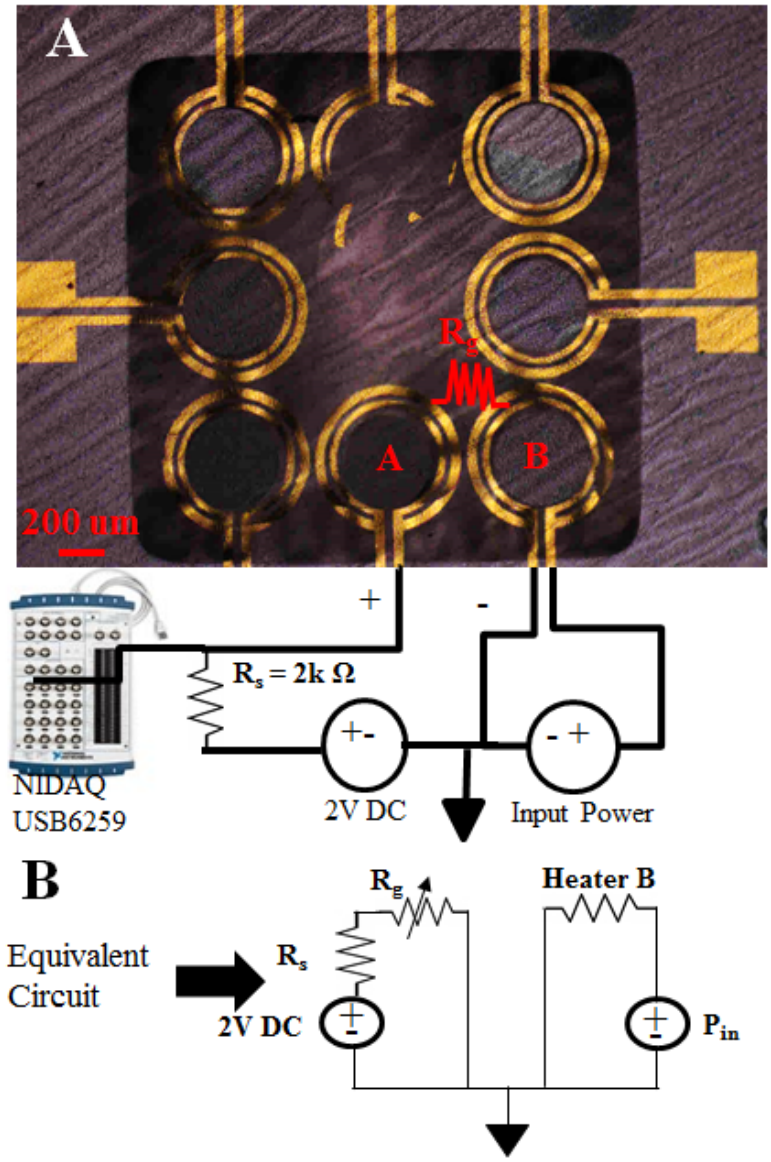

Figure 5.15: A. Setup for testing transience of interconnects between metal heaters associated with pillars A and B. A resistor of 3 $k\Omega$ was placed in series with the interconnect and the voltage across the interconnect was monitored. B. Equivalent circuit for the setup.

ing pillar B in and the resistance measured between resistive heaters, A and B. For this experiment, the PPC was not exposed to UV before transferring the PPC-graphene stack onto the pillar array. As the input power in the heater B

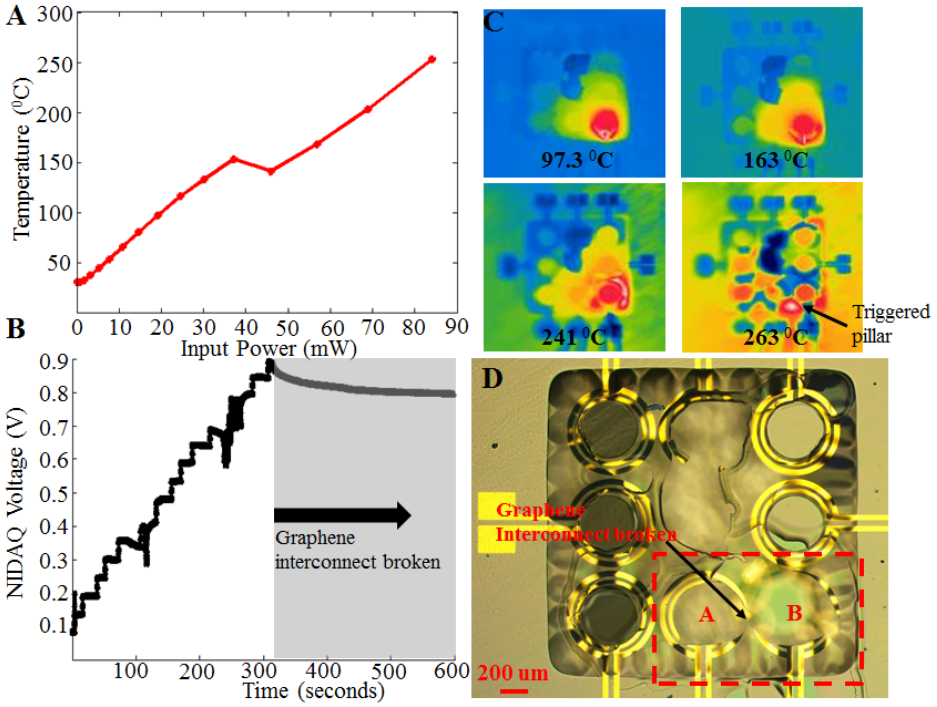

Figure 5.16: A). Temperature of pillar B versus input power for triggering and breaking graphene interconnect, measured using IR camera B). Increase in voltage measured across the series resistor as graphene interconnect is vaporized C). Optical micrograph of triggered devices D). Sequence of IR camera images during triggering

is increased, the PPC degrades and eventually vaporizes while simultaneously degrading the graphene interconnect between the pillars. The voltage across the graphene resistor rises as the interconnect degrades. The voltage across the interconnect follows a stepwise increase, in correspondence with the increase in power in heater B which causes the PPC-graphene to vaporize and eventually break. It is possible that strain induced in the graphene as the PPC temperature rises is also responsible for the change in resistance. At 262 ^{o}C, the pillar B is released from the frame and the PPC and graphene interconnect between the adjacent heaters is completely vaporized. After pillar release, the resistance is dominated by the smallest resistor between the heaters where the graphene is

intact - the bond-pads and metal leads connecting to the heater. This resistance was measured to be 1.21 $k\Omega$, nearly equal to the average expected resistance between the bond-pads calculated earlier. Table 5.2 compares the analytically expected results from this experiment, to the measured data. The experiment shows that interconnects between components of the PoP array can be controllably eliminated during the release of the silicon pillars.

Table 5.2: Summary of Interconnect Triggering

Parameter	**Analytical**	**Experimental**
Pillar release temperature (^oC)	270 ^oC	262 ^oC
Pillar release power (mW)	71.1	84.16
Interconnect resistance before pillar release (Ω)	120 – 300 Ω	154 Ω
Interconnect resistance after pillar release (Ω)	0.705 – 1.7 $k\Omega$	1.21 $k\Omega$

5.4.4 Graphene Piezoresistive Accelerometer

The accelerometer response was measured using the setup shown in Figure 5.17. The 3×3 PoP array with 100 μm radius pillars suspended on a PPC membrane of side 1.8 mm is placed on a shaker table with an acrylic spacer to prevent coupling of the magnetic field from the shaker table to the graphene resistors. Unreleased devices without DRIE etching were used for calibration with the shaker table (not shown), to subtract the electromagnetic coupling signal and

obtain the mechanical response of the device. The graphene resistance between the metal heaters was 190 $k\Omega$ and it is connected in series with a ceramic resistor of a similar value. A 100 $k\Omega$ potentiometer was used for the second branch of the Wheatstone bridge. An Analog Devices AMP04 amplifier with a gain of $G = 10\times$ was used to boost the signal from the piezoresistance modulation, followed by signal acquisition with a NIDAQ USB 6259. The frequency response of the accelerometer for a fixed input acceleration of 3g, was measured over frequencies of interest (Figure 5.17). The flat-band response of the accelerometer has an average amplitude of $A = 2.73\ mV$. The unamplified sensitivity of the graphene piezoresistor is:

$$A_{sense} = \frac{A}{G} \times \frac{1}{3g} = \frac{9.2\ \mu V}{m/s^2} \tag{5.10}$$

The resonance frequency of the structure is $\sim 180\ Hz$ close to that expected from COMSOL simulations. However, a second resonance is observed at 210 Hz. This is a potential consequence of the acrylic stage used to mitigate magnetic field coupling to the sensors producing a second resonance. The quality factor Q of the resonator is $Q \approx 7.2$ with the resonance centered at 180 Hz. The output voltage of the balanced Wheatone bridge is:

$$v_{out} = 12V(\frac{R_3}{R_3 + R_4} - \frac{R_{graphene}}{R_{graphene} + R_2}) = 9.2\ \mu V \tag{5.11}$$

The change in resistance per unit acceleration is:

$$\frac{\Delta R}{R_{graphene}} = \frac{9.2\mu V}{12V} = 7.6 \times 10^{-7} \tag{5.12}$$

From COMSOL simulations, the local strain produced in the PPC membrane between the pillars is $\epsilon = 4.7 \times 10^{-7}$ for a constant input acceleration of 3g in the flatband. The resultant gauge factor (GF) for the piezoresistors is estimated as $GF = \frac{\frac{\Delta R}{R_{graphene}}}{\epsilon} = 1.61$. This GF is within the range of values reported previously for graphene [150, 151, 152, 153]. The piezoresistance of the metal heaters

and wirebonds also contributes to this signal with GF for metals being ~ 2. So the change in the smaller resistance due to the metal does not influence the graphene piezo-resistance change which is much larger.

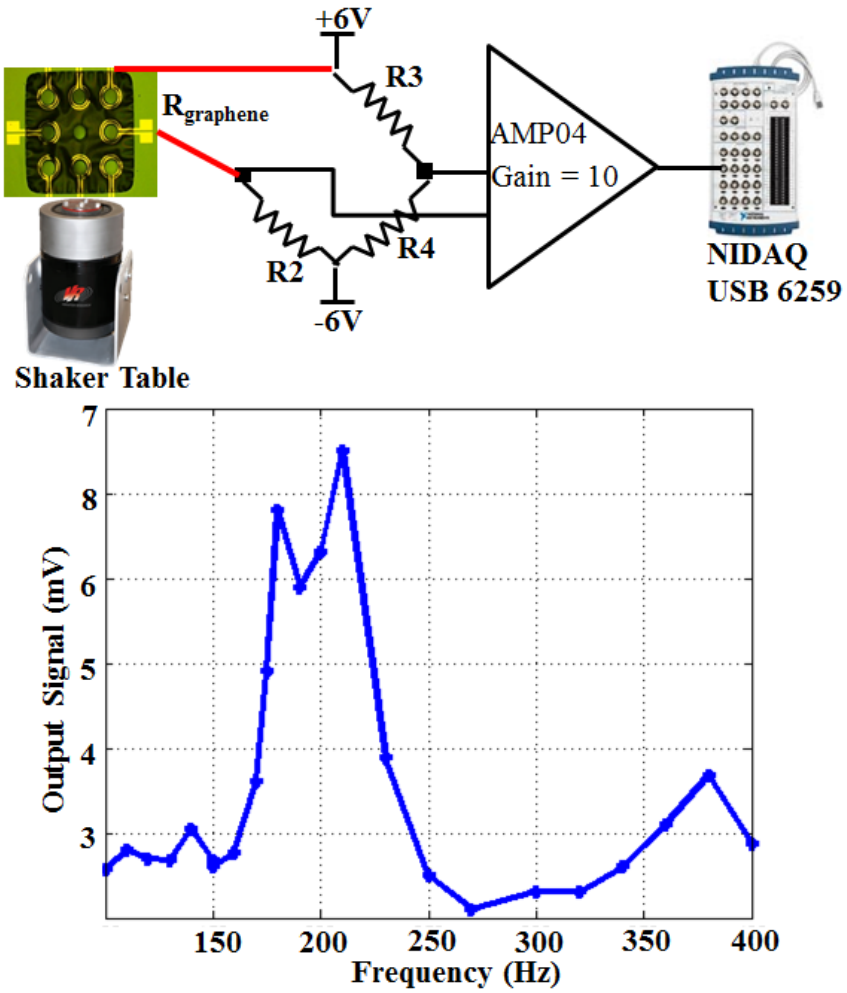

Figure 5.17: Shaker table setup for measuring the accelerometer response of the PoP membrane device with a 10× amplifier and 60 Hz notch filter followed by data acquisition.

5.5 Discussion

5.5.1 Technology Translation to CMOS

This chapter has presented the fabrication of MEMS devices with graphene and metal interconnects and sensors on a flexible polymer substrate. It is critical to integrate MEMS devices with CMOS circuits to provide capabilities for information processing as well as communication with the physical world [163]. Researchers have demonstrated CMOS circuits on flexible substrates using Thin Film Transistors (TFT). Several research groups demonstrated TFT-based CMOS circuits on different flexible substrates [164, 165]. More commonly used materials for TFT are: amorphous Si (a-Si:H), graphene, CNT, organic semiconducting material etc [166]. To integrate MEMS and CMOS in the PoP architecture, the planner interconnections can be made by patterning metal on top of polymer. Additionally, MEMS and CMOS can be integrated by stacking/sandwiching different layers and using conductive polymers. In such case, via connections will be formed by selectively exposing and vaporizing polymer substrate to deposit side wall metals. On the other end, the polymer used here is vaporizable after certain temperature range so the low temperature integration process need to be developed [167].

5.5.2 Graphene for Interconnects and Sensors

On-chip interconnects have been traditionally made with multi-layer metal-stacks [168] with dielectrics between the layers. Similarly, piezoresistors are fabricated using silicon which has a gauge factor in excess of 130 [169]. How-

ever, these interconnects and sensors are designed to be structurally robust, and cannot be reconfigured to be transient, thus making it difficult to design a transient substrate. Graphene has a very high Young's modulus of 1 TPa [170], but the atomically thin layer can be easily bent and broken out-of-plane making it suitable for transient electronics. In this work, the graphene has been shown to conform to highly strained flexible PPC substrates.

The graphene used for realizing interconnects between pillars must be defect-free and have low resistance in order to reduce Ohmic losses [171]. Previously, graphene has been specifically processed with high quality chemical vapor deposition growth (CVD) and thermal quenching for interconnects in high speed CMOS circuits [172] and for flexible electronics [173]. Hence, the graphene used for demonstrating interconnects in this paper was commercially obtained with large grain sizes and few defects.

In order to use graphene as a two-dimensional piezoresistive sensor, it is desirable to use polycrystalline graphene. The smaller grains and resultant traversing of carriers across grain-boundaries can be modulated to produce large piezoresistance changes in the graphene when the graphene is strained [174, 175]. Ultra high gauge factor (1.8×10^4) of graphene piezoresistors [150] has been previously demonstrated, using polycrystalline CVD graphene transferred on silicon nitride, patterned with metal electrodes. To demonstrate the use of graphene as a piezoresistor with the PoP architecture which has suspended silicon pillars as an accelerometer, polycrystalline CVD-grown graphene was used with large resistivity. In future iterations of the device, graphene for both, the interconnects and the sensor, can be transferred using PMMA [131] and then patterned with lithography. The PPC can then be spun-coat [157]. This can

achieve well-defined interconnects between different components of the chip as well as piezoresistors in high-strain regions of the PPC for maximum signal pick-up.

5.6 Conclusion

In conclusion, this work demonstrates a substrate consisting of individual silicon islands attached to a flexible substrate that can be vaporized. The pillars can be controllably detached from the substrate without affecting other components of the chip. Pulse-powered current driven heating of the PPC to vaporize the PPC and release silicon pillars demonstrates the potential for low-power substrate vaporization with electrical control. Graphene has been used as piezoresistor for acceleration sensing as well as for realizing interconnects between pillars. The graphene can be vaporized with the PPC, on demand, to realize vaporizable electrical interconnects and vaporizable inertial sensors.

CHAPTER 6

LOW-VOLTAGE ION MOBILITY SPECTROMETER ARRAY

Fast and reliable detection of toxic gas-phase industrial chemicals and warfare agents, which may be combustible, odorless, and colorless, necessitates the use of miniaturized multi-functional and portable gas analyzing systems. This chapter presents a silicon micro-machined ion-mobility spectrometer array (IMSA) using a versatile high aspect-ratio 3-D fabrication process and operating at less than 5V. The multi-electrode architecture facilitates simultaneous detection of more than one toxic gas species. Such a device has potential use for on-chip ion trapping in a quadrupole or hexapole electrode configuration. It also paves the way for a label-free gas analysis system that can be monolithically integrated with on-chip low-noise amplifiers to produce a low-cost mobile platform for detection and analysis of multiple gas species.

6.1 Introduction

Micro-scale gas sensors have been widely researched, owing to the advent of MEMS manufacturing capabilities and integration with CMOS circuits. Micro-gas analyzers (MGA) prove to be useful in separation of gases along long diffusion tubes followed by absorption on nm-thick metal films which changes the film conductance properties [176, 177]. MGAs do not necessarily require monolithic integration for high performance but rely solely on mass detection whereas both mass and ion-charge are important for differentiating gases. Micro-scale mass spectrometers (MS) can detect ions in B-fields [178] but require vacuum and large voltages for their operation. Since the principles of operation in IMS, which uses both ion-charge and mass are used for gas detection,

are well understood, the device can be miniaturized to the wafer level, and the same physics can be applied at the micro scale [179]. This chapter presents chip-scale multi-species ion detection, which uses high resolution and low voltages for pattern-based ion recognition.

6.2 Ion-Mobility Spectrometry

Ion-mobility Spectrometry (IMS) (shown in Figure 6.1) relies on the charge to mass ratio of ionized volatile organics, to separate and detect multiple species of gas-phase ionized molecules in a buffer gas. The analyte gas is ionized at the entrance of a drift tube and detected at its end with ion-detection electronics the time of travel for the ions and their charges enable determination of the gas species. A detailed description of the theory of charged-particle motion in electric fields is available in literature [180, 181]. For ion-flow across an electric field in a buffer gas mixture, the important parameters are the charge, mass and collision cross-section in the gas. The μ-scale acceleration and deceleration of a ion in an electric field E gives it a constant drift RMS velocity v_{drift} proportional to the field:

$$v_{drift} = \mu E \tag{6.1}$$

Here, μ is the ion-mobility which can be estimated by the Mason-Schamp equation [182]:

$$\mu = \frac{3}{16}\sqrt{\frac{2\pi}{m_{eff}kT}}\frac{q}{n\sigma} \tag{6.2}$$

m_{eff} is the reduced mass of the ion in the buffer gas, q is ion-charge, σ is collision cross-section of the ion and n is ambient air concentration. IMS detectors are highly accurate in multi-species detection of ppm and ppb gas concentra-

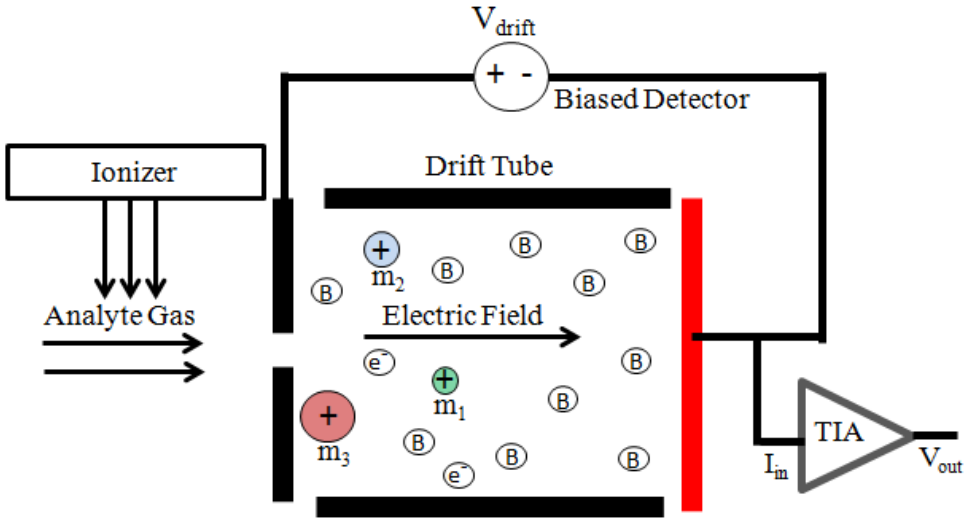

Figure 6.1: Ion-mobility analysis in drift tube with one planar electrode for measuring travel-time of different ions, $m_1 < m_2 < m_3$, in opposing buffer gas m_B. Electrons present in the drift tube are accelerated towards the positive electrode thereby producing no signal at the output

tions. However, they have traditionally been bulky table-top pieces of equipment, have a high cost of operation and maintenance and require high operating voltages.

6.3 Device Design

The key parameters for ion-mobility measurements are the mass and charge of analyte species. The ion-mobility based device concept presented here, is shown in Figure 6.2. The analyte gas mixture is ionized at the entrance of the flow channel. The ions have a constant lateral velocity (imparted by an off-the shelf pump) $u_{\|}$, and a transverse E-field is applied to this mixture. The ions undergo mobility-dependent segregation on the individual electrode islands which is detected as an output current - the ions with higher mobility (such as m_1) are sep-

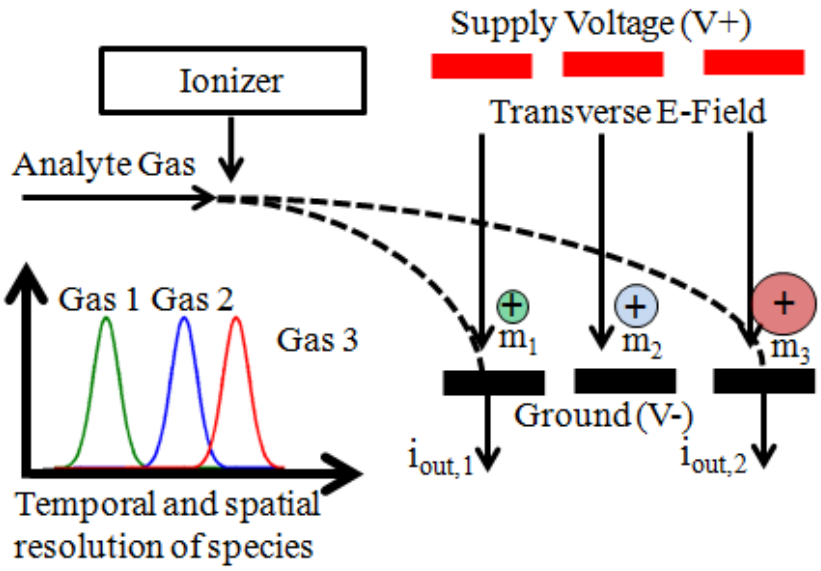

Figure 6.2: Ion-mobility analysis in constant lateral flow velocity with transverse E-field for spatial mass spectrometry providing spatial and temporal resolution of multiple species

arated on the earlier electrodes, since they have a larger transverse velocity and hence, shorter time of travel in the Y-direction. The lower mobility ions (such as m_3) travel further and reach the electrodes farther along the X-direction. In order to operate the device at low voltages ($< 5V$), the separation between opposite arrays of electrodes needs to be $\sim 1\ mm$. This allows generation of electric fields of $5 - 8\ kV/m$, sufficient to separate ions of different molecules on individual detector islands [183]. The resolution to separate multiple gas species needs consideration while fixing electrode widths and lateral separations between individual electrodes. The transverse time of travel in the channel, assuming an ion starts flight at the top of the channel is:

$$t_{\perp} = \frac{h}{\mu E} \tag{6.3}$$

The electric-field $E = \frac{V}{h}$, so the time of travel is:

$$t_{\perp} = \frac{h^2}{\mu V} \tag{6.4}$$

In this duration, the ion flows with a constant velocity in the X-direction along the channel as a result of the velocity imparted by the pump:

$$t_{\|} = \frac{L}{u_{\|}} \tag{6.5}$$

These two times of travel must be equal:

$$\frac{h^2}{L} = \frac{\mu V}{u_{\|}} \tag{6.6}$$

The above equation provides a design space to determine electrode dimensions and channel length, based on the applied voltage, flow produced by the pump and the mobility of gases to be detected. In this device, with transverse electric fields of few kV and ion-motion with air as the buffer gas, the electrode width and inter-electrode spacing were designed to be 800 μm each. Achievement of high aspect-ratio (> 1) of the electrode wall height with respect to the channel width is important in minimizing the loss of ion flux due to electric field curvature around the wall edges. This also helps in obtaining uniform temporal drift times of ions as they flow along the channel laterally. Figure 6.3 shows COMSOL simulations of electric field curvature for a $5V$ potential difference across the electrodes and the variation of curvature with wall height for a fixed channel width. The E-field curvature effect around the wall edges is also reduced as the aspect ratio is tripled from 1:2 to 3:2.

Thin metal sheets cannot be patterned effectively to produce high aspect ratios with vertical sidewalls. They also develop internal stresses after etching causing out of plane bending and inaccuracy in electrode-placement. In the device presented here, highly doped silicon was bulk micromachined to pattern the electrodes. Doped silicon is more resistive compared to conventional metals used for conduction such as copper or aluminum. However, it has sufficient

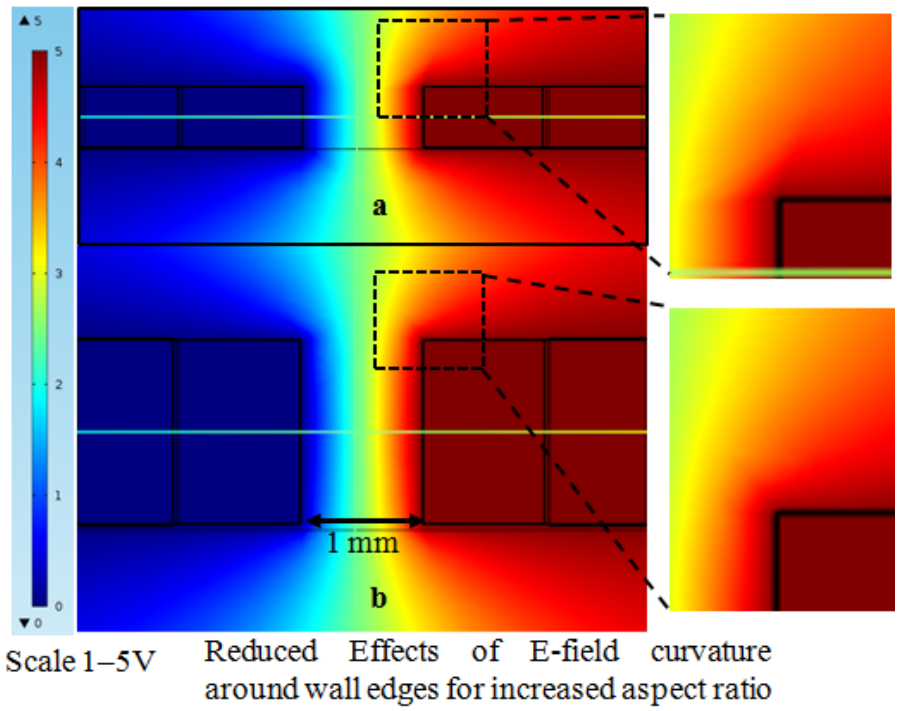

Figure 6.3: COMSOL simulations of E-field lines in the device showing a cross-section. The zoomed areas show the reduced effect of the E-field curvature effect around the edges as the aspect ratio is tripled from 0.5 to 1.5 for a fixed channel width of 1 mm

rigidity to allow bulk micromachining through the substrate without developing high stress or producing faults in the device layer. The required aspect ratios can then be achieved by stacking these layers of patterned silicon.

6.4 Device Fabrication

For etching and micromachining the device layer, laser-cutting was preferred to regular high aspect ratio etching by means of DRIE because it is available in-house and requires no lithography masks. Conventional DRIE is able to produce high aspect ratio (> 20) trenches and through-holes with surface scalloping

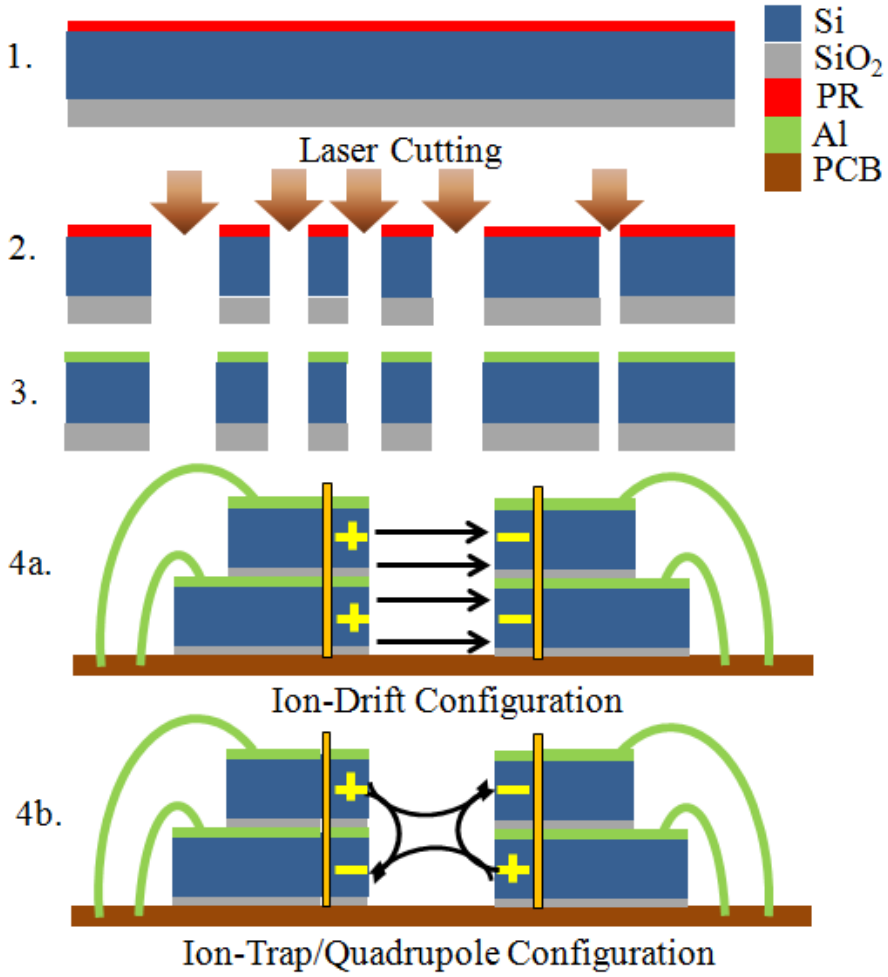

Figure 6.4: Fabrication process flow and assembly for stacked IMS array device.

of $< 50\ nm$. The beam resolution for laser cutting is about 100 μm with surface roughness of 10 μm . However, for the desired channel spacings of hundreds of microns, this produces very small variations in the electric field while providing a conductive wall surface.

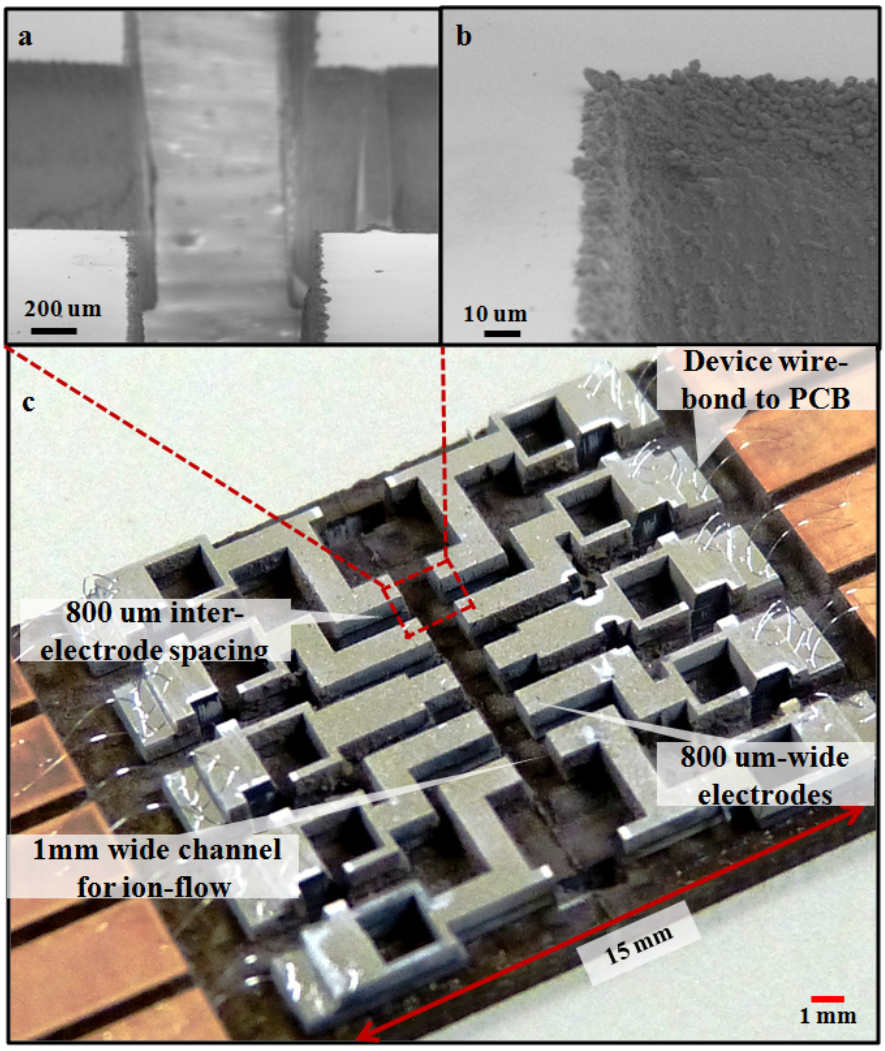

Figure 6.5: a). SEM images of laser cut device features for individual electrodes b). Surface roughness of 10 um due to laser cutting c). Photo of assembled 2-layer ion-mobility spectrometer array. Square through-holes were used for optical alignment of layers on the PCB with vertical pins, which were eventually removed

6.4.1 Direct-pattern Maskless Laser Micromachining

A novel fabrication process flow, shown in Figure 6.4, was developed to pattern and assemble device layers. A 600 *nm* plasma enhanced chemical vapor deposition (PECVD) silicon dioxide film was deposited on the unpolished side of a 0.5 mm highly doped SSP Si wafer with resistivity $0.001\Omega - cm$, for insulation. Photoresist was then spun on the polished side as protection for the device layer during etching (step 1). Arrays of the spectrometer electrodes were patterned by through-hole etching the wafer with a Class 1 laser LPKF Protolaser U (step 2). Individual electrodes on both sides were held together by solid silicon tethers which were left uncut at this stage for the purpose of device alignment. The photoresist was then stripped off the device layer, and aluminum was sputtered on it for contact (step 3). Two or three device layers were then stacked adhesively to achieve the high aspect ratio and stuck to a PCB layer. The tethers were then cut with the laser to isolate the electrodes each electrode island thus obtained has its individual layers insulated from each other due to the bottom oxide layer. The electrodes were then wirebonded to the PCB for electrical contact. The device can be used for mobility-based gas detection in the ion-drift configuration (step 4a) or for trapping ions with a quadrupole configuration (step 4b).

6.5 Device Test Setup

The final assembled device for testing is shown in Figure 6.5. SEM images of the device show wall roughness of 10 μm. A two-layer stacked IMSA with 1 mm channel width for ion flow that can be made as small as 150 μm with laser-

cutting. The inter-electrode spacing and electrode width are each 800 μm for a target resolution in gas molecular weights of 15, on 5 pairs of opposing electrodes. Every electrode on each layer has independent addressing for multiple voltage configurations. The device is symmetric and the electrode stack closest to the ion-channel input is labeled electrode 1, the furthest is electrode 5. For both devices, no detectable signal was observed on channel 5. Gas ionization occurs at the input of the channel with a commercial RPIF-34815B ionizer with ionizing beta-emitters of 670 keV, sufficient to produce ionized molecules as detectable signals for testing in air and in an air-acetone mixture. All current measurements for the device were done with Keithley 4200 SCS and a glass plate is used for confinement of the ions during experiments. For the purpose of testing, all layers on an isolated detector island are wire-bonded together to produce a high aspect-ratio channel. The device dielectric breakdown voltage in air is 2.4 kV, sufficiently large compared to operating voltage of 5V.

6.6 Experimental Results

With no ionization occurring at the channel input, the baseline noise current on each of the channels is approximately 10 pA. As a function of applied transverse voltage, the signal on each of the channels initially increases linearly till 1.9V and then saturates show in Figure 6.6. The voltage at which electrode current saturates is in close agreement with the predicted concentration-independent ion-mobility saturation for ion-flow in a large E-field from theory and simulation, as explained in [184].

For ionization in air, the detected current on each of the electrodes for a 5V

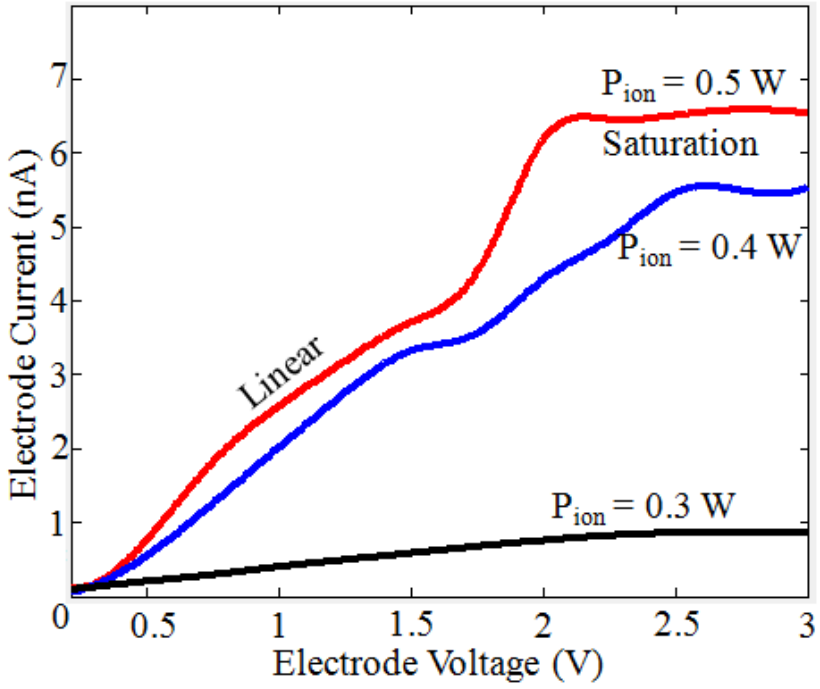

Figure 6.6: Device current as a function of electrode voltage (tested on electrode 2) for different ionizing powers which vary the ion-concentrations produced. Ion-current saturation occurs in transverse E-field at approx. 1.9V

bias is shown in Figure 6.7 and also compared to that of a single-layer device. For the stacked 2-wafer device, a strong signal of 6.8 nA on electrode 2 indicates gas species in the molecular weight range of 15 to 30, from nitrogen and oxygen which are majority components in air. The large 4.5 nA signal on channel 1 is not clearly understood based on the percentages of gas molecules in air with molecular masses in the range of 1 to 15, which is the target for that electrode pair. A possible explanation for this is the localized ionization of air close to the detector electrodes which is dependent on the placement of the ionizer. The ionizer flow in the device channel is not localized to the top and the ionization can lead to the formation of coordination complexes of charged ions with water molecules and other polar molecules. The two-layer device shows more than a

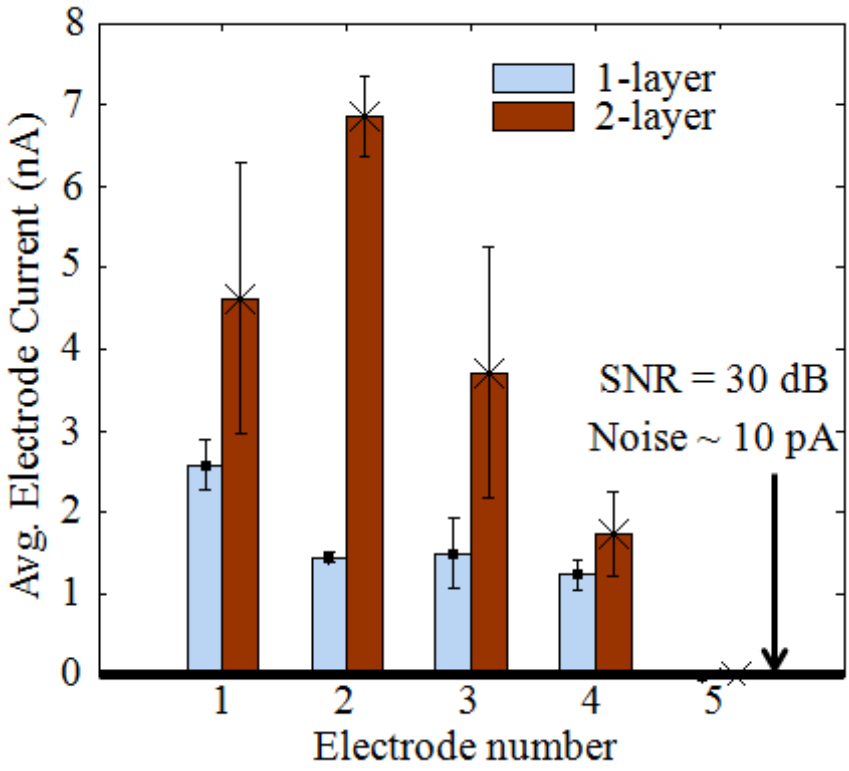

Figure 6.7: Spectrometry of ion-species based on ion mobility Comparison of average current (nA) sensed as a function of electrode number on one-layer(left) and two-layer(right) devices for ionization of air. The stacked-device device has enhanced sensing due to effective confinement of ions in channel

2x enhancement in case of some electrodes, a consequence of the more effective confinement of ions to the device channel.

Testing of the device with acetone-air mixture was performed by boiling 25 *ml* acetone and feeding the vapor through an attached tube to the ion-channel, while it is being ionized before entering into device. The observed signals on the 5 electrodes are shown in Figure 6.8 and compared to the signal from air for 5V DC bias across the electrodes. Electrode 2 shows a reduced current of 4.5 nA as a result of the relative reduction in concentration of nitrogen and oxygen due to the addition of high molecular weight acetone (molecular

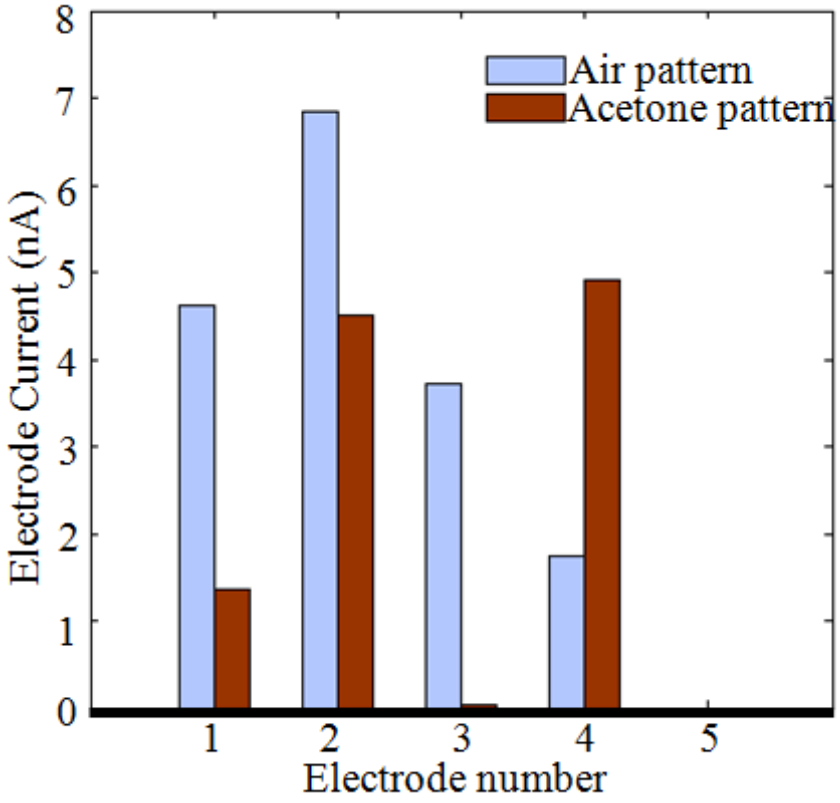

Figure 6.8: Detection of acetone-vapor in air comparison of the signals from ionization of air (left) and an air-acetone mixture (right). A strong current on electrode 4 in the air-acetone mixture indicates the acetone signal

weight = 58) in the mixture. Electrode 4 shows an enhanced current of 4.9 *nA* due in the acetone signal pattern. Signal on electrode 3 is almost completely suppressed, perhaps due to the buffer gas interaction with the ion plasma flow on electrodes 2 and 4.

6.7 Conclusion

Ion-mobility spectrometer array using a novel 3-D fabrication process, which paves the way for multi-species label-free ion detection, is presented. Results indicate that this device can achieve high resolution in molecular weight detection for gas species in air with maximum ionization power of 0.5W. By integrating this sensor with a benign radioactive ^{63}Ni source for power generator and ionization, that has been previously demonstrated [185], and on-chip amplifiers, the device can operate for several decades, limited only by the half-life of 100.3 years of the ^{63}Ni.

CHAPTER 7

THIN FILM PIEZOELECTRIC SENSE-ACTUATE FAN PAIR

For ion-mobility spectrometry-based gas sensing using the architecture describe in chapter 6, it is critical to produce specific ion-flow rates using low-power architectures in order to maximize sampled air volume for fast detection. In this chapter, a novel thin-film piezoelectric sense and actuate fan-pair for gas pumping is presented. This fan pair serves as a component for controlled ion flow in ion-mobility-based gas detectors. The highest flow-rate produced by actuating a 800 μm long beam at resonance is 7.01 cm/sec with a flow rate of 185.1 $\mu L/min$. The drive-fan achieves low-power operation (13.5 $mW/sccm$), low voltage (10.8 $V/sccm$) with sufficiently small form-factor (0.1 $mm^3/sccm$) along with feedback flow signal from the sense-fan to measure the flow and detect the onset of turbulent flow. This device has the potential for monolithic integration with CMOS circuits for chip-scale label-free gas detection.

7.1 Micro-scale Gas Pumping

Micro-scale gas pumps are important components of portable gas-sensors and gas chromatographs for emission content monitoring in industry, automation and food packing as well as environmental sensors for maintaining air quality [177]. Gas pumps also find applications in microfluidic devices for laminar flow control and manipulation of gases in microfluidic fuel cells with precise mass transport requirements to the electrodes, to reduce electrode size and improve power density [186]. Furthermore, convective air-flow generation for cooling and thermal management of electronic devices is a growing area of interest in order to optimize overall power requirements without affecting device perfor-

mance [187].

In ion-mobility gas sensors, high ion-flow rates are often required without any turbulence. Inertial fluid forces must be weaker than viscous shear forces in order to minimize turbulence and produce laminar flow in micro-channels. Flow is characterized using the Reynold's number Re [188] given by:

$$Re = \frac{QD_H}{\nu A} \tag{7.1}$$

Here, Q is the volumetric flow rate in m^3/s, ν is the kinematic viscosity of the fluid in m^2/s, A is the cross-section area of the channel and D_H is the hydraulic diameter of the flow channel, a characteristic length for fluid flow. The transition from laminar to turbulent flow occurs close to $Re = 2040$. D_H is nominally given by:

$$D_H = \frac{4A}{P} \tag{7.2}$$

Here, P is the channel perimeter. The effective Reynold's number Re is then given as:

$$Re = \frac{4Q}{\nu P} \tag{7.3}$$

For the IMS array described in chapter 2, the channel perimeter is $4\ mm$. The kinematic viscosity of air is $14.9 \times 10^{-6}\ m^2/s$ at room temperature and pressure. The corresponding Re for target flow-rates of the order of a few $100\ \mu L/min$ is close to 1. This is well within the laminar flow regime without producing creeping flow where viscous forces dominate inertial flow and $Re << 1$ [188].

Centrifugal pumps using scratch-drive rotary fans have been used for air-flow generation via conversion of rotational kinetic energy to hydrodynamic energy of air [189]. These fans have resonant frequencies in the few-kHz range and require 30 V_{pp} operation, but are prone to frictional wearing inherent in

their operational mechanism. In order to achieve high flow rates and large pressure differentials on chip for gas-chromatographs and ion-mobility based sensors, micro-valve based multi-stage gas pumps in mm-scale packages have been extensively explored [190]. To minimize device footprint and complexity for integration in miniaturized micro-packages, torsional axial fans based on resonant electrostatic actuation have been used to produce flow rates of up to 25 $\mu L/min$ using arrays of fans [191]. However, operation voltages required for electrostatically actuated device vary from $100 - 150\ V$.

Axial piezo-electric fans provide a low-power and low-voltage solution for chip-scale ion flow generation. Bulk lead zirconate titanate (more commonly know as PZT - $PbZr_xTi_{1-x}O_3$) plates with elastic non-piezoelectric mylar or steel plates attached to them have been previously used for cooling of electronic devices by convective removal of heat in confined spaces [187]. Such fans have low-power consumption and low-noise operation. However, their large size is not suitable for ultra-portable packaged sensors, used in the growing smartphone and tablet markets. This chapter presents the design, analysis and characterization of a micro-fabricated thin-film sense-actuate piezo-fan pair for chip-scale gas-sensors.

A schematic of the fan-pair with the gas-sensing system is shown in Figure 7.1. A laser micro-machined low-voltage ion-mobility spectrometer (IMS) array [192] which uses lateral electric fields for segregation of analytes on individual electrode islands, and high-aspect ratios for ion-flow confinement in the device channel, was presented in chapter 6. The sense-actuate fan pair in this work can be integrated at the input of the IMS channel, as shown, along with radioactive electron-emitting ^{63}Ni for ionizing analytes following initial pre-concentration

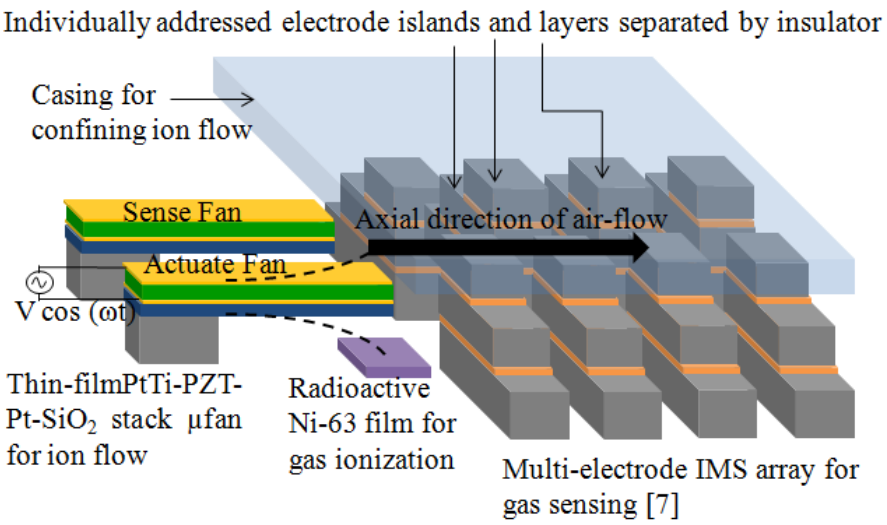

Figure 7.1: Chip scale ion-mobility gas sensor schematic - IMS array gas sensor, radioactive 63Ni film for gas ionization integrated with piezoelectric sense-actuate microfans for producing ion-flow

of analytes, if any. At resonance, the actuation fan-motion is amplified by the quality factor of the beam resonance (Q), and produces high ion flow via acoustic streaming. For very large driving voltage on the actuator, an electrical output signal is observed on the sense fan. This a result of the sense-fan experiencing a force due to lateral air-flow, which can be sensed with the reverse piezoelectric effect. The force on the sense-fan is a feedback signal which indicates a threshold drive on the actuator for transitioning out of low momentum convection. The "flutter" signal on the sense fan can be used for identifying and limiting the turbulent flow from the drive.

7.2 Piezo-fan Model

Flow generation from oscillating beams has been studied by several authors, particularly for larger beams, but not fully understood due to the complicated

non-linear flow dynamics. 2-D flow near the tips of flexible plates with large oscillation amplitudes have been investigated [193] and Toda et al. derived the theory for air-flow generation from a vibrating piezoelectric multi-morph under resonant operation [194]. For a piezoelectric film with an applied electric field E the strain vector s is given by :

$$s = DE \tag{7.4}$$

Here, s is a 6×1 column vector of three axial and shear strains each, E is a 3×1 column vector of electric-field and D is the 6×3 coupling coefficient matrix. For the fan presented here with metal electrodes patterned on the piezoelectric layer and an elastic layer of SiO_2, the d_{31} component is important for operation - vertical E-field in the PZT produces a longitudinal strain causing the multi-morph to bend. The modeling equation of motion for the 4-layer piezoelectric multimorph actuate fan is:

$$M\ddot{y} + ky + f_{air} = Fcos(\omega t) \tag{7.5}$$

Here, M is the effective mass of the oscillating fan concentrated at the center of the inertial force an effective length L away from the hinge, k is the spring constant of this beam, f_{air} is the force for driving the air-motion, F is the driving force for the fan by a sinusoidal AC signal for a flat-plate model as described in [194]. The force f_{air} is usually ignored in resonator analysis as a loss term. However, it is important in the analysis presented here to calculate the streaming flow produced by the fan since the damping is what drives the air-flow.

The width of air-region above and below the vibrating fan-edge that is streamed radially at resonance is $D \approx 2y_0$ where y_0 is the fan-edge amplitude. A radial torque T is required to accelerate this volume of air. At resonant opera-

tion, the air mass directed radially outwards in time dt near the fan edge is:

$$m_{air} = 2\rho_{air} W y_0 v_{\parallel} dt \tag{7.6}$$

Here, ρ_{air} is the density of air $1.225 kg/m^3$, W is the fan width and $v_{\parallel}$ is the air flow velocity. The time derivative of this mass multiplied by the lever arm i.e. fan length and maximum fan edge velocity is the required torque T, and the corresponding $f_{air} = \frac{T}{L}$ at the center of the inertial force [194]:

$$f_{air} = 1.57\rho_{air} W D v_{\parallel} v_{\perp} \tag{7.7}$$

The numerical factor is a normalization for the distance of the inertial force center from the anchor. The input mechanical power to the air mass is then:

$$P_M = T\frac{d\theta}{dt} = \rho_{air} W D v_{\parallel} v_{perp}^2 \tag{7.8}$$

For ideal coupling, all of this mechanical power is transferred to the air mass and used to produce streaming motion. However, some of this energy is dissipated as heat due to air viscosity [193]. Hence, there is an efficiency η which is the coupling coefficient between the mechanical input power and acoustic streaming power in the air-mass flown out radially. The output air-mass power is then the product of the static pressure p and volume flow-rate near the fan edge and is related to the input power as:

$$P_A = pDWv_{\parallel} = \eta P_M \tag{7.9}$$

The air-mass and fan-edge velocities can be estimated and related to each other using the Bernoulli energy equation while including the static pressure energy term produced by the fan. The velocities are related as $v_{\parallel} = \sqrt{2\eta}|v_{\perp}|$ for the case of incompressible flow assuming negligible resistance to air flow in the device channel. For an experimentally determined resonance frequency ω, and fan-edge amplitude y_0, $v_{\perp} = \omega y_0$. Thus, the measured air-velocity directly gives a

lower-bound estimate of the power-transfer efficiency from the fan to the air-mass.

In order to compute the air-mass velocity, f_{air} derived above is substituted in the non-linear equation of motion. The resonance frequency is $\omega = \sqrt{K/M}$ while the amplitude term is solved using Fourier analysis as in [194]. The forcing function E relates the applied voltage V across the piezoelectric to the fan-edge displacement at resonance which yields the expression for air-velocity [194] as:

$$v_{\|} = C\sqrt{\eta}\left(\frac{d_{31}V}{t_{PZT}\sqrt{eta}}\right)^{\frac{1}{3}}\frac{y_0^2}{L} \tag{7.10}$$

Here, C is constant with appropriate dimensions for lumping together numerical coefficients from the Fourier analysis and the densities of the air and beam materials. Finally the total volume flow-rate can be estimated as:

$$Q = 2y_0 W v_{\|} \tag{7.11}$$

Thus, for thin-film d_{31} coefficient values of the order of those for bulk PZT, the 500 nm thickness thin-film devices offer 30× enhancement in E-field for the same applied voltages, compared to 0.5 mm thick bulk PZT. This enables low-voltage operation for comparable flow-rate production.

7.3 Device Fabrication

The devices were fabricated using the thin-film PZT growth process at ARL[195] shown in Figure 7.2. Thermal oxidation was used to grow a 500 nm SiO_2 film as the elastic layer for the beam on a double-side polished silicon substrate. Sputtering was used to deposit the bottom electrode of TiO_2/Pt with thicknesses

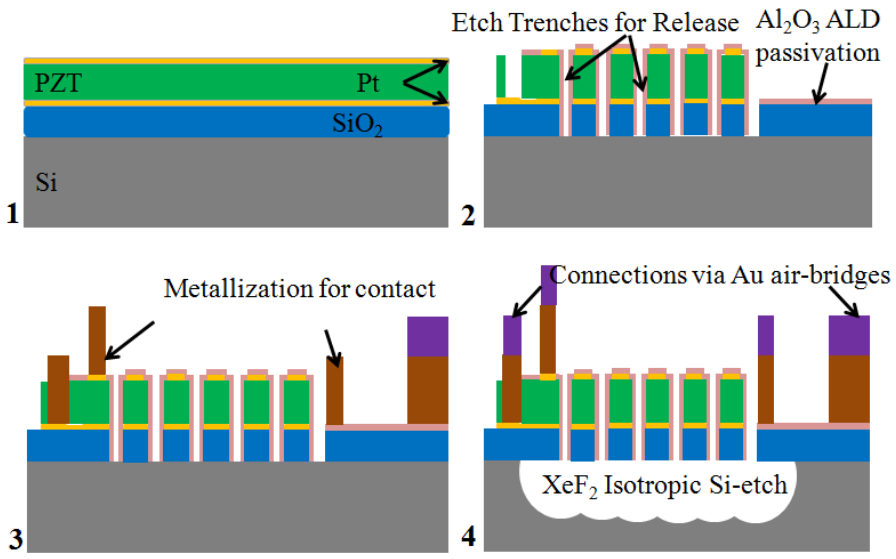

Figure 7.2: Process flow for fabrication of sense-actuate fan pairs

of 36 *nm* and 100 *nm* respectively. The PZT films were made using a custom sol-gel deposition process, and adding between 0 and 30% excess lead to account for losses during crystallization. The top Pt is also deposited using evaporation. Contact to the top Pt electrode was made with Cr/Pt/Au air-bridges followed by release via etch-trenches using XeF_2 for isotropic Si etch. Figure 7.3 shows a Transmission Electron Microscopy (TEM) image of the cross-section of the film-stack used to make the beam, before the final metal layer is deposited. Figure 7.4 shows a SEM of the sense-actuate fan pairs of widths 200 μm each and lengths 800 μm and 1000 μm with a separation of 300 μm that were tested.

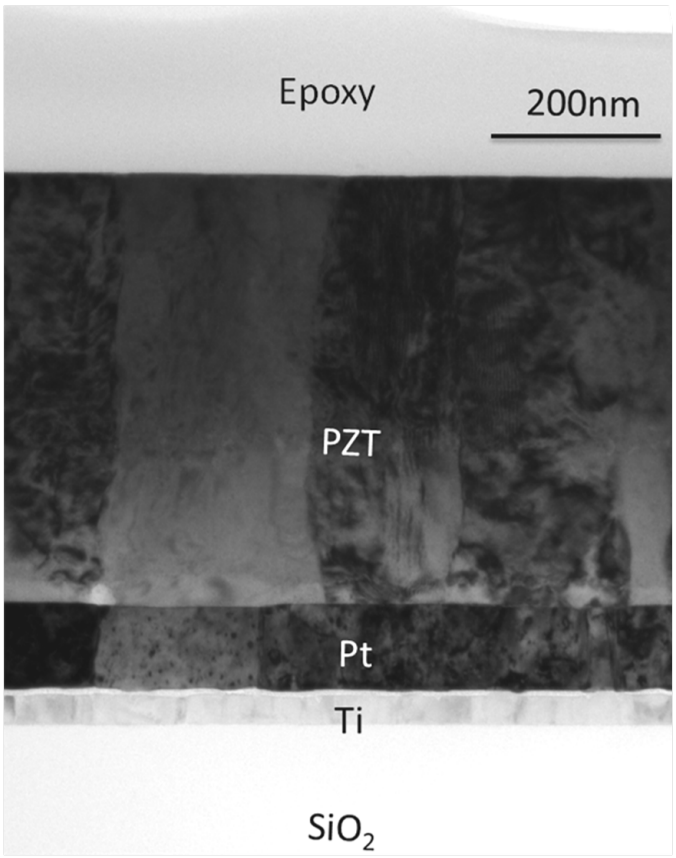

Figure 7.3: Transmission Electron Micrography (TEM) of the cross-section of the device layer stack

7.4 Device Testing

7.4.1 PZT Characterization

The fan edges bend and curve out of the wafer-plane due to residual film stresses after release, a consequence of the long axial dimension. As a result, optical profilometry or laser Doppler vibrometry cannot be used for direct displacement measurements since the laser light used in these systems does not return back to the detector due to angled incidence on the fan surface, the angle for each fan being a parameter which is difficult to control or tune. Hence

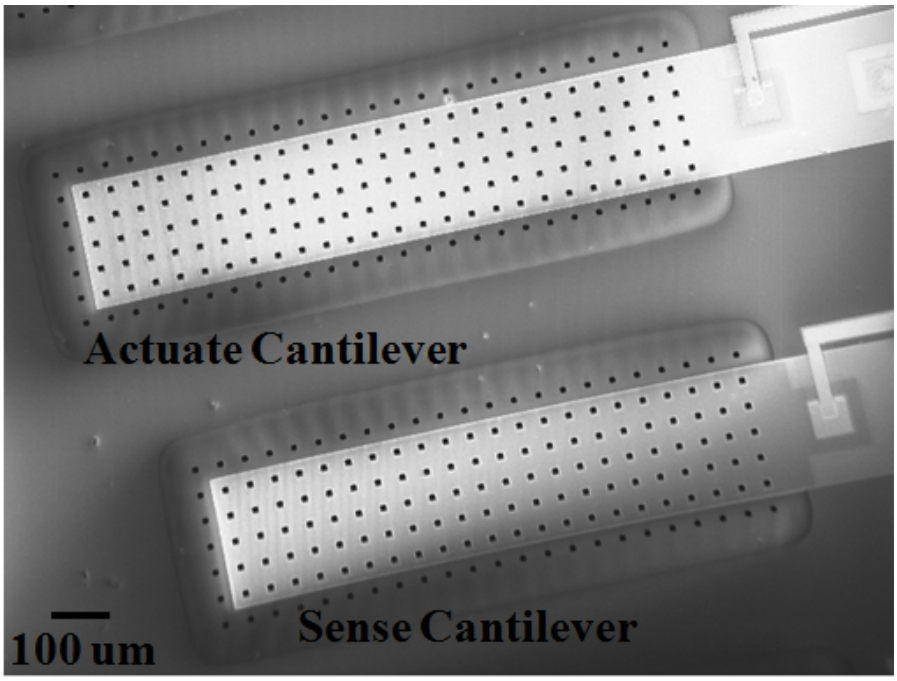

Figure 7.4: Scanning electron micrograph (SEM) of the unreleased sense-actuate fan-pair

for PZT characterization, fans were mounted at 90 degrees to the wafer-plane such that the fan bending, along its thickness when actuated, was in the plane of imaging to optically measure displacements accurately. This was used to extract the d_{31} co-efficient of PZT. In this analysis, it was assumed that shear-effects during bending are negligible and the residual stress-induced curvature was subtracted to remove the offset during actuation. DC actuation up to 6V was used to measure fan-edge displacement up to 121 μm (for the 800 μm long fan) and 148 μm (for 1000 μm long fan) following which, multilayer analysis for arbitrary piezoelectric-elastic layer stacks was used to calculate the d_{31} of PZT [196]. Typical poling field strengths for PZT are of the order of 300 kV/cm [197]. Hence, the actuation voltages are not expected to affect PZT performance or de-polarize it. For isotropic Poisson's ratio ν_i, the effective Young's moduli Y_i and coupling coefficients d_{31},i of the i-th layer in the multi-morph stack are modified

for this analysis as follows:

$$Y_i \rightarrow \frac{Y_i}{1-\nu_i^2} \tag{7.12}$$

$$d_{31,i} \rightarrow \frac{d_{31,i}}{1+\nu_i} \tag{7.13}$$

By using the fact that axial forces and moments at any cross-section for a DC-actuated beam are in equilibrium and assuming equal radius of curvature for all layers in the multi-morph, the $d_{31} = -85.8 \pm 5\ pC/N$. This value is less than typical d_{31} values of bulk PZT-5H close to $-275\ \ pC/N$ but within reasonable expectation given that the process isn't highly optimized and that multi-layer stressed thin-films add complexity to the polarization of the PZT.

7.5 Flow Measurements

Resonance frequencies for the 800 μm and 1000 μm fans were measured to be at 614 Hz and 505 Hz with 2.5 mW power input for charging-discharging the PZT capacitance. A commercial resistance temperature detector (RTD) element was used to measure air-velocity as a function of drive frequency. At each drive frequency, the RTD element stabilizes to a peak measured air-velocity which is plotted in Figure 7.5. The 800 μm long fan produces a peak air-velocity of 7.01 cm/sec at resonance. As expected from the piezo-fan model, this peak air-velocity produced by the fans varies inversely as the fan length. Also, the actuation frequency for peak air-velocity corresponds to the resonance frequency of the fans. Based on the measured fan velocities and fan-edge displacement at resonance, the calculated flow-rates and mechanical to air-mass flow power conversion efficiency are summarized in Table 7.1. The Reynolds numbers for

each of the flow rates produced from the beams is in the laminar flow regime, indicating that they are suitable for use in the IMS device.

Device Length (μm)	**Flow (cm/s)**	**Flow-Rate ($\mu L/min$)**	**Efficiency (η)**	**Reynold's Number**
800 μm	7.01	185.1	1.3%	1.24
1000 μm	4.97	167	0.7%	1.12

Table 7.1: Summary of flow-velocities, flow rates and mechanical to air-mass flow power transfer efficiencies

The piezo-fan model in [194] predicts a volume flow rate independent of length, assuming the Bernoulli equation holds true and no-resistance to air-flow. However, the measurements were done very close to the RTD sensor element which is housed in a metal casing, and is likely to add some resistance for air-flow. Also, the large vibration amplitude of 110 μm for 800 μm fan and 140 μm for 1000 μm fan, means that not all the air-flow is directed radially outwards towards the sensor. Figure 7.6 plots the voltage dependence of the measured peak air-velocity from the fan. The equation for air-velocity $v_{\|}$ predicts a $V^{\frac{5}{6}}$ voltage dependence - there is a $V^{\frac{1}{3}}$ in the equation derived and a further $V^{\frac{1}{2}}$ due to $y_0^{\frac{1}{2}}$ dependence on edge-displacement since y_0 is directly proportional to V. The data-fits for this dependence are plotted as dotted lines with the expected factor being $\frac{1}{L}$ for each curve. Table 7.2 summarizes the performance of this PZT-based fan and compares it to electrostatically actuated micro-fan and valve-based micro-pumps for chip-scale pumping. It is clear that the maximum flow-rate produced by the device in [190] is much higher than the one achieved here, but the checkerboard peristaltic pump used therein needs higher voltage operation as well as 30× more dynamic switching power. Higher flow-rates can be produced by PZT fans by optimizing the resonance frequencies and lengths and cascading arrays of fans to achieve a higher flow-rate.

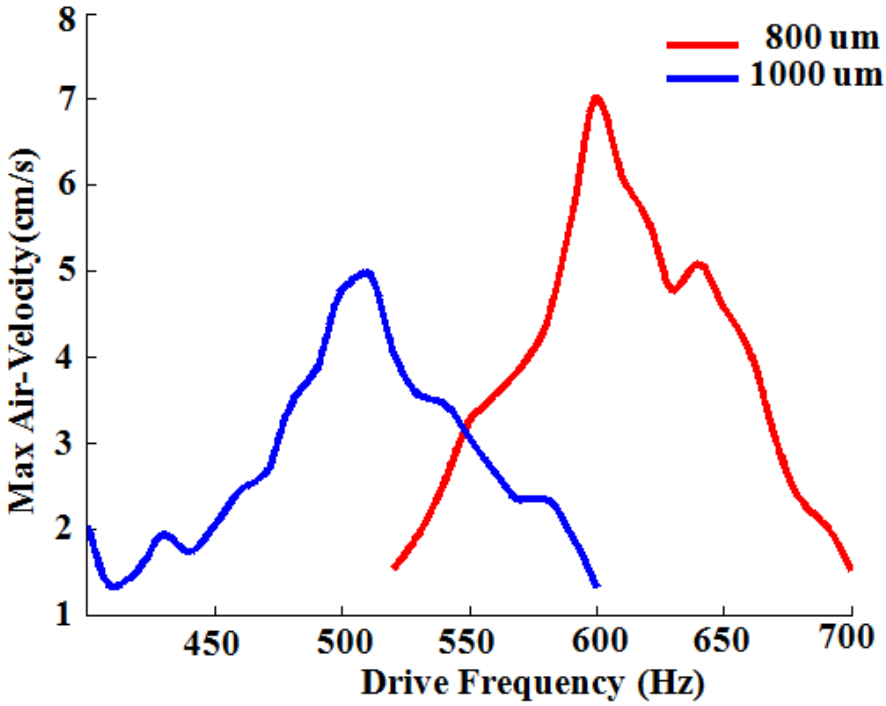

Figure 7.5: Plot of measured maximum air-velocity with RTD sensor element at the tip of the drive fan as a function of frequency for 800 μm and 1000 μm long piezofans

Work	Max Flow ($\mu L/min$)	Nominal Voltage	Power(mW)
Valve-based Micropump [190]	4000	100V	57
Electrostatic Microfan [191]	10	$100V_{p-p}$	–
This Work	185	$2V_{p-p}$	2.5

Table 7.2: Comparison of this work with previous reports for chip-scale fans and pumps

7.6 Sense Fan Measurements

The novel sensing scheme introduced in this pumping system is the sense fan which measures potential lateral turbulent air-flow, if any, due to large drive on the actuator. To prevent turbulence in micro-channels, inertial fluid forces

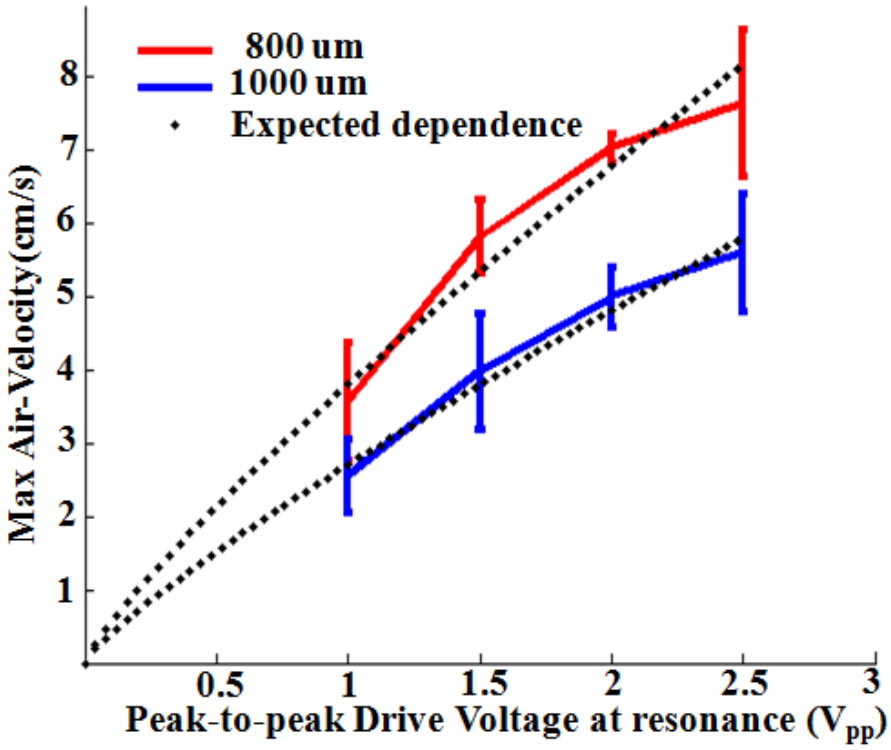

Figure 7.6: Plot of measured maximum air-velocity with RTD sensor element at the tip of the drive fan and expected $V^{\frac{5}{6}}$ dependence

must be weaker than viscous forces allowing layers of fluid air to slide. Any kind of lateral convection can be considered a signature of turbulence which is where the sense-fan provides a feedback signal via flutter. The experiments here demonstrate a proof-of-concept for this system, rigorous analysis of the turbulent air-flow is not discussed.

In the sense-actuate fan pair testing, the 1000 μm long actuate fan was driven with increasing drive amplitude. Correspondingly, the voltage developed across the sense fan due to a force applied by turbulent lateral air-flow, if any, was sensed via the reverse piezoelectric effect. Figure 7.7 plots direct time-domain signals obtained from the sense-fan flutter for various drive voltages on actuator at the resonance frequency of the actuator. Since the quality factors

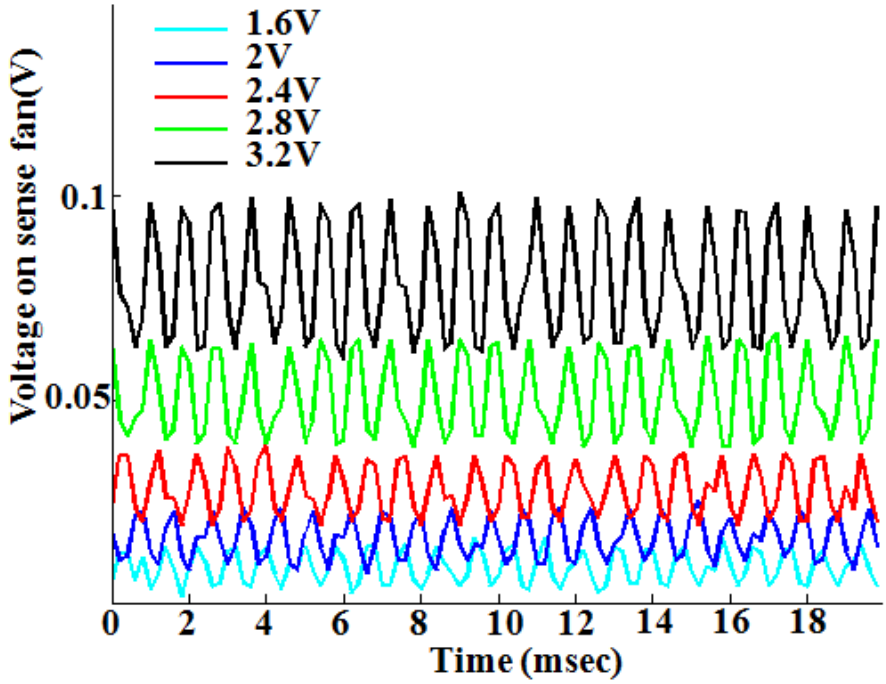

Figure 7.7: Sense-fan time-domain voltage output for different drive voltages on the actuator at resonance

for the resonant operation of these fans in air are low (~ 10), precise frequency matching was not required to overlap the enhanced motion of the drive fan at its resonance, with the enhanced sense motion of the sense fan.

Figure 7.8 plots the DC and AC voltage-signal levels as a function of drive voltage on the actuator at resonance. As the drive is increased both, a constant force (indicated by the DC signal level) and a flutter (indicated by the AC level), are seen on the sense and these increase with the drive. The FFT of the signals shows a peak at 1108 Hz in Figure 7.9, roughly twice the drive frequency, $2f$, and suppressed signal at the drive, f. It is possible that since the force due to lateral air-pressure pushes on the sense-fan in the same direction, the signal is a parametric resonance of the drive frequency at $2f$. The feedback from the sense can be used to control the drive on the actuation fan and maintain laminar flow.

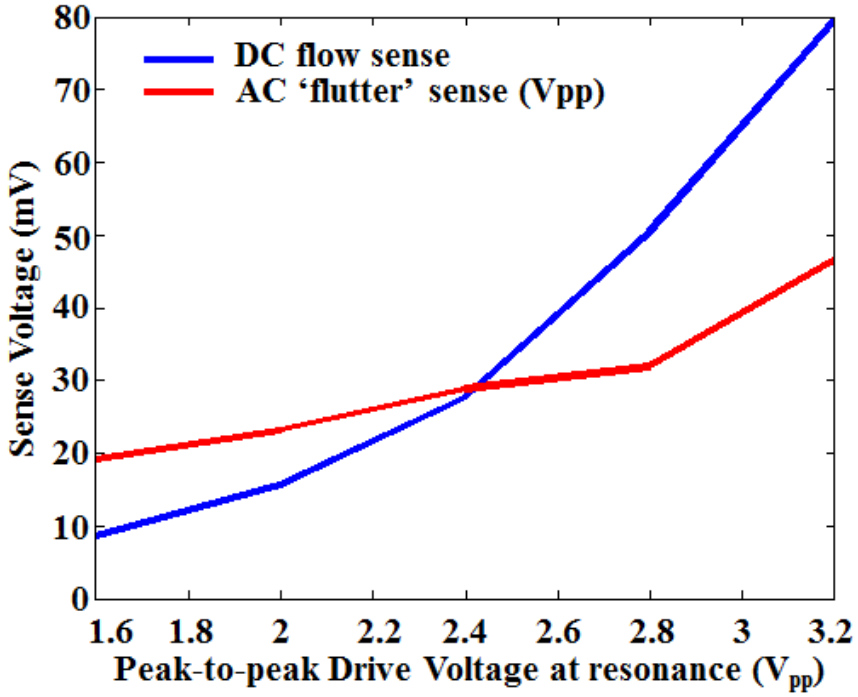

Figure 7.8: DC flow sense indicating constant lateral air-stream force and AC fluctuation showing increasing flutter/turbulence as actuator drive is increased

7.7 Conclusions

This chapter presented a novel low-voltage sense-actuate piezo-fan pair for potential integration in chip scale gas sensing applications. The thin-film PZT process enables scaling to achieve required electric fields with low voltage operation, for CMOS compatible operation. The sense-fan allows for feedback of turbulent flow sensing without complicated circuitry and extensive additional on-chip real-estate. By integrating the fan with ion-mobility-based sensors as in [192] and benign electron-emitting ^{63}Ni for ionization and self-powering as previously demonstrated [185], the system can have self-sustained performance for long periods limited only by the ionizer half-life.

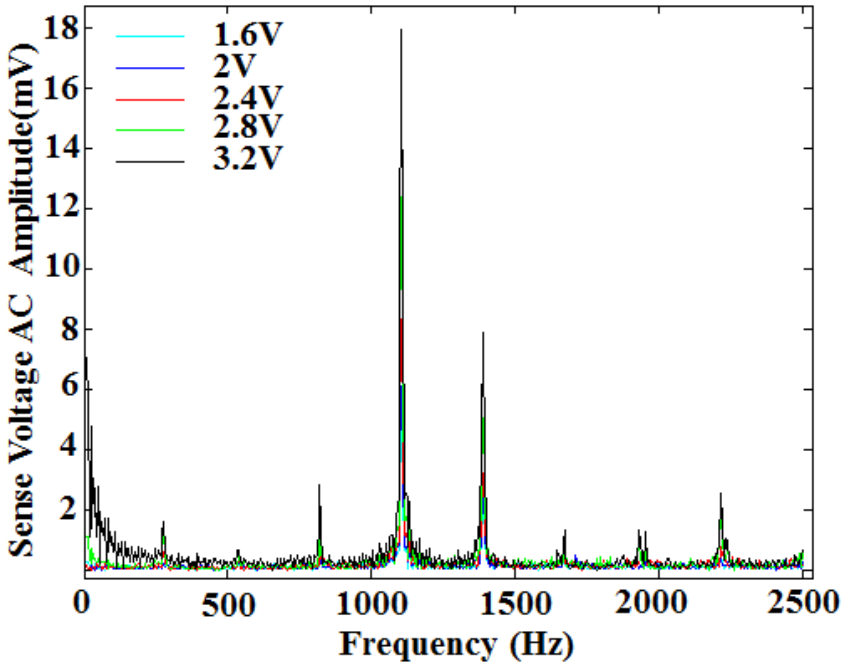

Figure 7.9: FFT of the AC signals with a peak at 1108Hz, which is twice the resonant drive frequency

CHAPTER 8

ENHANCED LITHIUM NIOBATE PYROELECTRIC IONIZER FOR CHIP-SCALE ION MOBILITY-BASED GAS SENSING

8.1 Introduction

Chapters 6 and 7 describe an ion-mobility based sensor used for gas detection and a piezoelectric fan which acts as a pump for producing air-flow in the channel of the sensor, have been described. The third key component of the gas sensing system is the ionizer, which produces ions from the neutral molecules in air as well as volatile organic compounds (VOCs) which need to be detected. This chapter presents the design, analysis and testing of a miniaturized ionizer based on the pyroelectricity of lithium niobate ($LiNbO_3$), suitable for integration in a low-voltage gas-sensor platform that the sensor and fan are compatible for.

Ambient ionization of air with applied electric fields has been used before, but it requires high voltages across narrow gaps [198]. Zero-power ionization using thin-film electron-emitting Nickel-63 (^{63}Ni) is an energy-efficient method of ionization [185], but the use of radioactive materials in commercial systems is not viable because of the additional protocols to be followed with incorporating radioactive materials and the possible negative health-effects of high doses of radiation. Pyroelectric ionization offers a low-voltage alternative to these techniques, and one which can be easily integrated with other components.

Rosenblum et al. first reported electron generation using thermally induced changes in the polarization of $LiNbO_3$, when it was heated or cooled [199]. In case of $LiNbO_3$, the heating and cooling produces a relative motion of the lithium

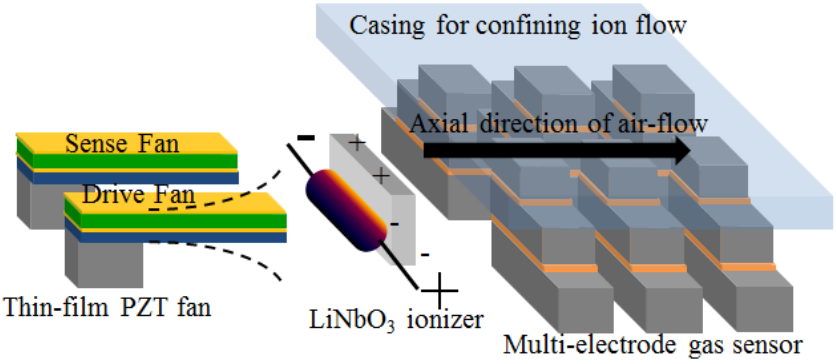

Figure 8.1: Ion-mobility based gas-sensor architecture modified to incorporate the $LiNbO_3$ ionizer.

atom in each unit cell with respect to the oxygen atoms. This ion displacement produces a polarization change in each unit cell [200, 201, 202], which in turn results in a net dipole moment in the material. Pyroelectric crystals have been used for ambient pressure ionization as ion sources for ion-mobility spectrometry [201]. Here, the electron or ion events due to temperature cycling were dependent on the exposure of the crystal surface to the ion-detector. In order to improve the signal to noise ratio (SNR) of the detected signal, it is critical to increase the total number of ionization events for detecting very low gas concentrations. This chapter presents a high throughput pyroelectric ionization source for such enhanced ionization. A $LiNbO_3$ crystal, with copper electrodes attached to it, was used to obtain a 2.4× increase in the number of ionization events. Additionally, the ionization counts at different heating powers have been also measured and compared.

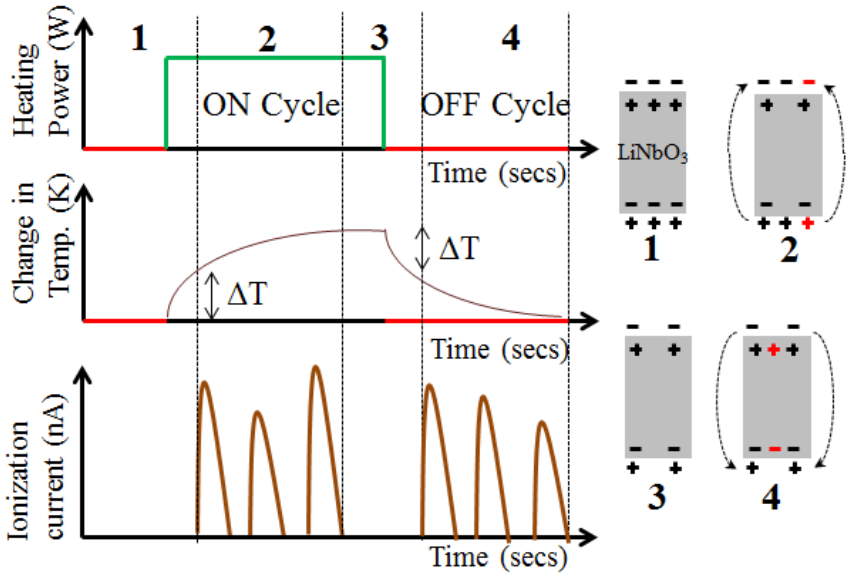

Figure 8.2: Schematic of thermal cycling of the crystal vs. time and corresponding ionization detected. The relative polarization of the $LiNBO_3$ crystal in the four different phases are also shown 1. room temperature; 2. heating cycle; 3. steady-state elevated temperature; 4. cooling cycle

8.2 Device Design

Upon heating or cooling, the net dipole moment produced in $LiNbO_3$ changes the surface charge on the crystal faces [201]. This produces net positive and negative charges on the crystal faces when it is not in thermal equilibrium, leading to a potential difference across the two faces. For sufficiently high voltages, the electric field is greater than breakdown of air which is 3 MV/m, which ionizes ambient air (Figure 8.2). The voltage V produced due to temperature changes in the crystal is [202]

$$V = \frac{d_{cr}\phi\Delta T}{\epsilon_{cr}} \tag{8.1}$$

Here, $\phi = 70\mu C/(m^2K)$ is the pyroelectric coefficient of $LiNbO_3$, $d_{cr} = 5\ mm$ is the thickness of the crystal, ΔT is the change in temperature, in K, and $\epsilon_{cr} = 30\epsilon_0$

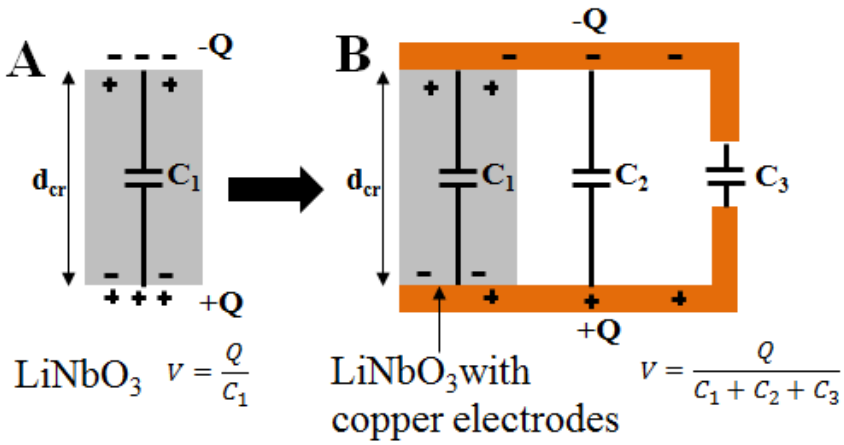

Figure 8.3: Equivalent circuit of the crystal before (A) and after (B) attaching copper electrodes to increase ionization events.

is the dielectric constant of $LiNbO_3$. Ionization results from dielectric discharge due to high electric fields caused by the separated charges on the crystal surfaces. For these parameters, it is possible to achieve the dielectric breakdown of air ($3 \times 10^6 V/m$) with a temperature change of as little as 11.3 K. To increase the number of ionization events, Figure 8.3 shows the modified crystal setup. Copper electrodes were adhesively attached to the Z and -Z faces of the crystal. The crystal and the electrodes hold the same charge Q as is produced over the crystal faces $Q = A\phi\Delta T$. However, this charge is now shared over the three capacitances of the lithium niobate crystal, the air capacitor formed by the copper electrodes, and the capacitor formed between the edges of the folded copper electrodes (g_2 in Figure 8.3) C_1, C_2, C_3. However, now the critical electric field for ambient ionization can be reached at lower temperatures by reducing the electrode distance $g_2 < g_1$. A derivation of the electric field across the bent electrodes versus the electric field without the copper electrodes is:

In this case, $g_1 = 5\ mm, g_2 = 1\ mm, w = 8\ mm, t = 0.1\ mm, A_p = 0.4\ cm^2, A_{cr} =$

0.56 cm^2 , the ratio of the electric field with and without electrodes for the device is 3.94. Because the dielectric constant of $LiNbO_3$ is much higher than that of air, the distribution of charge still leads to a significant magnification of the electric field. With this new electric field magnification, a change in temperature of only 2.28 K is needed to create ionization events.

8.3 Experimental Section

A 5 mm thick optical grade $LiNbO_3$ crystal from Precision Micro-Optics LLC was used for the experiments. Figure 8.4 shows the experimental setup used to detect the ionization events. A $4 \times 10 \times 5$ mm^3 crystal was attached to the resistive heater using two-part thermal epoxy on the cross-section of the crystal, thus exposing both faces. The nominal resistance of the heater was 150 Ω and it consumed 0.5 W. Copper electrodes of area 47.3 mm^2 were attached to the crystal faces. The change in temperature on the crystal surface was measured by mounting a temperature sensor with control circuitry on the heater and also monitored with an IR camera. Ionization events were detected by keeping a coaxial electrode near the crystal (3 mm from the crystal). A single voltage spike on the SRS is referred to as an event in this case. The detected ion current due to ionization events were amplified and measured with the Stanford Research Systems (SRS) 570 current preamplifier and the time-domain output was fed into a NIDAQ with 20 kHz sampling rate. The gain used for measurements was $20,000$ pA/V to ensure that the output is not saturated.

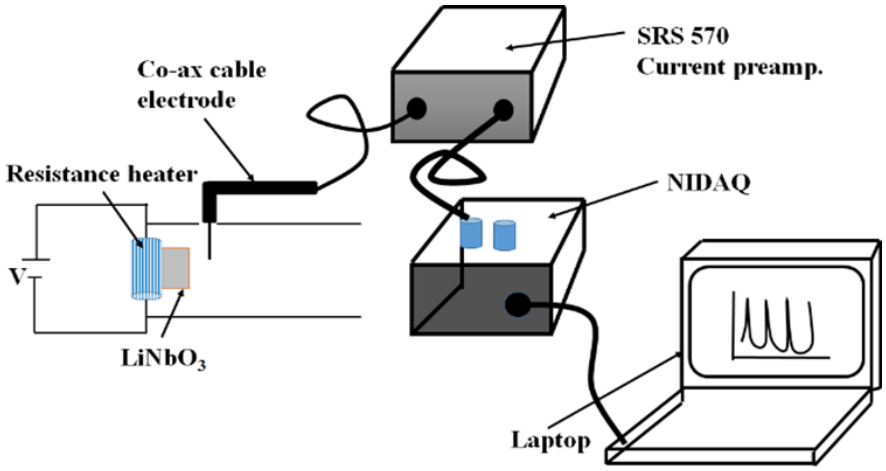

Figure 8.4: Experimental setup used to measure the ionization events

8.4 Results and Discussion

Figure 8.5 shows the output of voltage spikes produced due to ionization current amplified by SRS 570. It is seen clearly that after attaching the copper electrodes (B), the number of events is more than without any electrodes (A). Over a heating or cooling window of 120 seconds, the average number of ionization events measured with attached copper electrode is 60, which is 2.4x more compared to the 25 events (on average) without any electrodes. Additionally, the output voltage scales are the same i.e. the net current due to ionization is increased as a result of the electrodes and not simply distributed over more frequent smaller events. From Figure 8.5 it is also evident that, the ionization stops (after 55 seconds Figure 8.5A) once the surfaces charges are compensated. The crystal with copper foil has a large area for the charges to distribute. This helps in ionizing a larger volume of air around the electrodes, thus producing more ions. Most of the ionizations occurs away from the crystal, near the electrode tips due to the small radius of curvature of the surface there. Potentially, this also helps in increasing crystal lifetime by avoid dielectric discharge close to it.

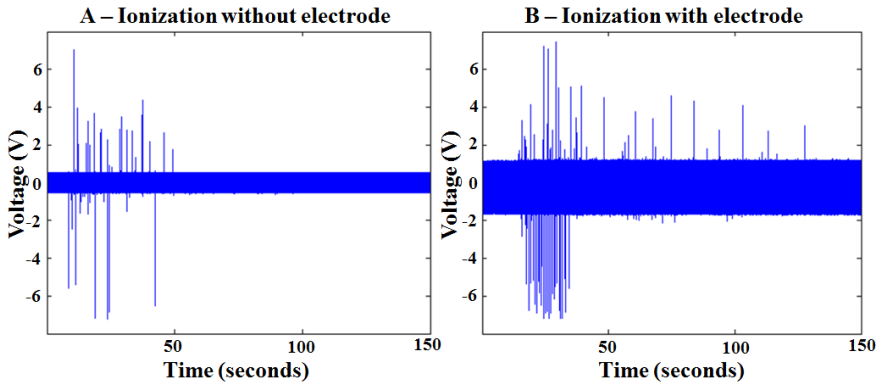

Figure 8.5: Measured ionization events (A) Crystal surface (B) Crystal with copper foils attached

At a given temperature, the electrical breakdown of the air can be controlled by controlling the distance between the copper electrodes. With the electrodes, the measured peak voltage is 2.24 V and with a gain of $G = 20,000\ pA/V$, corresponding to a peak ionization current

$$I_{peak} = VG = 2.24V \times 20000\frac{pA}{V} = 44.8\ nA \tag{8.2}$$

The average ion current over the heating cycle by integrating these spikes is 9.36 pA. Using the Paschen curve, it is possible to design for minimum breakdown voltage for a given electrode spacing to minimize the power that achieves this voltage [203].

Figure 8.7 shows the ionization peaks from the SRS output during both the heating and cooling cycle of the crystal. The number of ionization events occurring in each cycle is not the same due to the stochastic nature of the ionization and dependence on local variations in atmospheric humidity and pressure. This can be compensated by designing an appropriately calibrating ionizer and sensors for specific parameters. The ionization events can also be observed on the temperature data plotted. This is due to potential ion-current pickups from

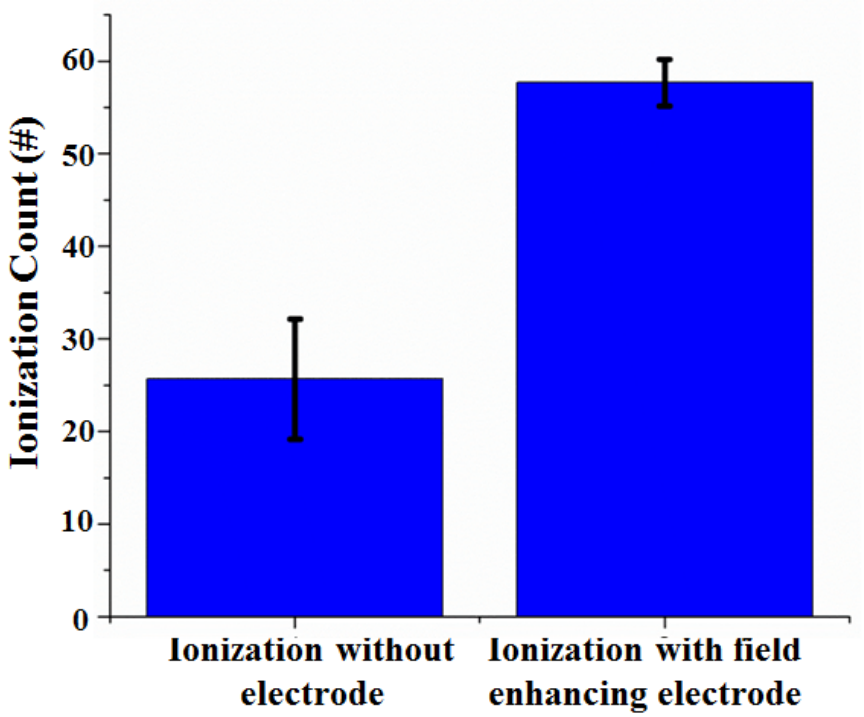

Figure 8.6: Increase in ionization events due to electrode

the temperature sensor electrodes which are on the crystal and sense the ion-charges. The number of ionization events per unit time, in this case over the nominal 120 second heating and cooling cycles, can be increased or decreased by controlling the temperature on the crystal and the rate of temperature ramping, as seen from Equation 8.1. Even small changes in temperature will lead to a huge potential build up on the crystal surface. Ionization events at different input powers to the resistive heater are plotted in Figure 8.8. A higher input power to the heater leads to a faster temperature-ramp, which in turn produces a larger change in polarization of the crystal and enhanced ionization. This showed a quadratic dependence on the number ionization events with resistive power.

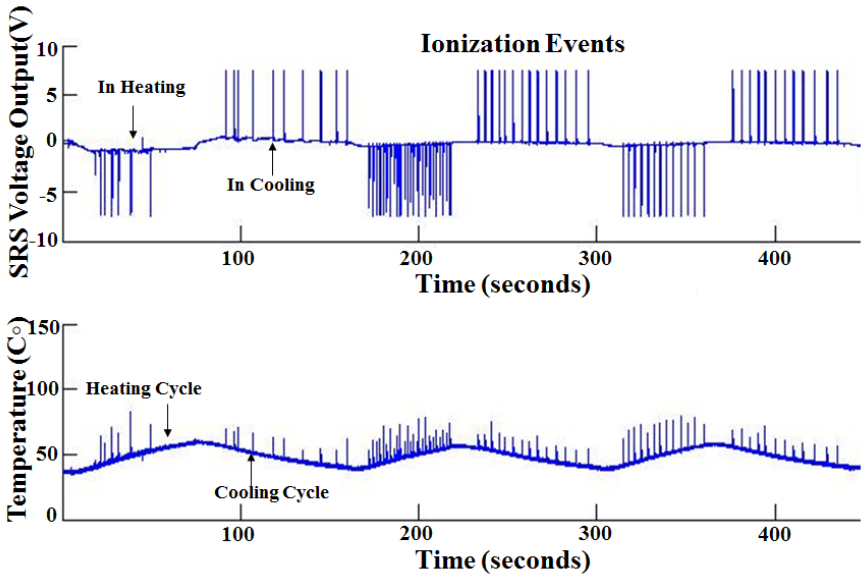

Figure 8.7: (A) Ionization events in heating and cooling cycle (B) Temperature control using control circuitry and an integrated temperature sensor

8.5 Conclusions and Future Work

An enhanced ionizer using a $LiNbO_3$ crystal for use in a miniaturized ion mobility-based gas sensor is presented in this chapter. This was achieved without increasing the system power by using copper electrodes on the crystal surface. Also, by reducing the distance between the copper electrodes it is possible to achieve the ionization events at much lower temperatures. This paves the way for precise gas detection with low gas concentrations due to the higher ionization counts. Using the demonstrated ionizer, it is possible to develop a modular gas sensor for volatile organic compound detection in exhaled human breath as a bio-sniffer.

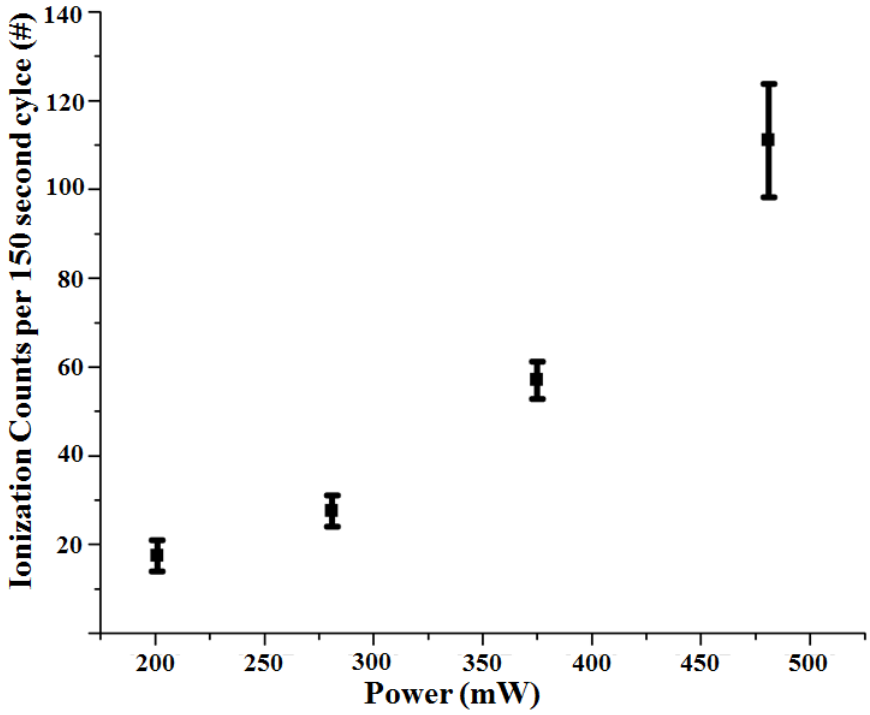

Figure 8.8: Ionization count per 150 second cycle as a function of heating power.

APPENDIX A

ELECTRICAL AND THERMO-MECHANICAL ANALYSIS OF GRAPHENE-ON-NITRIDE SINGLE-SHOT VALVES

The MATLAB code to analytically model the valve is included in this chapter of the Appendix.

```
'

close all; clear all; clc;
a = 750e-6;
t_gr = 4e-10;
t_sin = 360e-9;
t_ni = 45e-9;
n_finger = 7;


l = 110e-6;
w = 15e-6;
rho_gr = 2/1e6;
lf = 300e-6;
rho_ni = 1/13e6;


R1 = a*rho_gr/t_gr/(l-w)*2
R3 = R1;
R2 = (a-2*lf)*rho_gr/t_gr/w


R2a = 2*lf*rho_ni/45e-9/15e-6
```

```
% Checking ratios of resistances
R2a/R2
R1/R2

Rtotal = (1/R1+1/R2+1/R3)^(-1);
Rtotal = Rtotal/7

I = (0:.2e-3:7e-3)/n_finger;

Rsum = R1*R2+R2*R3+R3*R1;
I1 = I*R2*R3/Rsum;
I2 = I*R1*R3/Rsum;
I3 = I*R1*R2/Rsum;

P1 = I1.*I1*R1;
P2 = I2.*I2*R2;
P3 = I3.*I3*R3;

% Thermal Analysis

t_sin = 360e-9;
t_ni = 45e-9;
k_sin = 30;
k_ni = 90;
A1 = t_sin*(l - w)/2;
A2 = t_sin*w;
```

```
%------Late fix
Rth1 = a/2*1/2/k_sin/A1;

Rth2 = ((lf*1/2/k_ni/A2)^(-1) + (a/2/k_sin/t_sin/w/2)^(-1))^(-1);
% Coupling thermal resistance
Rthi = 7e4;

% -1.2 to -3.7 times e-3 from literature
alpha = -3.5e-3;

T1vec = [];
T2vec = [];
R1vec = [];
R2vec = [];
for j=1:length(I),
    syms delT1 delT2 I1 I2
    S = solve(I1^2*R1*(1+alpha*delT1) == delT1/Rth1 + (delT1 - delT2),
    T1vec = [T1vec S.delT1(1)];
    T2vec = [T2vec S.delT2(1)];
    R1vec = [R1vec R1*(1+alpha*S.delT1(1))];
    R2vec = [R2vec R2*(1+alpha*S.delT2(1))];
end


%{
```

```
subplot(3,2,1); plot(I/1e-3, T2vec, 'r*-', 'linewidth', 3);
hold on; grid on;
subplot(3,2,1); plot(I/1e-3, T1vec,'b*-', 'linewidth', 3);
%}

figure(1);
subplot(1,2,1); plot(I/1e-3, (T1vec+T2vec)/2, 'r*-', 'linewidth', 3);
hold on;



i1 = 0.1:.1:2;
i2 = [2.5 3 3.5 4 4.5 5 5.5 6.5];
i = [i1 i2]/7;
% Data from MEMS 2015
v = [0.326 0.659 0.979 1.28 1.56 1.84 2.1 2.3 2.58 2.76 2.98 3.16 3.38
T = [23.8 23.8 23.8 24.2 24.8 26.5 28.2 30.2 32.3 34.9 37.4 40.2 43.4
65.8 69.6 91 116 136 150 175 194 230 280]-23.8;
subplot(1,2,1); plot(i,T,'b*-','linewidth',3);
%{
xlabel('Input current (mA)');
ylabel(' Valve temperature (deg C)');
%}
subplot(1,2,2); plot(T,v./i,'b*-','linewidth',3);
%{
xlabel('Temperature (deg C)');
```

```
ylabel('Valve graphene resistance');
%}



Req = (2./R1vec+1./R2vec).^(-1);
subplot(1,2,2);
hold on; %grid on;
plot((T1vec+T2vec)/2,Req/1e3,'r*-','linewidth',3);
%grid on;


% Thermal stress and deflection
Tvec = (T1vec+T2vec)/2;
E_ni = 200e9;
E_sin = 310e9;
a_sin = 3.3e-6;
a_ni = 13e-6;
m = t_ni/t_sin;
n = E_ni/E_sin;
%{
m = .4/360;
n = 10/3.1;
%}

%figure();
```

```
y_x = 2/64*(a_sin - a_ni)*Tvec*(1+m)^2*(a/2)^2/(t_sin + t_ni)/(3*(1+m

figure(2); plot(Tvec, abs(y_x/1e-6),'r*-','linewidth',3);
hold on;

xlabel('Temperature (K)');
ylabel('Deflection (um)');



I1 = t_ni^3/12;
I2 = t_sin^3/12;
h = t_sin+t_ni;

stress_max = -(6/h^2*3/2*(E_ni*I1 + E_sin*I2)*(a_sin - a_ni)*(Tvec)/h



% Def Data
Tdef = [0 40 65 95 110 128 155 240];
Adef = [0 0.53 1.13 1.55 1.86 2.1 2.43 4.1]/2;
%figure();
figure(2); plot(Tdef,Adef,'b*-','linewidth',3);

xlabel('Temperature difference (C)');
```

```
ylabel('Amplitude of deflection (um)'); hold on;


figure(3); plot(I,stress_max,'r*-','linewidth',3);


%{
subplot(3,2,5);plot((T1vec+T2vec)/2,A*2/1e-6,'b','linewidth',3);
legend('Deflection data','Analytical model');


subplot(3,2,6); plot(I,R1vec,'b'); hold on;
subplot(3,2,6); plot(I,R2vec,'r');
xlabel('Current (A)');
ylabel('Resistance (ohms)');
%}

'
```

BIBLIOGRAPHY

[1] S. William, "Circuit element utilizing semiconductive material," 1951, uS Patent 2,569,347. [Online]. Available: https://www.google.com/patents/US2569347

[2] "Intel corporation form 10-k (annual report)," 2016. [Online]. Available: http://files.shareholder.com/downloads/INTC/867590276x0xS50863-16-105/50863/filing.pdf

[3] M. Ilegems, "Limits to miniaturization in microelectronics," in *Electronics and Microtechnology Workshop on the Limits of Miniaturization*, 1980, pp. 15–34.

[4] R. Howe and R. Muller, "Polycrystalline silicon micromechanical beams," *Journal of the Electrochemical Society*, vol. 130, no. 6, pp. 1420–1423, 1983.

[5] H. C. Nathanson, W. E. Newell, R. A. Wickstrom, and J. R. Davis, "The resonant gate transistor," *IEEE Transactions on Electron Devices*, vol. 14, no. 3, pp. 117–133, 1967.

[6] A. A. Seshia, M. Palaniapan, T. A. Roessig, R. T. Howe, R. W. Gooch, T. R. Schimert, and S. Montague, "A vacuum packaged surface micromachined resonant accelerometer," *Journal of Microelectromechanical systems*, vol. 11, no. 6, pp. 784–793, 2002.

[7] H. Xie and G. K. Fedder, "Fabrication, characterization, and analysis of a drie cmos-mems gyroscope," *IEEE Sensors Journal*, vol. 3, no. 5, pp. 622–631, 2003.

[8] K. Ikeda, H. Kuwayama, T. Kobayashi, T. Watanabe, T. Nishikawa, T. Yoshida, and K. Harada, "Silicon pressure sensor integrates resonant strain gauge on diaphragm," *Sensors and Actuators A: Physical*, vol. 21, no. 1-3, pp. 146–150, 1990.

[9] T.-W. Yeow, K. E. Law, and A. Goldenberg, "Mems optical switches," *IEEE Communications magazine*, vol. 39, no. 11, pp. 158–163, 2001.

[10] M.-H. Kiang, O. Solgaard, K. Y. Lau, and R. S. Muller, "Polysilicon optical microscanners for laser scanning displays," *Sensors and Actuators A: Physical*, vol. 70, no. 1-2, pp. 195–199, 1998.

[11] A. Lal and R. M. White, "Microfabricated structure to be used in surgery," Mar. 17 1998, uS Patent 5,728,089.

[12] G. Lammel, "The future of mems sensors in our connected world," in *Micro Electro Mechanical Systems (MEMS), 2015 28th IEEE International Conference on*. IEEE, 2015, pp. 61–64.

[13] E. Biham and A. Shamir, *Differential cryptanalysis of the data encryption standard*. Springer Science & Business Media, 2012.

[14] P. F. George, "Self-destructing metal structures," Dec. 21 1971, uS Patent 3,629,091.

[15] P. Roh and M. Strunk, "Self-destructing apparatus for impact-detonating explosive devices," Jun. 11 1974, uS Patent 3,815,505.

[16] S.-W. Hwang, H. Tao, D.-H. Kim, H. Cheng, J.-K. Song, E. Rill, M. A. Brenckle, B. Panilaitis, S. M. Won, Y.-S. Kim *et al.*, "A physically transient form of silicon electronics," *Science*, vol. 337, no. 6102, pp. 1640–1644, 2012.

[17] H. L. Hernandez, S.-K. Kang, O. P. Lee, S.-W. Hwang, J. A. Kaitz, B. Inci, C. W. Park, S. Chung, N. R. Sottos, J. S. Moore *et al.*, "Triggered transience of metastable poly (phthalaldehyde) for transient electronics," *Advanced Materials*, vol. 26, no. 45, pp. 7637–7642, 2014.

[18] N. Banerjee, Y. Xie, H. Kim, and C. H. Mastrangelo, "Microfluidic device for triggered chip transience," in *2013 IEEE SENSORS*, Nov 2013, pp. 1–4.

[19] N. Banerjee, Y. Xie, M. M. Rahman, H. Kim, and C. H. Mastrangelo, "From chips to dust: The mems shatter secure chip," in *2014 IEEE 27th International Conference on Micro Electro Mechanical Systems (MEMS)*, Jan 2014, pp. 1123–1126.

[20] K. L. Camera, B. Wenning, A. Lal, and C. K. Ober, "Transient materials from thermally-sensitive polycarbonates and polycarbonate nanocomposites," *Polymer*, vol. 101, pp. 59–66, 2016.

[21] X. Liu, S. Cheng, H. Liu, S. Hu, D. Zhang, and H. Ning, "A survey on gas sensing technology," *Sensors*, vol. 12, no. 7, pp. 9635–9665, 2012.

[22] M. E. Moragues, A. Toscani, F. Sancenon, R. Martınez-Manez, A. J. White, and J. D. Wilton-Ely, "A chromo-fluorogenic synthetic canary for co de-

tection based on a pyrenylvinyl ruthenium (ii) complex," *Journal of the American Chemical Society*, vol. 136, no. 34, pp. 11 930–11 933, 2014.

[23] C. Hoover, "The detection of carbon monoxide." *Industrial & Engineering Chemistry*, vol. 13, no. 9, pp. 770–772, 1921.

[24] A. Azad, S. Akbar, S. Mhaisalkar, L. Birkefeld, and K. Goto, "Solid-state gas sensors: A review," *Journal of the Electrochemical Society*, vol. 139, no. 12, pp. 3690–3704, 1992.

[25] K. Toda, T. Koga, J. Kosuge, M. Kashiwagi, H. Oguchi, and T. Arimoto, "Micro gas analyzer measurement of nitric oxide in breath by direct wet scrubbing and fluorescence detection," *Analytical chemistry*, vol. 81, no. 16, pp. 7031–7037, 2009.

[26] T. Maruyama, S. Sasaki, and Y. Saito, "Potentiometric gas sensor for carbon dioxide using solid electrolytes," *Solid State Ionics*, vol. 23, no. 1-2, pp. 107–112, 1987.

[27] J. S. Suehle, R. E. Cavicchi, M. Gaitan, and S. Semancik, "Tin oxide gas sensor fabricated using cmos micro-hotplates and in-situ processing," *IEEE Electron Device Letters*, vol. 14, no. 3, pp. 118–120, 1993.

[28] A. J. Ricco, R. C. Hughes, J. H. Smith, D. J. Moreno, R. P. Manginell, S. D. Senturia, and R. J. Huber, "Calorimetric gas sensor," Nov. 10 1998, uS Patent 5,834,627.

[29] P. Kirchner, J. Oberländer, P. Friedrich, J. Berger, G. Rysstad, M. Keusgen, and M. J. Schöning, "Realisation of a calorimetric gas sensor on polyimide foil for applications in aseptic food industry," *Sensors and Actuators B: Chemical*, vol. 170, pp. 60–66, 2012.

[30] Q. Zhou, D. Kritz, L. Bonnell, and G. H. Sigel, "Porous plastic optical fiber sensor for ammonia measurement," *Applied optics*, vol. 28, no. 11, pp. 2022–2025, 1989.

[31] H. E. Posch and O. S. Wolfbeis, "Optical sensors, 13: fibre-optic humidity sensor based on fluorescence quenching," *Sensors and Actuators*, vol. 15, no. 1, pp. 77–83, 1988.

[32] R. Gvishi and R. Reisfeld, "An investigation of the equilibrium between

various forms of oxazine-170 by means of absorption and fluorescence spectroscopy," *Chemical Physics Letters*, vol. 156, no. 2-3, pp. 181–186, 1989.

[33] Y. Sadaoka, Y. Sakai, and M. Yamada, "Optical properties of sulfonephthalein dyes entrapped within polymer matrices for quantification of ammonia vapour and humidity in air," *Journal of Materials Chemistry*, vol. 3, no. 8, pp. 877–881, 1993.

[34] K. Nakagawa, K. Tanaka, T. Kitagawa, and Y. Sadaoka, "Optochemical hcl gas sensor using substituted tetraphenylporphine–ethylcellulose composite films," *Journal of Materials Chemistry*, vol. 8, no. 5, pp. 1199–1204, 1998.

[35] J. Liu, X. Sun, P. Becla, L. C. Kimerling, and J. Michel, "Towards a ge-based laser for cmos applications," in *Group IV Photonics, 2008 5th IEEE International Conference on*. IEEE, 2008, pp. 16–18.

[36] R. C. Leveson and N. J. Barker, "Selective photoionization gas chromatograph detector," Nov. 1 1983, uS Patent 4,413,185.

[37] W. H. Brattain and J. Bardeen, "Surface properties of germanium," *Bell Labs Technical Journal*, vol. 32, no. 1, pp. 1–41, 1953.

[38] T. Seiyama, A. Kato, K. Fujiishi, and M. Nagatani, "A new detector for gaseous components using semiconductive thin films." *Analytical Chemistry*, vol. 34, no. 11, pp. 1502–1503, 1962.

[39] N. Taguchi, "Method for making a gas-sensing element," Dec. 7 1971, uS Patent 3,625,756.

[40] Y.-J. Choi, I.-S. Hwang, J.-G. Park, K. J. Choi, J.-H. Park, and J.-H. Lee, "Novel fabrication of an sno2 nanowire gas sensor with high sensitivity," *Nanotechnology*, vol. 19, no. 9, p. 095508, 2008.

[41] M.-W. Ahn, K.-S. Park, J.-H. Heo, J.-G. Park, D.-W. Kim, K. J. Choi, J.-H. Lee, and S.-H. Hong, "Gas sensing properties of defect-controlled zno-nanowire gas sensor," *Applied physics letters*, vol. 93, no. 26, p. 263103, 2008.

[42] E. Strelcov, Y. Lilach, and A. Kolmakov, "Gas sensor based on metal- insulator transition in vo2 nanowire thermistor," *Nano letters*, vol. 9, no. 6, pp. 2322–2326, 2009.

[43] U. Yogeswaran and S.-M. Chen, "A review on the electrochemical sensors and biosensors composed of nanowires as sensing material," *Sensors*, vol. 8, no. 1, pp. 290–313, 2008.

[44] J. Chen, L. Xu, W. Li, and X. Gou, "α-fe2o3 nanotubes in gas sensor and lithium-ion battery applications," *Advanced Materials*, vol. 17, no. 5, pp. 582–586, 2005.

[45] F. Schedin, A. Geim, S. Morozov, E. Hill, P. Blake, M. Katsnelson, and K. Novoselov, "Detection of individual gas molecules adsorbed on graphene," *Nature materials*, vol. 6, no. 9, pp. 652–655, 2007.

[46] J. D. Fowler, M. J. Allen, V. C. Tung, Y. Yang, R. B. Kaner, and B. H. Weiller, "Practical chemical sensors from chemically derived graphene," *ACS nano*, vol. 3, no. 2, pp. 301–306, 2009.

[47] B. A. Eckenrode, "The application of an integrated multifunctional field-portable gc/ms system," *Field Analytical Chemistry & Technology*, vol. 2, no. 1, pp. 3–20, 1998.

[48] C.-J. Lu, J. Whiting, R. D. Sacks, and E. T. Zellers, "Portable gas chromatograph with tunable retention and sensor array detection for determination of complex vapor mixtures," *Analytical chemistry*, vol. 75, no. 6, pp. 1400–1409, 2003.

[49] ——, "Portable gas chromatograph with tunable retention and sensor array detection for determination of complex vapor mixtures," *Analytical chemistry*, vol. 75, no. 6, pp. 1400–1409, 2003.

[50] H. Kim, W. H. Steinecker, S. Reidy, G. R. Lambertus, A. A. Astle, K. Najafi, E. T. Zellers, L. P. Bernal, P. D. Washabaugh, and K. D. Wise, "A micropump-driven high-speed mems gas chromatography system," in *Solid-State Sensors, Actuators and Microsystems Conference, 2007. TRANSDUCERS 2007. International*. IEEE, 2007, pp. 1505–1508.

[51] E. T. Zellers, S. Reidy, R. A. Veeneman, R. Gordenker, W. H. Steinecker, G. R. Lambertus, H. Kim, J. A. Potkay, M. P. Rowe, Q. Zhong *et al.*, "An integrated micro-analytical system for complex vapor mixtures," in *Solid-State Sensors, Actuators and Microsystems Conference, 2007. TRANSDUCERS 2007. International*. IEEE, 2007, pp. 1491–1496.

[52] W.-C. Tian, S. W. Pang, C.-J. Lu, and E. T. Zellers, "Microfabricated

preconcentrator-focuser for a microscale gas chromatograph," *Journal of microelectromechanical systems*, vol. 12, no. 3, pp. 264–272, 2003.

[53] Q.-Y. Cai, J. Park, D. Heldsinger, M.-D. Hsieh, and E. T. Zellers, "Vapor recognition with an integrated array of polymer-coated flexural plate wave sensors," *Sensors and Actuators B: Chemical*, vol. 62, no. 2, pp. 121–130, 2000.

[54] E. T. Zellers and M. Han, "Effects of temperature and humidity on the performance of polymer-coated surface acoustic wave vapor sensor arrays," *Analytical chemistry*, vol. 68, no. 14, pp. 2409–2418, 1996.

[55] E. T. Zellers, T.-S. Pan, S. J. Patrash, M. Han, and S. A. Batterman, "Extended disjoint principal-components regression analysis of saw vapor sensor-array responses," *Sensors and Actuators B: Chemical*, vol. 12, no. 2, pp. 123–133, 1993.

[56] M. Westhoff, P. Litterst, L. Freitag, W. Urfer, S. Bader, and J. I. Baumbach, "Ion mobility spectrometry for the detection of volatile organic compounds in exhaled breath of patients with lung cancer: results of a pilot study," *Thorax*, vol. 64, no. 9, pp. 744–748, 2009.

[57] G. A. Eiceman, Z. Karpas, and H. H. Hill Jr, *Ion mobility spectrometry*. CRC press, 2013.

[58] R. Guevremont, "High-field asymmetric waveform ion mobility spectrometry: a new tool for mass spectrometry," *Journal of Chromatography A*, vol. 1058, no. 1, pp. 3–19, 2004.

[59] C. Wu, W. F. Siems, G. R. Asbury, and H. H. Hill, "Electrospray ionization high-resolution ion mobility spectrometry- mass spectrometry," *Analytical chemistry*, vol. 70, no. 23, pp. 4929–4938, 1998.

[60] G. Gillen, C. Mahoney, S. Wight, and R. Lareau, "Characterization of high explosive particles using cluster secondary ion mass spectrometry," *Rapid communications in mass spectrometry*, vol. 20, no. 12, pp. 1949–1953, 2006.

[61] ——, "Characterization of high explosive particles using cluster secondary ion mass spectrometry," *Rapid communications in mass spectrometry*, vol. 20, no. 12, pp. 1949–1953, 2006.

[62] R. R. Syms and S. Wright, "Mems mass spectrometers: the next wave of

miniaturization," *Journal of Micromechanics and Microengineering*, vol. 26, no. 2, p. 023001, 2016.

[63] C. Rossi, D. Esteve, and C. Mingues, "Pyrotechnic actuator: a new generation of si integrated actuator," *Sensors and Actuators A: Physical*, vol. 74, no. 1, pp. 211–215, 1999.

[64] L. J. Guerin, O. Dubochet, J. F. Zeberli, P. Clot, and P. Renaud, "Miniature one-shot valve," in *Proceedings MEMS 98. IEEE. Eleventh Annual International Workshop on Micro Electro Mechanical Systems*, 1998, pp. 425–428.

[65] J. Bejhed, P. Rangsten, and J. Khler, "Demonstration of a single use microsystem valve for high gas pressure applications," *Journal of Micromechanics and Microengineering*, vol. 17, no. 3, p. 472.

[66] J. S. Bunch, S. S. Verbridge, J. S. Alden, A. M. van der Zande, J. M. Parpia, H. G. Craighead, and P. L. McEuen, "Impermeable atomic membranes from graphene sheets," *Nano Letters*, vol. 8, no. 8, pp. 2458–2462, 2008.

[67] A. Khan, J. Philip, and P. Hess, "Youngs modulus of silicon nitride used in scanning force microscope cantilevers," *Journal of Applied Physics*, vol. 95, no. 4, pp. 1667–1672, 2004.

[68] J. Zacharias, "The temperature dependence of young's modulus for nickel," *Physical Review*, vol. 44, no. 2, p. 116, 1933.

[69] L. Malard, M. Pimenta, G. Dresselhaus, and M. Dresselhaus, "Raman spectroscopy in graphene," *Physics Reports*, vol. 473, no. 5, pp. 51–87, 2009.

[70] X. Li, Y. Zhu, W. Cai, M. Borysiak, B. Han, D. Chen, R. D. Piner, L. Colombo, and R. S. Ruoff, "Transfer of large-area graphene films for high-performance transparent conductive electrodes," *Nano Letters*, vol. 9, no. 12, pp. 4359–4363, 2009.

[71] Q. Shao, G. Liu, D. Teweldebrhan, and A. A. Balandin, "High-temperature quenching of electrical resistance in graphene interconnects," *Applied Physics Letters*, vol. 92, no. 20, 2008.

[72] K. S. Novoselov, A. K. Geim, S. V. Morozov, D. Jiang, M. I. Katsnelson, I. V. Grigorieva, S. V. Dubonos, and A. A. Firsov, "Two-dimensional gas of massless dirac fermions in graphene," *Nature*, vol. 438, no. 7065, pp. 197–200, Nov 2005.

[73] F. Xia, D. B. Farmer, Y.-m. Lin, and P. Avouris, "Graphene field-effect transistors with high on/off current ratio and large transport band gap at room temperature," *Nano letters*, vol. 10, no. 2, pp. 715–718, 2010.

[74] S. Y. Zhou, G.-H. Gweon, A. Fedorov, P. First, W. De Heer, D.-H. Lee, F. Guinea, A. Neto, and A. Lanzara, "Substrate-induced band gap opening in epitaxial graphene," *arXiv preprint arXiv:0709.1706*, 2007.

[75] F. T. Vasko and V. Ryzhii, "Voltage and temperature dependencies of conductivity in gated graphene," *Phys. Rev. B*, vol. 76, p. 233404, Dec 2007.

[76] A. A. Balandin, S. Ghosh, W. Bao, I. Calizo, D. Teweldebrhan, F. Miao, and C. N. Lau, "Superior thermal conductivity of single-layer graphene," *Nano letters*, vol. 8, no. 3, pp. 902–907, 2008.

[77] Z. Ni, H. Wang, J. Kasim, H. Fan, T. Yu, Y. Wu, Y. Feng, and Z. Shen, "Graphene thickness determination using reflection and contrast spectroscopy," *Nano letters*, vol. 7, no. 9, pp. 2758–2763, 2007.

[78] J. G. Smits and W.-s. Choi, "The constituent equations of piezoelectric heterogeneous bimorphs," *IEEE transactions on ultrasonics, ferroelectrics, and frequency control*, vol. 38, no. 3, pp. 256–270, 1991.

[79] M. S. Weinberg, "Working equations for piezoelectric actuators and sensors," *Journal of Microelectromechanical Systems*, vol. 8, no. 4, pp. 529–533, 1999.

[80] D. L. DeVoe and A. P. Pisano, "Modeling and optimal design of piezoelectric cantilever microactuators," *Journal of Microelectromechanical systems*, vol. 6, no. 3, pp. 266–270, 1997.

[81] S. Timoshenko, "Analysis of bi-metal thermostats," *JOSA*, vol. 11, no. 3, pp. 233–255, 1925.

[82] W. C. Young and R. G. Budynas, *Roark's formulas for stress and strain*. McGraw-Hill New York, 2002, vol. 7.

[83] D. Thompson and P. Pratt, "The mechanical properties of reaction-sintered silicon nitride," in *Proc. Brit. Ceram. Soc*, vol. 6, 1966, pp. 37–47.

[84] A. Evans and R. Davidge, "The strength and oxidation of reaction-

sintered silicon nitride," *Journal of Materials Science*, vol. 5, no. 4, pp. 314–325, 1970.

[85] B. Merle and M. Göken, "Fracture toughness of silicon nitride thin films of different thicknesses as measured by bulge tests," *Acta Materialia*, vol. 59, no. 4, pp. 1772–1779, 2011.

[86] G. Deeley, J. Herbert, and N. Moore, "Dense silicon nitride," *Powder Metallurgy*, vol. 4, no. 8, pp. 145–151, 1961.

[87] V. Ziebart, O. Paul, and H. Baltes, "Strongly buckled square micromachined membranes," *Journal of Microelectromechanical Systems*, vol. 8, no. 4, pp. 423–432, 1999.

[88] V. Gund, A. Ruyack, S. Ardanuc, and A. Lal, "Graphene one-shot microvalve: Towards vaporizable electronics," in *2015 28th IEEE International Conference on Micro Electro Mechanical Systems (MEMS)*, 2015, pp. 1090–1093.

[89] J. Mueller, C. Marrese, J. Polk, E.-H. Yang, A. Green, V. White, D. Bame, I. Chadraborty, and S. Vargo, "An overview of mems-based micropropulsion developments at jpl," *Acta Astronautica*, vol. 52, no. 9, pp. 881–895, 2003.

[90] V. Gund, A. Ruyack, K. Camera, S. Ardanuc, C. Ober, and A. Lal, "Transient micropackets for silicon dioxide and polymer-based vaporizable electronics," in *2016 IEEE 29th International Conference on Micro Electro Mechanical Systems (MEMS)*, 2016, pp. 1153–1156.

[91] A. T. Evans, S. Chiravuri, and Y. B. Gianchandani, "A multidrug delivery system using a piezoelectrically actuated silicon valve manifold with embedded sensors," *Journal of Microelectromechanical Systems*, vol. 20, no. 1, pp. 231–238, 2011.

[92] S. Mutlu, C. Yu, F. Svec, C. H. Mastrangelo, J. M. Fréchet, and Y. B. Gianchandani, "A thermally responsive polymer microvalve without mechanical parts photo-patterned in a parylene channel," in *TRANSDUCERS, Solid-State Sensors, Actuators and Microsystems, 12th International Conference on, 2003*, vol. 1. IEEE, 2003, pp. 802–805.

[93] S. H. Goodwin-Johansson and G. E. McGuire, "Microelectromechanical flexible membrane electrostatic valve device and related fabrication methods," Jul. 8 2003, uS Patent 6,590,267.

[94] J. Moser, A. Barreiro, and A. Bachtold, "Current-induced cleaning of graphene," *Applied Physics Letters*, vol. 91, no. 16, p. 163513, 2007.

[95] F. M. d'Heurle, "Electromigration and failure in electronics: An introduction," *Proceedings of the IEEE*, vol. 59, no. 10, pp. 1409–1418, 1971.

[96] K. Stokbro, M. Engelund, and A. Blom, "Atomic-scale model for the contact resistance of the nickel-graphene interface," *Physical Review B*, vol. 85, no. 16, p. 165442, 2012.

[97] W. S. Leong, H. Gong, and J. T. Thong, "Low-contact-resistance graphene devices with nickel-etched-graphene contacts," *ACS nano*, vol. 8, no. 1, pp. 994–1001, 2013.

[98] G. Ziegler, J. Heinrich, and G. Wötting, "Relationships between processing, microstructure and properties of dense and reaction-bonded silicon nitride," *Journal of Materials Science*, vol. 22, no. 9, pp. 3041–3086, 1987.

[99] V. Gund, A. Ruyack, S. Ardanuc, and A. Lal, "Graphene one-shot microvalve: Towards vaporizable electronics," in *Micro Electro Mechanical Systems (MEMS), 2015 28th IEEE International Conference on*.

[100] F. Houlihan, F. Bouchard, J. Frechet, and C. Willson, "Thermally depolymerizable polycarbonates. ii: Synthesis of novel linear tertiary copolycarbonates by phase-transfer catalysis," *Macromolecules*, vol. 19, no. 1, pp. 13–19, 1986.

[101] K. L. Camera, B. Wenning, A. Lal, and C. K. Ober, "Transient materials from thermally-sensitive polycarbonates and polycarbonate nanocomposites," *Polymer*, vol. 101, pp. 59–66, 2016.

[102] S. Radhakrishnan and A. Lal, "Alkali metal-wax micropackets for chip-scale atomic clocks," in *Solid-State Sensors, Actuators and Microsystems, 2005. Digest of Technical Papers. TRANSDUCERS'05. The 13th International Conference on*.

[103] A. Ruyack, V. Gund, K. Camera, S. Ardanuç, C. Ober, and A. Lal, "Alkali metal based micro combustion using graphene micro-valve trigger," in *Journal of Physics: Conference Series*, vol. 660, no. 1. IOP Publishing, 2015, p. 012033.

[104] H. Lorenz, M. Despont, N. Fahrni, N. LaBianca, P. Renaud, and P. Vettiger,

"Su-8: a low-cost negative resist for mems," *Journal of Micromechanics and Microengineering*, vol. 7, no. 3, p. 121, 1997.

[105] I. Blakey, A. Yu, J. Blinco, K. S. Jack, H. Liu, M. Leeson, W. Yueh, T. Younkin, and A. K. Whittaker, "Polycarbonate based nonchemically amplified photoresists for extreme ultraviolet lithography," in *SPIE Advanced Lithography*. International Society for Optics and Photonics, 2010, pp. 763 635–763 635.

[106] J. T. Bendler, *Handbook of polycarbonate science and technology*. CRC Press, 1999.

[107] R. Berger, H. Lang, C. Gerber, J. Gimzewski, J. Fabian, L. Scandella, E. Meyer, and H.-J. Güntherodt, "Micromechanical thermogravimetry," *Chemical Physics Letters*, vol. 294, no. 4, pp. 363–369, 1998.

[108] S. Semancik, R. Cavicchi, M. Wheeler, J. Tiffany, G. Poirier, R. Walton, J. Suehle, B. Panchapakesan, and D. DeVoe, "Microhotplate platforms for chemical sensor research," *Sensors and Actuators B: Chemical*, vol. 77, no. 1, pp. 579–591, 2001.

[109] V. Kaajakari, S. Rodgers, and A. Lal, "Ultrasonically driven surface micromachined motor," in *Micro Electro Mechanical Systems, 2000. MEMS 2000. The Thirteenth Annual International Conference on*. IEEE, 2000, pp. 40–45.

[110] K. S. Novoselov, A. K. Geim, S. V. Morozov, D. Jiang, Y. Zhang, S. V. Dubonos, I. V. Grigorieva, and A. A. Firsov, "Electric field effect in atomically thin carbon films," *science*, vol. 306, no. 5696, pp. 666–669, 2004.

[111] V. Georgakilas, M. Otyepka, A. B. Bourlinos, V. Chandra, N. Kim, K. C. Kemp, P. Hobza, R. Zboril, and K. S. Kim, "Functionalization of graphene: covalent and non-covalent approaches, derivatives and applications," *Chemical reviews*, vol. 112, no. 11, pp. 6156–6214, 2012.

[112] K. F. Graff, *Wave motion in elastic solids*. Courier Corporation, 2012.

[113] V. Kaajakari *et al.*, "Practical mems: Design of microsystems, accelerometers, gyroscopes, rf mems, optical mems, and microfluidic systems," *Las Vegas, NV: Small Gear Publishing*, 2009.

[114] B. KRYCZKA and C. G. WILLSON, "Thermally depolymerizable polycarbonates v. acid catalyzed thermolysis of allylic and benzylic polycarbon-

ates: a new route to resist imaging," *Polymer Journal*, vol. 19, no. 1, pp. 31–49, 1987.

[115] J. Moser, A. Barreiro, and A. Bachtold, "Current-induced cleaning of graphene," *Applied Physics Letters*, vol. 91, no. 16, p. 163513, 2007.

[116] S. Lee, B. Koo, J.-G. Park, H. Moon, J. Hahn, and J. M. Kim, "Development of high-performance organic thin-film transistors for large-area displays," *MRS bulletin*, vol. 31, no. 6, pp. 455–459, 2006.

[117] T. Someya, Y. Kato, T. Sekitani, S. Iba, Y. Noguchi, Y. Murase, H. Kawaguchi, and T. Sakurai, "Conformable, flexible, large-area networks of pressure and thermal sensors with organic transistor active matrixes," *Proceedings of the National Academy of Sciences of the United States of America*, vol. 102, no. 35, pp. 12 321–12 325, 2005.

[118] A. Schmitz, P. Maiolino, M. Maggiali, L. Natale, G. Cannata, and G. Metta, "Methods and technologies for the implementation of large-scale robot tactile sensors," *IEEE Transactions on Robotics*, vol. 27, no. 3, pp. 389–400, 2011.

[119] S. Park, H. Kim, M. Vosgueritchian, S. Cheon, H. Kim, J. H. Koo, T. R. Kim, S. Lee, G. Schwartz, H. Chang *et al.*, "Stretchable energy-harvesting tactile electronic skin capable of differentiating multiple mechanical stimuli modes," *Advanced Materials*, vol. 26, no. 43, pp. 7324–7332, 2014.

[120] G. Yu, J. Gao, J. C. Hummelen, F. Wudl, and A. J. Heeger, "Polymer photovoltiac cells: Enhanced efficiencies via a network of internal donor-acceptor heterojunctions," *Science*, vol. 270, no. 5243, p. 1789, 1995.

[121] A. C. Mayer, S. R. Scully, B. E. Hardin, M. W. Rowell, and M. D. McGehee, "Polymer-based solar cells," *Materials today*, vol. 10, no. 11, pp. 28–33, 2007.

[122] D.-H. Kim, J.-H. Ahn, W. M. Choi, H.-S. Kim, T.-H. Kim, J. Song, Y. Y. Huang, Z. Liu, C. Lu, and J. A. Rogers, "Stretchable and foldable silicon integrated circuits," *Science*, vol. 320, no. 5875, pp. 507–511, 2008.

[123] D.-H. Kim, R. Ghaffari, N. Lu, and J. A. Rogers, "Flexible and stretchable electronics for biointegrated devices," *Annual review of biomedical engineering*, vol. 14, pp. 113–128, 2012.

[124] H. C. Ko, M. P. Stoykovich, J. Song, V. Malyarchuk, W. M. Choi, C.-J. Yu, J. B. Geddes Iii, J. Xiao, S. Wang, Y. Huang *et al.*, "A hemispherical electronic eye camera based on compressible silicon optoelectronics," *Nature*, vol. 454, no. 7205, pp. 748–753, 2008.

[125] S. R. Forrest, "The path to ubiquitous and low-cost organic electronic appliances on plastic," *Nature*, vol. 428, no. 6986, pp. 911–918, 2004.

[126] E. Menard, K. Lee, D.-Y. Khang, R. Nuzzo, and J. Rogers, "A printable form of silicon for high performance thin film transistors on plastic substrates," *Applied Physics Letters*, vol. 84, no. 26, pp. 5398–5400, 2004.

[127] Y. Chen, H. Li, and M. Li, "Flexible and tunable silicon photonic circuits on plastic substrates," *Scientific reports*, vol. 2, 2012.

[128] E. Biham and A. Shamir, *Differential cryptanalysis of the data encryption standard*. Springer Science & Business Media, 2012.

[129] S.-W. Hwang, D.-H. Kim, H. Tao, T.-i. Kim, S. Kim, K. J. Yu, B. Panilaitis, J.-W. Jeong, J.-K. Song, F. G. Omenetto, and J. A. Rogers, "Materials and fabrication processes for transient and bioresorbable high-performance electronics," *Advanced Functional Materials*, vol. 23, no. 33, 2013.

[130] M. Sisko, "Robotic aerial vehicle delivery system and method," Dec. 9 2014, uS Patent App. 14/565,348.

[131] X. Li, W. Cai, J. An, S. Kim, J. Nah, D. Yang, R. Piner, A. Velamakanni, I. Jung, E. Tutuc *et al.*, "Large-area synthesis of high-quality and uniform graphene films on copper foils," *Science*, vol. 324, no. 5932, pp. 1312–1314, 2009.

[132] Q. Zhu, Y. Z. Meng, S. C. Tjong, X. S. Zhao, and Y. L. Chen, "Thermally stable and high molecular weight poly (propylene carbonate) s from carbon dioxide and propylene oxide," *Polymer international*, vol. 51, no. 10, pp. 1079–1085, 2002.

[133] P. Song, M. Xiao, F. Du, S. Wang, L. Gan, G. Liu, and Y. Meng, "Synthesis and properties of aliphatic polycarbonates derived from carbon dioxide, propylene oxide and maleic anhydride," *Journal of applied polymer science*, vol. 109, no. 6, pp. 4121–4129, 2008.

[134] Z. Zhang, J.-H. Lee, S.-H. Lee, S.-B. Heo, and C. U. Pittman, "Morphology,

thermal stability and rheology of poly (propylene carbonate)/organoclay nanocomposites with different pillaring agents," *Polymer*, vol. 49, no. 12, pp. 2947–2956, 2008.

[135] H. Yan, W. R. Cannon, and D. J. Shanefield, "Thermal decomposition behaviour of poly (propylene carbonate)," *Ceramics international*, vol. 24, no. 6, pp. 433–439, 1998.

[136] H. A. Reed, C. E. White, V. Rao, S. A. B. Allen, C. L. Henderson, and P. A. Kohl, "Fabrication of microchannels using polycarbonates as sacrificial materials," *Journal of Micromechanics and Microengineering*, vol. 11, no. 6, p. 733, 2001.

[137] J. P. Jayachandran, H. A. Reed, H. Zhen, L. F. Rhodes, C. L. Henderson, S. B. Allen, and P. A. Kohl, "Air-channel fabrication for microelectromechanical systems via sacrificial photosensitive polycarbonates," *Journal of Microelectromechanical Systems*, vol. 12, no. 2, pp. 147–159, 2003.

[138] J. Chen, Y. Hu, Y.-C. Chen, R. Saha, R. Bashirullah, and P. Kohl, "Air cavity low-loss transmission lines for high speed serial link applications," in *Electronic Components and Technology Conference (ECTC), 2011 IEEE 61st*. IEEE, 2011, pp. 2146–2151.

[139] C. Huang, Q. Chen, D. Wu, and Z. Wang, "Implementation of air-gap through-silicon-vias (tsvs) using sacrificial technology," *IEEE Transactions on Components, Packaging and Manufacturing Technology*, vol. 3, no. 8, pp. 1430–1438, 2013.

[140] M. G. Cupta, P. J. Joseph, and P. A. Kohl, "Photoacid generators for catalytic decomposition of polycarbonate," *Journal of applied polymer science*, vol. 105, no. 5, pp. 2655–2662, 2007.

[141] O. Phillips, J. M. Schwartz, and P. A. Kohl, "Thermal decomposition of poly (propylene carbonate): End-capping, additives, and solvent effects," *Polymer Degradation and Stability*, vol. 125, pp. 129–139, 2016.

[142] T. J. Spencer and P. A. Kohl, "Decomposition of poly (propylene carbonate) with uv sensitive iodonium salts," *Polymer degradation and stability*, vol. 96, no. 4, pp. 686–702, 2011.

[143] M. N. Ozisik, *Heat conduction*. John Wiley & Sons, 1993.

[144] E. Sartori, "Convection coefficient equations for forced air flow over flat surfaces," *Solar Energy*, vol. 80, no. 9, pp. 1063–1071, 2006.

[145] J. Tao, C. Song, M. Cao, D. Hu, L. Liu, N. Liu, and S. Wang, "Thermal properties and degradability of poly (propylene carbonate)/poly (β-hydroxybutyrate-co-β-hydroxyvalerate)(ppc/phbv) blends," *Polymer Degradation and Stability*, vol. 94, no. 4, pp. 575–583, 2009.

[146] A. A. Balandin, S. Ghosh, W. Bao, I. Calizo, D. Teweldebrhan, F. Miao, and C. N. Lau, "Superior thermal conductivity of single-layer graphene," *Nano letters*, vol. 8, no. 3, pp. 902–907, 2008.

[147] Z. Ni, H. Wang, J. Kasim, H. Fan, T. Yu, Y. Wu, Y. Feng, and Z. Shen, "Graphene thickness determination using reflection and contrast spectroscopy," *Nano letters*, vol. 7, no. 9, pp. 2758–2763, 2007.

[148] K. L. Camera, B. Wenning, A. Lal, and C. K. Ober, "Transient materials from thermally-sensitive polycarbonates and polycarbonate nanocomposites," *Polymer*, vol. 101, pp. 59–66, 2016.

[149] "Graphene supermarket website," https://graphene-supermarket.com/Multilayer-Graphene-on-285-nm-Silicon-Dioxide-Wafer-5-pack.html, 2017.

[150] H. Hosseinzadegan, C. Todd, A. Lal, M. Pandey, M. Levendorf, and J. Park, "Graphene has ultra high piezoresistive gauge factor," in *Micro Electro Mechanical Systems (MEMS), 2012 IEEE 25th International Conference on*. IEEE, 2012, pp. 611–614.

[151] S.-H. Bae, Y. Lee, B. K. Sharma, H.-J. Lee, J.-H. Kim, and J.-H. Ahn, "Graphene-based transparent strain sensor," *Carbon*, vol. 51, pp. 236–242, 2013.

[152] C. Yan, J. Wang, W. Kang, M. Cui, X. Wang, C. Y. Foo, K. J. Chee, and P. S. Lee, "Highly stretchable piezoresistive graphene–nanocellulose nanopaper for strain sensors," *Advanced materials*, vol. 26, no. 13, pp. 2022–2027, 2014.

[153] M. Hempel, D. Nezich, J. Kong, and M. Hofmann, "A novel class of strain gauges based on layered percolative films of 2d materials," *Nano letters*, vol. 12, no. 11, pp. 5714–5718, 2012.

[154] E. S. Leland, E. M. Lai, and P. K. Wright, "A self-powered wireless sensor for indoor environmental monitoring," in *Wireless Networking Symposium, University of Texas at Austin Department of Electrical & Computer Engineering*, 2004.

[155] K. Owen, B. VanDerElzen, R. Peterson, and K. Najafi, "High aspect ratio deep silicon etching," in *Micro Electro Mechanical Systems (MEMS), 2012 IEEE 25th International Conference on*. IEEE, 2012, pp. 251–254.

[156] J. Yeom, Y. Wu, J. C. Selby, and M. A. Shannon, "Maximum achievable aspect ratio in deep reactive ion etching of silicon due to aspect ratio dependent transport and the microloading effect," *Journal of Vacuum Science & Technology B: Microelectronics and Nanometer Structures Processing, Measurement, and Phenomena*, vol. 23, no. 6, pp. 2319–2329, 2005.

[157] V. Gund, A. Ruyack, A. Leonardi, K. Vinayakumar, C. Ober, and A. Lal, "Individually detachable polymer-silicon micro-parts for vaporizable electronics," in *Solid-State Sensors, Actuators and Microsystems (TRANSDUCERS), 2017 Transducers: The 19th International Conference on*. IEEE, 2017.

[158] V. Gund, A. Ruyack, S. Ardanuc, and A. Lal, "Graphene one-shot microvalve: Towards vaporizable electronics," in *Micro Electro Mechanical Systems (MEMS), 2015 28th IEEE International Conference on*. IEEE, 2015, pp. 1090–1093.

[159] V. Gund, A. Ruyack, K. Camera, S. Ardanuc, C. Ober, and A. Lal, "Multimodal graphene polymer interface characterization platform for vaporizable electronics," in *Micro Electro Mechanical Systems (MEMS), 2015 28th IEEE International Conference on*. IEEE, 2015, pp. 873–876.

[160] K. Stokbro, M. Engelund, and A. Blom, "Atomic-scale model for the contact resistance of the nickel-graphene interface," *Physical Review B*, vol. 85, no. 16, p. 165442, 2012.

[161] W. S. Leong, H. Gong, and J. T. Thong, "Low-contact-resistance graphene devices with nickel-etched-graphene contacts," *ACS nano*, vol. 8, no. 1, pp. 994–1001, 2013.

[162] F. A. Doljack and R. Hoffman, "The origins of stress in thin nickel films," *Thin Solid Films*, vol. 12, no. 1, pp. 71–74, 1972.

[163] A. C. Fischer, F. Forsberg, M. Lapisa, S. J. Bleiker, G. Stemme, N. Roxhed, and F. Niklaus, "Integrating mems and ics," *arXiv preprint arXiv:1604.04843*, 2016.

[164] A. Dey, A. Avendanno, S. Venugopal, D. R. Allee, M. Quevedo, and B. Gnade, "Cmos tft op-amps: Performance and limitations," *IEEE Electron Device Letters*, vol. 32, no. 5, pp. 650–652, 2011.

[165] W. Honda, T. Arie, S. Akita, and K. Takei, "Mechanically flexible and high-performance cmos logic circuits," *Scientific reports*, vol. 5, 2015.

[166] Y. Kuo, "Thin film transistor technologypast, present, and future," *The Electrochemical Society Interface*, vol. 22, no. 1, pp. 55–61, 2013.

[167] S. Gowrisanker, M. Quevedo-Lopez, H. Alshareef, B. Gnade, S. Venugopal, R. Krishna, K. Kaftanoglu, and D. Allee, "A novel low temperature integration of hybrid cmos devices on flexible substrates," *Organic electronics*, vol. 10, no. 7, pp. 1217–1222, 2009.

[168] K. Fischer, M. Agostinelli, C. Allen, D. Bahr, M. Bost, P. Charvat, V. Chikarmane, Q. Fu, C. Ganpule, M. Haran *et al.*, "Low-k interconnect stack with multi-layer air gap and tri-metal-insulator-metal capacitors for 14nm high volume manufacturing," in *Interconnect Technology Conference and 2015 IEEE Materials for Advanced Metallization Conference (IITC/MAM), 2015 IEEE International*. IEEE, 2015, pp. 5–8.

[169] O. Tufte and E. Stelzer, "Piezoresistive properties of silicon diffused layers," *Journal of Applied Physics*, vol. 34, no. 2, pp. 313–318, 1963.

[170] J.-W. Jiang, J.-S. Wang, and B. Li, "Youngs modulus of graphene: a molecular dynamics study," *Physical Review B*, vol. 80, no. 11, p. 113405, 2009.

[171] Q. Shao, G. Liu, D. Teweldebrhan, and A. Balandin, "High-temperature quenching of electrical resistance in graphene interconnects," *Applied Physics Letters*, vol. 92, no. 20, p. 202108, 2008.

[172] X. Chen, D. Akinwande, K.-J. Lee, G. F. Close, S. Yasuda, B. C. Paul, S. Fujita, J. Kong, and H.-S. P. Wong, "Fully integrated graphene and carbon nanotube interconnects for gigahertz high-speed cmos electronics," *IEEE Transactions on Electron Devices*, vol. 57, no. 11, pp. 3137–3143, 2010.

[173] R.-H. Kim, M.-H. Bae, D. G. Kim, H. Cheng, B. H. Kim, D.-H. Kim, M. Li,

J. Wu, F. Du, H.-S. Kim *et al.*, "Stretchable, transparent graphene interconnects for arrays of microscale inorganic light emitting diodes on rubber substrates," *Nano letters*, vol. 11, no. 9, pp. 3881–3886, 2011.

[174] A. Isacsson, A. W. Cummings, L. Colombo, L. Colombo, J. M. Kinaret, and S. Roche, "Scaling properties of polycrystalline graphene: a review," *2D Materials*, vol. 4, no. 1, p. 012002, 2016.

[175] S.-E. Zhu, M. Krishna Ghatkesar, C. Zhang, and G. Janssen, "Graphene based piezoresistive pressure sensor," *Applied Physics Letters*, vol. 102, no. 16, p. 161904, 2013.

[176] K. Wise and N. Najafi, "The coming opportunities in microsensor systems," in *Solid-State Sensors and Actuators, 1991. Digest of Technical Papers, TRANSDUCERS'91., 1991 International Conference on*. IEEE, 1991, pp. 2–7.

[177] S.-I. Ohira and K. Toda, "Micro gas analyzers for environmental and medical applications," *Analytica Chimica Acta*, vol. 619, no. 2, pp. 143–156, 2008.

[178] J. A. Diaz, C. F. Giese, and W. R. Gentry, "Sub-miniature exb sector-field mass spectrometer," *Journal of the American Society for Mass Spectrometry*, vol. 12, no. 6, pp. 619–632, 2001.

[179] C.-M. Tassetti, R. Mahieu, J.-S. Danel, O. Peyssonneaux, F. Progent, J.-P. Polizzi, X. Machuron-Mandard, and L. Duraffourg, "A mems electron impact ion source integrated in a microtime-of-flight mass spectrometer," *Sensors and Actuators B: Chemical*, vol. 189, pp. 173–178, 2013.

[180] M. Reiser, *Theory and design of charged particle beams*. John Wiley & Sons, 2008.

[181] S. Humphries, *Charged particle beams*. Courier Corporation, 2013.

[182] H. Revercomb and E. A. Mason, "Theory of plasma chromatography/-gaseous electrophoresis. review," *Analytical Chemistry*, vol. 47, no. 7, pp. 970–983, 1975.

[183] M. Utriainen, E. Kärpänoja, and H. Paakkanen, "Combining miniaturized ion mobility spectrometer and metal oxide gas sensor for the fast detection of toxic chemical vapors," *Sensors and Actuators B: Chemical*, vol. 93, no. 1, pp. 17–24, 2003.

[184] R. Cumeras, I. Gracia, P. Ivanov, N. Sabate, and C. Cane, "Comsol simulation of acetone ions in planar ion mobility spectrometer," in *Electron Devices, 2009. CDE 2009. Spanish Conference on*. IEEE, 2009, pp. 323–326.

[185] R. Duggirala, R. G. Polcawich, M. Dubey, and A. Lal, "Radioisotope thin-film fueled microfabricated reciprocating electromechanical power generator," *Journal of Microelectromechanical systems*, vol. 17, no. 4, pp. 837–849, 2008.

[186] R. S. Jayashree, L. Gancs, E. R. Choban, A. Primak, D. Natarajan, L. J. Markoski, and P. J. Kenis, "Air-breathing laminar flow-based microfluidic fuel cell," *Journal of the American Chemical Society*, vol. 127, no. 48, pp. 16 758–16 759, 2005.

[187] S. M. Wait, S. Basak, S. V. Garimella, and A. Raman, "Piezoelectric fans using higher flexural modes for electronics cooling applications," *IEEE transactions on components and packaging technologies*, vol. 30, no. 1, pp. 119–128, 2007.

[188] B. R. Munson, D. F. Young, and T. H. Okiishi, "Fundamentals of fluid mechanics," *New York*, vol. 3, no. 4, 1990.

[189] R. J. Linderman, P. E. Kladitis, and V. M. Bright, "Development of the micro rotary fan," *Sensors and Actuators A: Physical*, vol. 95, no. 2, pp. 135–142, 2002.

[190] H. Kim, A. A. Astle, K. Najafi, L. P. Bernal, and P. D. Washabaugh, "A fully integrated high-efficiency peristaltic 18-stage gas micropump with active microvalves," in *Micro Electro Mechanical Systems, 2007. MEMS. IEEE 20th International Conference on*. IEEE, 2007, pp. 131–134.

[191] R. J. Linderman, O. Nilsen, and V. M. Bright, "The resonant micro fan gas pump for active breathing microchannels," in *TRANSDUCERS, Solid-State Sensors, Actuators and Microsystems, 12th International Conference on, 2003*, vol. 2. IEEE, 2003, pp. 1923–1926.

[192] V. Gund, S. Ardanuc, Y. Shi, and A. Lal, "Low-voltage (¡ 5v) ion-mobility spectrometer array for label-free gas detection," in *Solid-State Sensors, Actuators and Microsystems (TRANSDUCERS & EUROSENSORS XXVII), 2013 Transducers & Eurosensors XXVII: The 17th International Conference on*. IEEE, 2013, pp. 2767–2770.

[193] A. Ihara and H. Watanabe, "On the flow around flexible plates, oscillating with large amplitude," *Journal of Fluids and Structures*, vol. 8, no. 7, pp. 601–619, 1994.

[194] M. Toda, "Theory of air flow generation by a resonant type pvf2 bimorph cantilever vibrator," *Ferroelectrics*, vol. 22, no. 1, pp. 911–918, 1978.

[195] T. I. et al., "Analog rf mems attenuator with pzt actuators," in *Solid-State Sensors, Actuators and Microsystems (TRANSDUCERS & EUROSENSORS XXVII), 2013 Transducers & Eurosensors XXVII: The 17th International Conference on*. IEEE, 2013, pp. 2767–2770.

[196] D. L. DeVoe and A. P. Pisano, "Modeling and optimal design of piezoelectric cantilever microactuators," *Journal of Microelectromechanical systems*, vol. 6, no. 3, pp. 266–270, 1997.

[197] G.-T. Park, J.-J. Choi, J. Ryu, H. Fan, and H.-E. Kim, "Measurement of piezoelectric coefficients of lead zirconate titanate thin films by strain-monitoring pneumatic loading method," *Applied Physics Letters*, vol. 80, no. 24, pp. 4606–4608, 2002.

[198] R. B. Cole, "Electrospray ionization mass spectrometry: fundamentals, instrumentation, and applications," in *Electrospray ionization mass spectrometry: fundamentals, instrumentation, and applications*. Wiley-Interscience, 1997.

[199] B. Rosenblum, P. Bräunlich, and J. Carrico, "Thermally stimulated field emission from pyroelectric linbo3," *Applied physics letters*, vol. 25, no. 1, pp. 17–19, 1974.

[200] M. E. Lines and A. M. Glass, *Principles and applications of ferroelectrics and related materials*. Oxford university press, 1977.

[201] J. A. Geuther and Y. Danon, "Electron and positive ion acceleration with pyroelectric crystals," *Journal of applied physics*, vol. 97, no. 7, p. 074109, 2005.

[202] E. L. Neidholdt and J. Beauchamp, "Compact ambient pressure pyroelectric ion source for mass spectrometry," *Analytical chemistry*, vol. 79, no. 10, pp. 3945–3948, 2007.

[203] F. Paschen, "On the potential difference required for spark initiation in air,

hydrogen, and carbon dioxide at different pressures," *Annalen der Physik*, vol. 273, no. 5, pp. 69–75, 1889.